INVESTIGATIONS ON NaCl PARTICLE TEMPLATING METHOD FOR THE PREPARATION OF MICROCELLULAR CARBON AND SILICON CARBIDE FOAMS

A Thesis submitted
in partial fulfilment for the Degree of

Doctor of Philosophy

by

PRAVEEN WILSON

Department of Chemistry
INDIAN INSTITUTE OF SPACE SCIENCE AND TECHNOLOGY
Thiruvananthapuram – 695 547

June, 2020

To my mother & father,

my brothers,

and my friends…

CERTIFICATE

This is to certify that the thesis entitled **Investigations on NaCl particle templating method for the preparation of microcellular carbon and silicon carbide foams**, submitted by Praveen Wilson, to the Indian Institute of Space Science and Technology, Thiruvananthapuram, in partial fulfilment for the award of the degree of **Doctor of Philosophy**, is a *bona fide* record of research work carried out by him under my supervision. The contents of this thesis, in full or in parts, have not been submitted to any other Institution or University for the award of any degree or diploma.

Prof. K Prabhakaran
Supervisor
Professor
Department of Chemistry

Thiruvananthapuram

Counter signature of HOD with seal

June, 2020

DECLARATION

I declare that this thesis entitled **Investigations on NaCl particle templating method for the preparation of microcellular carbon and silicon carbide foams** submitted in partial fulfilment of the degree of **Doctor of Philosophy** is a record of original work carried out by me under the supervision of Prof. K. Prabhakaran, and has not formed the basis for the award of any other degree or diploma, in this or any other Institution or University. In keeping with the ethical practice in reporting scientific information, due acknowledgements have been made wherever the findings of others have been cited.

Thiruvananthapuram
June 2020

Praveen Wilson
SC15D007

ACKNOWLEDGEMENTS

I express my sincere gratitude to my guide, Prof. K. Prabhakaran, for giving me an opportunity to work in his group. His guidance and encouragement were the foundations of this thesis work. His wealth of knowledge, passion towards research and his work ethics have been sources of great inspiration to me and which I sincerely wish to emulate in my professional career.

I also take this opportunity to thank Dr. V. K. Dadhwal, Director, IIST, for providing all facilities to carry out my research. It is also a pleasure to extend my heartfelt gratitude to Prof. Kuruvilla Joseph, Dean (Student Activities, Student Welfare and Outreach) for his encouragement and kindness. I would like to thank all my doctoral committee members, Dr. Ilangovan (VSSC), Dr. Roy Joseph (SCTIMST), Dr. T.P.D Rajan (CSIR-NIIST), Prof. Parag Bhargava (IIT-Bombay), Dr. Bijudas C.R. (IIST), Prof. Nirmala R. James (IIST) and Dr. K. Y. Sandhya (IIST) for their valuable suggestions and encouragement in improving the quality of the thesis work. I thank the faculty members of the Department of Chemistry for their support. I am grateful to the members of VSSC, NIIST, SCTIMST, SAIF IIT-Madras, NCESS, Kerala University and Cochin University for helping in the characterization of my samples. I thank Dr. Sreeja Remani (ICMPD, VSSC) for sharing her lab resources and helping in processing of materials. I also thank Mrs. Aparna and Dr. Dijith (NIIST) for helping me with characterization.

I am grateful to my friends, Dr. Sujith Vijayan and Dr. Linsha Vazhayal for their help in my experimental work and for their fruitful discussions in writing this thesis. I am also thankful to Mr. Rakesh Krishnan P.P., Mrs. Chithra A., Dr. R. Narasimman, and Mr. Neeraj V.S., former and current members of my group, for their support during my tenure in IIST. I thank all my fellow research scholars for their love and support. I am thankful to have received assistance from valued members of the staff, Mr. Loveson Albert, Mrs. Bindu J.M., Mrs. Jayasree R, Mrs. Jayasree L and Mrs. Bindhu P.C.

I am forever indebted to my parents, brothers and sister for their endless love and encouragement. Words cannot express my love and affection towards my family for their

patience through the journey of my research work. I am blessed to have friends who have been a constant source of encouragement and support. I wish to extend my heartfelt gratitude to them for always being there for me. I thank each and everyone one who helped and inspired me in the last five years.

ABSTRACT

Carbon and silicon carbon (SiC) foams are three-dimensional porous materials comprising of uniformly dispersed pores within a solid matrix and porosity greater than 70%. Carbon foams are prepared from petroleum and coal tar pitches, synthetic polymers and natural organic molecules. They possess low density, tunable thermal and electrical and thermal conductivity, high specific surface area, chemical inertness, high permeability and electromagnetic interference (EMI) shielding. They find application in fields such as thermal insulation, thermal protection, gas and pollutant absorption, electrochemical devices, EMI shielding and catalysis. SiC foams are prepared from pre-ceramic polymers and aqueous suspensions. Properties of SiC foams include good oxidation resistance, high surface area, high permeability, high-temperature stability, excellent dielectric property, chemical inertness and high specific strength. Applications of SiC foams include catalyst support, hot-gas and molten metal filtration, membrane supports, gas-burner medium, lightweight structural parts for high-temperature applications and high-temperature EMI shielding materials. The properties of the foams depend on the porosity and pore size. Conventionally prepared foams possess large cells of size greater than 500 μm. To improve the mechanical and thermal insulation properties it is necessary to reduce the cell size. The main objective of this thesis is to produce and characterize carbon and SiC foams with microcellular (<100) microstructure through NaCl particle templating of molten sucrose resin. The porosity of the foams is tuned by varying the NaCl particle concentration.

A compression moulding process for the preparation of carbon foams with a triplex pore structure is studied. Pastes with mouldable consistency, prepared by hot-blending of sucrose-NaCl powder mixtures of NaCl to sucrose weight ratios ($\mathbf{W}_{N/S}$) in the range of 0.7 to 1.2, are set into solid bodies due to the caramelization of molten sucrose. The caramelization in presence of NaCl results in carbon-enriched polymeric structure due to the enhanced α-elimination reactions along with the –OH condensation as evidenced from the torque-time measurements, IR, TGA and elemental analysis. The pyrolysis of compression moulded bodies, followed by NaCl removal and further heat treatment produces carbon foams with a triplex pore structure. The volumetric shrinkage

during carbonization (28.5 to 24.2 vol.%), density (0.26 to 0.33 g cm^{-3}), compressive strength (2.84 to 8.37 MPa), Young's modulus (170 to 370 MPa) and thermal conductivity (0.348 to 0.257 W m^{-1} K^{-1}) of the carbon foams depend on the $\mathbf{W_{N/S}}$. The carbon foams exhibit high specific surface area of ~400 m^2 g^{-1} and a combination of macropores (414 to 70 μm), microcells (2 to 12 μm) and micropore texture.

Low-density microcellular carbon foams are prepared at $\mathbf{W_{N/S}}$ of 1.5 to 3 by using glycerol as a plasticizing additive. The glycerol required to form a mouldable paste increases from 8 to 64 g (per 100 g of sucrose) with an increase in $\mathbf{W_{N/S}}$. The slow setting of the pastes (5 – 13h) is due to the caramelization of molten sucrose as well as the slow evaporation of glycerol. The linear and volumetric shrinkages during carbonization of sucrose polymer-NaCl-glycerol composites lie in the range of 3.64 to 7.62% and 10.02 to 20.65%, respectively. The carbon-NaCl composites have adequate compressive strength (6.9 to 17.8 MPa) and ductility for machining using conventional machine tools. Machining of the carbon-NaCl composites followed by NaCl removal is used as a strategy to produce low-density carbon foams with desired contours. The glycerol not only decreases the density of carbon foams developed from the sucrose-NaCl system but also produces a remarkable change in the foam microstructure from a combination of macropores and microcells to only microcells of sizes predominantly in the range of 3 to 6 μm. Microcellular carbon foams prepared at $\mathbf{W_{N/S}}$ in the range of 1.5 to 3 show density, compressive strength, thermal conductivity and EMI shielding effectiveness in the ranges of 0.096 to 0.214 g cm^{-3}, 0.60 to 4.83 MPa, 0.087 to 0.235 W m^{-1} K^{-1} and 24.7 to 41.7 dB, respectively.

Thermally conducting microcellular carbon foams are prepared from sucrose with graphite as a conducting filler, NaCl particles as template and glycerol as plasticizing additive. The effect of graphite filler and NaCl template loading on density, porosity, thermal conductivity, and microstructure are carefully investigated. Microcellular conducting carbon foams (**MCCF**) exhibit high porosity (76.1 to 93.4 %) and adequate compressive strength (0.225 to 14.96 MPa). The high thermal conductivity (0.282 to 5.23 W m^{-1} K^{-1}), interconnected microcellular structure (cell size 2-12 μm) and hydrophobic nature make the foams ideal for hosting wax-based phase change materials for thermal energy storage and management applications. Composites of conducting carbon foam and paraffin wax (**PW**) are prepared with various wax loadings (50.5 to 82.6 wt%) which exhibit thermal conductivities in the range of 0.65 to 7.72 W m^{-1} K^{-1}. The melting and freezing characteristics and form stability of the composites are also studied. It is established that the microcellular structure is advantageous for easy wax-impregnation and retention during thermal cycling compared to macrocellular (cell size of 600 μm) foams of similar composition due to the enhanced capillary forces. Differential scanning calorimetry (DSC) study of **PW/MCCF** composites shows the highest melting enthalpy of 110.9 J g^{-1}.

Microcellular SiC foams (**MSiCFs**) are produced by the thermal setting of dispersions of silicon and NaCl powders in molten sucrose-glycerol solutions in a mould followed by carbonization, NaCl removal and reaction bonding at 1500 °C. The NaCl to sucrose weight ratio is varied from 1 to 3 to tune the porosity of the **MSiCFs**. The acidic silica layer on silicon particle surface catalyses the setting of the pastes by –OH condensation leading to setting times in the range of 1 to 3 h. The linear and volumetric shrinkages of sucrose polymer-silicon-NaCl composite bodies during carbonization at 750 °C, decrease from 4 to 1.36 % and 10.8 to 5%, respectively, when the NaCl to sucrose weight ratio increases from 1 to 3. Only a marginal linear and volumetric shrinkage of 0.2 to 2.3% and 1.17 to 7.7%, respectively, is observed during reaction bonding. The microcell size varies between 2 to 22 μm and are filled with SiC nanowires grown *in situ* by a catalyst-free vapour-solid (VS) mechanism. The **MSiCFs** with porosity in the range of 86.8 to 91.1 vol.% exhibit thermal conductivity and compressive strength in the ranges of 0.334 to 0.758 W m^{-1} K^{-1} and 0.97 to 2.38 MPa, respectively. The **MSiCFs** show excellent EMI shielding property in the X-band frequency region enhanced by the *in situ* grown SiC nanowires within microcells. The **MSiCFs** show highest EMI shielding effectiveness of 45.6 dB and specific shielding effectiveness of 137 dB g^{-1} cm^3.

TABLE OF CONTENTS

LIST OF TABLES

LIST OF FIGURES

ABBREVIATIONS

APCVD	Ambient Pressure Chemical Vapour Deposition
BET	Brunauer, Emmett and Teller
CVD	Chemical Vapour Deposition
CVI	Chemical Vapour Infiltration
CNF	Carbon Nanofiber
CNT	Carbon Nanotube
DSC	Differential Scanning Calorimetry
EDX	Energy Dispersive Spectroscopy
EMI	Electromagnetic Interference
FTIR	Fourier Transform Infrared Spectroscopy
GO	Graphene oxide
HIPE	High Internal Phase Emulsion
MCCF	Microcellular Conducting Carbon Foam
MSiCF	Microcellular Silicon carbide Foams
MWCNT	Multi-walled Carbon Nanotube
NASA	National Aerospace Agency
NLDFT	Non-linear Density Functional Theory
PAN	Polyacrylonitrile
PCM	Phase Change Material
PEO	Poly (ethylene oxide)
PMMA	Polymethyl methacrylate
PPO	Poly (propylene oxide)
PSD	Pore Size Distribution
PU	Polyurethane
PW	Paraffin Wax
RGO	Reduced graphene oxide
RPM	Rotations Per Minute
SEM	Scanning Electron Microscope

SF	Stacking Fault
TCR	Temperature Coefficient of Resistance
TEOS	Tetraethyl orthosilicate
TEM	Transmission Electron Microscope
TGA	Thermogravimetric Analyzer
TIPS	Thermally Induced Phase Separation
TPS	Thermal Protection System
TPS	Transient Plane Source
XRD	X-Ray Diffraction
SE	Shielding Effectiveness
SSE	Specific Shielding Effectiveness

NOTATIONS

ρ^*	Relative density
ρ_b	Bulk density
ρ_s	Skeletal/solid density
ρ_g	Density of gas
R_f	Resistivity of foam
R_s	Resistivity of solid
λ	Wavelength
d	D-spacing
θ	Angle of diffraction
V	Voltage drop
I	Current
s	Distance between pins
k_f	Thermal conductivity of foam
k_c	Thermal conductivity of sucrose-derived carbon
k_a	Thermal conductivity of air
k_g	Thermal conductivity of gas
γ	Surface tension of liquid
φ	Contact angle
g	Acceleration due to gravity
ρ	Density of liquid
h	Capillary rise
r	Capillary radius
ε_{eff}	Effective permittivity
ε_1	Permittivity of solid
ε_2	Permittivity of air
f	Volume fraction of air

CHAPTER 1

INTRODUCTION

The aim of this chapter is to provide insight into the conventional and state-of-the-art techniques used to prepare carbon and silicon carbide (SiC) foams. It also discusses the various precursors and reinforcing additives used to improve the structural and functional properties of carbon foams. A detailed description of applications of carbon and SiC foams is also given. This chapter introduces the motivation and objectives of the research work. At the end of the chapter, the organization of the thesis and a brief introduction of each chapter is provided.

1.1 Carbon

Carbon (atomic number: 6) is one of the most abundant elements in the universe. It is an essential element constituting the basic building block of life on earth and is found in all organisms. The carbon forms a variety of simple and complex organic molecules through its ability to bond with each other (catenation) and with other elements via single and multiple bonds using their sp, sp^2 and sp^3 hybridized and un-hybridized orbitals (McENANEY, 1999). The elemental carbon exists as bulk allotropic forms such as diamond and graphite and also forms a number of nano carbon materials such as carbon nanotubes, fullerene, graphene, carbon nanocone, carbon onions, and carbon quantum dots (Kharisov & Kharissova, 2019). In addition, carbon exists in bulk amorphous form called glassy carbon. Diamond has a cubic structure in which the carbon atoms are tetrahedrally bonded to each other through their sp^3 hybrid orbitals resulting in very low electrical conductivity and high hardness. On the other hand, graphite has a hexagonal sheet-like structure (sp^2 hybridized carbon) with extended conjugation and the sheets are stacked in the Z-direction by a weak van der Waals forces. This gives rise to high electrical conductivity and lubricating property. The nano allotropes of carbon also contain alternate carbon-carbon single and double bonds. A variety of electrical, optical, magnetic, mechanical and catalytic properties are invented on carbon-based nanomaterials due to their peculiar bonding and high surface to volume ratio. The glassy carbon contains a mixture of sp^3 and sp^2 hybridized carbon. Structurally, the glassy carbon is made up of ribbon-like stacks of graphene layers oriented randomly. A weak van der Waals force holds the graphene layers together and the ribbons are interconnected mostly through sp^3 carbon bonds. The restriction to shearing between the carbon ribbons of graphene layers as a result of the high degree of cross-link imparts high Young’s modulus and hardness in glassy carbon. **Figure 1.1** shows the structure of various allotropic forms of carbon.

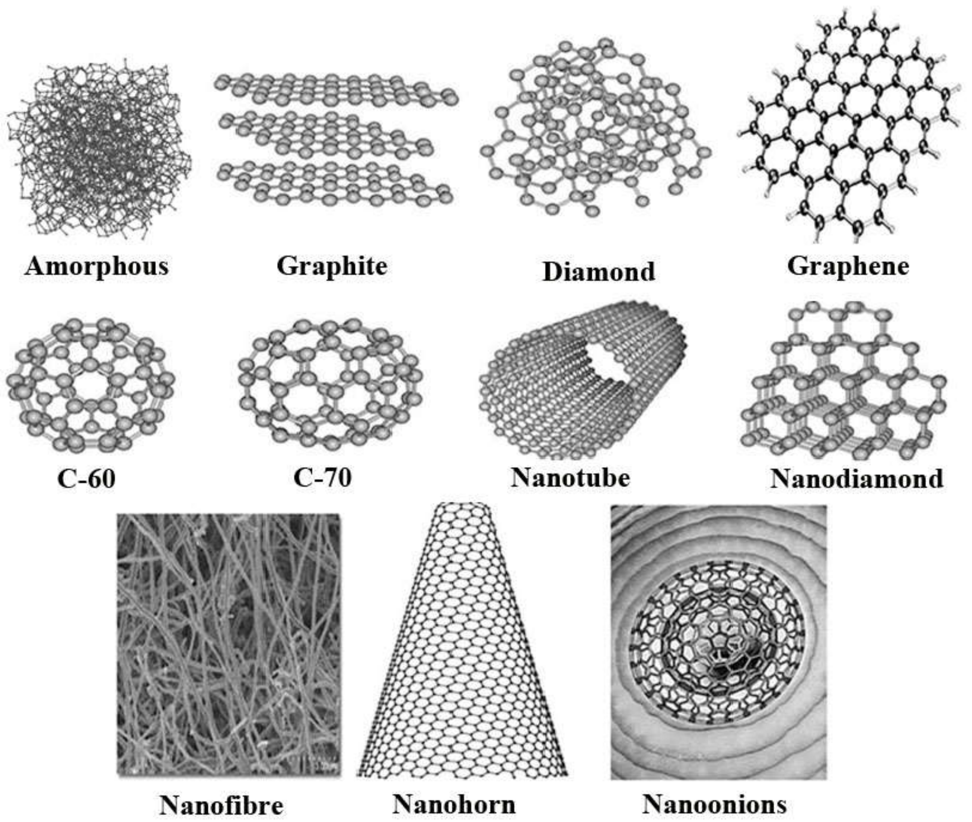

Figure 1.1 Various allotropes of carbon (Kharisov & Kharissova, 2019)

Carbon is a refractory element with a high melting point. The melting point of diamond and graphite are 4500 and 4450 °C, respectively (McEnaney, 1999). The carbon materials are chemically inert in ambient conditions. However, it starts to oxidize in an air atmosphere at temperatures exceeding 400 °C. Besides, carbon materials show high thermal stability in non-oxidizing environments. The chemical inertness of carbon in ambient conditions and high thermal stability in the inert atmosphere are attributed to highly covalent nature of the carbon-carbon bond. The carbon-carbon bond energy in diamond and graphite are 348 and 612 kJ mol^{-1}, respectively (McENANEY, 1999). In addition, the carbon materials show low thermal expansion coefficient and high thermal conductivity. The coefficient of thermal expansion of graphite and diamond are in the ranges of 4×10^{-6} to 8×10^{-6} and 1.1×10^{-6} to 1.3×10^{-6} mm^{-1} K^{-1}, respectively. The room temperature thermal conductivity of diamond and graphite are 15000 and 2800 W m^{-1} K^{-1}, respectively (McEnaney, 1999).

Carbon-based materials are prepared by heating organic polymeric materials which leave sufficient carbon during pyrolysis and the process is called carbonization. Chemical vapour deposition (CVD) is another technique which produces carbon-based nanostructure and pyrolytic carbon by the thermal decomposition of hydrocarbons (Delhaes, 2002; Manawi, Ihsanullah, Samara, Al-Ansari, & Atieh, 2018; Somani, Somani, & Umeno, 2006; Takikawa et al., 2000). Hydrocarbons such as methane, ethane, acetylene and benzene are used as carbon precursors in CVD.

1.2 Porous carbon

Porous carbon is a material with pores incorporated within the carbonaceous matrix where the matrix is composed of an assembly of defective graphene layers or aromatic sheets. Introduction of pores within the carbon matrix endow it with properties like high specific surface area and pore volume, low-density and tunable electrical, mechanical and thermal properties. The properties of porous carbon materials depend on the porosity, pore size, pore structure, as well as surface chemistry. Porous carbon materials are classified as microporous with pore size < 2nm, mesoporous with pore size in the range of 2 to 50 nm and macroporous with pore size >50 nm. Various porous carbon materials have found extensive application in gas adsorption and storage, water purification, catalytic supports, electrodes in energy storage devices, and thermal management.

Microporous carbon are generally prepared by (i) physical activation of carbon using CO_2 or steam (Chang, Chang, & Tsai, 2000; El Qada, Allen, & Walker, 2006; Guo et al., 2009; Lua & Guo, 2000; Molina-Sabio, Gonzalez, Rodriguez-Reinoso, & Sepúlveda-Escribano, 1996; Prakash Kumar, Shivakamy, Miranda, & Velan, 2006; San Miguel Guillermo, Fowler, & Sollars, 2003; H. Teng, Ho, & Hsu, 1997; T. Zhang et al.,

2004) and (ii) chemical activation of carbon-rich precursors using activating agents such as KOH, NaOH, $ZnCl_2$ and H_3PO_4 (J. Liu et al., 2018; Prauchner, Sapag, & Rodríguez-Reinoso, 2016; Rashidi & Yusup, 2016; Saha et al., 2017). They are synthesized in a powder form and are generally called as activated carbon. They are amorphous in nature due to the incorporation of a large number of defects in the carbon structure during the activation process. **Figure 1.2** shows the TEM image of a typical highly microporous carbon.

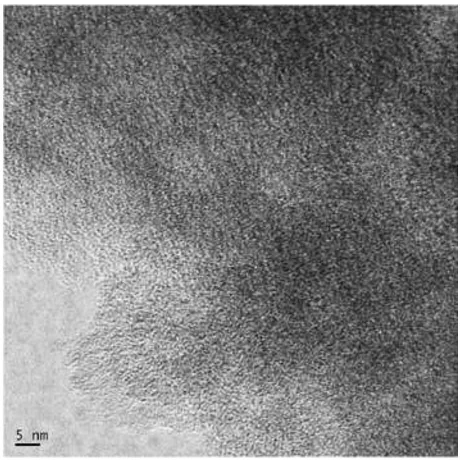

Figure 1.2 High-magnification TEM image of waste fish-derived activated carbon by KOH activation (Wilson, Vijayan, & Prabhakaran, 2018)

Alternately, ordered microporous carbons are derived using a template-based approach. In this, zeolites containing ordered rigid microporous architecture are used as templates. The carbon precursor resin is infiltrated into the zeolite, which is then carbonized in an inert atmosphere. The subsequent removal of the zeolite template by leaching with hydrofluoric acid (HF) solution produces ordered microporous carbon (Armandi, Bonelli, Bottero, Areán, & Garrone, 2007; Dubey et al., 2019; K. Kim, Kwon, Lee, Cho, & Ryoo, 2017; Ma, Kyotani, Liu, Terasaki, & Tomita, 2001; Ma, Kyotani, & Tomita, 2002; Stadie, Wang, Kravchyk, & Kovalenko, 2017; Xia, Yang, Gou, & Zhu, 2013). The schematic of the template-based method for the preparation of ordered microporous carbon and the respective TEM micrograph is given in **Figure 1.3**.

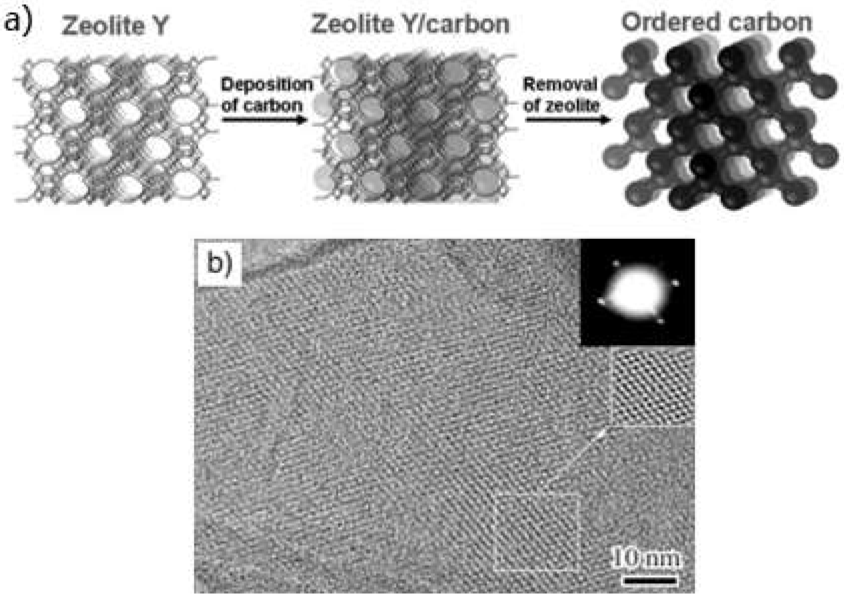

Figure 1.3 (a) Schematic of a template approach for the synthesis of ordered microporous carbon using zeolite-Y as a template (J. Lee, Kim, & Hyeon, 2006) and (b) High-resolution transmission electron microscopy (HRTEM) image of the ordered microporous carbon prepared following the procedure reported (Ma et al., 2001)

Mesoporous carbons are prepared by using simple inorganic or organic pore templates (Inagaki, Toyoda, Soneda, Tsujimura, & Morishita, 2016). Silica sol and aluminosilicates such as MCM-48, MCM-41, SBA-1 and SBA-15 are the inorganic templates used for the preparation of mesoporous carbon. (Inagaki et al., 2016; J. Lee, Han, & Hyeon, 2004; Ryoo, Joo, Kruk, & Jaroniec, 2001). On the other hand, self-assembled surfactant molecules such as amphiphilic block copolymers viz. poly(ethylene oxide)-block-poly(propylene oxide)-block-poly(ethylene oxide) (PEO106-PPO70-PEO106) (PluronicF127), PEO20-PPO70-PEO20 (Pluronic P123) and polystyrene-block-poly(4-vinylpyridine)(PS-P4VP) are employed as soft organic templates for the preparation of mesoporous carbons (Chengdu Liang & Dai, 2006; Chengdu Liang, Hong, Guiochon, Mays, & Dai, 2004; Mitome, Hirota, Uchida, & Nishiyama, 2016). The inorganic or organic template-incorporated precursor resin is set by further polymerization and cross-linking and subsequently carbonized. The inorganic templates are removed by etching with HF or NaOH after carbonization while the organic pore templates decompose out during carbonization. Carbon aerogels are monolithic mesoporous materials with porosity as high as 99%. They are obtained by the carbonization of organic aerogels produced mainly by sol-gel polycondensation of phenol and formaldehyde followed by supercritical drying (Rasines et al., 2015; Zu et al., 2016). **Figure 1.4** presents a schematic for the preparation of ordered mesoporous carbon from tannin.

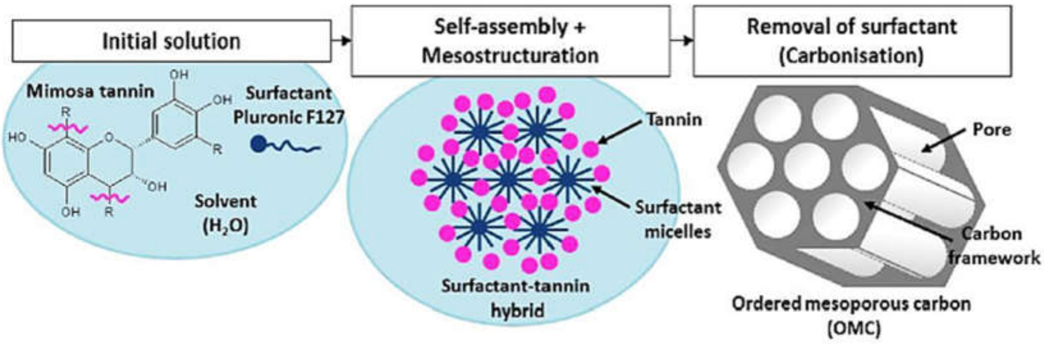

Figure 1.4 Schematic representation of the soft-templating method used to synthesize ordered mesoporous carbons (Sanchez-Sanchez et al., 2018)

Macroporous carbon (pore size > 50 nm) are conventionally prepared using three synthesis strategies; (i) foaming, setting and carbonization of carbon precursor resins, (ii) polymer foam replication and (iii) using sacrificial pore templates. These lightweight monolithic macroporous carbon materials with porosity >70% are called carbon foams. The details of properties, applications and synthesis methods of carbon foams are discussed in the subsequent sections.

1.3 Carbon foams

Carbon foam is defined as a rigid, macroporous material consisting of an interconnected network of carbonaceous ligaments (Gallego & Klett, 2003; Inagaki, Qiu, & Guo, 2015). The intervening space form cells of regular geometry distributed homogeneously as a three-dimensional array in the solid matrix. The cells can either be isolated from one another (closed cell) or be interconnected with the neighbouring cells via openings in the cell wall called cell windows (open cell). A third category of foams called reticulated foams also exists which consists of network-like struts and ligaments. **Figure 1.5** shows the high-magnification SEM images of the various types of carbon foams. Depending on the crystallinity of the carbon matrix they are classified as graphitic or non-graphitic foams which in turn depend on factors such as the carbon precursor used, processing conditions, heat-treatment temperature and use of a catalyst (R. Fu et al., 2005; M Karthik, Faik, Doppiu, Roddatis, & D'Aguanno, 2015; Maldonado-Hódar, Moreno-Castilla, Rivera-Utrilla, Hanzawa, & Yamada, 2000; Rodríguez, Cameán, García, & García, 2011; Yong Wang, Cao, Gao, & Wang, 2008). The carbon foams possess properties such as low density, tunable electrical and thermal conductivity, high surface area, flame resistance, and electromagnetic and acoustic absorption. The properties of the foams depend on the crystallinity, porosity, cell size, cell morphology and cell interconnectivity (Inagaki et al., 2015). A concise report of various processing methods for carbon foams and their applications is given in the following sections.

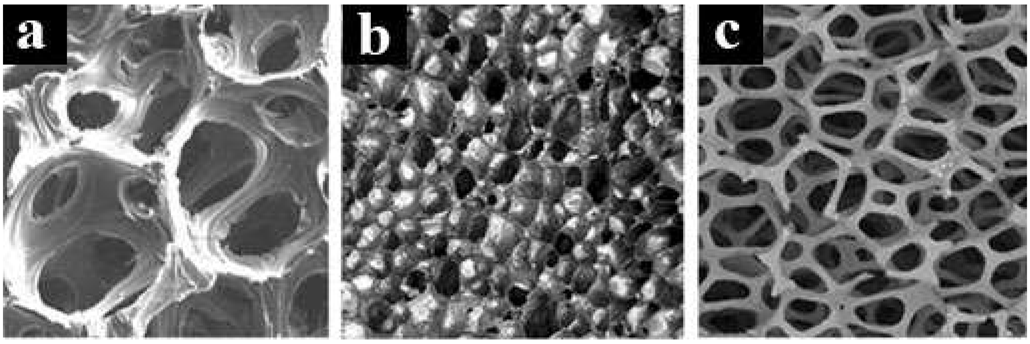

Figure 1.5 SEM images of (a) open cell, (b) closed cell and (c) reticulated carbon foams

1.3.1 Properties of carbon foams

The physical properties of carbon foams are defined by the crystallinity of the carbon matrix, cell size, cell interconnectivity, the morphology of the cells and thickness of the struts and ligaments. The properties of carbon foams can be tuned by processing methods, heat treatment temperature and choice of carbon precursor. The following sections discuss physical properties of carbon foams in terms of their relative density, mechanical properties, thermal conductivity and electrical conductivity.

1.3.1.1 Relative density and Porosity

Relative density (ρ^*) of a foam is defined as the ratio of the bulk density (ρ_b) of the foam to the density of the solid constituent material (ρ_s). The porosity of the foam is the fraction of voids within the foam and is related to the relative density by the relation:

$$\text{Porosity} = [(1-\rho^*)\times 100]\ \% \qquad (1.1)$$

For cellular foams, an upper limit of the relative density of 0.3 is considered (Gibson & Ashby, 1997). At relative densities >0.3, the cell walls become stocky and the pores are completely isolated by the solid matrix. Such solids are considered to be porous solids rather than cellular foams.

1.3.1.2 Mechanical strength

The mechanical strength of carbon foams depends largely on the relative density, cell size and the crystallinity of the solid matrix. Under compressive loading, carbon foams exhibit brittle behaviour. A typical stress-strain curve of carbon foam is comprised of three distinct regions. At low strains, a linear region signifying elastic deformation is observed and Young's modulus of the foams is calculated from the slope of this region. This is followed by a long plateau region where the stress remains constant over the applied strain. Here, the cells within the transverse planes successively collapse under the strain. Finally, the third region at high strains shows a drastic increase in stress corresponding to the densification of the collapsed foam. **Figure 1.6** shows a typical stress-strain plot of brittle cellular foams.

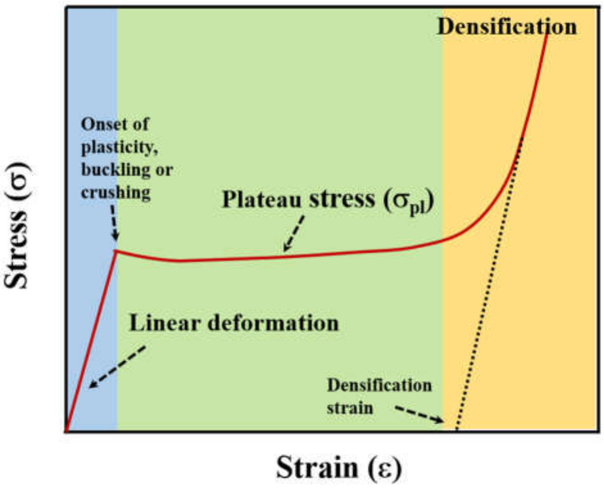

Figure 1.6 Typical stress-strain curve of a brittle elastic foam

Graphitic foams with highly ordered crystals derived from pitch exhibit comparatively high compressive strength over foams showing less ordered carbon structure. Pitch derived foams show compressive strength in the range of 1.47-23.7 MPa (Baran, Yardim, Atakül, & Ekinci, 2013; C. Chen, Kennel, Stiller, Stansberry, & Zondlo, 2006; Eksilioglu, Gencay, Yardim, & Ekinci, 2006; J. Klett, Hardy, Romine, Walls, &

Burchell, 2000; S. Li, Guo, Song, Shi, & Liu, 2010; S. Li et al., 2007; M. xian Wang, Wang, Li, & Hu, 2008; Yadav, Kumar, Bhatia, & Verma, 2011). Thermosetting precursors produce glassy or vitreous carbon foams with relatively lower compressive strengths. Polymer derived carbon foams show compressive strength in the range of 0.25 to 25.8 MPa (Q. Lin, Luo, Qu, Fang, & Chen, 2013; M. Liu et al., 2007; Lorjai, Wongkasemjit, & Chaisuwan, 2009; K. Wang et al., 2016; Liying Zhang et al., 2016; Zúñiga Ruiz et al., 2015) while biomass-derived foams exhibit compressive strength in the range of 0.08 to 12 MPa (P. Jana, Fierro, & Celzard, 2013, 2016; R Narasimman & Prabhakaran, 2012, 2013; Prabhakaran, Singh, Gokhale, & Sharma, 2007; Rios, Martínez-Escandell, Molina-Sabio, & Rodríguez-Reinoso, 2006; Seo et al., 2014; Tondi, Fierro, Pizzi, & Celzard, 2009). The compressive strengths of carbon foams derived from various precursors are presented in **Table 1.1**.

Table 1.1 Compressive strengths of carbon foams derived from various precursors

Precursor	Density (g cm^{-3})	Compressive strength	Thermal conductivity	Reference
Thermoplastic				
Mesophase pitch	0.38-0.56	1.47-3.31	-	(Eksilioglu et al., 2006)
Mesophase pitch	0.2-0.6		40-150	(J. Klett et al., 2000)
Mesophase pitch	0.6		182	(J. W. Klett, McMillan, Gallego,
Coal tar pitch-based	0.67	18.2	-	(C. Chen et al., 2006)
Petroleum pitch-based	0.34	3.9	-	(C. Chen et al., 2006)
Mesophase pitch	0.514–0.624	-	-	(M. xian Wang et al., 2008)
Asphaltene pitch	0.8	18.7		(Baran et al., 2013)
Mesophase pitch	0.51-0.55	-	79.25	(S. Li et al., 2010)
Mesophase pitch	0.23–0.58	3.0–5.0	60	(Yadav et al., 2011)
Mesophase pitch	0.75-0.78	23.7	43.7	(S. Li et al., 2007)

Coal tar pitch	0.249	0.46	21	(Focke et al., 2014)
Thermosetting				
Pthalonitrile	0.15	0.9	-	(Liying Zhang et al., 2016)
Diphenolic acid-based	0.02-0.09	~0.25-1	0.04-0.56	(Zúñiga Ruiz et al., 2015)
Polybenzoxazine	0.48	9.5	-	(Lorjai et al., 2009)
Allyl COPNA-modified	0.18-0.25	-~1.3-2.6	0.31-0.44	(K. Wang et al., 2016)
Polyarylacetylene	0.6	25.8		(M. Liu et al., 2007)
Cyanate ester	0.26	3.15	1.89	(Q. Lin et al., 2013)
Natural				
Lignin	0.39-0.58	2-12	-	(Seo et al., 2014)
Tannin	0.067	0.52	0.44	(Tondi, Fierro, et al., 2009)
Olive stones	0.22-0.32	-	-	(Rios et al., 2006)
Sucrose	0.14	0.53	0.19	(P. Jana, Fierro, et al., 2016)
Sucrose	0.04-0.075	0.11–0.23	0.042–0.065	(P. Jana et al., 2013)
Sucrose	0.115-0.145	0.89	-	(Prabhakaran et al., 2007)
Sucrose	0.053-0.085	-	-	(R Narasimman & Prabhakaran, 2012)
Sucrose	0.1-0.16	0.08-0.16	0.043-0.057	(R Narasimman & Prabhakaran, 2013)

The compressive strengths of carbon foams can be enhanced by incorporating various reinforcing additives. Herein, the reinforcing additives of superior mechanical strength carry the load applied to the carbon matrix. Carbon fibres, activated carbon, carbon nanotubes, graphite particles, graphene, clay and nanowhiskers are used as reinforcing additives (Chollon, Delettrez, & Langlais, 2014; W. Q. Li, Zhang, & Xiong, 2011; Q. Lin, Qu, Luo, Fang, & Luo, 2014; Luo, Ni, Li, Yang, & Wang, 2011; R Narasimman, Vijayan, Dijith, Surendran, & Prabhakaran, 2016; S. A. Song, Lee, Kim, &

Kim, 2017; S. Wang, Luo, & Ni, 2010; Xinying Wang, Zhong, Wang, & Yu, 2006; X. Wu, Liu, Fang, Mei, & Luo, 2011). Li et al produced carbon foams reinforced with multiwalled CNT (MWCNT) using mesophase pitch as a carbon source (W. Q. Li et al., 2011). With a reinforcement of 2 wt% of MWCNT, nearly 65% increase in compressive strength was observed. Luo et al reinforced phenolic resole resin derived carbon foams with $K_2Ti_6O_{13}$ whiskers (Luo et al., 2011). The compressive strength of the carbon foam was improved by 86% with the addition of 2wt% of $K_2Ti_6O_{13}$ whiskers. Hollow ceramic microspheres are used as reinforcement in phenolic resole resin-based carbon foams (S. Wang et al., 2010). A significant improvement in the compressive strength (~85 %) is achieved with 1wt% addition of hollow ceramic microspheres.

1.3.1.3 Thermal conductivity

The thermal conductivity of carbon foams depends on the crystallinity of the constituent carbon matrix. Graphitic carbon exhibits high thermal conductivity while amorphous carbon possesses low thermal conductivity. The crystallinity and thus the thermal conductivity of the carbon foams are influenced by the precursor materials as well as the heat-treatment temperature used in their preparation (C. Chen et al., 2006). Thermal conductivity in foams encompasses conduction, convection and radiation (Gibson & Ashby, 1997). The small cell size suppresses convective heat transfer and its contribution is negligible. Repeated absorption and reflection of radiation at the cell walls also diminishes radiative heat transfer. Heat conduction through the solid and the gas (usually air) within the cells are the major contributors to the thermal conductivity of foams. The conductivity in the cellular solids is usually described by Equation 1.2:

$$k_f = \frac{1}{3}\left(\left(\frac{\rho_g}{\rho_s}\right) + 2\left(\frac{\rho_g}{\rho_s}\right)^{\frac{3}{2}}\right)k_s + ((1 - \left(\frac{\rho_g}{\rho_s}\right))k_g \qquad (1.2)$$

where, k_s and k_g are the thermal conductivity of the solid and gas, respectively. The thermal conductivity of gas is very low (k_g= 0.025 W m^{-1} K^{-1} for air). Thus, it is the conductivity of the solid which mainly defines the thermal conductivity of the foam. The non-crystalline nature of the carbon obtained from thermosetting resins and naturally renewable precursors leads to low values of thermal conductivity (0.04 to 0.56 W m^{-1} K^{-1}) for the carbon foams derived from these precursors (P. Jana et al., 2013; P.

Jana, Fierro, et al., 2016; R Narasimman & Prabhakaran, 2013; Tondi, Fierro, et al., 2009; K. Wang et al., 2016; Zúñiga Ruiz et al., 2015). The carbon foams prepared from pitches can attain a high degree of graphitization and show high thermal conductivity in the range of 21-182 W m^{-1} K^{-1} (Focke et al., 2014; J. Klett et al., 2000; J. W. Klett et al., 2004; S. Li et al., 2010, 2007; Yadav et al., 2011). The thermal conductivity of carbon foams obtained from various precursors is given in **Table 1.1**.

1.3.1.4 Electrical conductivity

The electrical conductivity of a material decreases with the incorporation of pores as its relative density decreases. A decrease in relative density is associated with a decrease in the average cross-section available for conduction and the corresponding increase in the tortuosity of the current path (Gibson & Ashby, 1997). The resistivity of foam is related to the solid resistivity and relative density according to Equation 1.3.

$$R_f \propto \frac{R_S}{(\frac{\rho_b}{\rho_S})} \qquad (1.3)$$

Where, R_f is the resistivity of the foam, Rs is the resistivity of the solid, ρ_b/ρ_s is the relative density. The presence of conjugated π electrons in carbon foam endows it with good electrical conductivity. However, the electrical conductivity of carbon foams depends on the carbon precursors and heat treatment temperatures, as is observed with its thermal conductivity. A large disparity in the observed electrical conductivity in carbon foams is attributed to the dissimilarity in the crystallinity of the carbon matrix.

Carbon derived from synthetic polymers and natural renewable precursors are non-crystalline and the foams derived from these precursors show low electrical conductivity. An increase in the heat-treatment temperature increases the crystallinity of the obtained carbon foam which leads to improved electrical conductivity (Liying Zhang et al., 2016). The electrical conductivity of the carbon foams derived from synthetic polymers is reported in the range of 0.055 to 2450 S m^{-1} (Agarwal, Kumar, Kumari, & Dhakate, 2016; S. Chen et al., 2013; Rajeev Kumar, Dhakate, Saini, & Mathur, 2013; Lorjai et al., 2009; Liying Zhang et al., 2016). Carbon foams produced from natural renewable precursors like lignin, tannin and sucrose show the electrical conductivity in the range of 0.002 to 70 S m^{-1} (Letellier, Macutkevic, Paddubskaya, Klochkov, et al., 2015; Letellier, Macutkevic, Paddubskaya, Plyushch, et al., 2015; Prabhakaran et al., 2007; Seo et al., 2014; Zeng et al., 2018). Graphitic foams derived from pitch-based precursors exhibit high electrical conductivity on account of the presence of long-range order in the carbon matrix. The electrical conductivity for such foams ranges from 562 to 8.2×10^3 S m^{-1} (Rajeev Kumar, Dhakate, Gupta, et al., 2013; Rajeev Kumar, Dhakate, & Mathur, 2013; Heguang Liu, Li, Huang, & Zhao, 2015; Heguang Liu et al., 2016).

1.3.2 Applications of carbon foams

Carbon foams find application in numerous fields of industry and research owing to its multifaceted properties, which can be tuned by selecting the appropriate precursor and processing technique. Tunable porosity, thermal conductivity, electrical conductivity, textural property and surface chemistry have led to the diversification in the applications of carbon foams. The following sections will highlight some of the important applications of carbon foams.

1.3.2.1 High-temperature thermal insulation and ablative protection

Amorphous carbon foams prepared from synthetic polymers and natural renewable precursors possessing low thermal conductivity are good candidates for high-temperature thermal insulation. However, oxidation of carbon in the air atmosphere at high temperature limits their application. NASA used a carbon foam-based heat shield in their Parker Solar Probe mission (Garner, 2018). The heat shield is made of two panels of superheated carbon-carbon composite sandwiching a lightweight 4.5 inch-thick carbon foam core. The heat shield protects the probe from temperatures of nearly 1400 °C. **Figure 1.7** presents the schematic of the NASA's Parker solar probe.

In addition to the low thermal conductivity, carbon foams exhibit ablative property. The ablative materials are used as thermal protection systems (TPS) in re-entry space vehicles which encounter severe heating during hypersonic flight through a planet's or the earth's atmosphere (Rajeev Kumar et al., 2019; Ogasawara, Ayabe, Ishida, Aoki, & Kubota, 2018; Pulci et al., 2010; M. Yu, Li, Ao, & Chen, 2019). The ablative materials undergo decomposition under the harsh heating conditions during re-entry and thus protects the space vehicles. Pulci et al. developed composite ablative TPS which offered mechanical resistance and insulating performance using graphitic carbon foam (Grafoam) and graphitic carbon felt (Sigratherm) as reinforcements in phenolic resin. Design limitations mainly apply to an upper-density limit of 0.5 g cm^{-3}, and to the ability to withstand heat fluxes ranging from 2 to 9 MW m^{-2}, consistent with the moon–earth re-entry. **Figure 1.8** shows the thermal insulation performance of the Grafoam and Sigratherm based TPS.

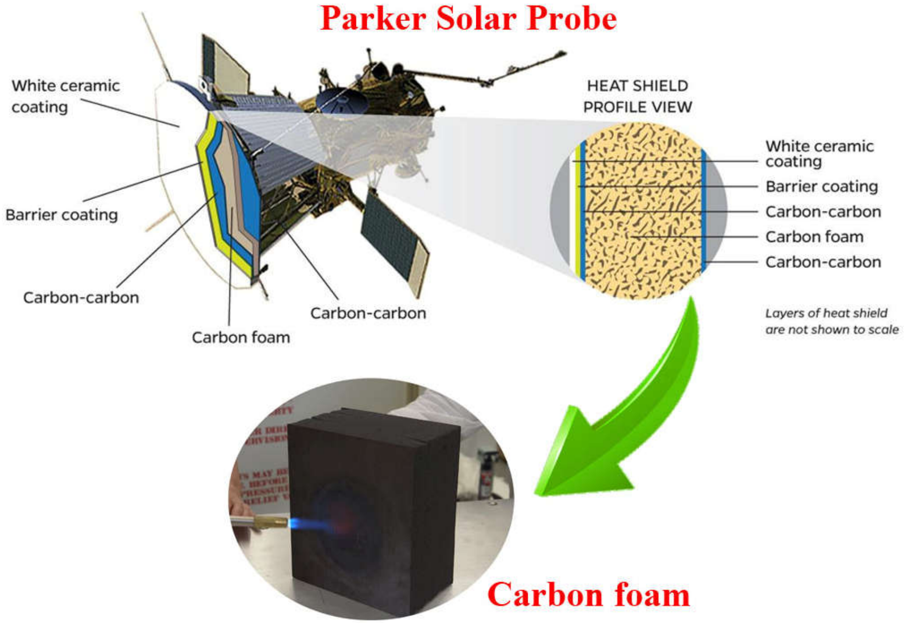

Figure 1.7 Schematic representation of NASA's Parker Solar Probe. The heat shield consists of a thick insulating carbon foam (Garner, 2018)

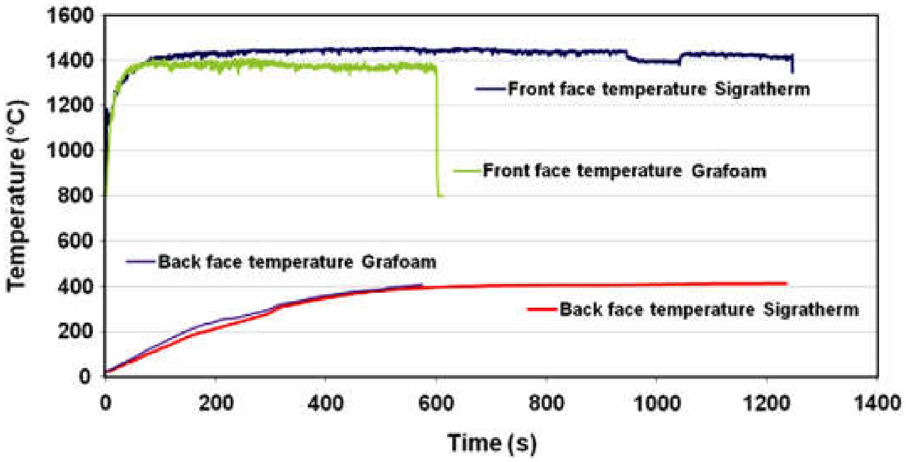

Figure 1.8 Temperature differential on the Front and Back faces of Sigratherm and Grafoam composites during oxyacetylene exposure test (Pulci et al., 2010)

1.3.2.2 Thermal management

Modern ultra-fast processors and power electronic devices generate significantly large amounts of heat. Heat sinks are used for dissipating the excess heat generated during the operation of these devices. Metal foams with high thermal conductivity have shown improved heat transfer efficiency by means of an increase in surface area. Researchers at the Oak Ridge National Laboratory (ORNL) developed graphitic carbon foam of density in the range of 0.2 to 0.6 g cm^{-3} with thermal conductivity between 40 and 180 W m^{-1} K^{-1} (Gallego & Klett, 2003). They demonstrated that the overall heat transfer coefficients of carbon foam-based heatsinks to be up to two orders of magnitude greater than those of conventional heat sinks. Carbon foams also showed a faster response to transient heat loads. Lin et al. developed high-effectiveness recuperative heat exchangers using solid and corrugated carbon foam blocks (Y. R. Lin, Du, Wu, Chow, & Notardonato, 2010). Heat transfer studies using carbon foams in various geometries and configuration showed that carbon foam can be an effective medium for heat transfer enhancement. Corrugated carbon foams exhibited a higher heat transfer coefficient and low-pressure drop in comparison to solid foams at all studied gas velocities. **Figure 1.9** shows a corrugated carbon foam and the illustration of airflow over it.

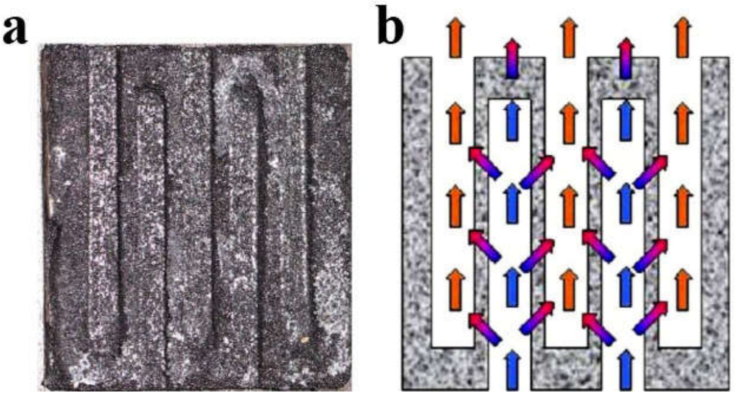

Figure 1.9 (a) Corrugated carbon foam and (b) illustration of airflow in a corrugated foam (Y. R. Lin et al., 2010)

Thermal conductivity of carbon foam could further be improved by incorporating graphite filler particles (J. Zhu et al., 2007). By the incorporation of the graphite particles (up to 5 wt%), the thermal conductivity of mesophase pitch-based carbon foam was increased from 70 to 110 W m^{-1} K^{-1}. The reinforcement also improved the compressive strength of the foams from 3.7 MPa to 12.5 MPa. Yadav et al. used polyurethane foam as a template and mesophase pitch as a precursor for producing carbon foams with a high thermal conductivity of 60 W m^{-1} K^{-1} (Yadav et al., 2011). Carbon foams of density in the range of 0.23–0.58 g cm^{-3} with compressive strength in the range of 3.0–5.0 MPa were obtained after heat treatment at 2400 °C.

1.3.2.3 Host for thermal energy storage materials

With growing energy demands and depleting natural gas reservoirs, there has been a gradual shift to explore sustainable energy sources. Solar thermal energy has been one of those sources of gathering widespread attention. Thermal energy storage system using phase change materials (PCM) is one of the technologies employed for the purpose of capturing and utilizing solar energy (Akeiber et al., 2016; Bose & Amirtham, 2016). The phase change materials store their thermal energy in the form of latent heat during solid to liquid or solid to solid phase transformation. The stored latent heat released during the reverse transformation is used for practical applications. **Figure 1.10** shows the schematic of the working of a PCM-based solar thermal energy storage system.

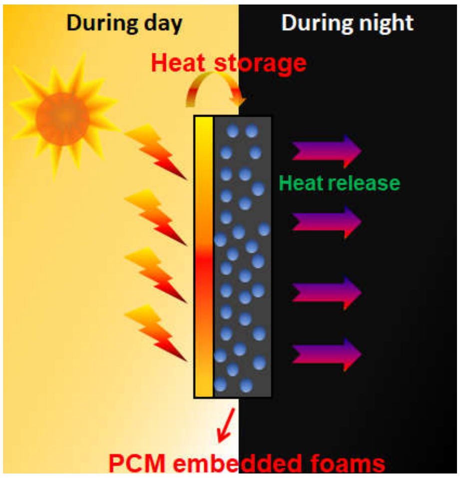

Figure 1.10 Schematic representation of the working of a thermal energy storage device

The solid to liquid phase change is preferred over solid to solid transition as the former is associated with high latent heat. The PCMs undergoing solid to liquid transition are contained in the pores of thermally conducting porous media to enhance the heat transfer and form stability. Thermally conducting carbon foams produced using coal, coal tar pitch, mesophase pitch, and synthetic organic polymers are appropriate for hosting PCM in thermal energy storage systems due to the high thermal conductivity of the foams. Zhong et al. developed mesophase pitch-based graphite foams (GFs) with high thermal diffusivity (90.42 – 230.2 mm^2 s^{-1}) and low pore-size to increase the thermal diffusivity of paraffin wax-based PCM (0.12 mm^2 s^{-1}) for thermal energy storage application (Zhong, Guo, Li, Shi, & Liu, 2010). The thermal diffusivity of the PCM/GF composite showed remarkable enhancement in the range of 24.94-74.31 mm^2 s^{-1}. A composite of paraffin wax and conducting carbon foam was developed by Karthik et al using resorcinol-formaldehyde and synthetic graphite filler as carbon precursors (Mani Karthik, Faik, & D'Aguanno, 2017). The thermal conductivity of the P-wax/G-foam composite with wax in both solid (2.6 W m^{-1} K^{-1}) and liquid (1.8 W m^{-1} K^{-1}) phases were higher than that of pristine paraffin wax in solid (0.24 W m^{-1} K^{-1}) and in liquid (0.11 W m^{-1} K^{-1}), respectively. The thermal conductivity of poorly conducting biomass-derived carbon foams are improved by incorporating graphite filler (P. Jana, Fierro, Pizzi, & Celzard, 2014) for making them suitable for hosting PCM.

1.3.2.4 Electromagnetic interference (EMI) shielding

Electronic devices, especially telecommunications and wireless devices, emit microwaves which interfere with commercial, military, aeronautical and other critical appliances (Aswathi, Rane, Ajitha, Thomas, & Jaroszewski, 2018). It is critical to provide barriers in these devices to isolate the EM waves internally or to shield from external interferences. Most appliances use conducting metal sheets, internally connected to the ground, to provide EM shielding. Though metal-based shielding materials are quite practical for ground-based equipment, however, the high density, low thermal stability and poor corrosion resistance make them rather unfeasible in aerospace, aeronautical and marine applications where the operating conditions are severe. In addition, the radar-based systems employ radio and microwaves for detection of aircraft and vessels, where the EM waves reflected from the metal shells are detected by a receiver. Hence, coating of costly EM wave absorbing materials is provided to avoid detection (Bae & Kim, 2014; Biscaro, Nohara, Peixoto, Faez, & Rezende, 2003; Truong, Turner, Muscat, & Russo, 1997).

The significance of porous structure in the absorption of microwave radiation is demonstrated in the literature (Fang, Li, Sun, Zhang, & Zhang, 2007; Qiulong Li et al., 2016; Moglie, Micheli, Laurenzi, Marchetti, & Mariani Primiani, 2012; Singh, Shishkin, Koppel, & Gupta, 2018). The pores create a darkroom effect thus enhancing absorption. Lightweight, conducting porous materials such as carbon foams have found to be suitable for EMI shielding application (Fang et al., 2007; Moglie et al., 2012; Shen et al., 2016; J. Yang, Shen, & Hao, 2004). The EMI shielding in carbon foams transpires through mechanisms such as reflection (SE_R), absorption (SE_A) and multiple internal reflections (SE_M) (Daniel & Thomas, 2018). The cumulative energy loss (SE_T) occurring by these phenomena gives rise to total shielding effectiveness of a material.

$$SE_T(dB) = SE_R + SE_A + SE_M \qquad (1.4)$$

In one of the first reported instances of application of carbon foams as EM shielding materials, Yang et al. developed mesophase pitch-derived carbon foam-based sandwich composites using glass fibre reinforced epoxy facing sheet. The carbon foams heat-treated at 700 °C showed good reflection loss (>-10 dB). Providing a glass fibre reinforced composite facing to the carbon foam enhanced the absorption significantly with a peak value of -35 dB and a broad bandwidth of 10.7 GHz (J. Yang et al., 2004). The ultralight (0.15 g cm^{-3}) carbon foam prepared by direct carbonization of phthalonitrile (PN) based polymer foam exhibited a high EMI SE of ~51.2 dB and excellent specific EMI SE of 341.1 dB cm^3 g^{-1} (Liying Zhang et al., 2016). Recently, lignin-derived carbon foams doped with reduced graphene oxide (RGO) having honeycomb-like morphology synthesized by ice templating followed freeze-drying showed EMI SE of 28.5 to 70.5 dB at 2 mm thickness (Zeng et al., 2018). The EMI shielding performance of some of the carbon foams and composites is provided in **Table 1.2**.

1.3.2.5 Electrodes in electrochemical systems

Energy is an essential commodity for human civilization. Conventional sources such as oil and coal are dwindling through inefficient overuse over the last century. Switching to renewable energy sources such as solar, wind, geothermal and ocean tides has become essential for a sustainable future. Though these sources are limitless, they are intermittent in nature and the energy produced by them needs to be stored efficiently for

Table 1.2 EMI shielding effectiveness of carbon foams reported in the literature

Precursor	**Thickness (mm)**	**EMI SE (dB)**	**Specific EMI SE (dB cm^3 g^{-1})**	**Reference**
Pthalonitrile	2	51.2	341.1	(Liying Zhang et al., 2016)
Graphene	0.3	25.2	-	(Shen et al., 2016)
Lignin+RGO	2	28.5-70.5		(Zeng et al., 2018)
Coal tar pitch + ferrocene	2.75	81	130	(Rajeev Kumar, Dhakate, Saini, et al., 2013)
Phenolic resin + Fe_3O_4 + ZnO	2.75	50	-	(R Kumar et al., 2014)
Coal tar pitch + MWCNT	2.75	50-85	85-163	(Rajeev Kumar, Dhakate, Gupta, et al., 2013)
Sucrose + GO	5	21.2-38.6	80-160	(R Narasimman, Vijayan, & Prabhakaran, 2015)
CNT + chitosan	2.5	37.6	2149	(M. Z. Li et al., 2018)

use on demand. Batteries store electrical energy through reversible chemical reactions. Hence, efficiency, reliability, high energy density and power density are indispensable qualities of batteries for the future. Carbon-based electrode materials have been used since the inception of batteries and supercapacitors. Improving the performance and storage capacity using carbon-based nanomaterials is an area of intense research.

Porous electrode materials have attracted progressively more attention because an increase in the electrode/electrolyte interfaces improves the electrochemical properties by enhancing the charge transport (Doherty, Caruso, Smarsly, Adelhelm, & Drummond, 2009; Hasegawa et al., 2011). Porous carbons, usually in their powdered state, are well-known electrode material designed for applications such as batteries and supercapacitors, electrochemical sensors, and oxygen reduction (Arroyo-Gómez, Villarroel-Rocha, de Freitas-Araújo, Martínez-Huitle, & Sapag, 2018; Imoto et al., 2003; Koskun, Şavk, Şen, & Şen, 2018; B. Liang et al., 2020; Si et al., 2013; Yongfang Wang, Zuo, & Liu, 2018; C. Zhao et al., 2018; T. Zhu et al., 2014; Y. Zhu, Hu, Li, & Zhang, 2007). In this approach, porous carbon is mixed with a binder and a conducting phase in a solvent and coated over copper or aluminium foil to form electrodes. However, in such a construction, a large fraction of pores would remain inaccessible to the electrolyte and thus prevent or diminish efficient ion transport and reduce rate capability of the batteries (Z. Wang, Li, Ergang, & Stein, 2006). In contrast, a hierarchical porous structure would improve the performance of electrodes where the presence of micropores provides a high specific surface area, increasing the interfacial area between the electrode and electrolyte while that of meso- and macropores allow the efficient mass transport of the electrolyte throughout the electrode (Hasegawa et al., 2011).

Ji et al. reported the use of free-standing, lightweight, and highly conductive ultrathin graphite foam (UGF), loaded with lithium iron phosphate (LFP), as a cathode in a lithium-ion battery (H. Ji et al., 2012). The LFP loaded UGF showed high rate capability and specific capacity due to the high conductivity ($\sim 1.3 \times 10^5$ S m^{-1}) and low density ($\sim$9.5 mg cm^{-3}) of the 3-dimensional graphene network in comparison to LFP loaded on Aluminium foil and Nickel foam.

With interest peaking in wearable electronics, there is a demand for power source devices that are flexible, stretchable/compressible, and durable. To achieve this end, Xiao et al. developed a new type of free-standing and hydrophilic nitrogen-doped carbon foams (NCFs) as high-performance electrodes for compressible supercapacitors (K. Xiao et al., 2016). The NCFs were prepared by single-step pyrolysis of commercially available melamine sponges. The interconnected carbon network endowed NCFs to bear a reversible compressive strain as high as 80% and superior long-term durability even after compression for as many as 1000 cycles. The areal and specific capacitance of NCFs electrode were 332 mF cm^{-2} and 52 F g^{-1}, respectively, at a current density of 1 mA cm^{-2}.

Carbon foam with large mesopores prepared by combining hard- and soft-templating method (silica nanoparticles and triblock copolymer P-123) was used as a cathode for lithium-sulfur batteries (L. Fu et al., 2013). Graphene foam doped with nitrogen was directly used as counter electrode for dye-sensitized solar cells, showing conversion efficiency of 7.07%, comparable to that of the platinum counter electrode (Y. Xue et al., 2012).

1.3.2.6 Acoustic absorption

Sound is considered as a major environmental pollutant in industry, transportation and residential establishments. To mitigate the adverse effects of noise pollution, sound-absorbing materials are used in the construction of buildings and vehicles. Materials in the form of fibres, foams, and grains are currently used for sound absorption. Carbon foams are widely studied as acoustic absorption materials (Amaral-Labat, Gourdon, Fierro, Pizzi, & Celzard, 2013; Muehleisen, Beamer, & Tinianov, 2005).

Reticulated carbon foams were investigated for sound absorption in harsh environments of heat engines (Muehleisen et al., 2005). Cellular vitreous carbon foams derived from flavonoid tannins was investigated for acoustic absorption in the frequency range of 50–4300 Hz (Amaral-Labat et al., 2013). The low-frequency acoustic absorption characteristics of mesophase pitch-based carbon foams were studied by Gao et al (Gao, Cheng, Hou, & Zhang, 2018). A sound absorption coefficient of 0.5 at a frequency below 400 Hz was obtained for carbon foams of thickness 25 mm and back cavity depth of 40 mm.

1.3.2.7 Fire resistant structures

Fire-resistant materials are an important component in the construction of buildings, ships and automotive. Traditionally polymer-based fire retardant coatings are used to protect the structure. These coatings exhibit poor tolerance to oxidants, strong acidic/alkaline reagents, organic solvents, as well as release toxic gases. Use of carbon as structural material avoids such fire retardant coatings as carbon-based materials inherently resistant to fire as they do not produce volatile matters responsible for the flame propagation.

Hu et al. developed the highly fire-retardant ultralight graphene foam by mixing graphene oxide solution with hexachlorocyclotriphosphazene (HCTP, molecular formula: $P_3N_3Cl_6$) to form a continuous GO-HCTP foam (Hu et al., 2016). The incorporation of phosphorus and nitrides in the foam enhanced the flame retardation property. Narasimman et al. prepared carbon foams with cell size and foam density in the ranges of 0.33–2.34 mm and 0.1151–0.2281 g cm^{-3} from aqueous sucrose resin using activated carbon as fillers (Rajaram Narasimman, Vijayan, & Prabhakaran, 2015). The carbon foams showed good flame resistance. The oxyacetylene flame took 60–70 s to penetrate 15 mm thick carbon foam. Carbon foams derived from tannin also showed excellent fire-resistant property (Tondi, Fierro, et al., 2009). It took nearly 30 s of exposure of the carbon foam to a neutral oxyacetylene flame (2750–3050 °C) to get a hole across a material of thickness 2 cm. Photographic images showing flame resistant property of tannin-derived carbon foams are presented in **Figure 1.11**.

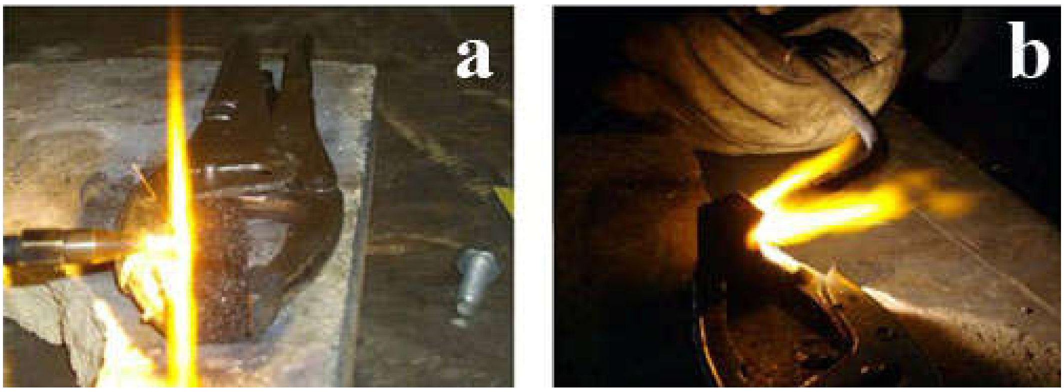

Figure 1.11 Carbon foam exposed to a neutral 2750–3050 °C oxyacetylene flame (a) Beginning of the test of fire resistance and (b) after 15 s (Tondi, Fierro, et al., 2009)

1.4 Preparation of carbon foams

Carbon foams are prepared from organic precursor resins providing a considerable amount of carbon during pyrolysis. The properties of carbon foams depend on the nature of precursors employed for their production. Thermoplastic and thermosetting resins and plant-based naturally renewable molecules are used as precursors for carbon foams. Thermoplastic precursors form a liquid phase during carbonization resulting in a more ordered structure that leads to easy graphitization on high-temperature heat treatment. On the other hand, thermosetting precursors upon carbonization yield carbon with rigid cross-linked structure without the long-range order which restrict graphitization. Some of the organic precursors commonly used for the preparation of carbon foams are described in the following section.

1.4.1 Thermoplastic precursors

Thermoplastic precursors mainly include petroleum pitch and coal tar pitch. Petroleum pitch is the residue obtained during the fractional distillation of crude oil (Savage, 1993) while coal tar pitch is the residue obtained during the distillation of coat tar. The coal-tar is produced by coking of bituminous coals at high temperatures (900-1000 °C). Both coal tar pitch and petroleum pitch consist of polynuclear aromatic and alicyclic hydrocarbons of molecular masses in the range of 300-400 g mol^{-1}. The major difference between the two is that the coal tar pitch contains more aromatic fraction compared to petroleum pitch. Pitches are commonly converted to mesophase pitch by prolonged heat-treatment nearly 375 °C to facilitate easy graphitization of the carbon products (J. W. Klett et al., 2004; S. Li et al., 2007; Savage, 1993; Yadav et al., 2011). During the heat-treatment, the polynuclear hydrocarbons further condense and aromatize to produce sheet-like structures. The alignment of these lamellar molecules leads to nematic discotic liquid crystals. The molecular weight of the mesophase pitch is in the range of 1200 to 1300 g mol^{-1}. The structures of typical polynuclear hydrocarbons present in petroleum pitch and coal tar pitch are given in **Figure1.12**. The schematic of the molecular arrangement in the mesophase pitch is shown in **Figure 1.13**.

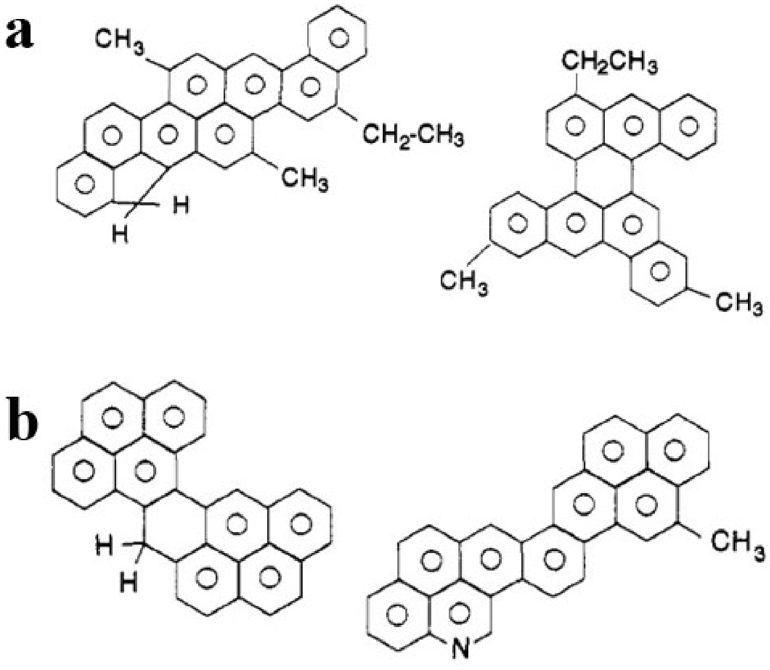

Figure 1.12 Molecular structures of (a) petroleum pitches and (b) coal tar pitches (Kershaw & Black, 1993)

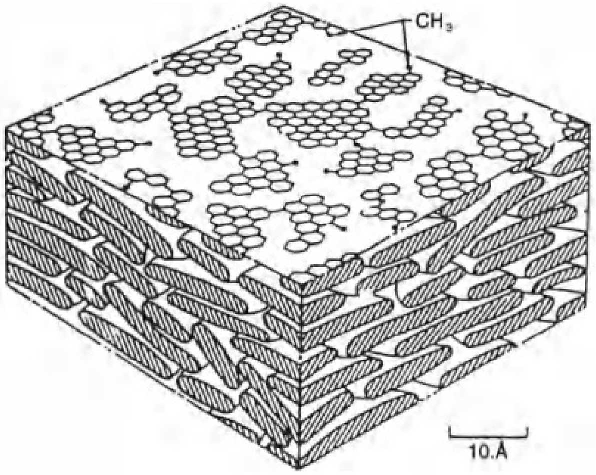

Figure 1.13 Schematic representation of molecular arrangement within the mesophase pitch (Savage, 1993)

1.4.2 Thermosetting precursors

Most synthetic polymers used as carbon precursors are thermosetting in nature. These are produced in low molecular weight form called resins. They undergo further polymerization and cross-linking during the processing to produce polymer foams. The polymer foams produced are subjected to carbonization heat treatment to form carbon foams. Unlike thermoplastic resins, the thermosets do not soften on reheating. This results in the formation of glassy carbon during pyrolysis which cannot be graphitized even by high-temperature heat treatments. The non-graphitic carbon derived from thermosetting polymers has a low density and the carbon yield is in the range of 50-60%. Phenol-formaldehyde resin, furfural resin, polyimides, polybenzoxazine, pthalonitrile and melamine-formaldehyde are widely studied as precursors for the preparation of carbon foams (Farhan, Wang, & Zhang, 2017; Ghani, Maya, & Cerdà, 2016; Hao et al., 2011; Lei, Guo, Shi, & Liu, 2010; Q. Lin et al., 2013; M. Liu et al., 2007; Lorjai et al., 2009; Pekala & Hopper, 1987; Roy et al., 2016; Liying Zhang et al., 2016; Zúñiga Ruiz et al., 2015). The structures of thermosetting resins used for the preparation of carbon foams and their carbon yield are shown in **Figure 1.14**.

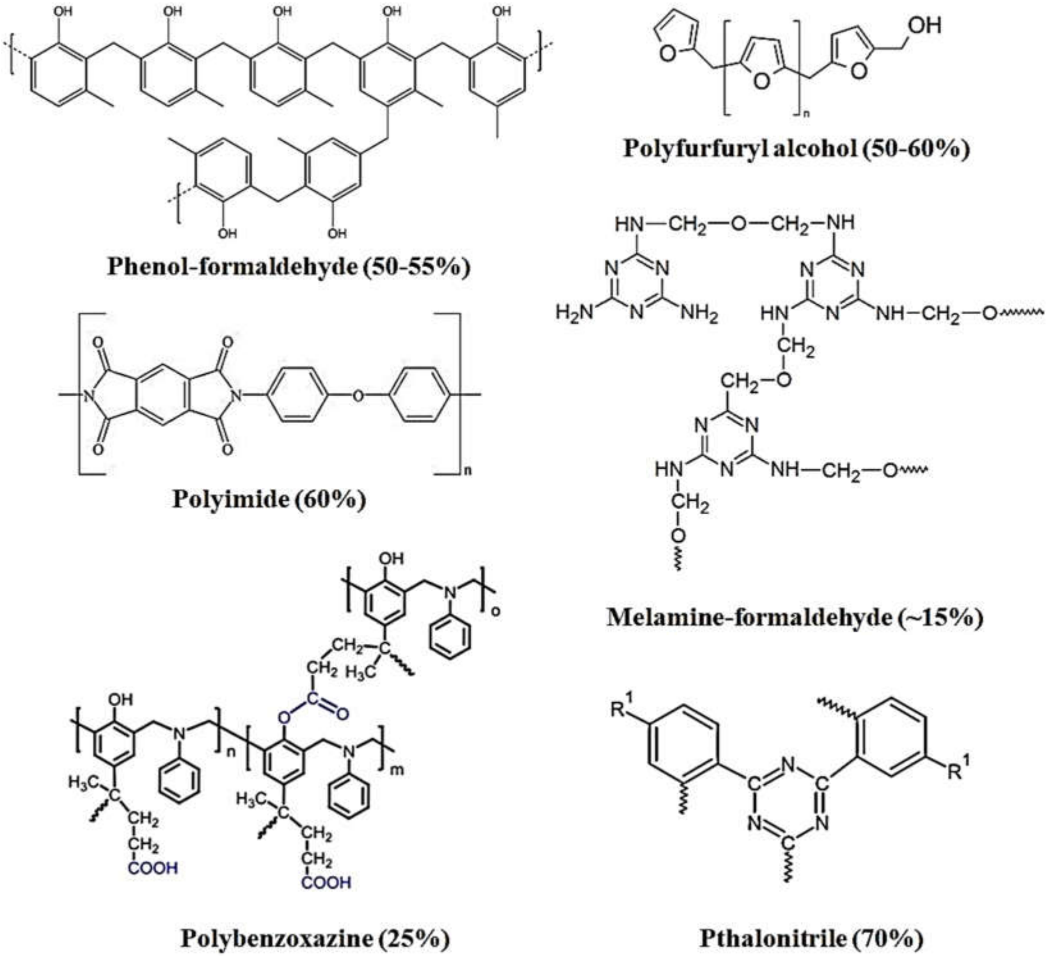

Figure 1.14 Some common synthetic polymers used as carbon foam precursors. The values in the bracket indicate the reported carbon yields (Lorjai et al., 2009; Savage & Savage, 1993; Y. Wu, Fang, & Jiang, 1998; Liying Zhang et al., 2016)

1.4.3 Naturally renewable precursors

Depleting petroleum and coal-based resources has led to an exploration of carbon-rich biomolecules as alternate precursors for the preparation of carbon foams in the recent past. Among the most researched biomolecules tannin, lignin and sugars are of prime importance (P. Jana et al., 2013; P. Jana, Palomo del Barrio, Fierro, Medjahdi, & Celzard, 2016; R Narasimman & Prabhakaran, 2012, 2013; R Narasimman et al., 2015; Prabhakaran et al., 2007; Seo et al., 2014; Tondi, Fierro, et al., 2009).

Tannin is a resin extracted from the bark of trees (Tondi, Fierro, et al., 2009). It is composed of 75 to 80% polyflavonoids, while carbohydrate monomers and oligomers make up the rest of the composition. The phenolic nuclei in the polyflavonoids can undergo reaction with formaldehyde as in phenol-formaldehyde reactions which provide a handle for resinification and further processing into various carbon products. The research group associated with Celzard has widely studied tannin for the preparation of carbon foams (Celzard, Zhao, Pizzi, & Fierro, 2010; X. Li et al., 2012; Szczurek, Fierro, Pizzi, & Celzard, 2014; Szczurek, Fierro, Pizzi, Stauber, & Celzard, 2013; Tondi, Blacher, et al., 2009). Lignin, the main by-product of pulp and paper industries, is an abundant, cheap, renewable, and nontoxic natural polymer.

Lignin is composed of phenyl propane units and has a highly cross-linked structure close to the network of phenolic resin (Chatterjee & Saito, 2015). The phenolic units of lignin can react with formaldehyde to form methylol derivatives that condense internally or with other phenols under alkaline condition. Lignin has been used in the preparation of carbon foams (Qu, Han, Gao, & Qiu, 2017; Seo et al., 2014; Zeng et al., 2018).

Sucrose is a widely studied carbohydrate for the preparation of carbon foams (Farhan, Wang, Jiang, Li, & Wang, 2016; P. Jana et al., 2013; P. Jana, Fierro, et al., 2016; R. Narasimman, Vijayan, & Prabhakaran, 2014; R Narasimman & Prabhakaran, 2013; R Narasimman et al., 2016; R Narasimman, Vijayan, & Prabhakaran, 2014; R Narasimman et al., 2015; Rajaram Narasimman et al., 2015). It is a disaccharide obtained in abundance from sugar cane. It is composed of two monosaccharides- glucose and fructose. Sucrose is considered as a hydrate of carbon with chemical formula $C_{12}(H_2O)_{11}$. **Figure 1.15** depicts the molecular structures of tannin, lignin and sucrose.

1.4.4 Carbon foam preparation methods

The carbon foams are prepared by the carbonization of polymer foams formed from their precursor resins. The methods such as foaming and setting, polymer foam replication and sacrificial templating are used for the conversion of precursor resins to polymer foams. The carbon foam preparation methods are described in the following section.

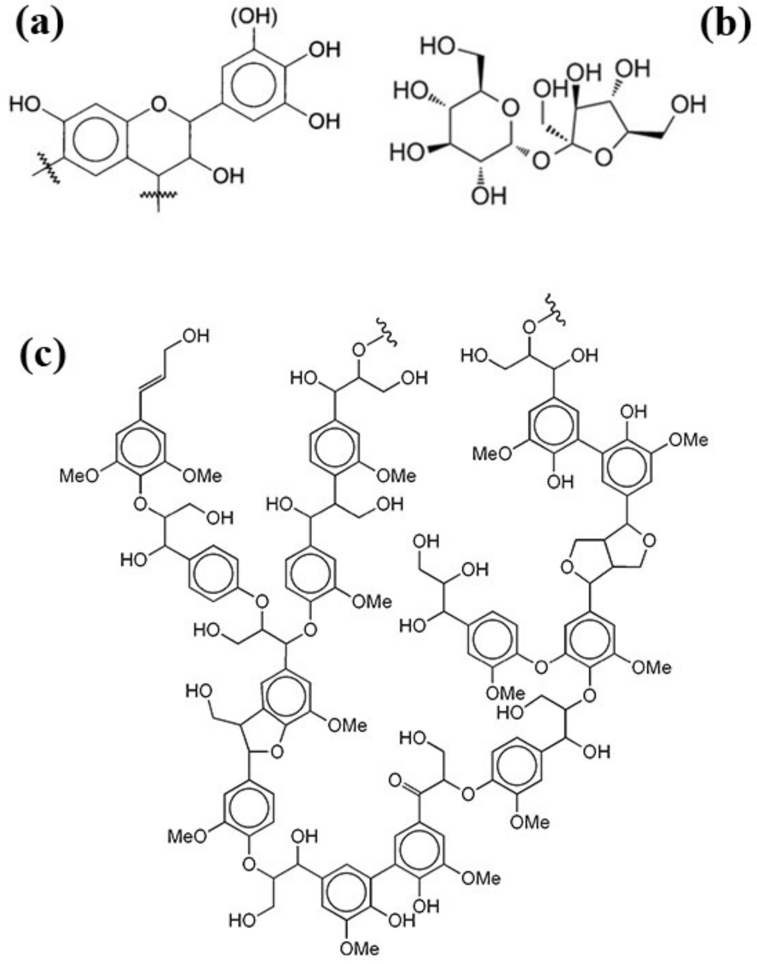

Figure 1.15 Molecular structures of (a) tannin (b) sucrose and (c) lignin (Gandini, 1989; “Lignin - American Chemical Society,” n.d.)

1.4.4.1 Foaming and setting of carbon precursor resins

This method uses pitch or polymer resin as precursors for the preparation of carbon foams. Foaming involves the creation of gas bubbles in the liquid carbon precursor followed by stabilizing them by further polymerization and cross-linking to a rigid solid. The gas bubbles are generated either by using a blowing agent or partial decomposition of the carbon precursor resin itself. Surfactants are often used for the interim stabilization of the gas bubbles in the liquid precursor resin. There are low pressure and high-pressure methods for the foaming of carbon precursor resins. In low-pressure method, the carbon precursor resin containing the blowing agent and surfactant is heated for foaming (Qiulong Li et al., 2016; R Narasimman & Prabhakaran, 2012; Prabhakaran et al., 2007; Szczurek et al., 2013; Liying Zhang et al., 2016; Zúñiga Ruiz et al., 2015). In this, evaporation or decomposition of the blowing agent creates bubbles which are stabilized by the surfactant and finally set by further polymerization and cross-linking. In high-pressure method, the precursor resin/pitch is heated in a closed chamber under pressure (C. Chen et al., 2006; Eksilioglu et al., 2006; Gallego & Klett, 2003; Khan et al., 2017; J. Klett et al., 2000; Lei et al., 2010; S. Li et al., 2011). The foaming is achieved by lowering pressure and temperature in a controlled fashion. Heating the carbon precursor resins at high-temperature releases low molecular weight gaseous molecules which dissolve in the liquid resin under the pressure. Upon releasing the pressure, these dissolved gases nucleate into bubbles. The bubbles are stabilized by solidification of the molten precursors by cooling. The organic foam thus obtained is then oxidative-stabilized by heating in air. This is followed by carbonization and graphitization in an inert atmosphere to obtain carbon foams. The flow chart of the foaming method is provided in **Figure 1.16**.

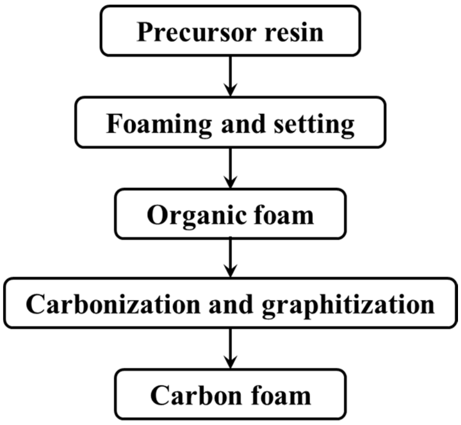

Figure 1.16 Flow chart of the foaming technique used in the preparation of carbon foams

The parameters controlling the foaming time, porosity, pore size and pore size distribution of carbon foams are foaming temperature, the concentration of blowing agent and surfactant concentration. The conventionally used blowing agents are pentane, azodicarbonamide, diethyl ether and borneol (M. Liu et al., 2007; Tondi, Fierro, et al., 2009; Tondi, Pizzi, Masson, & Celzard, 2008; Tondi, Pizzi, Pasch, & Celzard, 2008; J.-H. Yang et al., 2013; S. P. Zhang et al., 2010). Blowing agents such as boric acid, aluminium nitrate, silver nitrate and iron nitrate are used in the thermo-foaming of sucrose (De Araújo, Villarroel-Rocha, De Souza, Sapag, & Pergher, 2019; R Narasimman &

Prabhakaran, 2012, 2013). In these, faster foaming is due to the catalytic activity of H^+ formed either by complexation of boric acid with polyols or hydrolysis of metal nitrates. **Figure 1.17** shows the SEM image of a typical carbon foam derived from coal tar pitch.

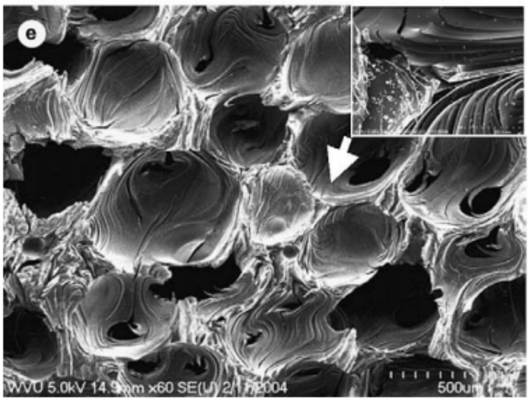

Figure 1.17 SEM image of carbon foam derived from coal tar pitch (C. Chen et al., 2006)

Lorjai et al. reported the preparation of carbon foams by carbonizing polybenzoxazine foams at 800 °C (Lorjai et al., 2009). The carbon foams exhibited density and compressive strength of 0.48 g cm^{-3} and 9.5 MPa, respectively. Preparation of polybenzoxazine-derived vitreous carbon foams was also reported by Ruiz et al. and by Hao et al through a self-induced foaming process followed by carbonization (Hao et al., 2011; Zúñiga Ruiz et al., 2015). Low-density carbon foam (0.15 g $cm^{-3)}$ with intrinsically nitrogen-doped structure was prepared from phthalonitrile using azodicarbonamide as a blowing agent (Liying Zhang et al., 2016). The foamed phthalonitrile resin was cured and carbonized at temperatures in the range of 600-1000 °C to obtain carbon foams. One of the earliest attempts to synthesize carbon foam from sucrose was reported by Prabhakaran et al (Prabhakaran et al., 2007). The method involved foaming and setting of a resin obtained by heating acidic aqueous sucrose solution followed by carbonization. The low-density foams (115–145 mg cm^{-3}) exhibited electrical conductivity in the range 1.5×10^{-5} to 0.2 ohm^{-1} cm^{-1}. The aqueous sucrose resin was also used as a precursor in the preparation of carbon foams in the works reported by Jana et al (P. Jana et al., 2013; P. Jana, Palomo del Barrio, et al., 2016). Narasimman et al. reported the preparation of carbon foams by thermo-foaming of molten sucrose followed by carbonization. (R Narasimman & Prabhakaran, 2012, 2013; R Narasimman et al., 2015). A self-blowing system based on low-cost precursors, mainly tannin and furfuryl alcohol, was used to obtain glass-like carbon foams (Tondi, Fierro, et al., 2009). The foams exhibited compressive strength of 2.4 MPa and anisotropic thermal conductivities with a value of 0.44 W m^{-1} K^{-1} in the z-direction and 0.35 W m^{-1} K^{-1} in the transverse direction. The SEM image of carbon foam derived from aqueous sucrose resin by thermo-foaming is provided in **Figure 1.18**.

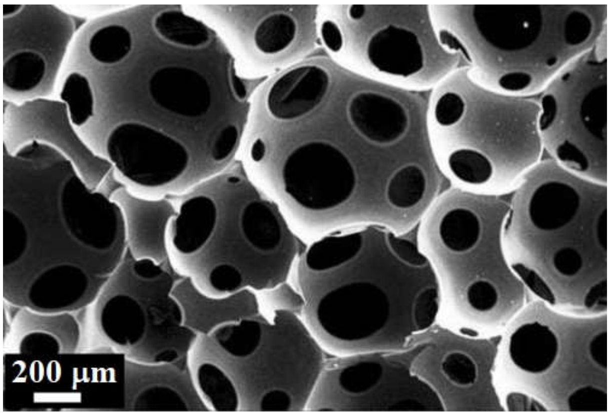

Figure 1.18 SEM photomicrograph of carbon foam prepared from aqueous sucrose resin (Prabhakaran et al., 2007)

One major limitation of the foaming method is the heterogeneity of the pore structure. During foaming, the polymerization of the precursor and/or the decomposition of the foaming agent generate volatile gases, causing an increase in the foam volume. The pressure within the foam, however, is rarely uniform. The lower regions of the foam (near the bottom of the mould) experience higher pressures than the regions near the surface (W. Zhao, Pizzi, Fierro, Du, & Celzard, 2010). This results in a large variation in the cell size within the foam. The bottom region of the foams has predominantly larger cells and exhibits large heterogeneity than the top region. The cell size-dependent properties, viz. apparent density, mechanical and thermal properties, would also show large variations in foam samples obtained from the same large foam body.

1.4.4.2 Replication technique

The polymer foam replication method is used for the preparation of reticulated carbon foams. Replication is a technique where the carbon precursor resin is impregnated into a polymeric foam template followed by squeezing to obtain a thick layer of the precursor over the surface of the polymer foam ligaments. This process is repeated several times to obtain a uniform and thick resin coating. Subsequently, the resin-impregnated polymer foam is heated to cross-link the resin and carbonized/graphitized to obtain carbon foams with pore structure analogous to that of the polymer foam. The polymer foam template decomposes during the carbonization. The flowchart of the synthesis process is provided in **Figure 1.19**.

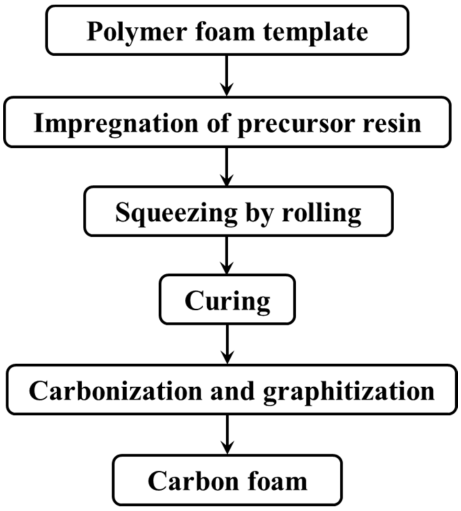

Figure 1.19 Flowchart of the preparation of carbon foams via replication method

Polyurethane (PU) foams of a range of pore sizes have been utilized as templates for the preparation of reticulated carbon foams. Carbon precursor resins such as coal tar pitch, phenol-formaldehyde, polyimide and poly furfuryl alcohol are used for the preparation of reticulated carbon foams (Y. Chen et al., 2007; Farhan, Wang, Jiang, & Li, 2016; P. Jana et al., 2013; M. Karthik, Faik, Doppiu, Roddatis, & D'Aguanno, 2015; Rajeev Kumar, Dhakate, & Mathur, 2013; Rajeev Kumar, Kumari, Mathur, & Dhakate, 2015). Jana et al reported the preparation of reticulated amorphous carbon foams from aqueous sucrose solution using household cleaning pad as foam template (P. Jana et al., 2013). On the other hand, reticulated graphitic carbon foams are prepared by coating slurry of mesophase pitch powder on PU template followed by drying, oxidative stabilization, carbonization and graphitization (Rajeev Kumar, Dhakate, & Mathur, 2013; Rajeev Kumar et al., 2015). **Figure 1.20** shows the SEM image of reticulated carbon foam derived from sucrose using household cleaning pad as a template.

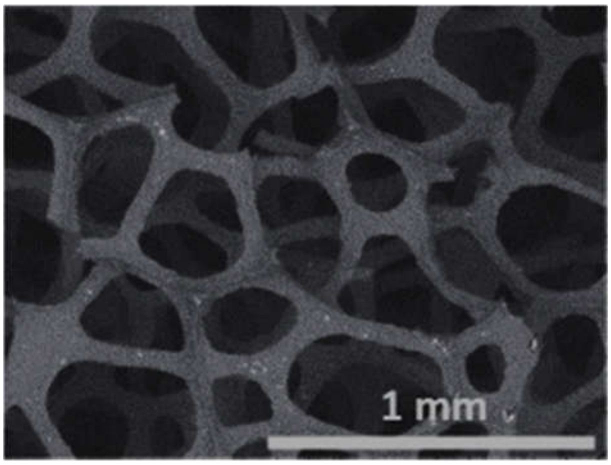

Figure 1.20 SEM image of reticulated carbon foam derived from sucrose prepared via replication technique (P. Jana et al., 2013)

1.4.4.3 Sacrificial templating method

In sacrificial templating, the pores are generated by the extraction/decomposition of uniformly dispersed templates in the carbon precursor resin. Various types of sacrificial templating methods are employed in the processing of carbon foams viz, (i) particle templating (ii) emulsion templating and (iii) ice templating. In particle templating, polymeric beads such as polymethyl methacrylate (PMMA) or inorganic silica particles are dispersed in the carbon precursor resin by mechanical or ultrasonic agitation. The precursor is then set by further polymerization and cross-linking. The set precursor containing the pore template is then pyrolyzed in an inert atmosphere. The polymeric bead templates decompose during pyrolysis thus generating pores in the carbon matrix (K. T. Lee, Lytle, Ergang, Oh, & Stein, 2005; Seo et al., 2014). On the other hand, the silica particle templates are leached out either using strong NaOH or HF solution (Eltmimi et al., 2010; He et al., 2013; Chengdu Liang, Dai, & Guiochon, 2003). A flow chart representing the steps involved in the preparation of carbon foams by sacrificial templating is provided in **Figure 1.21**.

Seo et al. reported the synthesis of carbon foams from an integrated cross-linked network of lignin–resorcinol–formaldehyde in the presence of PMMA particles as the pore generator, followed by carbonization (Seo et al., 2014). The prepared lignin-derived carbon foams had partially open cell structures. The carbon foams had bulk densities in the range of 0.37–0.60 g cm^{-3}.

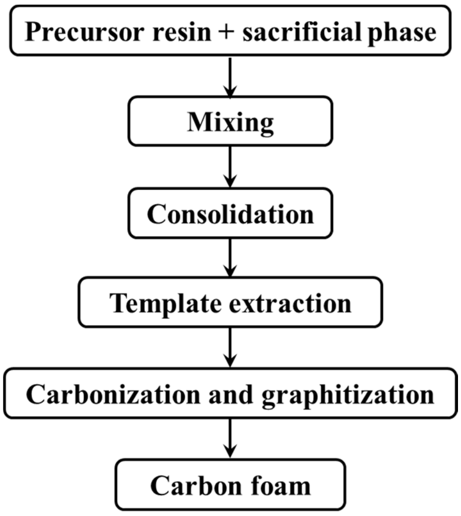

Figure 1.21 Flowchart of the sacrificial template method used in the preparation of carbon foams

In emulsion templating, an immiscible organic liquid is dispersed in an aqueous carbon precursor resin with the help of a suitable surfactant to form an emulsion (Alam et al., 2013; Gross & Nowak, 2010; Patil et al., 2016; Szczurek et al., 2014; Thongprachan, Yamamoto, Chaichanawong, Ohmori, & Endo, 2011; R. T. Woodward et al., 2016, 2017, 2018; T. R. Woodward, De Luca, Roberts, & Bismarck, 2016). After the emulsion is formed the carbon precursor resin is cured by further polymerization and cross-linking. Subsequent drying and carbonization produce the carbon foam. This method is particularly useful in producing carbon foams with spherical, micrometre-sized cells. The porosity is controlled by varying the organic to the aqueous liquid volume ratio. Very low-density foams are achieved by forming high internal phase emulsions (HIPE) (Patil et al., 2016; R. T. Woodward et al., 2017; T. R. Woodward et al., 2016).

Ice-templating involves the preparation of a cross-linked hydrogel from an aqueous polymeric resin (Mukai, Nishihara, Yoshida, Taniguchi, & Tamon, 2005; Murakami, Satoh, Ogino, & Mukai, 2013; Nishihara, Mukai, & Tamon, 2004; Zeng et al., 2018). The water present in the hydrogel is frozen by cooling. The removal of ice crystals by freeze-drying followed by carbonization produces carbon foam. Murakami et al. used the ice-templating method to form a honeycomb-type carbon foam of straight macropores of a few tens of micrometres in diameter using various resorcinol-formaldehyde (RF) hydrogels (Murakami et al., 2013). An aqueous solution of resorcinol and formaldehyde was heated at 303 K to polymerize and the hydrogels obtained were immersed in liquid nitrogen to freeze water. The frozen gels were immersed in tertbutyl alcohol (t-BuOH) to exchange the water included in their structure with t-BuOH. The materials washed with tBuOH were freeze-dried at 263 K, cut into small pieces using a razor blade, and carbonized to obtain carbon foams. SEM images of carbon foams produced using sacrificial polymer bead templating, emulsion templating and ice templating are provided in **Figure 1.22**.

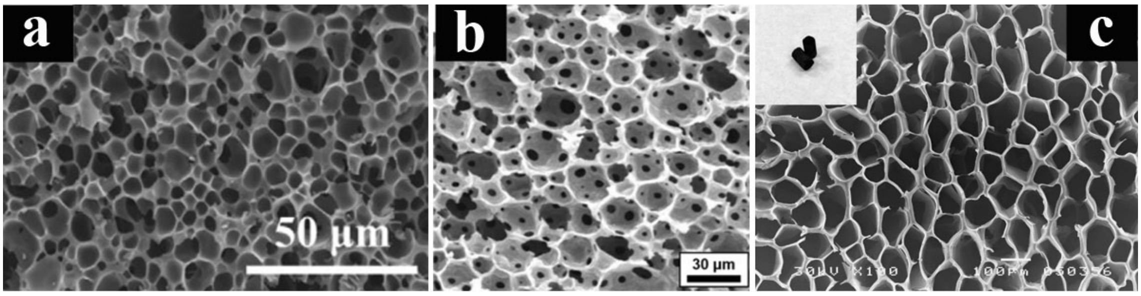

Figure 1.22 SEM Images of carbon foams prepared via (a) particle templating using PMMA beads (b) emulsion templating using poly (DVB) HIPE and (c) ice templating of resorcinol-formaldehyde resin (Murakami et al., 2013; Seo et al., 2014; T. R. Woodward et al., 2016)

1.5 Silicon carbide (SiC) foams

Silicon carbide (SiC) is an important ceramic material used in a wide range of commercial and industrial applications. The Si-C bond in SiC is highly covalent in nature. The SiC ceramic is a wide bandgap semiconductor with a room temperature thermal conductivity of 41 and 25.5 W m^{-1} K^{-1} for α-SiC and β-SiC, respectively (Davis, 2017; Pierson, 1996). This makes it suitable for electronic applications requiring high-power, high-frequency, and high-temperature (Casady, 2000). In the manufacturing industry, it is one of the most popular abrasive materials used in grinding wheels, water jet cutting, sandblasting and sandpapers (Rowe, 2014). Composites of SiC with carbon are used as structural materials in the aerospace industry and also as brake discs in the automotive industry.

Porous SiC ceramics have shown exceptional efficacy as catalytic supports, hot-gas and molten metal filters, membrane supports, gas-burner media, and lightweight structural parts for high-temperature applications (Afsharvahid, Ashman, & Dally, 2008;

Bai, 2010; Biamino et al., 2010; Bolivar et al., 2010; Brockmeyer & Aubrey, 2008; S. Dong et al., 2018; Duan et al., 2014; Duong-Viet et al., 2016; Eom, Kim, & Raju, 2013; Gianella, Gaia, & Ortona, 2012; Jiao, Jiang, Yang, & Zhang, 2012; Jiao et al., 2015; Caiyun Liang et al., 2017; Ou et al., 2019, 2017; Trimis & Durst, 1996; Vega Bolivar et al., 2010; Vogt, Györfy, Herzog, Graule, & Plesch, 2007; Wood & Harris, 2008). The high-temperature stability, low thermal expansion coefficient, high oxidation resistance and excellent dielectric behaviour are some of the key properties of SiC which makes it attractive in high-temperature applications. Properties of porous SiC ceramics such as porosity, pore size, and degree of interconnectivity are influenced by the processing techniques involved.

SiC ceramic foams are prepared either from SiC fine powders or pre-ceramic polymers. Processing techniques such as foaming, polymer foam replication and sacrificial templating are used for the preparation of SiC foams. In the foaming method, a suspension of SiC powder in an aqueous medium containing a surfactant is foamed by incorporating a gas (D. C. Jana, Sundararajan, & Chattopadhyay, 2017). The surfactant provides interim stabilization to the bubbles in the suspension medium. The foamed suspension is permanently set into a gelled body either by polymerization of some organic monomers or coagulation of the suspension. The gelled body is further dried and sintered to produce the SiC foam. Partially hydrophobized particles are used instead of surfactants to produce wet foams with superior stability in direct foaming method and such foams are called particle-stabilized foams (Jang et al., 2017). The direct foaming of molten pre-ceramic polymers is also used for the preparation of SiC ceramics (Bao, Nangrejo, & Edirisinghe, 1999; Fukushima & Colombo, 2012; Hossain, Sarkar, Oraon, & Ranjan, 2016; Matthews, Edirisinghe, & Folkes, 1999; Mishra, Kumar, Ranjan, & Prasad, 2018). In this, a pre-ceramic polymer such as polycarbosilane is foamed by heating in the presence of a blowing agent that evaporates at low temperature. Subsequent curing and pyrolysis of the foamed green body produce SiC foams. Fukushima and Colombo prepared macrocellular SiC foams using a polycarbosilane pre-ceramic polymer and a chemical blowing agent - azodicarbonamide (Fukushima & Colombo, 2012).

Replication is the most common technique for synthesizing SiC ceramic foams with reticulated microstructure. The process involves impregnation of porous templates such as polyurethane foams with aqueous SiC powder slurries or pre-ceramic polymers followed by pyrolysis and pressure-less sintering at elevated temperatures (Bao, Nangrejo, & Edirisinghe, 2000; R Mouazer, Mullens, Thijs, Luyten, & Buekenhoudt, 2005; Vogt et al., 2007; X. Zhu, Jiang, & Tan, 2002; X. Zhu, Jiang, Tan, & Zhang, 2001). SiC foams with anisotropic pore structure are also prepared using wood-derived carbon foams as templates (Esposito, Sciti, Piancastelli, & Bellosi, 2004; Greil, Lifka, & Kaindl, 1998; Herzog, Klingner, Vogt, & Graule, 2004; Ota et al., 1995; Varela-Feria, Martínez-Fernández, De Arellano-López, & Singh, 2002). Typically, the synthesis involves (i) pyrolysis of wood for making carbon foams and (ii) infiltration of the carbon foams with gaseous or liquid Si, SiO_2, or TEOS to form SiC or Si-SiC ceramics. Porous SiC derived from wood templates exhibit much smaller pore size (10-300 µm) in comparison to templating approach using polymer foams. **Figure 1.23** shows the SEM image of porous SiC derived using carbonized pine wood as a template.

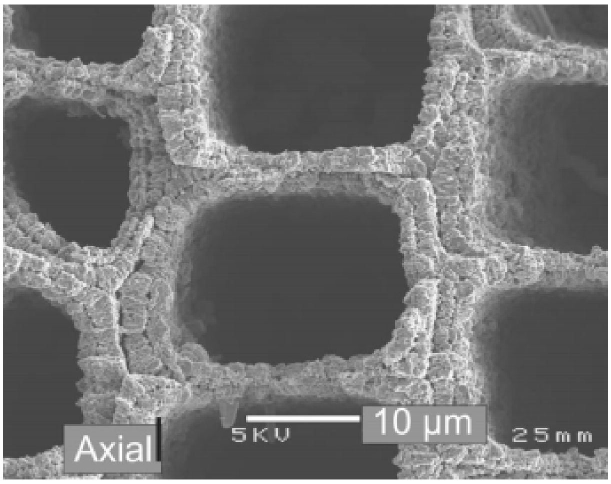

Figure 1.23 Porous SiC derived from carbonized pine (autumn section) shown in the axial direction (Herzog et al., 2004)

Freeze-casting and emulsion templating methods are also used for the preparation of SiC ceramic foams. In freeze casting, the SiC powder suspension or pre-ceramic polymer solution is frozen to crystallize the solvent medium and the solvent crystals are subsequently removed by freeze-drying (Ferraro et al., 2018; Fukushima, Nakata, Zhou, Ohji, & Yoshizawa, 2010; F. Wang et al., 2016; F. Xue et al., 2018; Yoon, Lee, Kim, & Koh, 2007; Yoon, Park, Kim, & Koh, 2007). The porous green ceramic/pre-ceramic polymer thus obtained is heat-treated in an inert atmosphere at high temperature to produce SiC ceramic foams. The pore size is tailored by controlling the freezing process. In this, the crystallized solvent acts as a pore template. The unidirectional freezing is often used to create foams with unidirectionally aligned pores. In emulsion templating, an oil phase is dispersed in an aqueous slurry of SiC powder containing an organic monomer using a suitable emulsifying agent (Ferraro et al., 2018; Ge, Wang, Yuan, Dong, & Li, 2014). Subsequent setting by polymerization of the organic monomer followed by drying and sintering produce SiC ceramic foam. In this, the dispersed oil phase acts as a pore template. Emulsion templating is also used for the preparation of SiC foams from pre-ceramic polymers (Frind, Oschatz, & Kaskel, 2011; Ungureanu et al., 2011; Vakifahmetoglu, Balliana, & Colombo, 2011). In this, water is dispersed in a solution of pre-ceramic polymers in an oil medium. The emulsion produced is stabilized by cross-linking of the pre-ceramic polymer followed drying and high-temperature heat treatment to produce SiC ceramic foams. The formation of high internal phase emulsion (emulsions with > 74 vol.% dispersed phase) facilitates the preparation of SiC foams of ultrahigh porosity. **Figure 1.24** shows the SEM images of SiC foams prepared by freeze casting and emulsion templating.

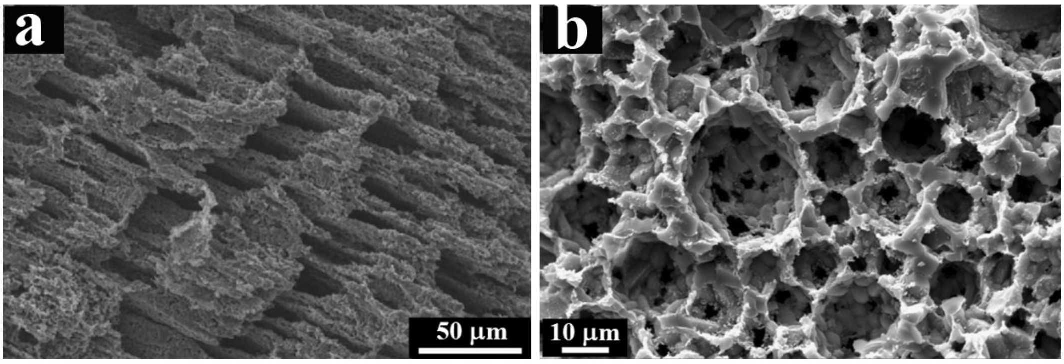

Figure 1.24 SEM micrographs of porous SiC obtained by (a) freeze-casting (F. Wang et al., 2016) and (b) emulsion templating techniques (Ge et al., 2014)

Porous SiC with controlled porosity and pore structure is synthesized by homogeneously dispersing a solid sacrificial phase such as polymer microbeads within a pre-ceramic polymer matrix. The sacrificial phase is then extracted by leaching or by decomposition to yield interconnected porous ceramic structures after pyrolysis (Chae, Kim, Song, Kim, & Narisawa, 2009; Colombo & Bernardo, 2003; Eom, Kim, Song, & Kim, 2008; Y.-W. Kim, Eom, Wang, & Park, 2008; Y.-W. Kim, Kim, Song, Kim, & Park, 2005; Resmi et al., 2015; I.-H. Song, Kwon, Kim, & Kim, 2010). Poly(methyl methacrylate) and poly(methylmethacrylate-co-ethylene glycol dimethacrylate) microbeads have been used as sacrificial templates (Colombo & Bernardo, 2003; Y.-W. Kim et al., 2005). The SEM image of porous SiC prepared using sacrificial microbeads as pore template is presented in **Figure 1.25**.

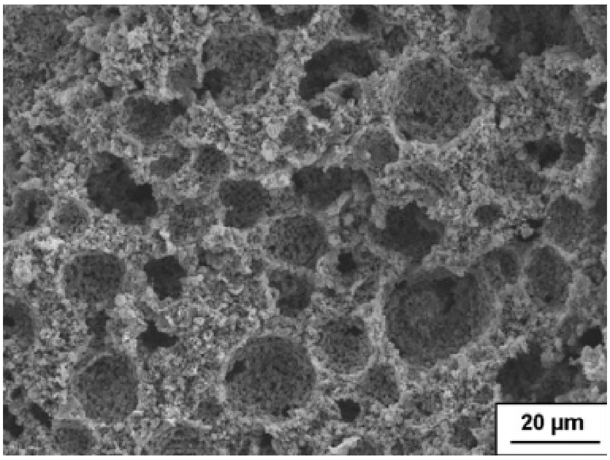

Figure 1.25 Porous SiC ceramics prepared sacrificial templating method using 5 wt% hollow microspheres and sintered at 1800 °C (Eom et al., 2008)

The high thermal conductivity, high resistance towards oxidation, high mechanical strength and chemical inertness of silicon carbide (SiC) foam ceramics offer great advantage in applications such as catalyst support (Duong-Viet et al., 2016; Jiao et al., 2012, 2015; Ledoux & Pham-Huu, 2001; Ou et al., 2019). The open cellular nature along with high porosity also significantly improves the diffusivity of the gaseous precursors and products with minimal pressure drop. Porous SiC ceramics have been widely used in burner technologies as it provides stabilization for the combustion process and improves effective heating (Afsharvahid et al., 2008; AL-Hamamre, Diezinger, Talukdar, Von Issendorff, & Trimis, 2006; Gianella et al., 2012; Kamal & Mohamad, 2005; Wood & Harris, 2008). Stabilized combustion is superior over conventional combustion processes in terms of reduced NOx and CO emissions and allows the control of the reaction zone temperature. Porous SiC shows promise for TPS application, owing to its thermal stability at very high temperature, low density, high stiffness and fairly good strength, high hardness, erosion resistance and self-passivating behaviour in oxidising environment (Biamino et al., 2010; Vega Bolivar et al., 2010; Xiuwu Wang et al., 2019). The porous SiCs have been investigated as high-temperature EMI shielding materials owing to its excellent dielectric property and thermal stability (S. Dong et al., 2018; Duan et al., 2014, 2017; Quan Li et al., 2013; Caiyun Liang et al., 2017). In the recent past, Si-SiC foams have been investigated as a volumetric absorber in concentrated solar power plants for sustainable energy production (Bai, 2010; Rousseau et al., 2013; Sano, Iwase, & Nakayama, 2012; Z. Wu, Caliot, Flamant, & Wang, 2011). **Figure 1.26** shows the photographic images of SiC foams used as catalyst support and gas burner.

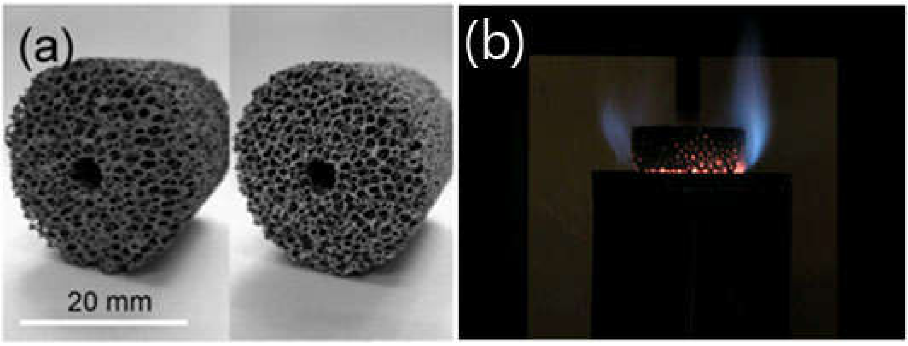

Figure 1.26 (a) Optical image of porous SiC support (left) and ZSM-5 catalyst coated SiC foam (right) (Jiao et al., 2012) and (b) Photographic image of porous SiC ceramic as a medium for combustion (Kamal & Mohamad, 2005)

1.6 Microcellular carbon and silicon carbide foams

The majority of the foaming and template-based methods reported in the literature produce carbon and SiC foams with relatively large cell size. The large cell size makes the foams fragile. This results in debris formation during storage and transportation of carbon and SiC foam bundles. The debris formation is a serious concern during construction, maintenance and cleaning of carbon and SiC foam-based structures. Decreasing the cell size is the way to increase the compressive strength and debris formation resistance of carbon and SiC foams. Foams with cell sizes in the range of 0.1 to 100 mm are called microcellular foams. In smaller cells, the strut strength is higher because the strut surface area is much smaller, which decreases the probability of finding a flaw with critical dimension (Colombo & Bernardo, 2003). Reducing the cell size offers an advantage in terms of higher surface area to volume ratio. In addition, the smaller cells walls in these foams restrict the heat transfer by conduction due to enhanced phonon scattering (Alvarez, Jou, & Sellitto, 2010; Sumirat, Ando, & Shimamura, 2006; Sundarram & Li, 2013).

A few methods have been reported for the preparation of microcellular carbon foams. One of the methods was the pyrolysis (1100-1200 °C) of microcellular poly (acrylonitrile) foam obtained by a phase inversion process (Aubert & Sylwester, 1991). The process involved preparation of the PAN precursor foams by thermally induced phase separation (TIPS) of PAN solutions followed by gelation, freezing followed by freeze-drying. Prior to carbonization, the PAN foams were subjected to thermal pre-treatment in the air for cyclization of PAN to the "ladder polymer" structure. The density of the foams varied in the range of 0.02-0.2 g cm^{-3} with cell size in the sub-micrometre to 20 μm range.

Infiltration of phenol-formaldehyde resin into a sintered NaCl powder compact followed by curing, pyrolysis and NaCl removal was another method reported for the preparation of microcellular carbon foam (Pekala & Hopper, 1987). The preparation of NaCl powder compact for infiltration involved classification of sodium chloride (NaCl) particles in the desired size range followed by cold pressing into bars and sintering. The pyrolysis temperature was restricted below the melting point of NaCl. The NaCl removal was achieved by extraction using water. The density of the carbon foam obtained was in the range of 0.03 to 0.1 g cm^{-3} with cell sizes less than 20 μm. SEM image of microcellular carbon foam prepared via this method is shown in **Figure 1.27**.

High-pressure foaming of an ethanol solution of phenol-formaldehyde resin in an autoclave followed by pyrolysis at 1073 K was used for the preparation of microcellular carbon foams with high compressive strength (Lei et al., 2010). Phenol–formaldehyde (PF) novolac resin prepared by the polymerization of phenol and formaldehyde (mole ratio1:0.8) with oxalic acid as catalyst was employed as raw material with hexamine as curing agent. The carbon foam produced had bulk density, average pore size, compressive strength and thermal conductivity of 0.73 g cm^{-3}, 20 nm, 98.3 MPa and 0.24 W m^{-1}K^{-1}, respectively.

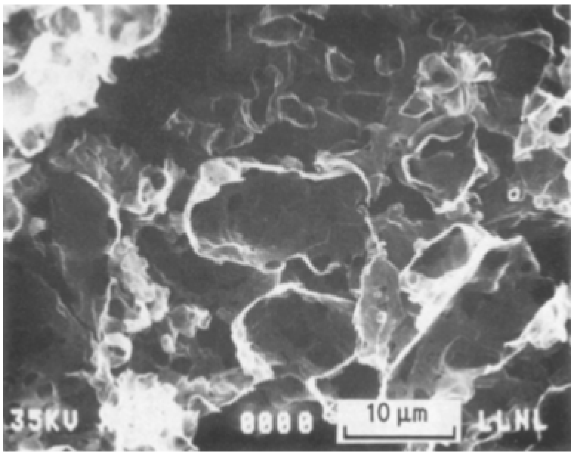

Figure 1.27 High-magnification SEM image of microcellular carbon foams prepared from the phenol-formaldehyde resin by sacrificial templating (Pekala & Hopper, 1987)

Anderson et al. produced microcellular graphitic foams with the graphitic planes aligned along the struts from the anisotropic pitch (Anderson, Kearns, Klett, & Roy, 2000). The process involved jet-milling of pitch pellets into particles of size in the range of 1-3 μm and then pressing into pre-forms. The pitch pre-forms were subsequently heated in a pressure vessel under nitrogen pressure. The as-obtained foam materials were removed, oxygen stabilized, carbonized in a nitrogen environment at 900 °C and graphitized at 2700°C. The authors were able to control the pore size by varying the pressure, temperature and hold time. It was observed that the foams prepared at lower temperature and pressure and longer hold time yielded smaller cell size and higher density. On the other hand, foams prepared at a higher temperature, lower pressure, and shorter hold time possessed large cell size and lower density. The graphitized foams exhibited thermal conductivity in the range of 16.9 to 74.8 W m^{-1} K^{-1}. Using a similar approach, Klett et al. prepared high thermal conductivity microcellular carbon foams from Conoco dry mesophase with cell size in the range of 60 to 90 μm (J. Klett et al., 2000). The graphitized (2800 °C) carbon foams exhibited a density range and a maximum thermal conductivity of 0.35 to 0.59 g cm^{-3} and 134 W m^{-1} K^{-1}, respectively.

Preparation of microcellular graphene foams was reported by Shen et al. and Jiang et al. (Jiang, Xin, & Li, 2016; Shen et al., 2016). Microcellular graphene foam prepared by reducing and foaming graphene oxide film showed EMI shielding effectiveness of 26.3 dB over a frequency range of 8.2-59.6 GHz (Shen et al., 2016). Jiang et al fabricated microcellular 3D graphene foams via ambient pressure chemical vapour deposition (APCVD) with electroless plated nickel (Ni) foam templates (Jiang et al., 2016) using methane as carbon source. The graphene foams exhibited pore size less than 100 µm, density of 0.0020 g cm^{-3}, and a pore wall thickness of about 5 nm.

Microcellular SiC foams are primarily prepared through gas blowing and sacrificial bead techniques. In the gas blowing technique, pre-ceramic polymers are used as precursors and carbon dioxide is used for blowing. (Y.-W. Kim, Kim, Wang, & Park, 2003; Y.-W. Kim & Park, 2003; Wolff, Ceron Nicolat, Fey, Greil, & Münstedt, 2012; Wolff & Münstedt, 2011). A typical gas blowing technique involves: (i) saturating pre-ceramic polymers using gaseous, liquid, or supercritical CO_2, (ii) nucleating and growing a large number of bubbles by creating thermodynamic instability via a rapid pressure drop or heating, and (iii) transforming the microcellular pre-ceramics into microcellular ceramics by pyrolysis and subsequent sintering (Y.-W. Kim et al., 2005). Supercritical and gaseous CO_2 were found to be more effective as blowing agents than liquid CO_2, yielding a higher cell density. The microcellular porous SiC ceramics prepared by CO_2 blowing method using a 55% polycarbosilane and 45% polysiloxane formulation have cell density, cell size and porosity of 9.4×10^9 cells cm^{-3}, ~2–4 µm and 45.0%, respectively.

Replication method using sintered NaCl powder compact as pore template and polycarbosilane as SiC precursor was also reported for the preparation of microcellular SiC foams (Fitzgerald, Michaud, & Mortensen, 2005). In this, a porous sodium chloride compact formed by sintering was first pressure-infiltrated with molten polycarbosilane. The polymer was cured by heating at 435 °C under 7 MPa in an argon atmosphere. The salt template was leached with distilled water. After the dissolution of the salt, the resulting polymer foam was pyrolyzed to form a silicon carbide foam. The porous SiC obtained had cell sizes in the range of 10-100 µm.

A polymer-based sacrificial template was also investigated for the preparation of microcellular SiC ceramics (Kultayeva, Ha, Malik, Kim, & Kim, 2019). In this, thoroughly mixed β-SiC powder and PMMA microbeads (~8 µm) were pressed in a mould under 30 MPa of pressure. Subsequent heating to remove the PMMA template and sintering at 1800-2000°C produced microcellular SiC ceramics. The porosity of the microcellular SiC ceramic could be controlled in the range of 28–64% by adjusting the sacrificial PMMA microbeads content (0–30 wt%) and sintering temperature (1800–2000 °C). Both electrical and thermal conductivities of the porous SiC ceramics decreased, from 7.7 to 1.7 Ω^{-1} $cm^{-1}$and from 37.9 to 5.8 W m^{-1} K^{-1}, respectively, with an increase in the porosity from 30 to 63%.

1.7 Objectives and Scope of the thesis

Preparation by foaming and carbonization of precursor resins yields carbon foams with large cell sizes. The large cell sizes result in highly brittle foams with low compressive strength. The thermal conductivity of foams is also largely dependent on cell size. Smaller cell size restricts heat conduction by phonon-phonon interactions and subdued convectional heat transfer of gases in the cells. Moreover, the large cell sizes limit the adhesion of carbon foams on ceramics-based facing sheets used in the preparation of sandwich composites for aerospace applications. To improve the compressive strength, thermal insulation and adhesion of facing sheets on foam surfaces; it is essential to reduce the cell size of the carbon foams. While petroleum or coal-based pitches and synthetic polymers are conventionally used as precursors, the rapidly depleting petroleum sources and the highly expensive synthetic polymers have necessitated the use of renewable biomolecules such as tannin, lignin and sucrose as carbon precursors. The preparation of SiC foams by foaming of pre-ceramic polymers and ceramic powder slurries also suffer from complicated synthesis procedures and expensive precursors in addition to the issues associated with large cell size. The objectives of this thesis are the preparation of microcellular carbon and SiC foams using a simple NaCl particle templating method by using sucrose as a carbon source and their microstructure, compressive strength and thermal conductivity characterization.

The specific objectives of the thesis are summarized thus:

1. To prepare microcellular carbon foams by compression moulding using sucrose as carbon precursor and NaCl particle as pore template.
2. To use glycerol as a plasticising additive to widen the porosity range of microcellular carbon foams from sucrose and NaCl particle template

3. To prepare thermally conducting microcellular carbon foams using graphite powder as conductive filler by NaCl templating for using as a host for wax-based phase change materials
4. To prepare microcellular SiC foams from sucrose and silicon powder by NaCl particle templating
5. To characterize the microcellular carbon and SiC foams by microstructure, compressive strength, electrical conductivity, thermal conductivity and textural property measurements

1.8 Organization of the thesis

This thesis describes the processing methodology for the preparation of microcellular carbon and SiC foams from sucrose, a naturally renewable carbon precursor, using a simple NaCl particle templating method. The research focuses on the effect of template concentration on microstructure, density, compressive strength and thermal conductivity of the microcellular foams. The thesis is organized into six chapters.

Chapter 1 discusses the state-of-the-art literature survey on porous carbon, carbon foams and SiC foams in view of their preparation technique, properties and applications. Definition of the research problem and objectives of the thesis is contained within **Chapter 1**.

In **Chapter 2**, the preparation of microcellular carbon foams from molten-sucrose-NaCl pastes via a compression moulding technique is described. The effect of NaCl particles on the setting by polymerization of molten sucrose and the carbon yield is investigated. The influence of NaCl powder concentration on density, microstructure, compressive strength and thermal conductivity of microcellular carbon foams is studied and the results are discussed. The limitation of the process to achieve low-density microcellular carbon foams is also discussed.

In **Chapter 3**, glycerol is used as a plasticising additive to overcome the limitation of the sucrose-NaCl system to achieve low-density microcellular carbon foams. Molten sucrose-NaCl-glycerol pastes of mouldable constancy with NaCl to sucrose weight ratios in the range of 1.5 to 3 are studied for their setting characteristics. The low-density microcellular carbon foams prepared from these pastes are characterized by density, microstructure, compressive strength and thermal conductivity measurements. The application of low-density microcellular carbon foams for EMI shielding is also studied.

Chapter 4 deals with the preparation of thermally conducting microcellular carbon foams from sucrose using graphite powder as a conducting filler, NaCl particles as a pore template and glycerol as a plasticizing additive. These foams, prepared at various NaCl to sucrose and graphite to sucrose weight ratios are characterized by density, microstructure, thermal conductivity, compressive strength and contact angle measurements. The form stable carbon foam-wax composites fabricated by infiltration of molten wax are also characterized by microstructure, thermal conductivity and differential scanning calorimetry analysis.

In **Chapter 5**, the preparation of microcellular SiC foams from sucrose and silicon powder using NaCl particle as a pore template and glycerol as a plasticising additive is described. The setting characteristic of the molten sucrose-silicon-NaCl-glycerol pastes is studied by torque-time measurements. The microcellular SiC foams are also characterized with respect to their density, microstructure, compressive strength and thermal conductivity as a function of NaCl to sucrose weight ratio. The EMI shielding property of the foams is characterized for possible application in high-temperature EMI shielding.

In **Chapter 6**, the results of the current work are summarized. A mention of the scope for future research on this subject is also made.

CHAPTER 2

MICROCELLULAR CARBON FOAMS BY COMPRESSION MOULDING OF MOLTEN SUCROSE-NaCl PASTES

2.1 Introduction

Carbon foams are getting renewed interest due to their lightweight, tunable electrical and thermal conductivities, fire resistance, high electromagnetic interference shielding effectiveness and acoustic absorption property (Amaral-Labat et al., 2013; Amini, Aguey-Zinsou, & Guo, 2011; Chung, 2001; Gallego & Klett, 2003; Mesalhy, Lafdi, & Elgafy, 2006). Conventionally, carbon foams are prepared from petroleum/coal tar pitch and synthetic polymers using foaming and polymer foam replication methods (C. Chen et al., 2006; Inagaki et al., 2004; Lorjai et al., 2009; M. xian Wang et al., 2008; X. Wu et al., 2011; Yadav et al., 2011; S. P. Zhang et al., 2010; Zúñiga Ruiz et al., 2015). The depletion of petroleum-based products through overuse and the inherently expensive synthetic polymers have led to a shift in the preparation of carbon foams using renewable plant-based precursors such as sucrose, lignin and tannin (P. Jana, Palomo del Barrio, et al., 2016; Prabhakaran et al., 2007; Seo et al., 2014; Tondi, Fierro, et al., 2009). The foaming and polymer foam replication methods produce carbon foams with large cell sizes. Carbon foams produced via foaming of the carbon precursors contain inhomogeneous pore size distribution and density on account of the variation of cell size in the foaming direction (W. Zhao et al., 2010). Foams possessing large cells have lower mechanical strength and are prone to disintegration during handling and usage which limits their application. Moreover, the bulk thermal conductivity of the foams is inversely related to the cell size as smaller cells restrict the heat transfer via both conduction and convection mechanisms. Small cells enhance the phonon-phonon scattering phenomenon leading to poor thermal conductivity and also restrict convectional heat transfer in the gases residing in the pores (Sundarram & Li, 2013). A decrease in cell size consequently increases the mechanical strength and decreases the thermal conductivity of carbon foams. The foams with cell size smaller than 100 µm are called microcellular foams.

Though a number of reports on the processing of microcellular polymer and ceramic foams are available, preparation of microcellular carbon foams is seldom reported.

The present chapter reports the preparation of microcellular carbon foams from sucrose using NaCl particle as pore templates. Herein, pastes produced by mixing molten sucrose and NaCl powder are compression moulded to form sucrose polymer-NaCl composites. Carbonization of the sucrose polymer-NaCl composite followed by NaCl extraction and high-temperature heat-treatment produce microcellular carbon foams. The NaCl to sucrose weight ratio is adjusted to obtain foams with a wide range of porosities. The setting characteristics of the molten sucrose-NaCl pastes, the NaCl removal kinetics and the carbon yield at various NaCl to sucrose weight ratios are studied. The density, compressive strength, thermal conductivity and textural properties of the carbon foams as a function of the NaCl to sucrose weight ratio are also analysed.

2.2 Experimental

2.2.1 Preparation of microcellular carbon foams

Analytical reagent grade sucrose, NaCl and acetone were procured from Merck India Ltd. Mumbai. The flowchart of the process for the preparation of carbon foams is shown in **Figure 2.1**.

Various amounts of sucrose and NaCl powders were mixed by planetary ball milling (Fritsch, Germany) in an acetone medium for 2 h at a speed of 200 RPM using zirconia grinding balls of 10 mm diameter and zirconia jar of 500 ml capacity. The powder to ball and powder to acetone weight ratios were 1:2 and 3:4, respectively. The selection of acetone as a medium for ball milling was due to the low solubility of NaCl (0.00042 g Kg^{-1}) and sucrose (7 g Kg^{-1}) in acetone. The slurries obtained after ball milling were dried in an air oven at 70 °C in borosilicate glass trays. The compositions of the sucrose-NaCl mixtures used in the study are given in **Table 2.1**.

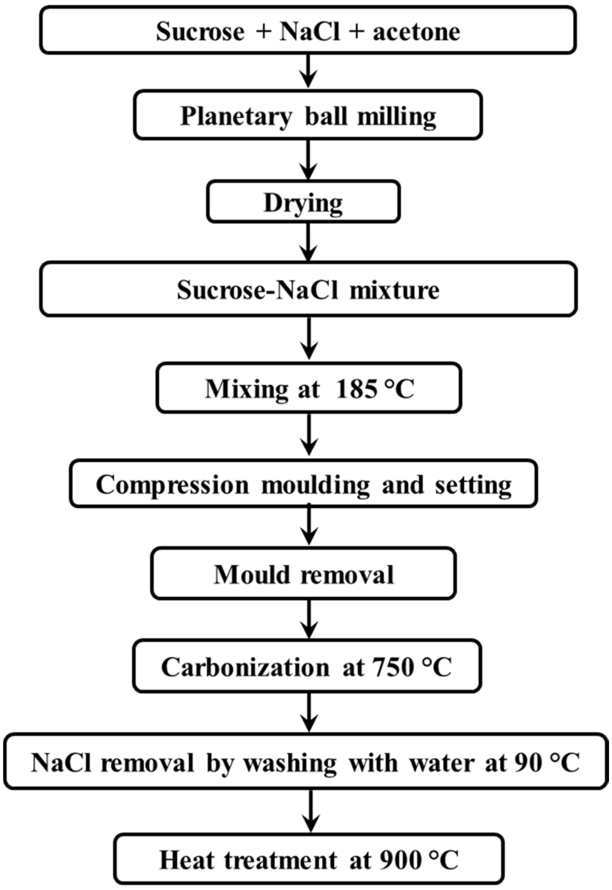

Figure 2.1 Flowchart for the preparation of carbon foams

Table 2.1 Compositions used in the preparation of microcellular carbon foams

Sucrose (g)	**NaCl** (g)	**Sucrose to NaCl weight ratio** ($W_{N/S}$)
100	70	0.7
100	80	0.8
100	90	0.9
100	100	1
100	110	1.1
100	120	1.2

The sucrose-NaCl mixtures thus obtained were heated in an air oven at 185 °C to melt the sucrose and thoroughly mixed with a wooden ladle to form a homogeneous paste. The photograph of molten sucrose-NaCl paste in a glass tray is shown in **Figure 2.2a**. A rectangular stainless steel mould of 10 cm x 10 cm x 2.5 cm size (**Figure 2.2b**) fabricated in-house was used for compression moulding. The molten sucrose-NaCl paste was transferred into the mould cavity, then covered with its lid and gently hot-pressed in a hydraulic press for 3 h. The temperature of the upper and lower platens of the press was kept at 195 °C. The sample was removed from the mould after cooling to room temperature and annealed at 200 °C for 2 h in an air oven. Subsequently, the sample was heated in a box furnace in an argon atmosphere at 750 °C for 2 h using a temperature ramp of 1 °C min^{-1}. The sample was removed from the furnace after cooling down to room temperature in the same inert atmosphere. The sample heat-treated at 750 °C was immersed in distilled water at 90 °C until the whole NaCl present in the body was leached out. The carbon foam produced after NaCl extraction was further heat-treated at 900 °C in the inert atmosphere furnace for 2 h at a temperature ramp of 1 °C min^{-1}.

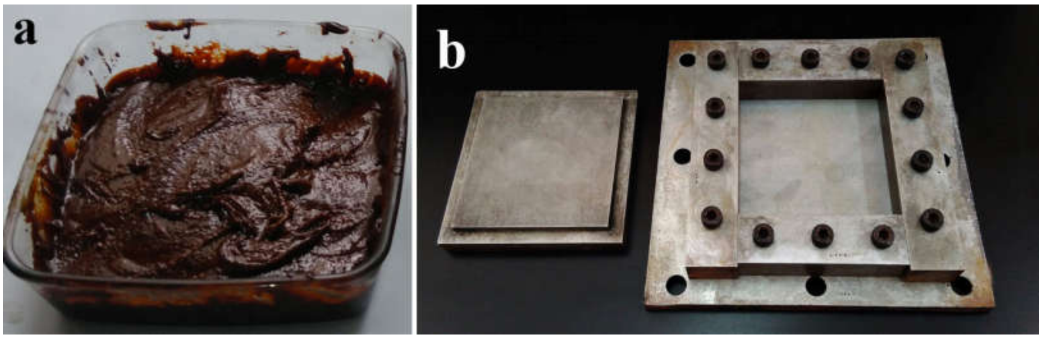

Figure 2.2 Photographic images of (a) molten sucrose-NaCl paste and (b) stainless steel mould used for the compression moulding of molten sucrose-NaCl pastes

2.2.2 Characterization

2.2.2.1 Torque measurements

The variation of torque with time of the NaCl paste was studied at 160 °C using a torque rheometer (Brabender Plasti-Corder, GmbH, Germany). Nearly 50 cm^3 of the sucrose-NaCl powder mixture prepared by planetary ball milling was loaded into the internal mixing unit of the rheometer set at a temperature of 185 °C and a rotor speed of 10 RPM. The temperature was lowered to 160 °C after 5 min during which sucrose in the mixture properly melted and mixed well with the NaCl to form a paste. The torque data was recorded with time until it reached 100 Nm.

2.2.2.2 NaCl extraction kinetics

The compression moulded sucrose-NaCl paste after carbonization at 750 °C was immersed in 800 ml distilled water taken in a 1 L beaker. The mouth of the beaker was covered with an aluminium foil and tied with a nylon rope (**Figure 2.3**) to avoid evaporation loss of water. The beaker containing the carbonized body immersed in water was then heated in an air oven at 90 °C. The water was replaced with fresh water after every 4 h until the removal of the whole NaCl present. The completion of NaCl removal was confirmed by testing the spent water for chloride ion using $AgNO_3$ solution. NaCl reacts with $AgNO_3$ to form a white precipitate of AgCl. The NaCl content in the spent water was estimated by titrating against standard $AgNO_3$ solution using potassium chromate indicator (Vogel, 1989). The spent water was first made up to 1 L and then appropriately diluted with distilled water before the titration.

Figure 2.3 Photograph showing the setup used for the NaCl removal from carbon-NaCl composite body

2.2.2.3 Thermogravimetric analysis

Thermogravimetric analysis (TGA) was carried out in air and nitrogen atmosphere using a thermogravimetric analyzer (Q-50, TA Instruments, USA). The heating rate used was 5 °C min^{-1}. The sucrose polymer sample for TGA was obtained by NaCl removal by soxhlet extraction of sucrose polymer-NaCl composite body followed by drying.

2.2.2.4 Fourier Transform Infrared spectroscopy

The infrared spectrum of the sucrose polymer was recorded using a Fourier Transform Infrared (FTIR) spectrophotometer (Spectrum-150, Perkin Elmer, USA) at wavenumbers in the range of 450-4000 cm^{-1}. The sucrose polymer for recording FTIR spectrum was obtained by removing the NaCl present in the sucrose polymer-NaCl composite body by soxhlet extraction with water. The sample for IR measurements was prepared by mixing the sucrose polymer with KBr using a mortar and pestle and pressing into pellets at a pressure of 5 kg cm^{-2}. Any adsorbed moisture from the sample was removed by heating the pellets under an IR lamp for 30 min before the analysis.

2.2.2.5 X-Ray diffraction analysis

The X-ray Diffraction (XRD) analysis of the carbon foam samples was carried out in an X-ray diffractometer (X'pert Pro, Philips, USA) using Cu Kα radiation (λ=1.54056 Å). The samples for XRD were obtained by crushing the carbon foam using a mortar and pestle. The diffraction patterns were recorded at 2θ values in the range of 5 to 90° with a step size of 0.017° using monochromatic X-rays. The d-spacing was calculated using Bragg's equation:

$$n\lambda = 2d\ sin\theta \qquad (2.1)$$

Where, λ is the wavelength, d is the distance between the lattice planes and θ is the angle of diffraction

2.2.2.6 Elemental analysis

Elemental analysis of the sucrose polymer was carried out using Perkin Elmer 2400 Series II CHNS analyzer. For the analysis, nearly 0.3 g of the sample was combusted in excess oxygen and the resultant gases were reduced to elemental gases such as CO_2, N_2, H_2O and SO_2. The gases are separated in a gas chromatography column and concentrations of individual components are determined using a thermal conductivity detector.

2.2.2.7 Scanning electron microscopy

The microstructure of the samples was analyzed on fractured surfaces using a high-resolution scanning electron microscope (HRSEM, FEI Quanta FEG 200, USA).

The samples were sputter-coated for 15 min with gold using a sputter coating instrument for improving the conductivity of the samples. Secondary Electron (SE) images were used for the analysis. The pore sizes were measured from the SEM images using the ImageJ software.

2.2.2.8 Transmission electron microscopy

Transmission electron microscopy (TEM) images were obtained using a high-resolution transmission electron microscope (HRTEM, JEOL-JEM 2100, USA) operating at 200 kV. The samples were crushed and dispersed in isopropanol by sonicating for 15 min using a probe sonicator. The dispersions were then drop-cast on the carbon-coated copper grid and dried at room temperature for 30 min.

2.2.2.9 Bulk and skeletal density measurements

The bulk density was calculated from the weight and dimensions of small cuboid samples cut from the foam bodies using a hacksaw blade. The samples were polished using a fine emery paper. A digital Vernier calliper with a least count of 0.01 mm was used for the measurement of dimensions. The skeletal density of the foams was measured using a helium pycnometer (AccuPyc II 1340 Pycnometer, Micromeritics, USA). The porosity of the foam was calculated from the bulk and skeletal densities using Equation 2.2,

$$\text{Porosity (\%)} = \left(1 - \frac{\rho_b}{\rho_s}\right) * 100 \qquad (2.2)$$

where, ρ_b and ρ_s are the bulk and skeletal density of the foams.

2.2.2.10 Compressive strength measurements

The compressive strength measurement of carbon foam samples of dimensions 25 mm x 25 mm x 12 mm (ASTM standard C365/C365M-05) was carried out using a Universal Testing Machine (Instron5050, Instron, USA) at a crosshead speed of 0.5 mm min^{-1}. The stress at the plateau region of the stress-strain plot was taken as the compressive strength and Young’s modulus was calculated from the slope of the linear elastic region of the plot.

2.2.2.11 Thermal conductivity measurement

The room temperature thermal conductivity of the carbon foam samples was measured using the transient plane source (TPS) method (Hot Disk, TPS2500S, Sweden). TPS method is widely used for the measurement of thermal conductivity, thermal diffusivity and specific heat capacity of materials. It uses a resistive element of known temperature coefficient of resistance (TCR) as both the heat source and temperature sensor. The resistive element, nickel, is patterned into a continuous double spiral by etching out of a thin foil. The spiral is reinforced on both sides by thin insulating layers of polyimide (Kapton).

Rectangular carbon foams samples of 40 mm x 40 mm x 15 mm size were used for the measurement. Two identical samples from each set were cut and then polished using a fine emery paper to obtain perfectly flat surfaces. The Kapton sensor of the instrument was sandwiched between the two foam samples with perfect contact. A schematic of the thermal conductivity measurement set up is shown in **Figure 2.4**.

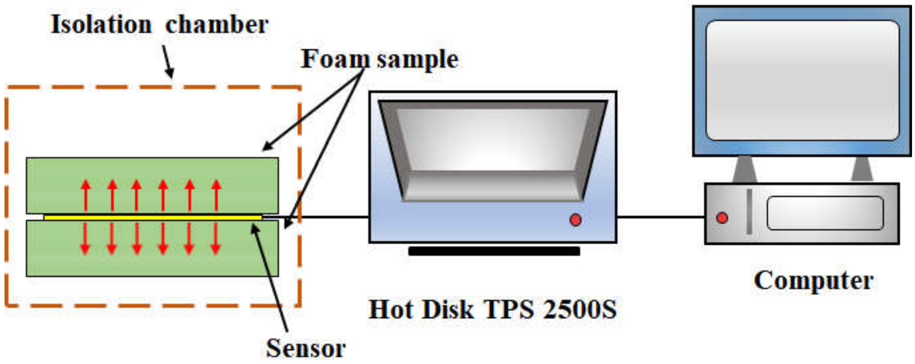

Figure 2.4 Schematic representation of thermal conductivity measurement

2.2.2.12 Textural properties

The textural properties of the carbon foams were analyzed using volumetric N_2 adsorption at -196 °C using a surface area analyzer (Micromeritics Tristar II, USA). The samples were degassed at 300 °C for 16 h under flowing N_2 prior to the analysis. The BET (Brunauer-Emmett-Teller) method was used for the calculation of the surface area. The total pore volume was estimated from the amount of N_2 adsorbed at a relative pressure of 0.99. The micropore volume was obtained by using the t-plot method from N_2 adsorption at -196 °C. The pore size distribution (PSD) was calculated using non-local density functional theory (NLDFT) using carbon-N_2 standard slit model (SAIEUS Program, Micromeritics Instrument Corp.) from the N_2 adsorption isotherm.

2.3 Results and Discussion

2.3.1 Paste preparation and moulding

The NaCl powder obtained from the supplier contains cubic particles of nearly 500 µm size as shown in **Figure 2.5**. During the planetary ball milling, the NaCl particles break into smaller sizes and mix well with the sucrose. Upon heating the dry sucrose-NaCl powder mixture in a borosilicate glass tray at 185 °C, the sucrose melts and the NaCl particles are uniformly dispersed in it by stirring with a wooden ladle to form a paste. The consistency of the paste depends on the NaCl to sucrose weight ratio ($\mathbf{W_{N/S}}$). The paste prepared at $\mathbf{W_{N/S}}$ less than 0.7 is too fluid to be moulded by compression. On the other hand, at $\mathbf{W_{N/S}}$ higher than 1.2, the paste produced is too viscous to fill in the mould cavity. The pastes prepared at $\mathbf{W_{N/S}}$ in the rage of 0.7 to 1.2 easily flows and completely fills the mould when gently pressed with the lid using a hydraulic press whose platens are maintained at 195 °C. The paste within the mould sets into a solid sucrose polymer-NaCl composite body by polymerization of sucrose on heating the same for nearly 3 h. The solidified bodies could be easily removed by dismantling the mould after cooling it to room temperature. A photograph of the sucrose polymer-NaCl composite body is shown in **Figure 2.6**.

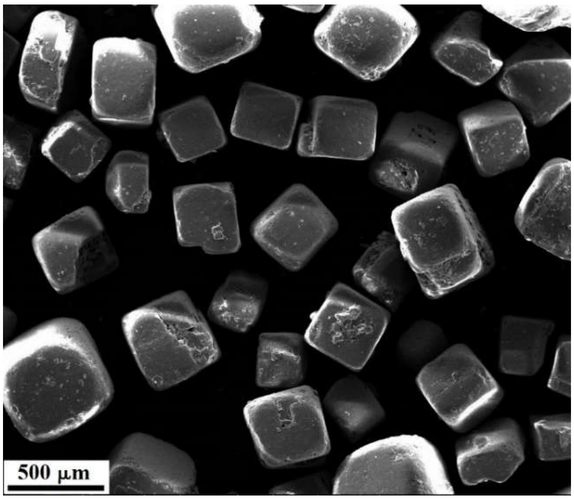

Figure 2.5 SEM photomicrograph of as-received NaCl powder

Figure 2.6 Photographic image of sucrose polymer-NaCl composite body obtained after compression moulding and setting

The uniform melting of sucrose in the sucrose-NaCl powder mixture during the preparation of the paste requires periodic stirring. Without proper stirring, the sucrose either in contact with the walls of the glass tray or on the surface of the heap preferentially melts. This results in the advancement of the curing reactions in the local regions leading to the formation of an inhomogeneous paste. The sucrose-NaCl mixtures at $\mathbf{W_{N/S}}$ less than 1.2 can be easily stirred with a ladle during the preparation of paste. However, stirring with a wooden ladle is tougher at $\mathbf{W_{N/S}}$ higher than 1.2 due to the high viscosity of the paste as a result of higher NaCl loading. Further, filling the mould with pastes of $\mathbf{W_{N/S}}$ higher than 1.2 is difficult, due to their high viscosity. On the other hand, the molten sucrose without NaCl ($\mathbf{W_{N/S}}$=0) has liquid-like behaviour against the paste-like consistency required for compression moulding. Attempts made for the compression moulding at $\mathbf{W_{N/S}}$ in the range of 0 to 0.6 produce bodies with large voids. Moreover, the bodies produced show large shrinkage during setting due to insufficient filler (NaCl) content which results in the uneven shape of the sucrose polymer-NaCl composite bodies. A photograph of a compression-moulded body at $\mathbf{W_{N/S}}$ of 0.5 is shown in **Figure 2.7**. Therefore, molten sucrose-NaCl pastes of $\mathbf{W_{N/S}}$ in the range of 0.7-1.2 are used for the compression moulding.

Figure 2.7 Photograph of compression-moulded body at **$W_{N/S}$** of 0.5 showing large voids

2.3.2 Setting of molten sucrose- NaCl paste

Though the platens of the hydraulic press were set at 195 °C for compression moulding, the temperature of the molten sucrose-NaCl paste inside the mould cavity measured using a thermocouple was only 160 °C. Therefore, setting studies of the molten sucrose-NaCl pastes were carried out at 160 °C. The polymerization leading to the setting of molten sucrose-NaCl pastes is studied by torque measurement using the torque rheometer. **Figure 2.8** shows the torque-time graph of molten sucrose-NaCl pastes prepared at **$W_{N/S}$** in the range of 0.7-1.2 measured at 160 °C.

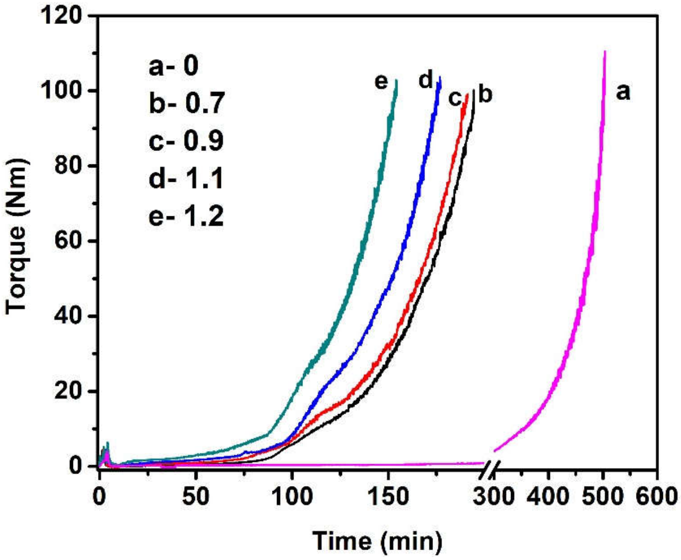

Figure 2.8 Torque-time graph of molten sucrose-NaCl pastes of various **$W_{N/S}$** at 160 ºC

The torque of the pastes increases gradually up to about 90 min and then rises rapidly. The time required for the paste to reach a torque value of 100 Nm decreases from 195 to 155 min when the $\mathbf{W_{N/S}}$ increases from 0.7 to 1.2. On the other hand, in the case of molten sucrose alone, the increase in torque with time is sluggish up to 300 min and then rapid beyond 300 min. It took nearly 500 min to reach a torque value of 100 Nm.

It is well known that the molten sucrose on heating undergoes caramelization, which involves polymerization of glucose and fructose anhydrides, formed by the thermal decomposition of sucrose, through intermolecular -OH condensation to form infusible polymeric structures (humin or caramelin) of average molecular formula $C_{125}H_{188}O_{80}$ (Darder & Ruiz-Hitzky, 2005; R. Narasimman & Prabhakaran, 2012). The large difference in the torque-time graph of molten sucrose-NaCl pastes and neat molten sucrose indicates a difference in their setting mechanisms. In effect, the NaCl in the mixture catalyzes the polymerisation of molten sucrose. The acceleration of hydrothermal carbonization of biomass such as sucrose in the presence of sodium salts is already reported in the literature (Ming et al., 2013). In this, the sodium salts are reported to play a catalytic role in the process of intra/intermolecular dehydration, aromatization, cross-polymerization, and carbonization of the intermediates produced from the biomass to form carbon materials. It has also been reported that the NaCl catalyzes both the degradation of starch to lower carbohydrates and their subsequent caramelization (Ming et al., 2013; Moreau, Bindzus, & Hill, 2011).

In order to understand the difference in setting reactions in the presence and absence of NaCl, the sucrose polymer formed in the presence and absence of NaCl under identical temperature is characterized by FTIR, TGA and elemental analysis. **Figure 2.9** shows the FTIR spectra of sucrose polymer formed in the presence and absence of NaCl. The FTIR spectrum of both polymers shows peaks at 3430, 2925, 1717, 1610, 1503 and 1022 cm^{-1} corresponding to absorption due to -OH, C-H, C=O, C=C and C-O-C stretching vibrations, respectively (Ming et al., 2013; R. Narasimman & Prabhakaran, 2012). It is interesting to note that the intensity of -OH and C-H peaks is lower and intensity of C=C peak is higher for sucrose polymer formed in the presence of NaCl even though both FTIR spectra were recorded with KBr pellets containing the same concentration of the respective polymers. There are two possible reactions such as (i) intermolecular -OH condensation leading to polymerization through C-O-C linkage and (ii) intramolecular water elimination leading to the formation of C=C. The decrease in intensity of -OH and C-H peaks and an increase in the intensity of C=C peak indicate that the elimination reaction leading to C=C formation is more favourable in the presence of NaCl along with polymerization through -OH condensation. This is further supported by the fact that the sucrose in molten sucrose-NaCl paste shows a total weight loss of 19.7% during setting and annealing at 200 °C compared to 15.4% weight loss observed for neat sucrose. The higher weight loss in the presence of NaCl is due to the intramolecular water elimination facilitated by NaCl.

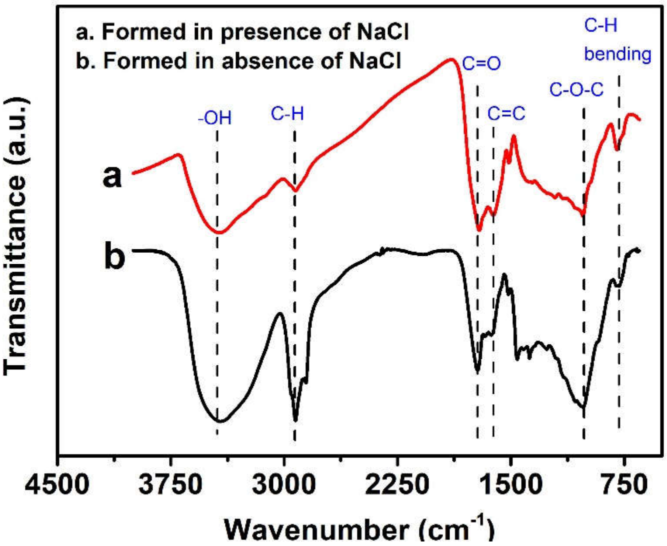

Figure 2.9 FTIR spectra of sucrose polymer formed in the presence and absence of NaCl

The elemental analysis of the sucrose polymer formed in the presence and absence of NaCl also supports the above mechanism. The sucrose polymer formed in the presence of NaCl is carbon-rich compared to that formed in the absence of NaCl. The sucrose polymer formed in the presence of NaCl contains 56.7 wt% carbon whereas that formed in the absence of NaCl contains 49.8 wt% carbon. The elemental composition of sucrose polymers formed in the presence and absence of NaCl under identical temperature is given in **Table 2.2**. The polymerization of sucrose in the presence of NaCl results in a carbon-enriched polymeric structure which is further confirmed from the carbon yield at

900 °C. The carbon yield at 900 °C of sucrose polymer formed in the presence and absence of NaCl is 41 and 28 wt%, respectively. **Figure 2.10** shows the TGA graph in nitrogen atmosphere of sucrose polymer formed in the presence and absence of NaCl. The higher carbon yield is due to the carbon-enriched polymeric structures formed due to the intramolecular water elimination reaction facilitated by NaCl. The -OH condensation reduces the carbon yield as the oxygen incorporated in the structure as C-O-C linkage will be removed as CO at higher temperatures (R Narasimman et al., 2014).

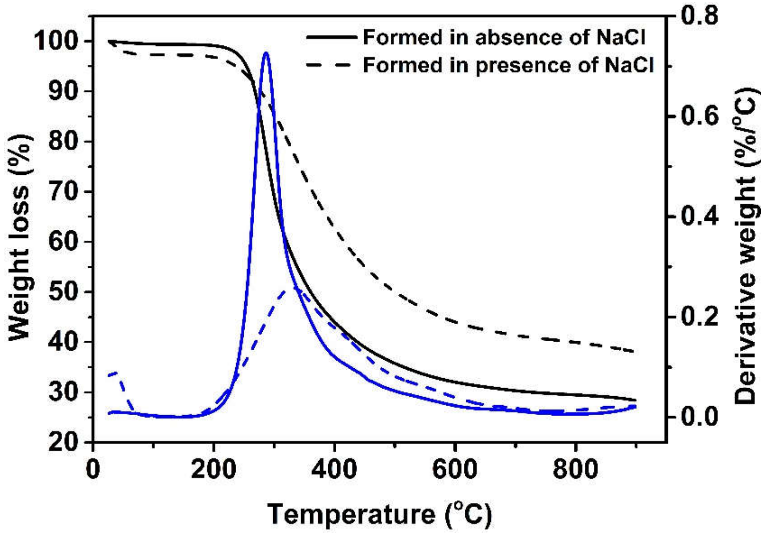

Figure 2.10 TGA of sucrose polymer formed in the presence and absence of NaCl

Table 2.2 Elemental composition of sucrose polymer formed in the presence and absence of NaCl

Sample designation	Carbon (wt%)	Hydrogen (wt%)	Oxygen (wt%)
Sucrose polymer formed in the presence of NaCl	56.7	4.8	38.5
Sucrose polymer formed in the absence of NaCl	49.8	5.3	44.9

2.3.3. Carbonization shrinkage

The polymer present in the sucrose polymer-NaCl composite bodies undergoes carbonization when heated at 750 °C in an inert atmosphere to form carbon-NaCl composite bodies. The carbonization temperature is limited to 750 °C as the NaCl in the body melts and oozes out when carbonization is attempted at 800 °C. The sucrose polymer-NaCl composite bodies obtained at $\mathbf{W_{N/S}}$ in the range of 0.8-1.2 show no deformation or crack during carbonization though they undergo uniform shrinkage. In contrast, the composite body obtained at $\mathbf{W_{N/S}}$ of 0.7 shows large deformation during the pyrolysis. **Figure 2.11** shows the linear and volume shrinkages during carbonization of the sucrose polymer-NaCl composite bodies at various $\mathbf{W_{N/S}}$. The linear and volumetric shrinkages rapidly decrease from 12 to 10.14% and 28.50 to 25.73%, respectively, when the $\mathbf{W_{N/S}}$ increases from 0.7 to 0.8. Further increase in $\mathbf{W_{N/S}}$ to 1.2 slowly decreases the linear and volume shrinkages to 8.9 and 24.3%, respectively. The NaCl particles present in the sucrose polymer-NaCl composite body resists the shrinkage and deformation of the body during pyrolysis. It appears that at $\mathbf{W_{N/S}}$ of 0.7, the NaCl particle loading is not sufficient to resist the deformation of the body during the pyrolysis.

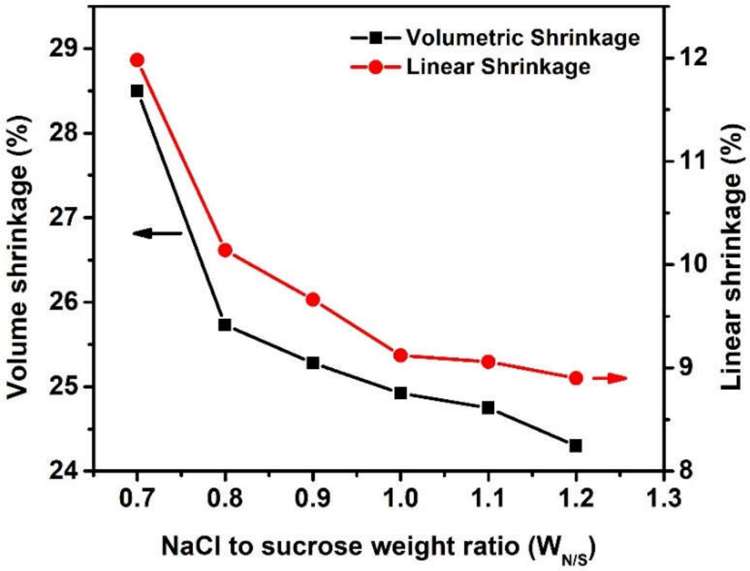

Figure 2.11 Effect of $\mathbf{W_{N/S}}$ on the shrinkage during carbonization of sucrose polymer-NaCl composite bodies

2.3.4 Microstructure of sucrose polymer-NaCl and carbon NaCl composites

Figure 2.12 shows SEM images of the fractured surface of sucrose polymer-NaCl and carbon-NaCl composite bodies prepared at a $\mathbf{W_{N/S}}$ of 1. The large pores observed in the low-magnification image of sucrose polymer-NaCl composite body are formed due to the entrapment of water vapour produced by -OH condensation as well as the elimination reactions during setting. The high-magnification images show the uniform distribution of NaCl particle in the sucrose polymer as well as in the carbon matrix. The breakdown of large cubic particles in the as-received NaCl powder to fine particles of irregular shape during milling is clearly evidenced in the high-magnification images. The sizes of fine NaCl particles in the composite body are approximately in the range of 2-13 μm. The macropores created by the entrapment of water vapour become evident after carbonization. It is interesting to note that the NaCl particles in sucrose polymer-NaCl composite and carbon-NaCl composite have more or less the same size indicating negligible NaCl particle growth during the carbonization. However, the rounding of sharp edges and corners of the NaCl particles takes place during the carbonization due to diffusion of NaCl from the sharp edges and corners to the faces. The strong sucrose polymer-NaCl particle and carbon-NaCl particle interfaces are clearly evidenced in the high-magnification SEM photomicrograph of the sucrose polymer-NaCl particle and carbon-NaCl particle composite bodies, respectively, as shown in **Figure 2.13**.

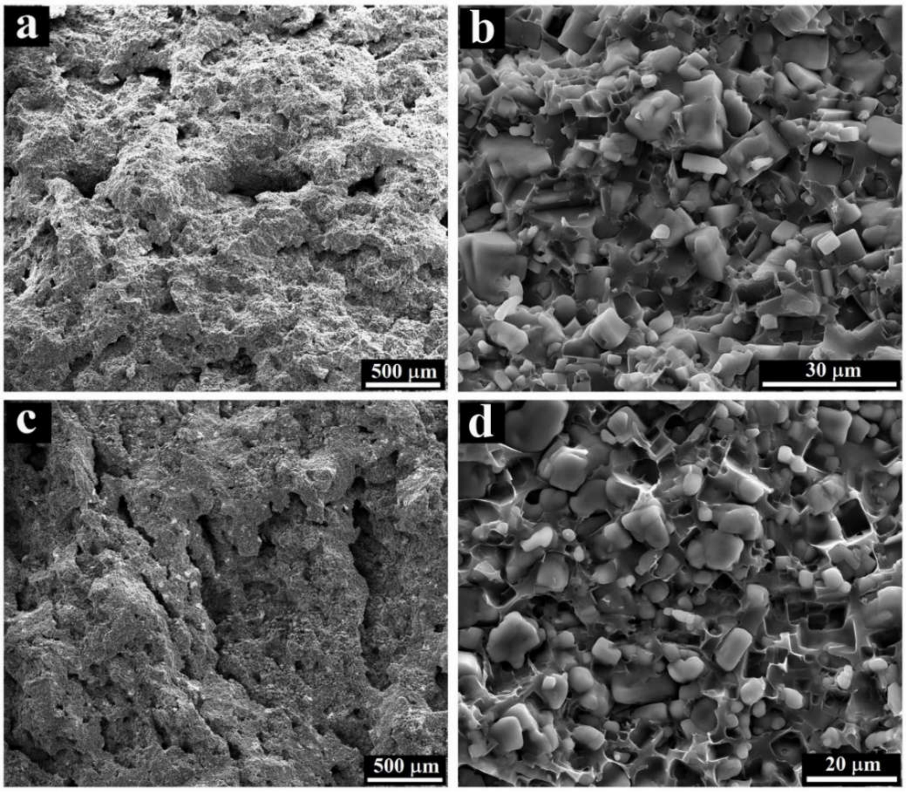

Figure 2.12 SEM photomicrograph of the fractured surface of sucrose polymer-NaCl and carbon-NaCl composite bodies prepared at a $\mathbf{W_{N/S}}$ of 1. a & b are sucrose polymer-NaCl composite and c & d are carbon-NaCl composite

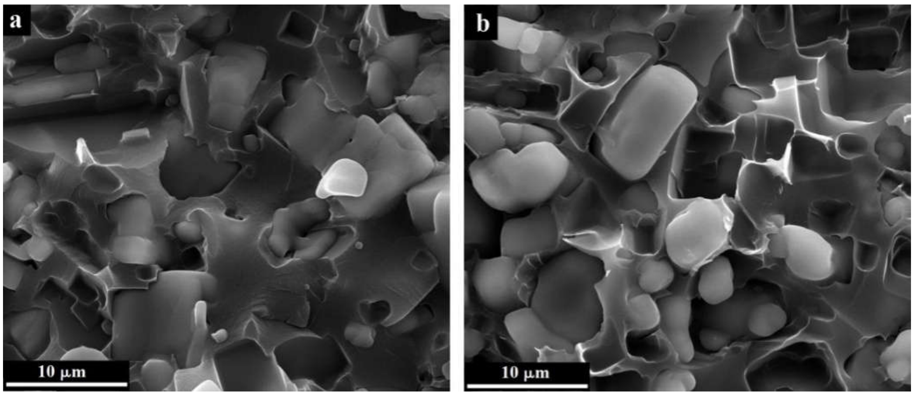

Figure 2.13 High-magnification SEM photomicrograph of (a) sucrose polymer-NaCl composite and (b) carbon-NaCl composite showing strong sucrose polymer-NaCl and carbon-NaCl interfaces

2.3.5 NaCl removal

The NaCl particles embedded in the carbon matrix are leached out by washing with water. In order to speed up the NaCl removal, washing is carried out with water at 90 °C, though the complete removal of NaCl is possible by washing at room temperature. **Figure 2.14** shows the amount of NaCl removed with time from a carbon-NaCl composite body of size 9 cm x 9 cm x 1.7 cm prepared at a $\mathbf{W_{N/S}}$ of 1.

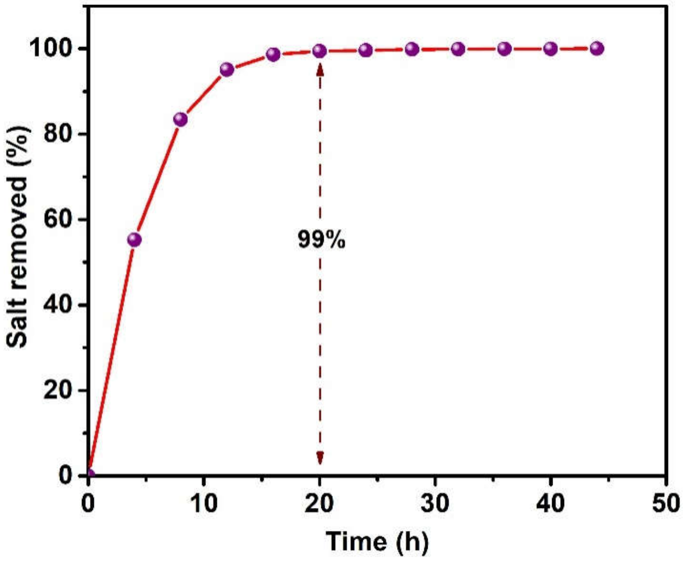

Figure 2.14 NaCl removal kinetics from the carbon-NaCl composite body ($\mathbf{W_{N/S}}$=1)

The percentage of NaCl removed in each washing was calculated based on the total amount of NaCl present in the carbon-NaCl composite estimated gravimetrically by burning off the carbon at 600 °C in a muffle furnace. Nearly 55% of the NaCl present in the body is removed in the first 4 h. Further, the rate of NaCl removal decreases with time. More than 99% of the NaCl is removed within 20 h. It appears that the NaCl particles embedded in the carbon matrix completely dissolve in 20 h and the remaining less than 1% NaCl may be adsorbed on the carbon surface. The complete removal of NaCl is possible in 44 h. On the other hand, continuous washing of a carbon-NaCl composite body of size 5 cm x 3 cm x 2 cm with water using a soxhlet extraction unit results in the complete removal of NaCl in 11 h. The carbon-NaCl composite body retains its shape and size during the NaCl removal and subsequent drying at 100 °C.

Generally, the use of pore templates with a wide range of particle sizes poses difficulty in their complete removal by leaching with a solvent. The smaller particles completely covered by the matrix material is hard to be removed by a solvent. It has been reported that sucrose polymer on carbonization produces a large volume of micropores due to the reaction between the retained oxygen as C-O-C linkage and carbon to form CO (R Narasimman et al., 2014). In the present case, complete removal of NaCl is achieved even though we use NaCl powder with a broad particle size distribution (2-13 μm). It appears that the water molecules can access the smaller NaCl particles covered by the carbon matrix through the micropores formed in the carbon matrix thus facilitating complete NaCl template removal.

The carbon foam bodies obtained after NaCl removal are further heat-treated at 900 °C for 2 h. The carbon foam bodies exhibit weight-loss in the range of 1.5-2.8% during heat-treatment at 900 °C. A linear shrinkage in the range of 0.8-1.2% is also observed. However, no cracks or deformation during the heat-treatment at 900 °C are observed. The photograph of a sucrose polymer-NaCl composite, a carbon-NaCl composite and a carbon foam body after the heat-treatment at 900 °C prepared at a $\mathbf{W_{N/S}}$ of 1 showing their relative sizes is presented in **Figure 2.15**.

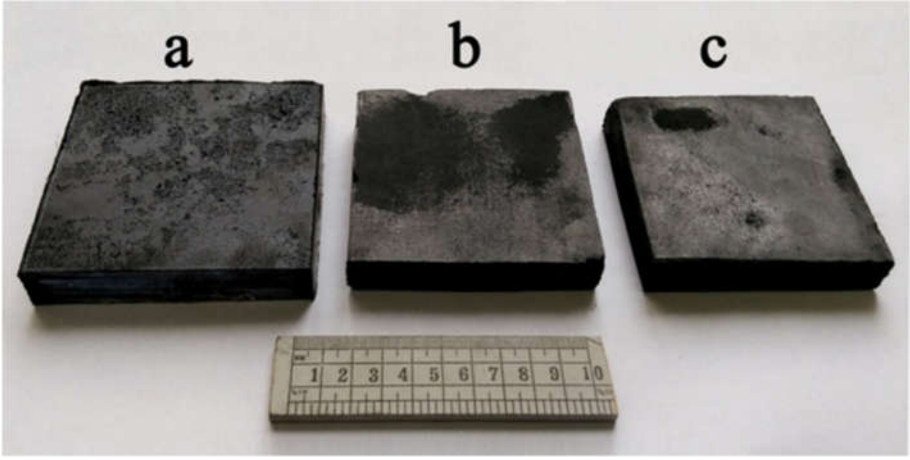

Figure 2.15 Photograph of (a) sucrose polymer-NaCl composite body, (b) carbon-NaCl composite body and (c) carbon foam body showing their relative size (**W**$_{N/S}$=1)

2.3.6 Phase analysis

The carbonization of polymer precursors generally produces amorphous carbon materials. The carbonization of sucrose polymer produces carbon with turbostratic graphite structure as evidenced by the broad peaks at 2θ values of ~25 and ~44° in the XRD diffraction pattern corresponding to the reflections from (002) and (101) planes, respectively (Z. Q. Li, Lu, Xia, Zhou, & Luo, 2007; R Narasimman & Prabhakaran, 2012). The XRD diffraction pattern of the carbon foam in comparison with the carbon produced by carbonization of sucrose polymer prepared in the absence of NaCl is shown in **Figure 2.16**. The carbon foam obtained after NaCl removal from the carbon-NaCl composite body gives reflection corresponding to the (002) peak at a 2θ value of 25°. The peak shifted to 25.4° upon further heat-treatment at 900 °C. In comparison, the carbon obtained by carbonization at 750 and 900 °C of the sucrose polymer prepared in the absence of NaCl shows (002) reflections at 23.3 and 24.4°, respectively. The d-spacing calculated from Bragg's equation gives values of 3.56 and 3.50 Å for the carbon foam obtained after NaCl removal and further heat-treatment at 900 °C, respectively. Correspondingly, the d-spacing calculated for the carbon prepared by carbonization at 750 and 900 °C of sucrose polymer prepared in the absence of NaCl shows higher values of 3.81 and 3.65 Å, respectively. This indicates that the carbon-rich polymer, with a large number of C=C bonds obtained by the polymerization of sucrose in the presence of NaCl, produces carbon with more closely packed graphene layers at lower carbonization temperature.

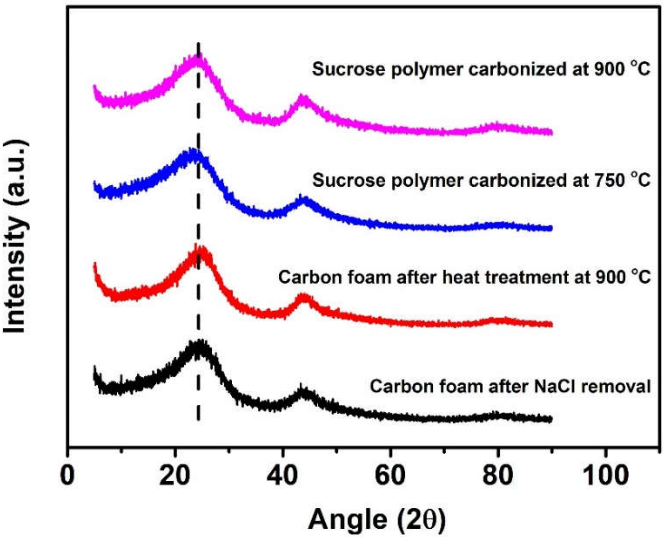

Figure 2.16 XRD diffraction pattern of carbon foam carbonized at 750 and 900 °C

2.3.7 Microstructure of carbon foams

The SEM analysis of the carbon foams prepared at $\mathbf{W_{N/S}}$ in the range of 0.7-1.2 reveals two types of pores. Large irregular pores of width >50 μm formed by the entrapment of water vapour during the setting of molten sucrose-NaCl paste within the mould are termed as macropores. Moreover, the pores of size <15 μm formed by the removal of NaCl particle are termed as microcells. The low-magnification images clearly show the presence of macropores. **Figure 2.17** shows the low-magnification SEM photomicrograph of the fractured surface of the carbon foam bodies prepared at $\mathbf{W_{N/S}}$ in the range of 0.7-1.2. The macropores have elongated and irregular shapes. The determination of the exact size of these macropores from the SEM images is difficult due to their irregular shape. The width of the elongated pores measured using ImageJ software is taken as the macropore width. The average macropore width is calculated from a minimum of four SEM images of the same sample. It is clear from the microstructure that the width and volume of the macropores decrease with an increase in $\mathbf{W_{N/S}}$. The approximate average macropore width is given in **Table 2.3**. The average width of the macropores decreases drastically from 414 to 128 μm when the $\mathbf{W_{N/S}}$ increases from 0.7 to 0.9. Further increase in $\mathbf{W_{N/S}}$ to 1.2 slowly decreases the macropore width to 70 μm.

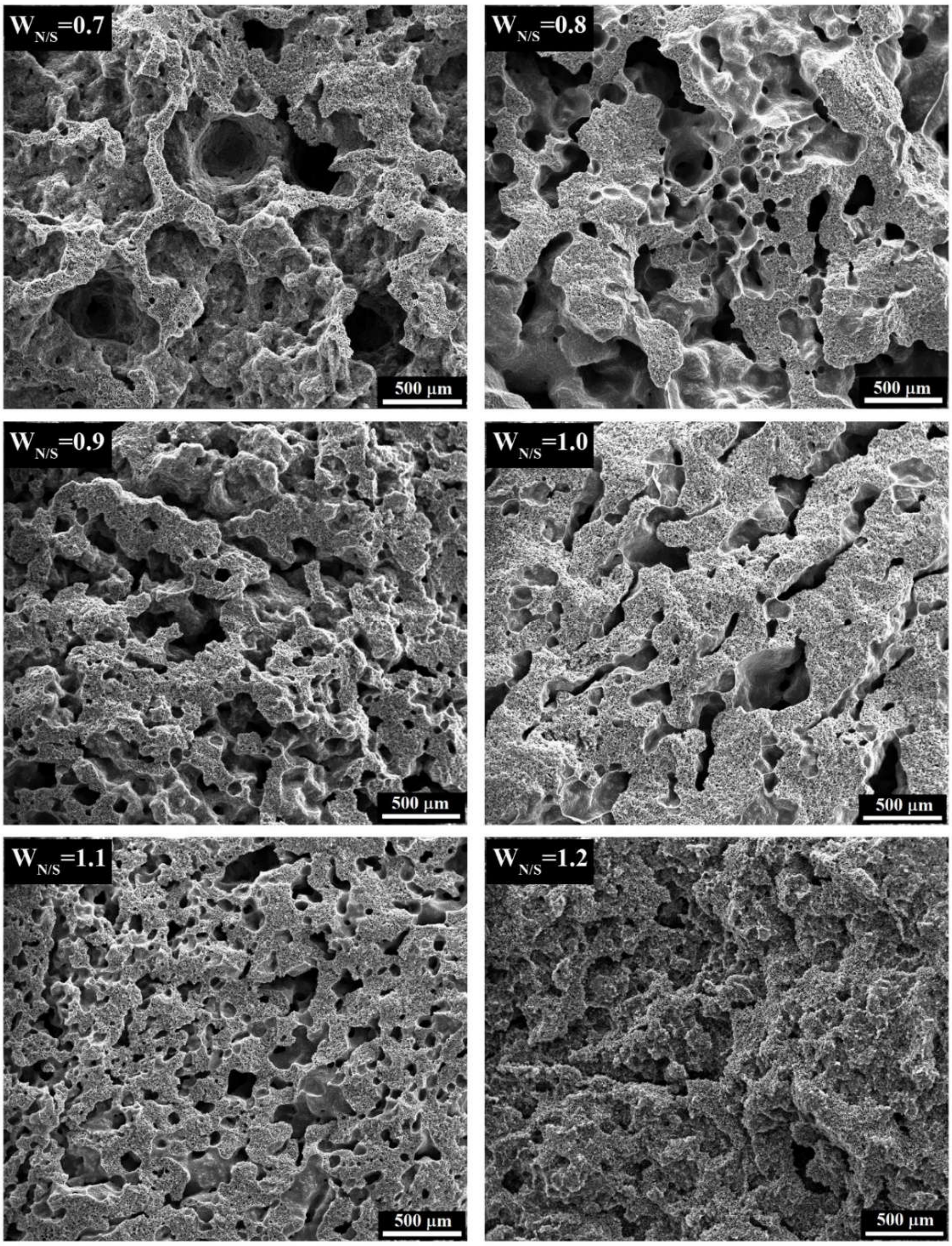

Figure 2.17 Low-magnification SEM photomicrograph of microcellular carbon foams prepared at $\mathbf{W_{N/S}}$ of 0.7, 0.8, 0.9, 1.0, 1.1 and 1.2

Table 2.3 Average macropore size of carbon foams prepared at various $\mathbf{W_{N/S}}$

NaCl to sucrose weight ratio ($\mathbf{W_{N/S}}$)	0.7	0.8	0.9	1	1.1	1.2
Average macro pore size (μm)	414	221	128	116	78	70

The macropores in the carbon foam bodies are separated by thick regions. High-magnification SEM images of these regions show the presence of microcells which are formed by the removal of NaCl particles from the carbon-NaCl composites. The connection between the neighbouring microcells was rarely visible in the high-magnification SEM image. At all studied $\mathbf{W_{N/S}}$, the microcells are irregular in shape. The SEM images of the carbon foams prepared at various $\mathbf{W_{N/S}}$ shows uniform distribution of the microcells. The high-magnification SEM images of carbon foams prepared at $\mathbf{W_{N/S}}$ of 0.7 and 1.2 are shown in **Figure 2.18**.

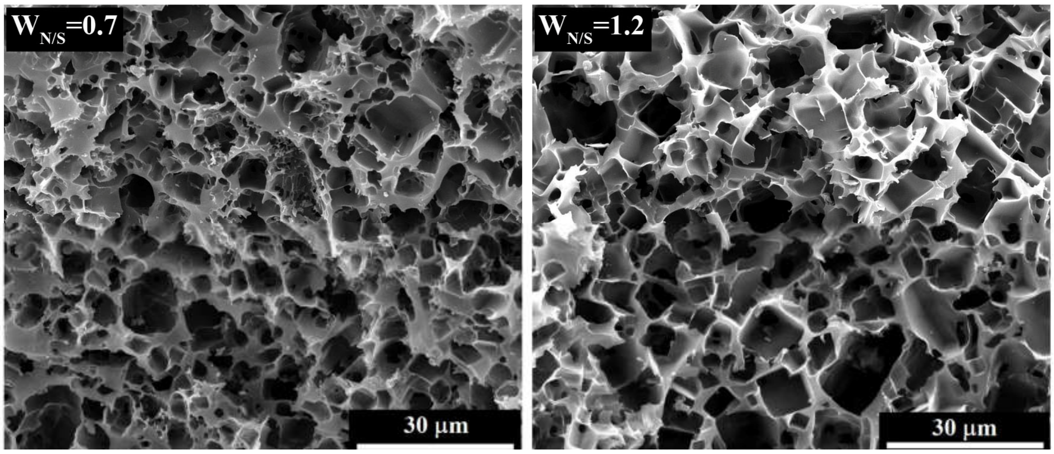

Figure 2.18 High-magnification SEM images of microcellular carbon foams prepared at $\mathbf{W_{N/S}}$ of 0.7 and 1.2

The size and size distribution of microcells are measured from the high-magnification SEM images using ImageJ software. The carbon foam samples prepared at $\mathbf{W_{N/S}}$ in the range of 0.7 to 1.2 have microcells size in the range of 2-14 μm. A majority of the microcells have sizes in the range of 2-4 μm. The average cell size observed is nearly 5 μm. The typical size distribution of the microcells is given in **Figure 2.19**.

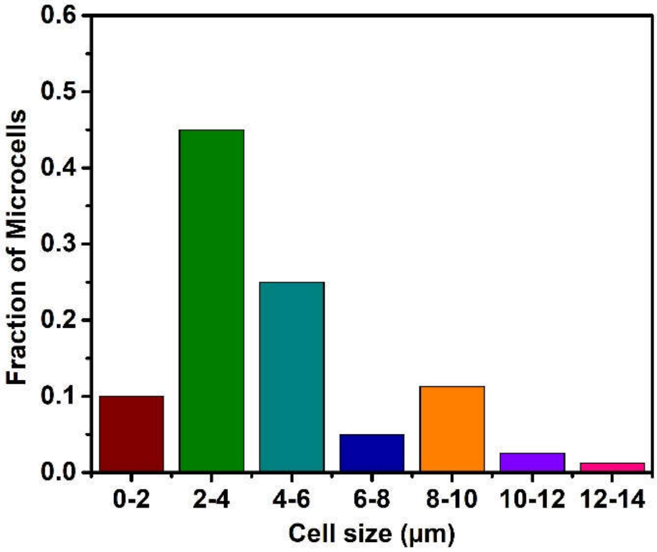

Figure 2.19 The typical size distribution of microcells in carbon foams

2.3.8. Carbon foam density

The carbon foams obtained at $\mathbf{W_{N/S}}$ in the range of 0.7-1.2 show densities within a narrow range of 0.26-0.33 g cm^{-3}. The increase in pore template (NaCl) concentration is expected to decrease the density of the carbon foam. Contrary to this, the foam density increases from 0.26 to 0.33 g cm^{-3} when the $\mathbf{W_{N/S}}$ increases from 0.7 to 1. Further increase in $\mathbf{W_{N/S}}$ to 1.2 marginally decreases the carbon foam density to 0.31 g cm^{-3}. The increase in the concentration of NaCl particles increases the volume of microcells and decreases the volume of the macropores in the carbon foam bodies as evidenced by the microstructure. At $\mathbf{W_{N/S}}$ in the range of 0.7-1, the decrease in the volume of macropores is much higher than the increase in the volume of microcells which results in an increase in the foam density from 0.26 to 0.33 g cm^{-3}. On the other hand, the decrease in density from 0.33 to 0.31 g cm^{-3} indicates that the increase in the volume of microcells dominates the decrease in the volume of macropores when the $\mathbf{W_{N/S}}$ increases from 1 to 1.2. This is clearly visible in the change in microstructure at $\mathbf{W_{N/S}}$ above 1. The density of the carbon foams as a function of $\mathbf{W_{N/S}}$ is shown in **Figure 2.20**. The skeletal density of the carbon foams prepared at $\mathbf{W_{N/S}}$ in the range of 0. 7 to 1.2 measured using a helium pycnometer is given **Table 2.4**. The carbon foams showed skeletal density in a narrow range with an average value of 2.04 ± 0.03 g cm^{-3}. The skeletal density observed is comparable to that of disordered carbons reported in the literature (X. Li et al., 2012; Tondi, Fierro, et al., 2009). There is no considerable change in the skeletal density by repeating the measurement after powdering the carbon foam samples, indicating a negligible contribution of pores which are inaccessible to helium (closed pores) to the total porosity (Zúñiga Ruiz et al., 2015). The total porosity calculated from the observed bulk density and skeletal density of the carbon foams is in the range of 83.83 to 87.26 vol.%.

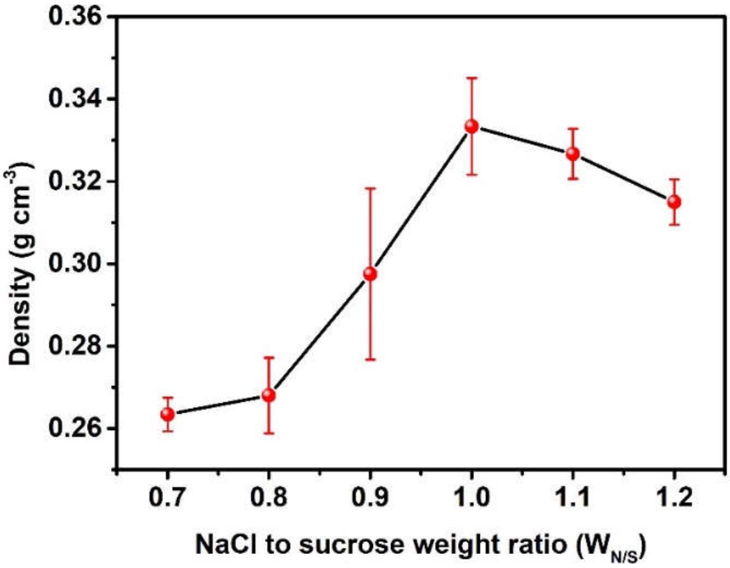

Figure 2.20 The effect of $\mathbf{W_{N/S}}$ on the density of carbon foams

Table 2.4 Skeletal density of carbon foams prepared at various $\mathbf{W_{N/S}}$

$\mathbf{W_{N/S}}$	0.7	0.8	0.9	1	1.1	1.2
Skeletal density (g cm^{-3})	2.05	2.03	2.07	2.06	2.01	2.04

2.3.9 Compressive strength and Machinability

Thermo-structural applications require carbon foam with reasonably high compressive strength. The compressive stress-strain graph of the microcellular carbon foam samples is shown in **Figure 2.21**a. The microcellular carbon foam samples show stress-strain behaviour analogous to typical brittle foams with an initial linear region at low strains followed by a near plateau and a region of densification at high strains in the stress-strain graph. The slope of the initial linear region is taken as Young's modulus and stress corresponding to the plateau region is taken as the compressive strength. Brittle carbon foams with large cell size show highly serrated plateau region in the compressive stress-strain graph. The serrated nature of the plateau region is due to the fracture of successive cell walls (Celzard et al., 2010; Tondi, Fierro, et al., 2009; Zúñiga Ruiz et al., 2015). The major difference between the stress-strain graphs of the microcellular carbon foams and the carbon foams with large cell sizes reported in the literature is the less serrated nature of the plateau region in the former compared to the latter. The compressive strength increases from 2.84 to 8.37 MPa when the $\mathbf{W_{N/S}}$ increases from 0.7 to 1.2. The increase in the compressive strength with an increase in $\mathbf{W_{N/S}}$ up to 1 is due to the combined effect of the increase in foam density and the decrease in the size of the macropores. The increase in compressive strength at $\mathbf{W_{N/S}}$ from 1 to 1.2 in spite of an observed decrease in the density is due to the decrease in the width and volume of the macropores. On the other hand, Young's modulus of the carbon foams increases gradually from 225 to 370 MPa when the $\mathbf{W_{N/S}}$ increases from 0.7 to 1. A further increase in the $\mathbf{W_{N/S}}$ to 1.2 results in a gradual decrease in Young's modulus of the carbon foam samples to 240 MPa. The compressive strength and Young's modulus of the carbon foams as a function of $\mathbf{W_{N/S}}$ are shown in **Figure 2.21**b.

The variation in compressive strength as a function of the density of the carbon foams is exhibited in **Figure 2.21**c. An overall increase in the compressive strength with density is observed. Linear fitting of the data points with an R^2 value of 0.8919 suggests a linear relation between compressive strength and density exists as reported in various literature (Celzard et al., 2010; Eksilioglu et al., 2006; Lei et al., 2010). The specific compressive strength of the carbon foams increases from 10.74 to 26.57 MPa/g cm^{-3} when the $\mathbf{W_{N/S}}$ increases from 0.7 to 1.2. The carbon foam prepared by thermo-foaming of molten sucrose and aqueous sucrose resin without any reinforcing additives showed maximum specific compressive strengths of 5 and 6.18 MPa/g cm^{-3}, respectively (R. Narasimman et al., 2014; Prabhakaran et al., 2007). It is interesting to note that the maximum specific compressive strength obtained for the carbon foam is roughly 5 and 4 times higher than that obtained for carbon foams prepared by thermo-foaming of molten sucrose and aqueous sucrose resin, respectively. Moreover, the highest specific compressive strength achieved is comparable with those reported for carbon foams prepared from tannin (28 MPa/g.cm^{-3}) (Tondi, Fierro, et al., 2009), coal tar pitch (27.16 MPa/g.cm^{-3}) (S. Li et al., 2007) and mesophase pitch reinforced with mesocarbon microbeads (30.38 MPa/g.cm^{-3}) (C. Chen et al., 2006). The high compressive strength of the carbon foams makes them suitable to undergo machining with conventional machines and tools. This facet of the carbon foams is demonstrated successfully by subjecting the foams prepared at $\mathbf{W_{N/S}}$ in the range of 0.7 to 1.2 to drilling and milling in a drilling machine and milling machine, respectively, using high-speed steel tools. Holes with a diameter of 8 mm and a slot with a width and depth of 5 mm are produced by drilling and milling, respectively. **Figure 2.21**d shows the carbon foam with the drilled holes and a milled slot.

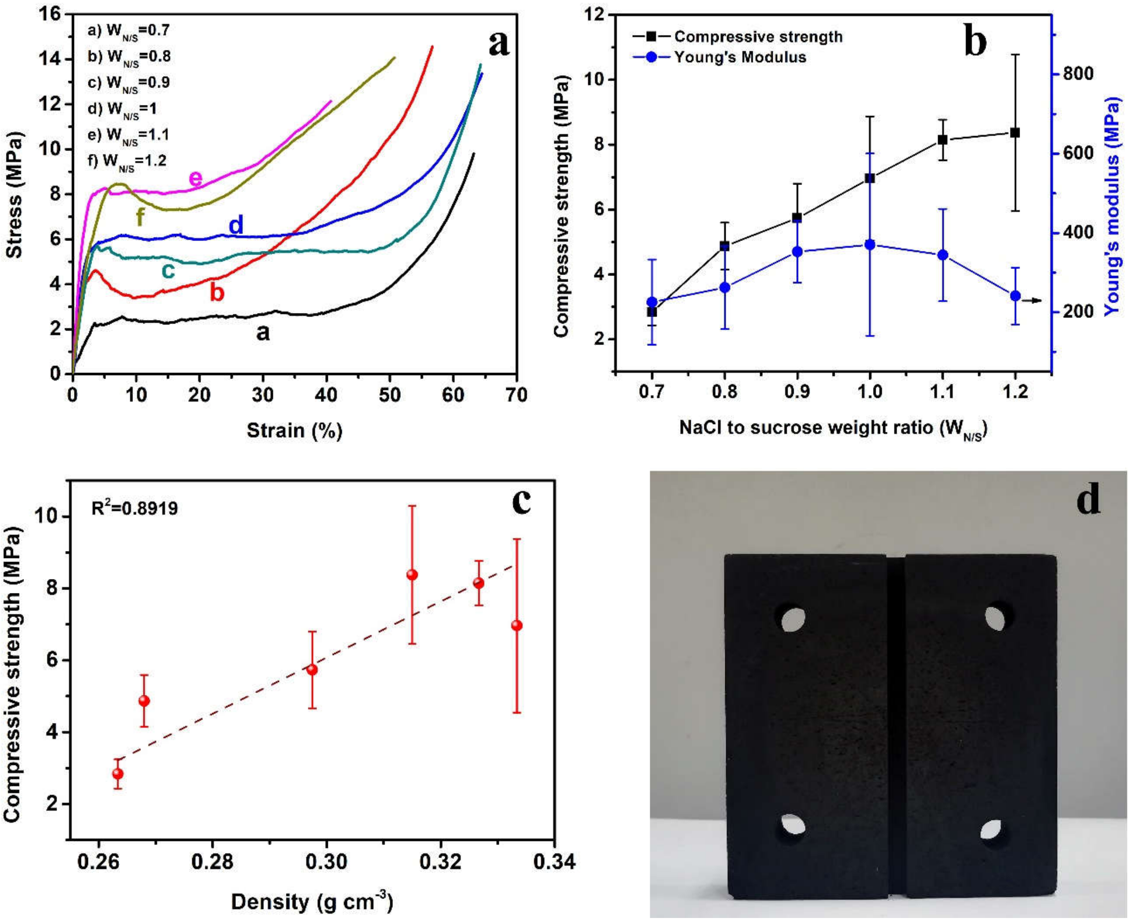

Figure 2.21 (a) Compressive stress-strain graph of the carbon foams at various $\mathbf{W_{N/S}}$, (b) The effect of $\mathbf{W_{N/S}}$ on the compressive strength and modulus of carbon foams, (c) variation of compressive strength with density and (d) photographic image of carbon foam prepared at $\mathbf{W_{N/S}}$=1.2 with holes made by drilling and slot produced by milling

2.3.10 Thermal conductivity

Thermal protection applications require carbon foams with low thermal conductivity. Generally, amorphous carbon foams show very low thermal conductivity. The thermal conductivity value of insulating foam materials depends on their bulk density and pore size (P. Jana et al., 2013; P. Jana, Fierro, et al., 2016; Tondi, Fierro, et al., 2009; K. Wang et al., 2016; Zúñiga Ruiz et al., 2015). The carbon foams prepared at various $\mathbf{W_{N/S}}$ show thermal conductivity within a close range as shown in **Figure 2.22**. The thermal conductivity decreases from 0.348 to 0.257 W m^{-1} K^{-1} when the $\mathbf{W_{N/S}}$ increases from 0.7 to 1.2. In general, the thermal conductivity of amorphous carbon foam decreases with a decrease in bulk density (Farhan et al., 2017; Zúñiga Ruiz et al., 2015). However, in spite of an observed increase in foam density from 0.26 to 0.33 g cm^{-3}, the thermal conductivity of carbon foams decreases from 0.348 to 0.283 W m^{-1} K^{-1} when the $\mathbf{W_{N/S}}$ increases from 0.7 to 1. Further, the density and thermal conductivity decrease to 0.31 g cm^{-3} and 0.257 W m^{-1} K^{-1}, respectively, when the $\mathbf{W_{N/S}}$ increases to 1.2.

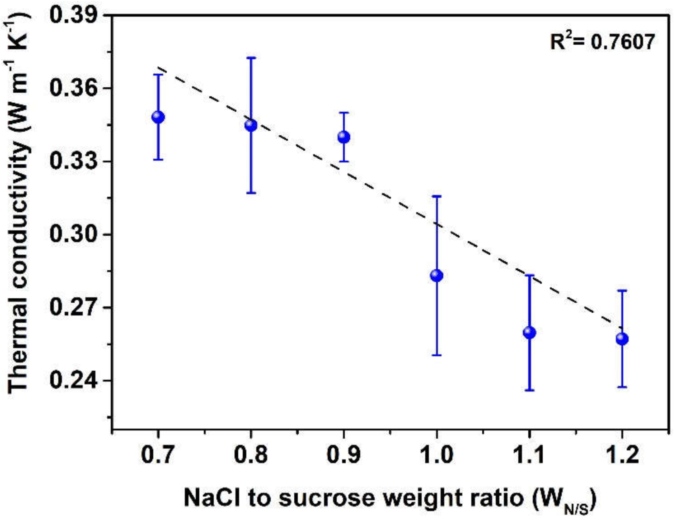

Figure 2.22 Thermal conductivity of carbon foam samples at various $\mathbf{W_{N/S}}$

The effect of pore size on thermal conductivity of porous materials has been studied by various authors (Alvarez-Lainez, Rodriguez-Perez, & DE Saja, 2008; Alvarez et al., 2010; Han et al., 2009; Sumirat et al., 2006; Sundarram & Li, 2013). Alvarez et al. reported a decrease in thermal conductivity of porous silicon with a decrease in pore size due to phonon ballistic effects (Alvarez et al., 2010). The phenomenon of phonon scattering by smaller pores is further supported by Sumirat et al. (Sumirat et al., 2006). Han et al. reported a decrease in thermal conductivity with a decrease in pore size of rigid polyurethane foam (Han et al., 2009). Theoretical studies using finite element and molecular dynamics models by Sundarram et al. demonstrated a decrease in thermal conductivity with a decrease in pore size due to extensive diffusive scattering of heat carriers in the solid phase of polymer matrix at lower pore sizes (Sundarram & Li, 2013). Alvarez-Lainez et al. also reported a decrease in thermal conductivity with a decrease in pore size in open cell polyolefin foams prepared by compression moulding (Alvarez-Lainez et al., 2008). In the present work, the decrease in thermal conductivity observed with an increase of foam density is attributed to the pore size effect. It is clear from the microstructure of the carbon foam that the size and volume of the macropores produced due to the entrapped water vapour decreases and the volume of microcells produced by the removal of NaCl templates increase with an increase in $\mathbf{W}_{\mathbf{N/S}}$. The decrease in thermal conductivity with an increase in $\mathbf{W}_{\mathbf{N/S}}$ is due to an increase in the volume of microcells.

2.3.11 Textural properties

Carbon foams are used for adsorption of dyes, organic pollutants and gases and absorption of oil (B. Chen et al., 2015; X. Dong et al., 2012; Gupta & Tai, 2016; C. Ji et al., 2017; Mi et al., 2018; R Narasimman et al., 2014; Qu et al., 2017; H. Zhu et al., 2015). The carbon foams used for the above purposes require high surface area and hierarchical pore structure. The typical N_2 adsorption isotherm of a carbon foam sample is shown in **Figure 2.23a**. The carbon foam samples show steep uptake of N_2 gas at low relative pressures indicating the presence of micropores. The non-local density functional theory (NLDFT) pore size distribution of a carbon foam sample is shown in **Figure 2.23b**. The NLDFT graph shows a peak corresponding to a pore width of ~1.04 nm. These micropores are formed by the *in situ* activation proposed by Narasimman et al. in carbon foam prepared by thermo-foaming of molten sucrose (R Narasimman et al., 2014). The carbon foam prepared by thermo-foaming of molten sucrose followed by carbonization at 900 °C showed a specific surface area of 367 m^2 g^{-1}, micropore volume of 0.18 $cm^3 g^{-1}$ and pore width of 1 nm. In comparison, the carbon foams prepared from molten sucrose-NaCl paste showed the specific surface area in a range of 379-442 m^2 g^{-1}, micropore volume in the range of 0.13-0.15 cm^3 g^{-1} and total pore volume in the range of 0.16-0.21

$cm^3\ g^{-1}$. The textural properties of carbon foams are given in **Table 2.5**. The hydroxyl condensation and α-elimination reactions are expected to be completed below 400 °C. Therefore, the carbon obtained by heating the sucrose polymer and sucrose polymer-NaCl composites at 400 °C are analyzed for oxygen content. The carbon obtained by heating sucrose polymer at 400 °C in the absence of NaCl shows an oxygen concentration of 19.7 wt%. On the other hand, the carbon obtained from the sucrose polymer-NaCl composite bodies show oxygen content in the range of 16.7-18.9 wt%. The lower micropore volume observed in carbon foams prepared from molten sucrose-NaCl pastes is due to the lower concentration of oxygen retained as C-O-C linkage as a considerable amount of hydroxyl groups is removed by α-elimination. The micropore texture of the carbon foam is further evidenced by the TEM photomicrograph as shown in **Figure 2.24**.

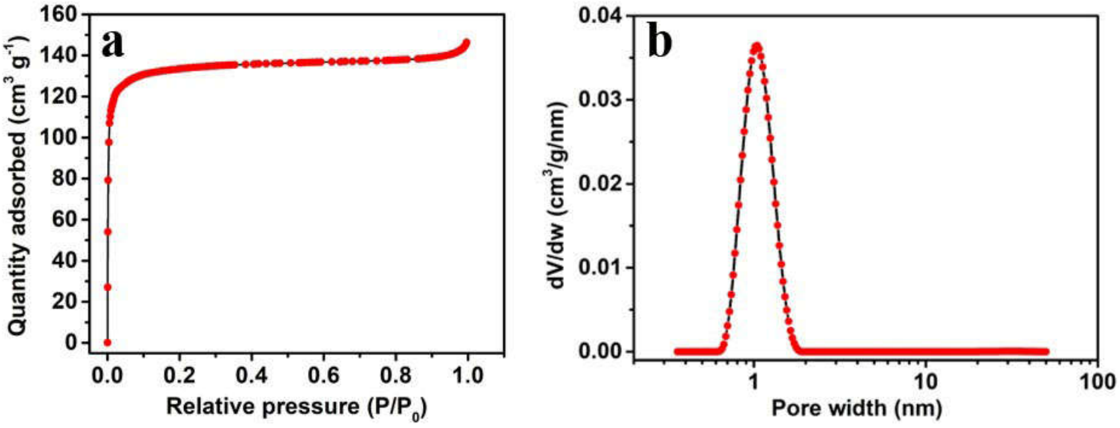

Figure 2.23 (a) Typical N_2 adsorption isotherm and (b) NLDFT pore size distribution of a microcellular carbon foam sample (**$W_{N/S}$** =1)

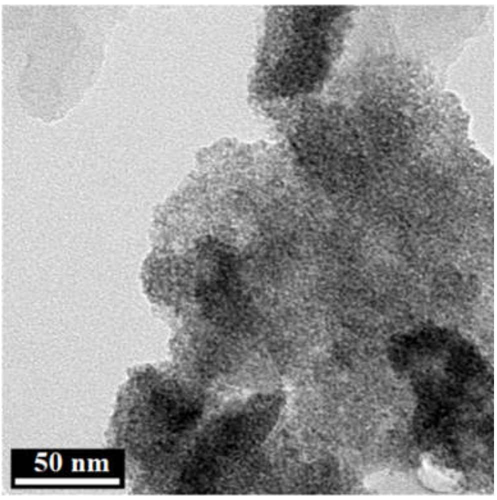

Figure 2.24 TEM photomicrograph of a carbon foam sample (**$W_{N/S}$**=1)

Table 2.5 Textural properties of carbon foams prepared at different $\mathbf{W_{N/S}}$

($\mathbf{W_{N/S}}$)	**Total surface area ($\mathbf{m^2\ g^{-1}}$)**	**Micropore area ($\mathbf{m^2\ g^{-1}}$)**	**Total pore volume ($\mathbf{cm^3\ g^{-1}}$)**	**Micropore volume ($\mathbf{cm^3\ g^{-1}}$)**	**NLDFT Pore size (nm)**
0.7	385	307	0.16	0.13	1.01
0.8	394	339	0.18	0.14	1.04
0.9	442	363	0.21	0.15	0.96
1.0	408	340	0.19	0.14	0.98
1.1	379	315	0.18	0.14	0.96
1.2	416	348	0.19	0.14	1.00

2.4 Conclusions

Carbon foams with a triplex pore structure consisting of large macropores (70-414 μm), microcells (2-14μm) and micropores (< 2 nm) have been prepared by the compression moulding of molten sucrose-NaCl powder pastes followed by pyrolysis at 750 °C, NaCl removal by leaching with water and subsequent heat-treatment at 900 °C. The setting of the paste during compression moulding is achieved by the caramelization of molten sucrose. The setting of the sucrose is catalysed in the presence of NaCl as evidenced by the torque-time graph measured in a torque rheometer. The NaCl facilitates the intramolecular water elimination reaction during caramelization leading to the carbon-enriched polymeric structures as evidenced by the elemental analysis, IR, TGA and torque-time measurement. The NaCl-sucrose mixtures with $\mathbf{W_{N/S}}$ in the range of 0.7-1.2 are used as $\mathbf{W_{N/S}}$ below 0.7 produces large voids during compression moulding and large shrinkage with warpage during pyrolysis. On the other hand, the preparation of pastes at $\mathbf{W_{N/S}}$ above 1.2 is tough by hot-blending with a ladle. The microcellular carbon foams show density in the range of 0.26-0.33 g cm^{-3} with a maximum at $\mathbf{W_{N/S}}$ of 1. The XRD analysis indicates the turbostratic nature of carbon produced by the carbonization of sucrose with broad peaks at 25 and 44° corresponding to reflections from (002) and (101) planes. The microcellular carbon foams have a hierarchical triplex pore structure with macropores created by the entrapment of water vapour produced during caramelization, microcells created by the removal of NaCl template and micropore texture created by *in* *situ* activation. The average macropore width decreases from 414 to 70 µm when the $\mathbf{W_{N/S}}$ increases from 0.7 to 1.2. On the other hand, the average microcell size remains more or less constant with a value of ~5 µm, irrespective of $\mathbf{W_{N/S}}$. The compressive strength of the carbon foams increases from 2.8 to 8.4 MPa when the $\mathbf{W_{N/S}}$ increases from 0.7 to 1.2. The compressive strength shows a near-linear dependence on the bulk density of the foams with an R^2 value of 0.8919. The thermal conductivity of the carbon foams decreases from 0.348 to 0.257 W m^{-1} K^{-1} when the $\mathbf{W_{N/S}}$ increases from 0.7 to 1.2. The carbon foams prepared at $\mathbf{W_{N/S}}$ in the range of 0.7-1.2 show specific surface area and micropore volume in close ranges of 379-442 m^2 g^{-1} and 0.13-0.15 cm^3 g^{-1}, respectively. The DFT pore size analysis shows a peak corresponding to a pore size of 1.04 nm. The presence of micropore is supported by the TEM analysis of the carbon foam sample.

CHAPTER 3

LOW-DENSITY MICROCELLULAR CARBON FOAMS FROM SUCROSE BY NaCl PARTICLE TEMPLATING USING GLYCEROL AS A PLASTICIZING ADDITIVE

3.1 Introduction

A major limitation of the microcellular carbon foam prepared by NaCl templating method reported in **Chapter 2** was the presence of large macropores formed by the entrapped water vapour generated during polymerisation of sucrose. This created a heterogeneity in the microstructure of the microcellular carbon foam. However, the macropore size and volume decrease with an increase in the NaCl to sucrose weight ratio ($\mathbf{W_{N/S}}$). The reason is that at higher concentrations of solid NaCl particles, the space for the water vapour to coalesce in the molten sucrose-NaCl paste is restricted. Nevertheless, increasing the $\mathbf{W_{N/S}}$ beyond 1.2 resulted in molten sucrose-NaCl pastes with very high viscosity as the quantity of molten sucrose is not sufficient to create an adequately thick layer around the NaCl particles to induce flow. This limits the achievable lower density and thermal conductivity of the carbon foams to 0.31 g cm^{-3} and 0.257 W m^{-1} K^{-1}, respectively. The versatility of a foam preparation process depends on its ability to produce foams with a wide range of density and homogenous pore structure. In the present chapter, low-density microcellular carbon foams of uniform pore structure (devoid of macropores) with density and thermal conductivity as low as 0.095 g cm^{-3} and 0.088 W m^{-1} K^{-1}, respectively, is achieved by increasing the NaCl template loading in the composition and using glycerol as a plasticizing additive. Machining of carbon-NaCl composites using conventional machine tools followed by NaCl removal by leaching with water is used as a strategy to produce low-density carbon foams with desired contours.

3.2 Experimental

3.2.1 Preparation of low-density microcellular carbon foams

The analytical reagent grade sucrose, NaCl, glycerol, and methanol were procured from Merck India Ltd. Mumbai. Methanol was selected as a ball-milling medium in this work based on two reasons; (i) NaCl is only sparingly soluble (14.9 g L^{-1}) in methanol and (ii) glycerol is completely miscible with methanol. The preparation methodology was similar to the work reported in **Chapter 2**. The flowchart of the process is given in **Figure 3.1**. The sucrose, NaCl powder, and glycerol were mixed by planetary ball milling (Fritsch, Germany) in methanol medium for 2 h at a speed of 200 RPM. Zirconia grinding balls of 10 mm diameter and zirconia jar of 500 ml capacity were used for ball milling. The powder to ball and powder to methanol weight ratios were 1:2 and 3:4, respectively. The slurry obtained after ball milling was dried in an air oven at 70 °C in a borosilicate glass tray for 12 h. The sucrose-NaCl-glycerol mixtures thus-obtained were heated in an air oven at 185 °C to melt the sucrose and thoroughly blended with a wooden ladle to form pastes. The pastes were transferred into the stainless steel mould with a rectangular cavity of size 10 cm × 10 cm × 2.5 cm. The mould was then covered with its lid and gently pressed at 160 °C in a hydraulic press for the setting. The samples were removed from the mould after cooling to room temperature. The samples removed from the mould were annealed at 200 °C for 2 h in an air oven and heated in an argon atmosphere at 750 °C for 2 h at a heating rate of 1 °C min^{-1}.

The samples were removed from the furnace after cooling naturally to room temperature. The same inert atmosphere was maintained during the cooling as well. The samples heat-treated at 750 °C were washed with distilled water at 90 °C until the whole NaCl present in the body was leached out. The NaCl-removed bodies were further heat-treated at 900 °C in the inert atmosphere furnace for 2 h at a rate of 1 °C min^{-1}. Shrinkage during the heat-treatments was calculated from the dimensions measured before and after the heat-treatment processes. The large pores formed by the entrapment of water vapour, smaller pores formed by the removal of NaCl template and nanometer-size pores formed by *in situ* activation are named as macropores, microcells, and micropores, respectively.

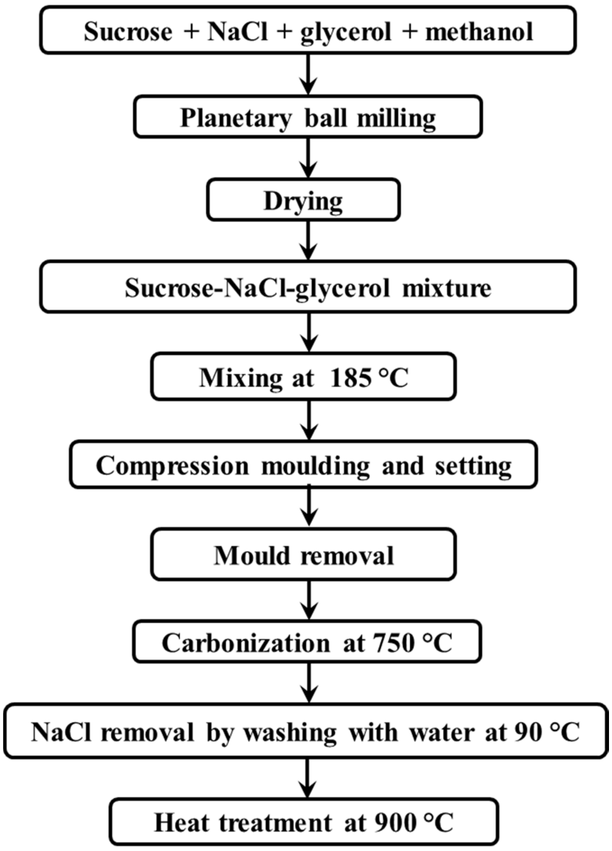

Figure 3.1 Flow chart of processing of low-density microcellular carbon foam

3.2.2 Characterization

3.2.2.1 Rheological measurements

The viscosity measurement of the molten sucrose-NaCl-glycerol pastes was carried out at various shear rates at 160 °C using a rheometer (MCR 102 Modular Compact Rheometer, Anton Paar, USA) with a cone and plate measurement system (CP-25, 25 mm diameter and angle 2°). The samples for viscosity measurements were prepared by blending sucrose-NaCl-glycerol mixtures in a borosilicate glass beaker at 185 °C.

3.2.2.2 Setting characteristics of pastes

The torque-time measurement of the molten sucrose-NaCl-glycerol pastes was also carried out in a torque rheometer (Brabender PlastiCorder, GmbH, Germany) with a rotor speed of 10 RPM at 160 °C. The setting time of the pastes for each $\mathbf{W_{N/S}}$ was determined by trial and error method. Specifically, the bodies removed from the mould after compression moulding the paste at various time intervals were reheated at 160 °C in an air oven. The properly-set bodies did not soften while reheating at 160 °C and the corresponding pressing time was taken as the setting time.

3.2.2.3 Machinability

The machinability of the carbon-NaCl composites was tested by producing holes and slots on rectangular bodies by drilling and milling, respectively. The conventional drilling and milling machines and high-speed steel tools were used for the machining operations.

3.2.2.4 Density measurement

The bulk density of microcellular carbon foams was calculated from the weight and dimensions of polished rectangular samples derived from the foam bodies. The skeletal density was measured using a helium pycnometer (AccuPyc II 1340 Pycnometer, Micromeritics, USA). The porosity of the foams was calculated from the relative density using Equation 2.2 (**Chapter 2**).

3.2.2.5 SEM analysis

The microstructure of the low-density microcellular foams was analyzed on fractured surfaces using a high-resolution scanning electron microscope (HRSEM, FEI QuantaFEG200, USA). The microcell size was measured from the high-magnification SEM images using the ImageJ software. The cell sizes measured from a minimum of three SEM images of the same sample was used for the calculation of the average cell size.

3.2.2.6 Measurement of textural properties

The volumetric N_2 adsorption-desorption measurement of the low-density microcellular foams was carried out using a surface area analyzer (Micromeritics Tristar II, USA). The details of the measurements are the same as reported in **Chapter 2**.

3.2.2.7 Compressive strength measurements

The compressive strength measurement was carried out using a Universal Testing Machine (Instron 5050, Instron, USA) at a crosshead speed of 0.5 mm min^{-1}. The foam samples of 24 mm × 24 mm × 12 mm (ASTM standard C365/C365M-05) size were used for the measurement. Furthermore, the compressive strength measurement of carbon-NaCl composites was also carried out using a rectangular sample of 10 mm × 10 mm × 20 mm size at the same crosshead speed.

3.2.2.8 Thermal conductivity measurements

The thermal conductivity of the microcellular carbon foams was measured using the transient plane source method (Hot Disk, TPS 2500S, Sweden) at room temperature. Rectangular samples of dimension 40 mm × 40 mm × 15 mm were used for the measurement.

3.2.2.9 Electrical conductivity measurement

The electrical conductivity of the foams was measured using the four probe method. A programmable current source (Keithley 6221) and a digital voltmeter were used. The probes used were the spring-loaded type and a minimum pressure was applied to ensure proper electrical contact between the sample and the probes. The voltage (V) between two pins separated by a distance (s) of 2 mm was measured using a nanovoltmeter. A digital photograph of the electrical conductivity measurement setup is shown in **Figure 3.2**. The bulk resistivity (R_f) was calculated from the current and voltage readings using the equation:

$$R_f = 2\pi s \left(\frac{V}{I}\right) \qquad (3.1)$$

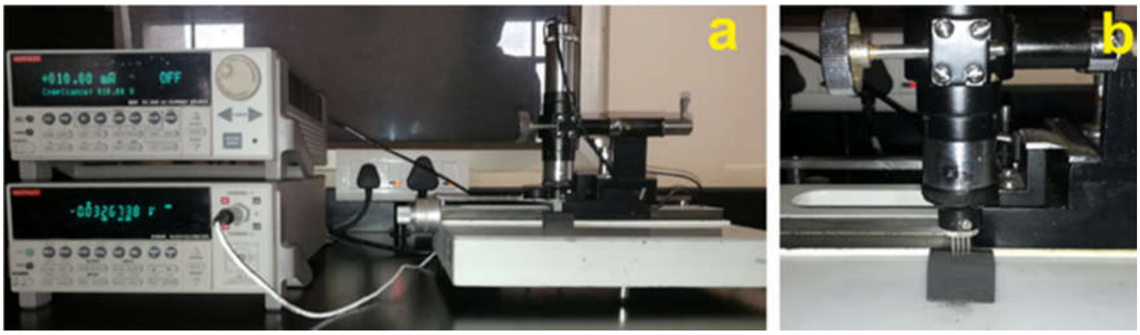

Figure 3.2 Digital photograph of (a) Four probe electrical conductivity measurement setup and (b) probes placed firmly in contact with the foam sample

3.2.2.10 Measurement of EMI shielding effectiveness

The electromagnetic interference (EMI) shielding effectiveness (SE) of the low-density microcellular carbon `foams was measured for the X-band (8.2–12.4 GHz) in the microwave region using a vector network analyzer (E5071C, Agilent) and a corresponding waveguide. Rectangular foam samples of dimensions 22.7 mm × 10.2 mm × 5 mm were used. The samples were cut and polished corresponding to the dimensions of the cavity of the shim and then push fitted to establish proper electrical contact with the internal walls and to minimize the spurious leakage of the microwave. A full two-port VNA calibration was performed at the beginning of each test to avoid the measurement error. The scattering parameters S_{11}, S_{12}, S_{21} and S_{22} were recorded and EMI shielding effectiveness (EMI SE) was deduced from the scattering parameters. **Figure 3.3** shows the schematic of the s-parameters measured using a 2 port network analyzer.

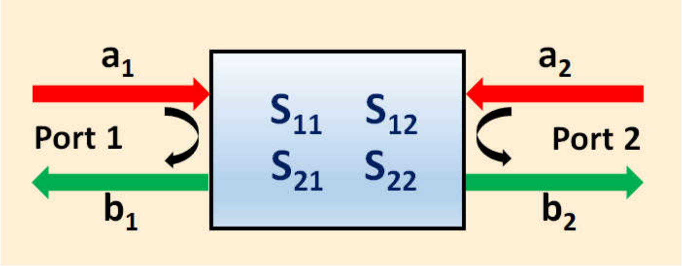

$$S_{11} = \frac{b_1}{a_1} \quad S_{21} = \frac{b_2}{a_1} \quad (a_2 = 0)$$

$$S_{22} = \frac{b_2}{a_2} \quad S_{12} = \frac{b_1}{a_2} \quad (a_1 = 0)$$

Figure 3.3 S-parameters in a 2 port vector network analyzer

3.3 Results and discussion

3.3.1 Preparation molten sucrose-NaCl-glycerol pastes

Carbon-NaCl composites with high NaCl loading are required to achieve low-density microcellular carbon foams. Preparation of carbon-NaCl composites with high NaCl loading is not possible from sucrose-NaCl mixtures as the sucrose-NaCl mixtures of $\mathbf{W_{N/S}}$ beyond 1.2 do not produce mouldable paste upon hot blending at 185 °C. At $\mathbf{W_{N/S}}$ higher than 1.2, the molten sucrose is insufficient to produce an adequately thick layer on NaCl particle surface to induce plasticity. Thus, the incorporation of a plasticizing additive enables higher NaCl powder loading. The criteria for the selection of a plasticizing additive are (i) it should be completely miscible with molten sucrose (ii) its boiling point should be higher than the processing temperature (185 °C), and (iii) the

NaCl template should be poorly soluble in the plasticizing additive. Glycerol satisfies all the above criteria as it is completely miscible with molten sucrose and has a boiling point of 290 °C. The NaCl has a poor solubility of 10 g/100 ml in glycerol at room temperature. In addition, the glycerol is expected to polymerize with the sucrose through -OH to -OH condensation during curing of the paste and become part of the polymeric structure.

The amount of glycerol required for forming a paste with a mouldable consistency depends on the $\mathbf{W_{N/S}}$. It is determined using the following procedure: a known weight (300 g) of sucrose–NaCl mixtures of various $\mathbf{W_{N/S}}$ was heated in a 1 L borosilicate glass beaker using a heating mantle to melt the sucrose. The glycerol is progressively added to the hot mixture under continuous blending with a wooden ladle by keeping the beaker in the heating mantle until the sucrose-NaCl powder mixture forms a paste of mouldable consistency. The amount of glycerol required to plasticize sucrose-NaCl powder mixture containing 100 g sucrose increases from 14 g to 74 g when the $\mathbf{W_{N/S}}$ increases from 1.5 to 3. The composition of the sucrose-NaCl-glycerol mixtures forming a paste with mouldable consistency is given in **Table 3.1**.

Table 3.1 Compositions used for the preparation of low-density microcellular carbon foams

Sucrose (g)	**NaCl (g)**	**Glycerol (g)**	**Sucrose to NaCl weight ratio ($\mathbf{W_{N/S}}$)**
100	150	14	1.5
100	175	20	1.75
100	200	26	2
100	225	34	2.25
100	250	45	2.5
100	275	56	2.75
100	300	74	3

During hot blending of the sucrose-NaCl-glycerol mixtures, the molten sucrose and glycerol form a homogeneous solution. The molten sucrose-glycerol solutions have a lower viscosity than that of molten sucrose. The viscosity at 160 °C of molten sucrose measured at a shear rate of 10 s^{-1} decreases from 1230 mPa.s to 28 mPa.s with the incorporation of 42.5 wt% glycerol (sucrose-glycerol of a composition equivalent to $\mathbf{W_{N/S}}$ of 3). The low viscous sucrose-glycerol solutions easily coat over the NaCl particles to form pastes of the required consistency. The prepared molten sucrose-NaCl-glycerol pastes show highly shear thinning flow behaviour at 160 °C. The viscosity of the pastes does not show a regular trend with the **W$_{N/S}$**. The pastes prepared at **W$_{N/S}$** in the range of 1.5 to 3 show a very high viscosity in the range of 7.5 to 25 kPa.s at a low shear rate of 2 s^{-1}. On the other hand, the viscosity decreases to the range of 0.1 to 20 Pa.s when the shear rate increases to 100 s^{-1}. The viscosity of the pastes measured at 160 °C as a function of shear rate is shown in **Figure 3.4**.

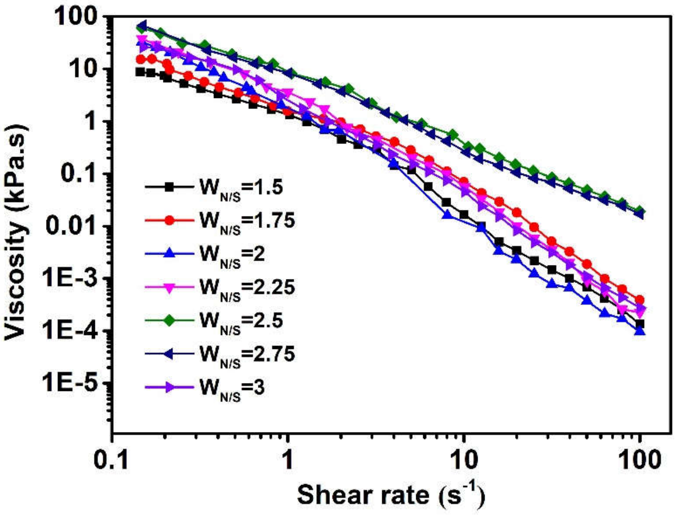

Figure 3.4 The viscosity-shear rate plot of the molten sucrose-NaCl-glycerol pastes prepared at various **W$_{N/S}$** measured at160 °C

The shear thinning nature of the paste enables easy mould filling whereas the high viscosity at low shear rate prevents oozing of the paste out of the mould during the setting. The lack of a regular trend in viscosity of the paste with **W$_{N/S}$** and a broad range of observed viscosity at a particular shear rate indicates the inadequacy of the manual method used for the determination of the amount of glycerol required for the formation of a mouldable paste. In spite of this, all the prepared pastes are very much suitable for compression moulding.

3.3.2 Setting characteristics of molten sucrose-NaCl-glycerol pastes

Compression moulding of the molten sucrose-NaCl-glycerol paste in a steel mould at 160 °C results in setting due to the polymerization of glucose and fructose anhydride formed from sucrose (Darder & Ruiz-Hitzky, 2005; R. Narasimman &

Prabhakaran, 2012). The approximate time required for the setting of sucrose-NaCl-glycerol paste was determined by trial and error method. Setting time increases from 5 to 13 hours when the $\mathbf{W_{N/S}}$ increases from 1.5 to 3 (**Table 3.2**). The increase in setting time with an increase in $\mathbf{W_{N/S}}$ indicates the sluggish polymerization of glucose and fructose anhydride in glycerol medium. This is further evidenced by the torque-time measurements. The variation of torque with time of molten sucrose-NaCl-glycerol pastes of various $\mathbf{W_{N/S}}$ measured at 160 °C is shown in **Figure 3.5**. The torque remains steady up to a certain time and then increases slowly with time. The molten sucrose-NaCl paste at a $\mathbf{W_{N/S}}$ of 1.2 reaches a torque of 100 Nm in ~155 min (**Chapter 2**). However, in the present case, molten sucrose-NaCl-glycerol pastes take a longer time for reaching a torque of 100 Nm. The time required for reaching a torque of 100 Nm increases from 288 to 461 min when the $\mathbf{W_{N/S}}$ increases from 1.5 to 2. The pastes prepared at $\mathbf{W_{N/S}}$ of 2.25, 2.5, 2.75 and 3 reaches a torque value of 74, 39, 36 and 7.5 Nm, respectively, in nearly 530 min. The measurement of torque is restricted to 530 min as the continuous measurement is possible only up to 9 h with the available torque rheometer. The increase in torque with time is due to the increase in molecular weight of the sucrose polymer. An early torque build-up is observed in molten sucrose-NaCl-glycerol pastes of lower $\mathbf{W_{N/S}}$ indicating a faster increase in molecular weight of the sucrose polymer. The study suggests that the glycerol in molten sucrose-NaCl-glycerol pastes retard the polymerization of glucose and fructose anhydride formed from sucrose.

Table 3.2 Approximate setting time of molten sucrose-NaCl-glycerol pastes prepared at various $\mathbf{W_{N/S}}$

$\mathbf{W_{N/S}}$	1.5	1.75	2	2.25	2.5	2.75	3
Setting time (h)	5	6	7	8	9.5	11	13

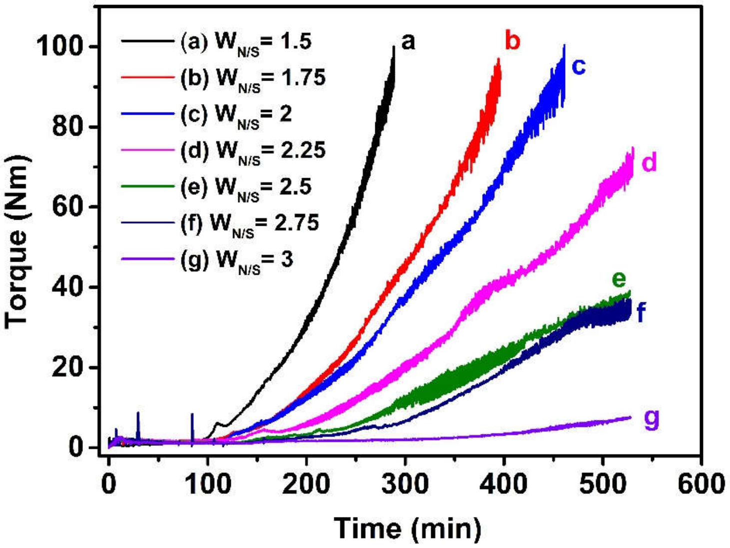

Figure 3.5 Torque-time graph of molten sucrose-NaCl-glycerol pastes of various $\mathbf{W_{N/S}}$ measured at 160 °C

3.3.3 Composition of sucrose polymer-NaCl and Carbon-NaCl composites

The polymer content in the sucrose polymer-NaCl composite bodies estimated from their weight losses at 650 °C in air atmosphere decreases from 32.8 to 18.8 wt% when the $\mathbf{W_{N/S}}$ increases from 1.5 to 3. The sucrose in sucrose-NaCl mixture undergoes a total weight loss of 19.7 wt% during heating at 160 °C for 6 h and subsequent annealing at 200 °C for 2 h. The polymer content calculated by considering the weight retention from sucrose alone contributes to 34.8 to 21.1 wt%. That is, the estimated polymer content is slightly lower than the polymer content calculated by considering the sucrose alone. This indicates that contrary to our expectation of co-polymerization with sucrose through –OH condensation, the glycerol in the sucrose-NaCl-glycerol mixture escapes during compression moulding and subsequent annealing at 200 °C. This is further confirmed by the fact that the majority of the glycerol in NaCl-glycerol mixture (15 wt% glycerol) taken in a beaker slowly evaporates when heated in an air oven at 160 °C for 6 h. This result suggests that the setting of molten sucrose-NaCl-glycerol pastes is not due to the polymerization of glucose and fructose anhydride alone but also due to the slow removal of the glycerol by evaporation. It is inferred that both the polymerization of glucose & fructose anhydride and removal of glycerol increase the viscosity with time which converts the paste to the solid body.

The carbon content in carbon-NaCl composite bodies estimated from their weight losses at 650 °C in air atmosphere decreases from 16.6 to 7.8 wt% when the $\mathbf{W_{N/S}}$ increases from 1.5 to 3. The polymer content in polymer-NaCl composite and carbon content in the carbon-NaCl composite at various $\mathbf{W_{N/S}}$ are given in **Table 3.3**. The carbon yield of the sucrose polymer calculated from the polymer content of the polymer-NaCl composites and carbon content of the carbon-NaCl composites is also given in **Table 3.3**. The sucrose polymer in the polymer-NaCl composite at a $\mathbf{W_{N/S}}$ of 1.5 shows a carbon yield of 40.9 wt%. On the other hand, the sucrose polymer in polymer-NaCl composites at $\mathbf{W_{N/S}}$ in the range of 1.75 to 3 is in a close range of 36.2 to 36.9 wt%. It is well known that the carbon yield from a precursor polymer increases with an increase in molecular weight. The lower carbon yield from the sucrose polymer at higher $\mathbf{W_{N/S}}$ indicates that the sucrose polymer formed at higher glycerol concentration has lower molecular weight.

Table 3.3 The polymer content in polymer-NaCl composite and carbon content in the carbon-NaCl composite

$\mathbf{W_{N/S}}$	**Polymer content in Polymer-NaCl composite (wt%)***	**Carbon content in Carbon-NaCl composite (wt%)**	**Carbon yield (wt%)**
1.5	32.8 (34.8)	16.6	40.9
1.75	29.2 (31.4)	13.0	36.2
2	27.4 (28.6)	12.0	36.3
2.25	23.4 (26.3)	9.3	36.6
2.5	21.9 (24.3)	8.6	36.9
2.75	19.5 (22.6)	8.2	36.7
3	18.8 (21.1)	7.8	36.5

*Values in the parenthesis are polymer content calculated based on 19.7% of weight loss from sucrose

3.3.4 Carbonization shrinkage

The shrinkage of the sucrose polymer-NaCl composites during the carbonization at 750 °C decreases with an increase in $\mathbf{W_{N/S}}$. The linear shrinkage decreases from 7.62 to 3.64% whereas the volume shrinkage decreases from 20.65 to 10.02% when the $\mathbf{W_{N/S}}$

increases from 1.5 to 3. The effect of **$W_{N/S}$** on the shrinkage during carbonization is shown in **Figure 3.6**.

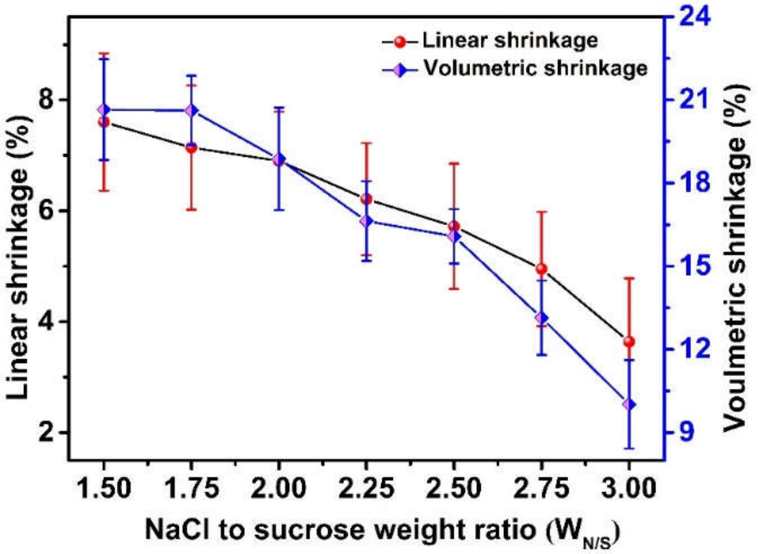

Figure 3.6 Effect of **$W_{N/S}$** on the carbonization shrinkage of sucrose polymer-NaCl composites

During the heat-treatment, the size of NaCl particles in the composite body remains unchanged whereas the sucrose polymer shrinks due to carbonization. That is, the observed shrinkage of the body is due to the shrinkage of sucrose polymer. The decrease in shrinkage of the body with an increase in **$W_{N/S}$** is due to the decrease in sucrose polymer concentration. The carbon-NaCl composites contain a uniform distribution of NaCl particles in the carbon matrix. Typical SEM image of a fractured surface of the carbon-NaCl composite is shown in **Figure 3.7**. The size of NaCl particles observed in the carbon-NaCl composites, which decides the size of microcells in the final carbon foam, is in the range of 1 to 17 µm. The size of NaCl particles observed is slightly higher than that observed in carbon–NaCl composites prepared from sucrose-NaCl mixture alone. This indicates that ball milling in the presence of glycerol adversely affects the particle size reduction of NaCl due to the higher viscosity of the slurry.

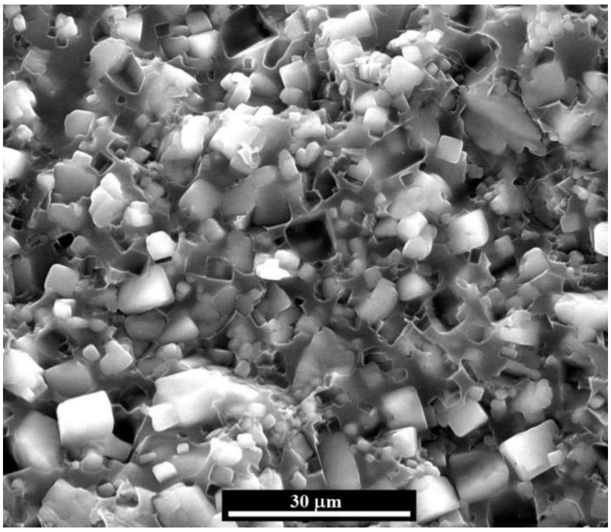

Figure 3.7 SEM photomicrograph of the fractured surface of a carbon-NaCl composite

3.3.5 Foam density

Figure 3.8 shows the effect of **$W_{N/S}$** on the bulk density of low-density microcellular carbon foams. The bulk density of the foam decreases linearly from 0.214 to 0.096 g cm^{-3} when the **$W_{N/S}$** increases from 1.5 to 3. The skeletal density of the carbon foams prepared at **$W_{N/S}$** in the range of 1.5 to 3 is given in **Table 3.4**. The skeletal density observed is in the range of 1.94 to 2.04 g cm^{-3} with an average value of 1.98 ± 0.04 g cm^{-3}. The porosity calculated from the bulk density and average skeletal density of the low-density microcellular foams increases from 89.19 to 95.15 vol.% when the **$W_{N/S}$** increases from 1.5 to 3.

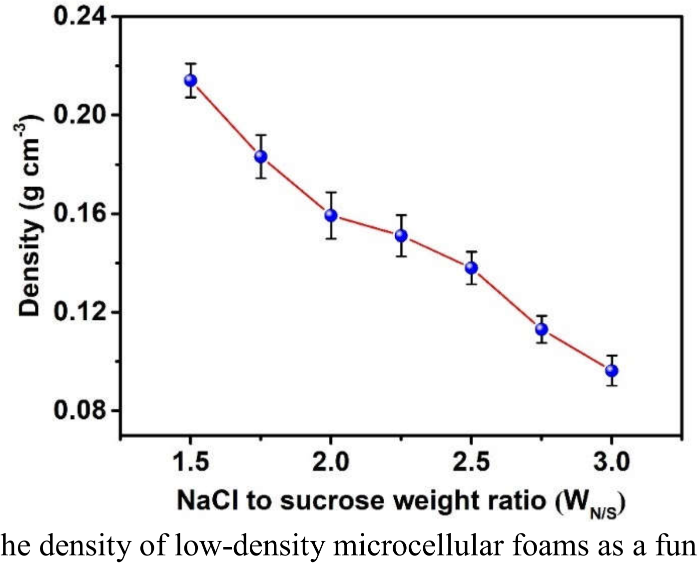

Figure 3.8 The density of low-density microcellular foams as a function of **$W_{N/S}$**

Table 3.4 Skeletal density of carbon foams prepared at various $\mathbf{W_{N/S}}$

$\mathbf{W_{N/S}}$	1.5	1.75	2	2.25	2.5	5.75	3
Skeletal density (g cm^{-3})	2.03	2.04	1.97	1.98	1.96	1.96	1.94

3.3.6 Compressive strength

The compressive stress-strain behaviour of low-density microcellular carbon foams prepared at various $\mathbf{W_{N/S}}$ is shown in **Figure 3.9**a. The stress-strain graph shows typical behaviour of brittle foam materials: an initial linear region at low strain followed by a stress maximum, a near plateau region and a region of densification at high strain (Letellier, Delgado-Sanchez, Khelifa, Fierro, & Celzard, 2017; Tondi, Fierro, et al., 2009; Zúñiga Ruiz et al., 2015). The slope of the initial linear region is taken as Young's modulus and the stress corresponding to the plateau region (except for $\mathbf{W_{N/S}}$=1.5) in the stress-strain graph is taken as the compressive strength. At $\mathbf{W_{N/S}}$=1.5, there is a rapid decline in the stress after a maximum. The stress corresponding to this maximum is taken as its compressive strength. The variation of compressive strength and Young's modulus as a function of $\mathbf{W_{N/S}}$ is shown in **Figure 3.9**b. The average compressive strength decreases from 4.84 to 0.60 MPa when the $\mathbf{W_{N/S}}$ increases from 1.5 to 3. The corresponding decrease in Young's modulus is from 345 to 35 MPa. The compressive strength of the foams shows a linear relationship with density with an R^2 value of 0.9816 (**Figure 3.9**c). Generally, the compressive strength and Young's modulus of brittle foam materials decreases with an increase in porosity and cell size. In addition, a decrease in strut and cell wall thickness also decreases the compressive strength and Young's modulus (Letellier, Delgado-Sanchez, et al., 2017). In the present case, the decrease in compressive strength and Young's modulus with an increase in $\mathbf{W_{N/S}}$ is due to the increase in porosity and decrease in the cell wall and the strut thickness, as the foams prepared at all $\mathbf{W_{N/S}}$ exhibit more or less the same microcell size distribution. The compressive strength observed for the microcellular carbon foams are much higher than that of macrocellular foams prepared from the same precursor material.

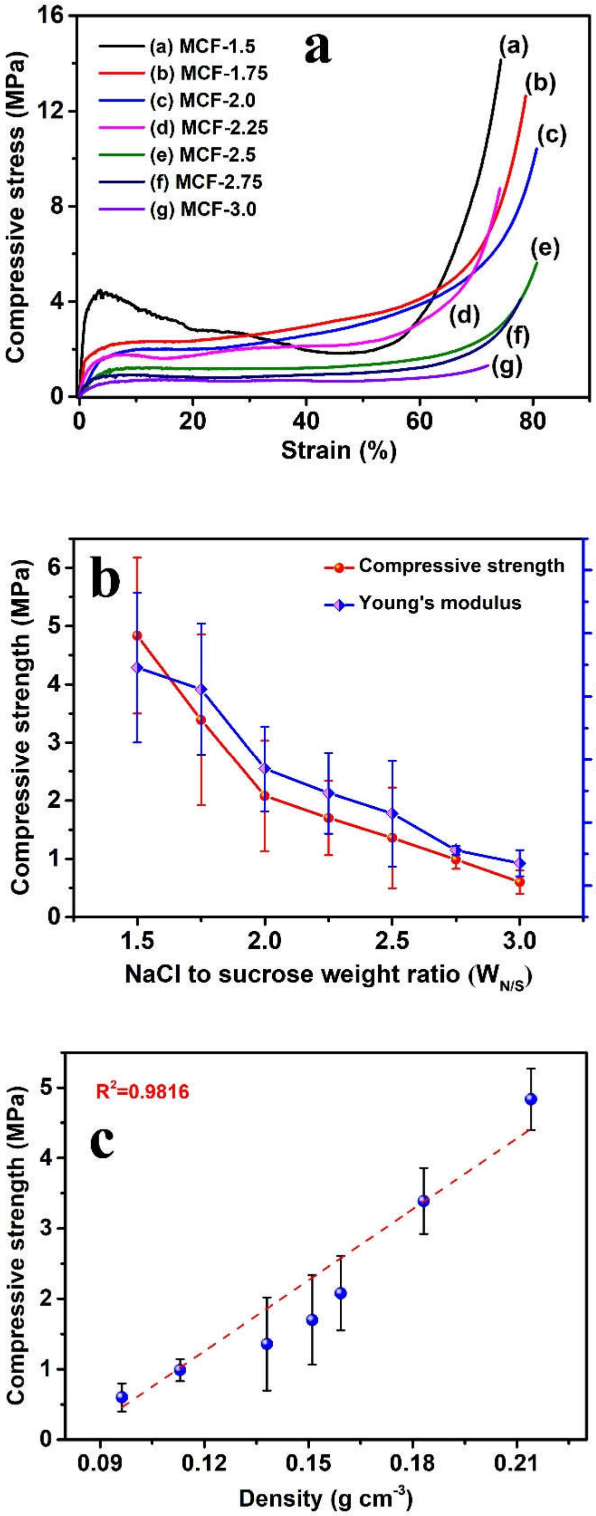

Figure 3.9 (a) Stress-strain plot of low-density microcellular foams (b) compressive strength and Young's modulus as a function of $\mathbf{W}_{\mathbf{N/S}}$ and (c) relationship between compressive strength and density of foams

Macrocellular carbon foams of density 0.22 and 0.14 g cm^{-3} possessing a cell size of ~890 µm prepared by thermo-foaming of molten sucrose showed compressive strength value of 1.30 and 0.90MPa, respectively (R Narasimman et al., 2016, 2015). The low-density microcellular foams of comparable density, 0.214 and 0.138 g cm^{-3}, show compressive strengths of 4.8 and 1.4 MPa, respectively. That is, nearly 55 to 269 % increase in compressive strength is observed in the density range of 0.138 to 0.214 g cm^{-3} because of the change in cell size from the macrocellular to the microcellular range.

3.3.7 Microstructure

The carbon foams of higher density reported from molten sucrose-NaCl pastes contain macropores of size in the range of 414 to 70 µm in addition to the microcells created by the NaCl templates (**Chapter 2**). These macropores are formed by the entrapment of water vapour produced by –OH condensation during caramelization. The introduction of glycerol in the molten sucrose-NaCl system results in a remarkable change in the foam microstructure. The macropores observed in carbon foams obtained from molten sucrose-NaCl pastes are absent in carbon foams prepared from the molten sucrose-NaCl-glycerol paste. This is clearly evidenced by the low-magnification SEM photomicrograph of the foams shown in **Figure 3.10**. It appears that the water vapour produced by –OH condensation in molten sucrose-NaCl-glycerol pastes diffuses out rather than producing bubbles in the body. One reason for this is the slow formation of water vapour during the setting of molten sucrose-NaCl-glycerol paste compared to that of molten sucrose-NaCl paste as evidenced by the high setting time and slow torque build-up. It appears that the rate of formation of water vapour by –OH condensation is the same as its rate of diffusion. To be precise, during setting, the concentration of water vapour in the paste never reaches the level required for the nucleation of bubbles. Alternate reason can be the modification of surface tension and viscosity of the molten sucrose by the incorporation of glycerol. It is well known that high viscosity and low surface tension are favourable for stabilization of bubbles. The decrease in viscosity of molten sucrose by the addition of glycerol as well as the gradual increase in viscosity with time due to sluggish polymerization of glucose and fructose anhydride in glycerol medium do not favour the formation of bubbles.

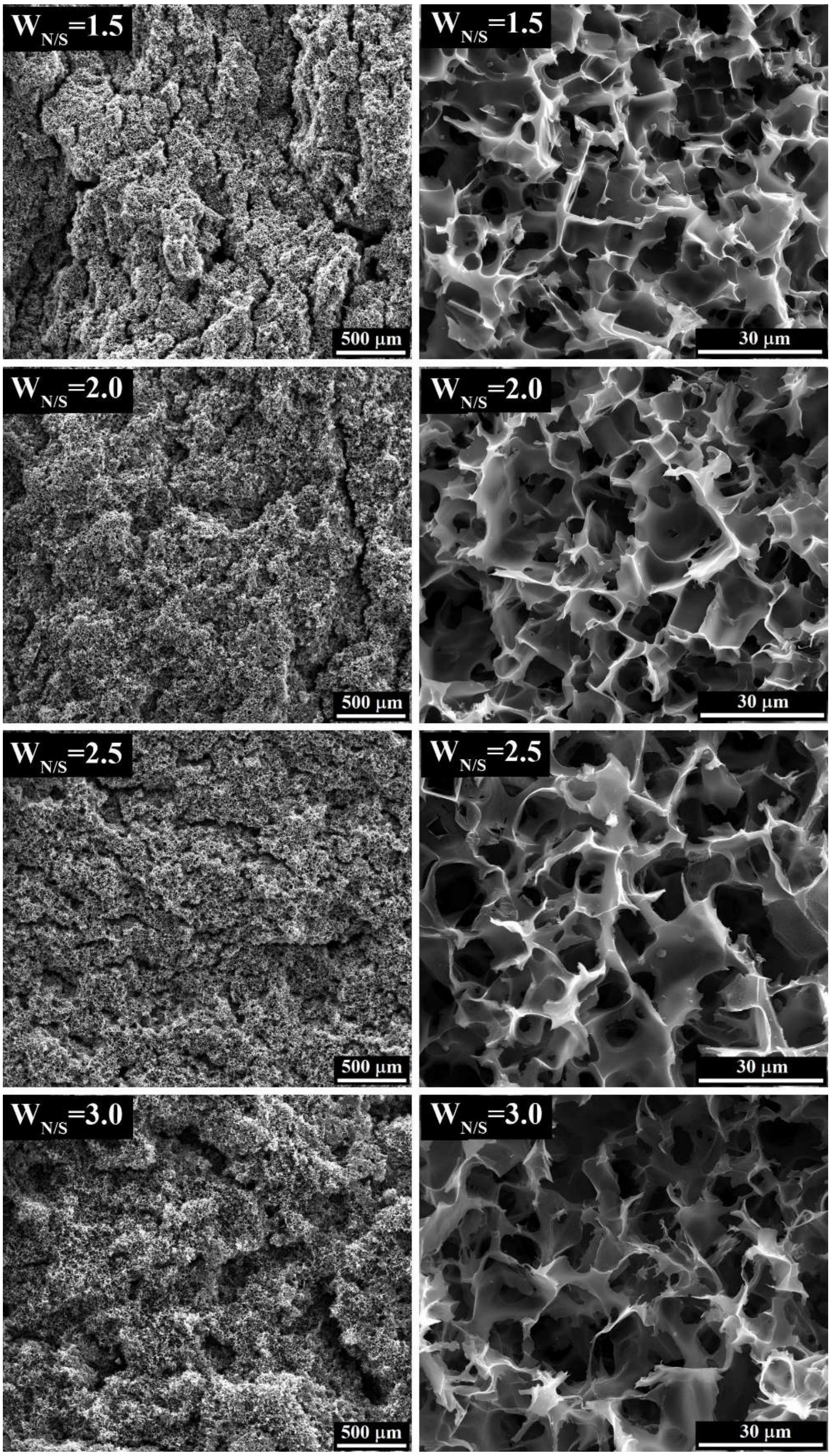

Figure 3.10 The low-magnification (left) and high-magnification (right) SEM images of microcellular carbon foams prepared at $\mathbf{W}_{N/S}$ of 1.5, 2, 2.5 and 3, respectively

The high-magnification images in **Figure 3.10** show the microcells formed by the removal of NaCl templates. The microcells have an irregular shape. The range of microcell sizes observed in all the prepared low-density microcellular carbon foams is more or less identical. However, the thickness of microcell walls decreases with an increase in $\mathbf{W_{N/S}}$. This is because the same amount of molten sucrose produces a thinner layer of sucrose polymer over the NaCl particle surface with an increase in $\mathbf{W_{N/S}}$. The approximate estimation of microcell size distribution obtained from the SEM images by ImageJ software is shown in **Figure 3.11**.

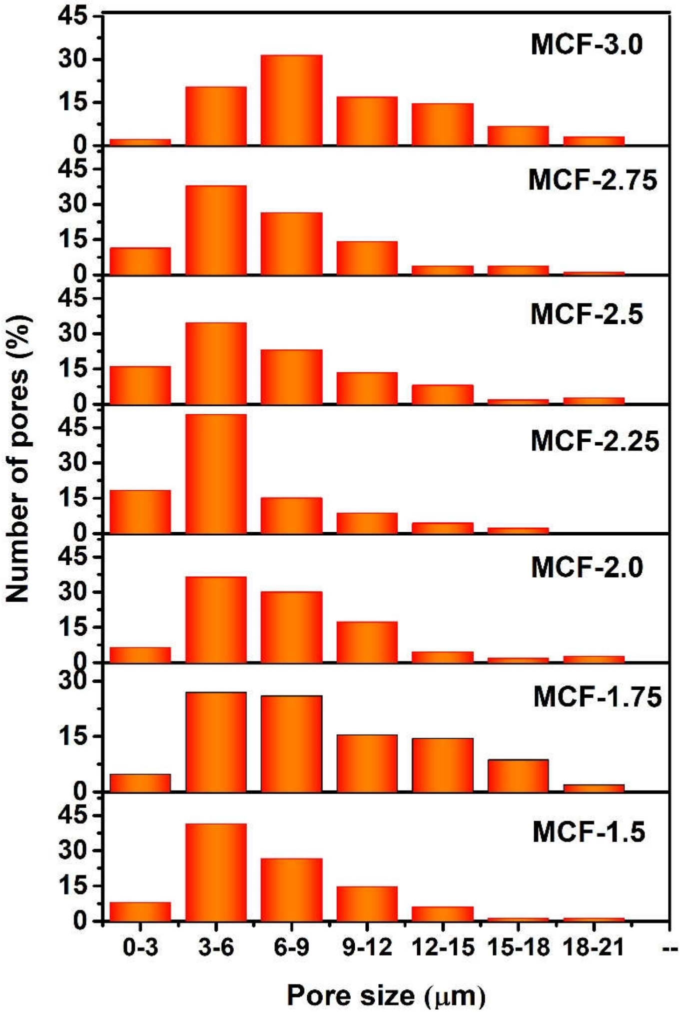

Figure 3.11 Microcell size distribution of low-density microcellular carbon foam determined from the SEM images

The sizes of microcells observed are in the range of 2 to 20 µm. The majority of the microcells are in the size range of 3 to 6 µm. The average microcell sizes observed for the low-density microcellular carbon foams are in the range of 5.8 to 7.9 µm. The carbon foams prepared from molten sucrose-NaCl pastes showed microcell sizes in the range of 2 to 12 µm with an average cell size of nearly 5 µm (**Chapter 2**). The observed higher microcell size in low-density foams is due to the less effective particle size reduction of NaCl during ball milling in the more viscous methanol-glycerol medium.

3.3.8 Machinability of carbon-NaCl composites

The carbon foams intended for structural, thermo-structural and EMI shielding applications should be made in required contours. The carbon foams prepared in simple shapes are converted into the required complex shapes by machining (Y. R. Lin et al., 2010; Q. Yu, Straatman, & Thompson, 2006). For successful machining, the carbon foams should have adequate strength for holding them in machines and to withstand the stresses during machining. Moreover, the machined surface should have a very good finish. Though the carbon foams prepared from coal and mesophase pitch are reported to have good machinability characteristics, machining of thin-walled fins in structures used for heat exchanger applications is reported to be troublesome. Special techniques were developed to produce such thin-walled structures by Klett et al. in Oak Ridge National Laboratory, USA (Gallego & Klett, 2003). However, the technique is not disclosed in the open literature. The low-density carbon foams are extremely susceptible to damage while holding in machines and during the machining. One way to overcome this problem is the machining of the carbon-NaCl composite body and subsequent removal of NaCl by leaching with water as the carbon-NaCl composites are sturdy. **Figure 3.12** shows the stress-strain graph of the carbon-NaCl composite bodies prepared at various $\mathbf{W_{N/S}}$. The stress-strain graph shows an initial linear region and a stress maximum. The stress maximum is followed by a slow decline in stress. The stress corresponding to the maximum in the stress-strain graph is taken as the compressive strength and slope of the initial linear region is taken as Young's modulus. The stress-strain graph indicates that the carbon-NaCl composites are sufficiently ductile to resist cracking while holding them in milling and drilling machines and during the machining.

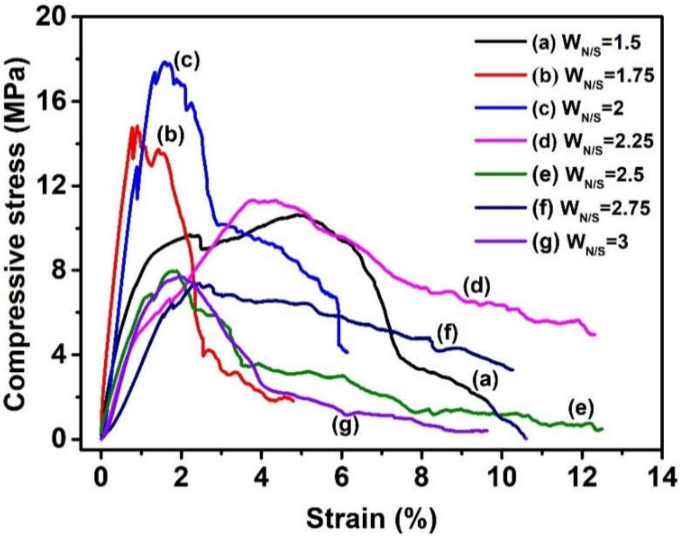

Figure 3.12 Compressive stress-strain graph of the carbon-NaCl composites prepared at various $\mathbf{W_{N/S}}$

The compressive strength of carbon-NaCl composite body increases from 10.7 to 17.8 MPa when the $\mathbf{W_{N/S}}$ increases from 1.5 to 2. Further increase in $\mathbf{W_{N/S}}$ decreases the compressive strength of the carbon-NaCl composite. The compressive strength decreases from 17.8 to 6.9 MPa when the $\mathbf{W_{N/S}}$ increases from 2 to 3. Young's modulus also follows the same trend. That is, Young's modulus increases from 1006 to 1964 MPa when the $\mathbf{W_{N/S}}$ increases from 1.5 to 2 and then decreases to 521 MPa when the $\mathbf{W_{N/S}}$ further increases to 3. The effect of $\mathbf{W_{N/S}}$ on the compressive strength and Young's modulus of carbon-NaCl composites is shown in **Figure 3.13**. In carbon-NaCl composites, the brittle NaCl matrix is reinforced by the soft turbostratic graphite. Each NaCl particles in the carbon-NaCl composite are surrounded by a layer of the carbon. The strength of the composites depends on the thickness of the soft carbon phase around the brittle NaCl particles. The maximum compressive strength and Young's modulus are expected at an optimum thickness of the soft phase. It appears that an optimum thickness of soft carbon phase around the NaCl particles is produced at a $\mathbf{W_{N/S}}$ of 2. The compressive strengths of the carbon-NaCl composites prepared at $\mathbf{W_{N/S}}$ in the range of 1.5 to 3 are sufficiently high for holding them in milling and drilling machines. **Figure 3.14**a shows the photograph of rectangular carbon-NaCl composite bodies subjected to machining. The holes are made by drilling and slots are made by milling using conventional drilling and milling machines and high-speed steel tools. The fins of thickness 5 and 3 mm produced on the rectangular carbon-NaCl composite body by milling are clearly seen. The machined surfaces have a very good finish.

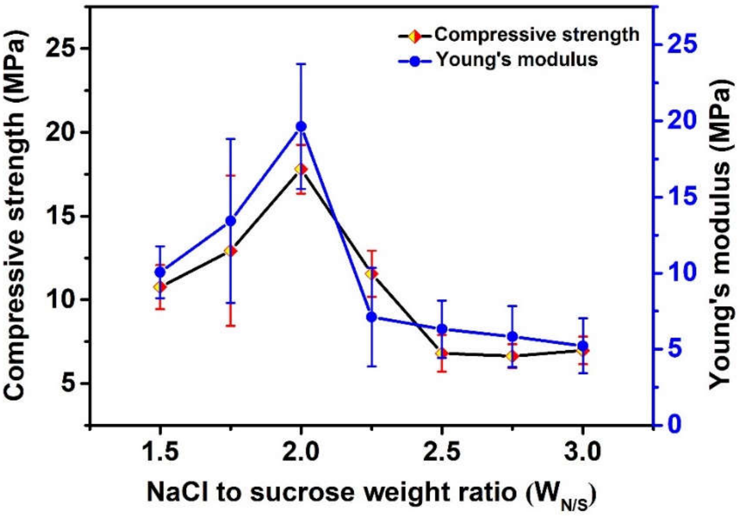

Figure 3.13 The effect of $\mathbf{W_{N/S}}$ on the compressive strength and Young's modulus of carbon-NaCl composites

The NaCl from the machined carbon-NaCl composite body is completely removed by washing with water at 90 °C without creating any damage to the body. The machined carbon-NaCl composite body prepared up to a $\mathbf{W_{N/S}}$ of 3 does not lose the sharp edges or smooth surface during subsequent washing with water at 90 °C for NaCl removal. **Figure 3.14**b shows the photograph of the machined carbon-NaCl composites after NaCl removal and subsequent heat-treatment at 900 °C. However, attempts made at $\mathbf{W_{N/S}}$ higher than 3 (with and without machining) results in the disintegration of the carbon-NaCl composite bodies of size 10 cm × 10 cm × 2 cm during repeated washing with water for NaCl removal due to the poor strength of the resultant carbon foam. That is, the low-density carbon foams obtained at $\mathbf{W_{N/S}}$ higher than 3 are unable to withstand their weight when saturated with water during washing. On the other hand, NaCl from smaller bodies prepared by cutting the large carbon-NaCl composites can be successfully removed using soxhlet extraction without any disintegration. This suggests that the fabrication of microcellular carbon foams of a larger size useful for practical applications is possible at $\mathbf{W_{N/S}}$ less than 3.

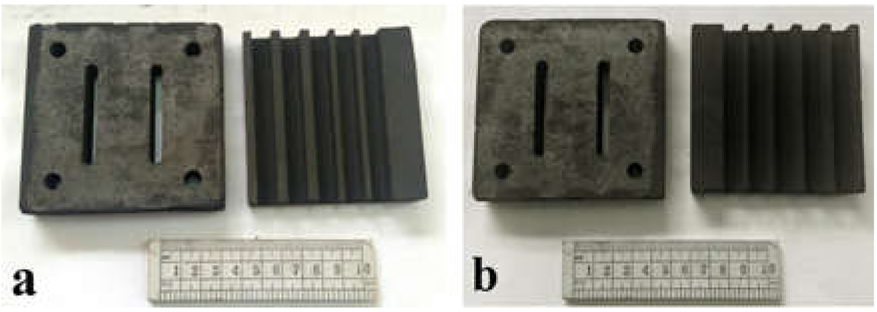

Figure 3.14 Photographs of (a) carbon-NaCl composite bodies after machining and (b) carbon foam obtained by NaCl removal and subsequent heat-treatment at 900 ºC of the machined bodies. The slots & fins are produced by milling and holes are produced by drilling

3.3.9 Textural properties

The typical N_2 adsorption-desorption isotherm and pore size distribution obtained using non-local density functional theory (NLDFT) of a low-density microcellular carbon foam are shown in **Figure 3.15**. The foams prepared at all $\mathbf{W_{N/S}}$ show similar N_2 adsorption-desorption isotherm and NLDFT pore size distribution. The isotherms of the low-density microcellular carbon foam show a steep uptake of N_2 at low relative pressures indicating the presence of micropores in the material. The BET surface area and textural properties of the foams are given **Table 3.5**. The low-density microcellular carbon foam prepared at various $\mathbf{W_{N/S}}$ show specific surface area, total pore volume and micropore volume in close ranges of 422 to 441 $m^2\ g^{-1}$, 0.21 to 0.23 $cm^3\ g^{-1}$ and 0.16 to 0.18 $cm^3\ g^{-1}$, respectively. The NLDFT pore size distribution graph shows a single peak. The median micropore size is in the range of 0.58 to 0.61 nm.

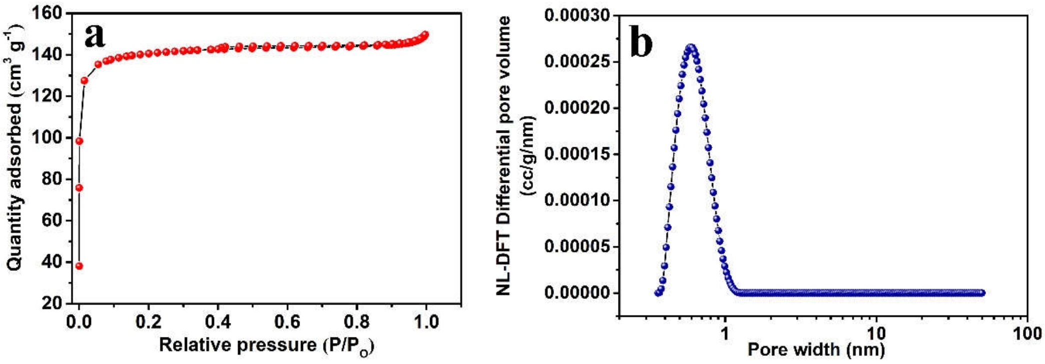

Figure 3.15 (a) Typical N_2 adsorption-desorption isotherm of low density microcellular carbon foam and (b) NLDFT pore size distribution

Table 3.5 Textural properties of microcellular carbon foams prepared at various $\mathbf{W_{N/S}}$

$\mathbf{W_{N/S}}$	**BET Surface area (m^2 g^{-1})**	**Micropore area (m^2 g^{-1})**	**Total pore volume (cm^3 g^{-1})**	**Micropore volume (cm^3 g^{-1})**	**Micropore size (nm)**
1.5	439	356	0.23	0.17	0.61
1.75	441	369	0.23	0.18	0.60
2	431	360	0.22	0.17	0.59
2.25	422	351	0.21	0.16	0.59
2.5	429	354	0.21	0.16	0.61
2.75	440	371	0.21	0.16	0.60
3	428	358	0.21	0.16	0.58

The formation of micropores is due to an *in situ* activation by the reaction of oxygen retained in the carbon materials as C-O-C linkages with the carbon to form carbon monoxide (**Chapter 2**). More or less similar surface area and textural properties observed for all low-density microcellular carbon foam further confirm that the glycerol used as a plasticizing additive is not retained in the polymer structure and has no role in creating the microporosity.

3.3.10 Thermal conductivity

The thermal conductivity of carbon foams depends on the porosity, pore size, pore interconnectivity and crystallinity of the carbon skeleton (X. Li et al., 2012; S. A. Song et al., 2017). Amorphous carbon foams with smaller pore size and less pore interconnectivity are expected to show low thermal conductivity. **Figure 3.16**a shows the effect of $\mathbf{W_{N/S}}$ on the thermal conductivity of the low-density microcellular carbon foam. The thermal conductivity decreases from 0.235 to 0.088 W m^{-1} K^{-1} when the $\mathbf{W_{N/S}}$ increases from 1.5 to 3. The foams exhibit a linear relationship between the thermal conductivity and density with an R^2 value of 0.9655 (**Figure 3.16**b). A set of images illustrating the thermal insulation property of the microcellular carbon foams is given in **Figure 3.17**. A fresh flower directly placed over a 15 mm thick microcellular carbon foam ($\mathbf{W_{N/S}}$=1.5) exposed to Bunsen flame remains fresh ever after 120 seconds.

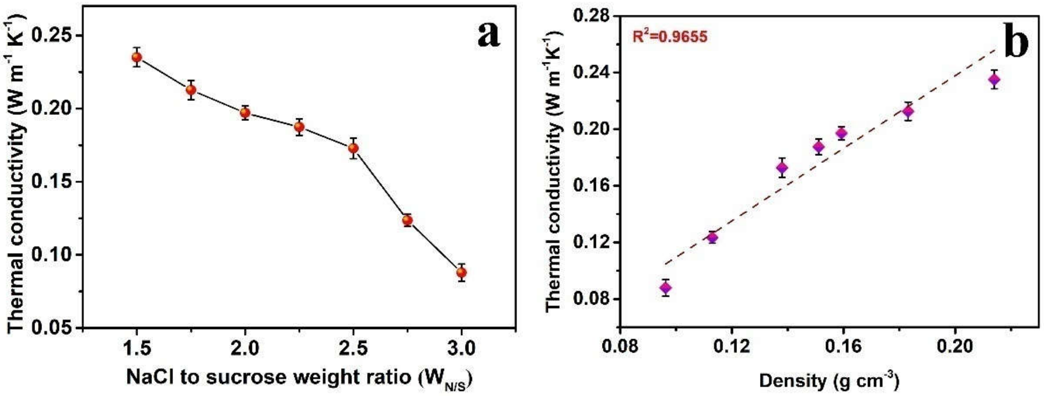

Figure 3.16 (a) Variation of thermal conductivity of low-density microcellular carbon foam with **W$_{N/S}$** and (b) the relationship between thermal conductivity and density of low-density microcellular carbon foam

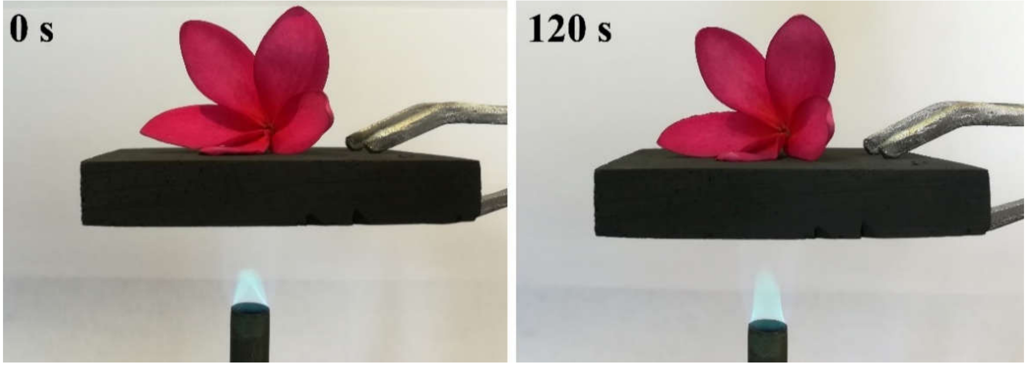

Figure 3.17 Photographic images depicting the thermal insulation property of microcellular carbon foams

The carbon foams prepared from sucrose-NaCl-glycerol pastes at all studied **W$_{N/S}$** have turbostratic graphite structure with more or less the same microcell size distribution. The turbostratic structure is evidenced by the broad peak observed at 2θ value of nearly 23.5° in the XRD diffraction pattern corresponding to the reflection from (002) plane. The XRD diffraction pattern of microcellular carbon foams is shown in **Figure 3.18**. The decrease in thermal conductivity with an increase in **W$_{N/S}$** is solely due to the increase in porosity. The observed values are in the range of thermal conductivity of insulating carbon foam materials reported in the literature (X. Li et al., 2012; S. A. Song et al., 2017).

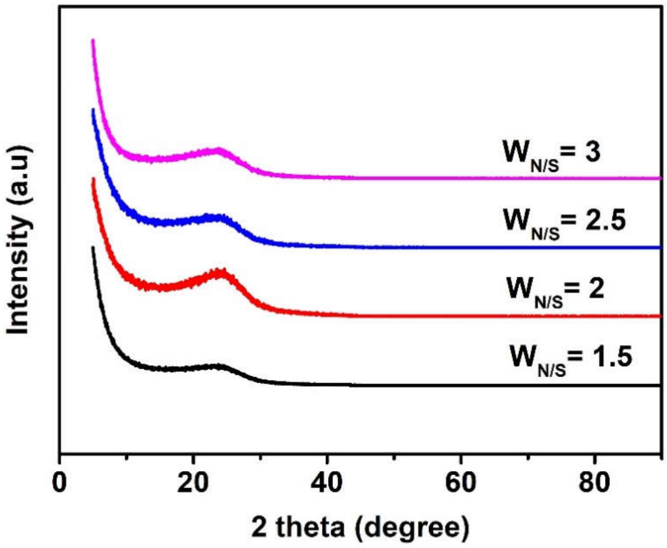

Figure 3.18 XRD diffraction pattern of low-density microcellular carbon foams prepared at **$W_{N/S}$** of 1.5, 2, 2.5 and 3

3.3.11 EMI shielding

The EMI shielding materials are used to prevent the interference of radiations emitted from the electrical instruments with the working of other appliances. They also protect the environment from the severe electromagnetic pollution produced from the modern wireless communication devices which are a threat to the human health (Acharya, Kumar, & Mathur, 2018; Anyaka & Akuru, 2012). Carbon foams are considered as a superior candidate for EMI shielding due to their lightweight, high electrical conductivity and porous nature (Letellier, Macutkevic, et al., 2017; Qiulong Li et al., 2016; W.-L. Song et al., 2015). The electrical conductivity of carbon foams is due to the disordered graphitic structure formed during the carbonization heat-treatment. The electrical conductivity of low-density microcellular carbon foams decreases from 5.5 to 2.7 S cm^{-1} when the **$W_{N/S}$** increases from 1.5 to 3. The decrease in electrical conductivity is due to the decrease in foam density. The electrical conductivity values of microcellular carbon foams are given in **Table 3.6**.

Table 3.6 Electrical conductivity of low density microcellular carbon foams prepared at various **$W_{N/S}$**

$W_{N/S}$	1.5	1.75	2	2.25	2.5	2.75	3
Electrical conductivity (S m^{-1})	5.49	4.66	4.14	3.16	3.36	3.15	2.7

The mechanism of EMI shielding by carbon foams includes absorption, reflection and multiple internal reflections within the cells (Letellier, Macutkevic, et al., 2017; Y. Q. Li, Samad, Polychronopoulou, & Liao, 2015; W.-L. Song et al., 2015). The reflection of the EM wave is due to the impedance mismatch between air and carbon foam surface. On the other hand, EM absorption is mainly due to the dielectric loss that involves relaxation and conduction losses. The relaxation losses are influenced by the polarization caused by defects and functional groups present whereas the conduction losses are due to the electrical conductivity of the carbon foam (Letellier, Macutkevic, et al., 2017; Qiulong Li et al., 2016; Zeng et al., 2018; Liying Zhang et al., 2016). The total shielding effectiveness is the sum of all these contributions. **Figure 3.19** shows the EMI shielding effectiveness (EMI SE) of low-density microcellular carbon foams measured as a function of frequency in the X-band (8.2 -12.4 GHz) region. The shielding effectiveness remains more or less constant for the entire X-band region for the foams prepared at a particular **$W_{N/S}$**. The effect of **$W_{N/S}$** on the EMI SE of low-density microcellular carbon foams at a frequency of 11 GHz is shown in **Figure 3.19**. The EMI SE of the foams decreases from 41.7 to 24.7 dB when the **$W_{N/S}$** increases from 1.5 to 3. The decrease in EMI SE is due to the decrease in the bulk density of the carbon foams. The microcellular carbon foams prepared at all **$W_{N/S}$** show absorption contribution higher than the reflection contribution. The absorption and reflection contributions to the total EMI SE of the microcellular carbon foams are in the ranges 18.5 to 33.3 and 6.2 to 8.5 dB, respectively.

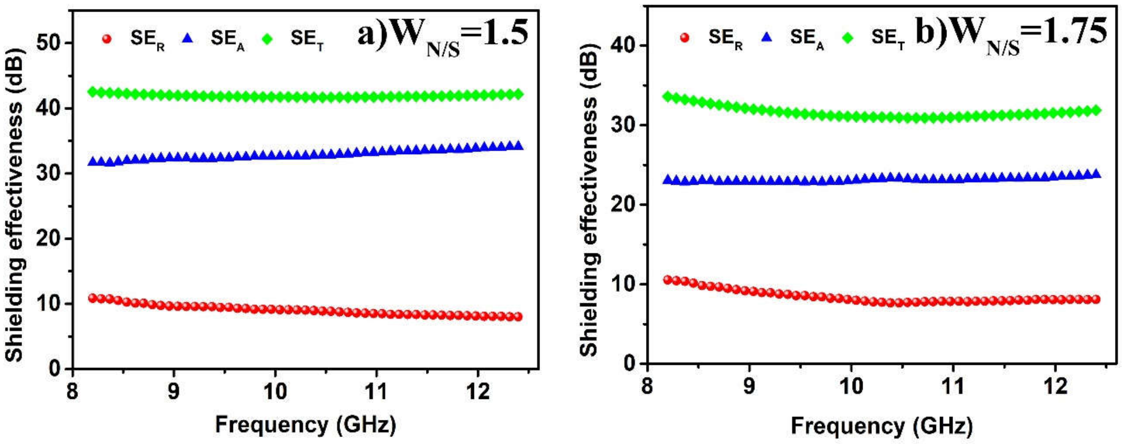

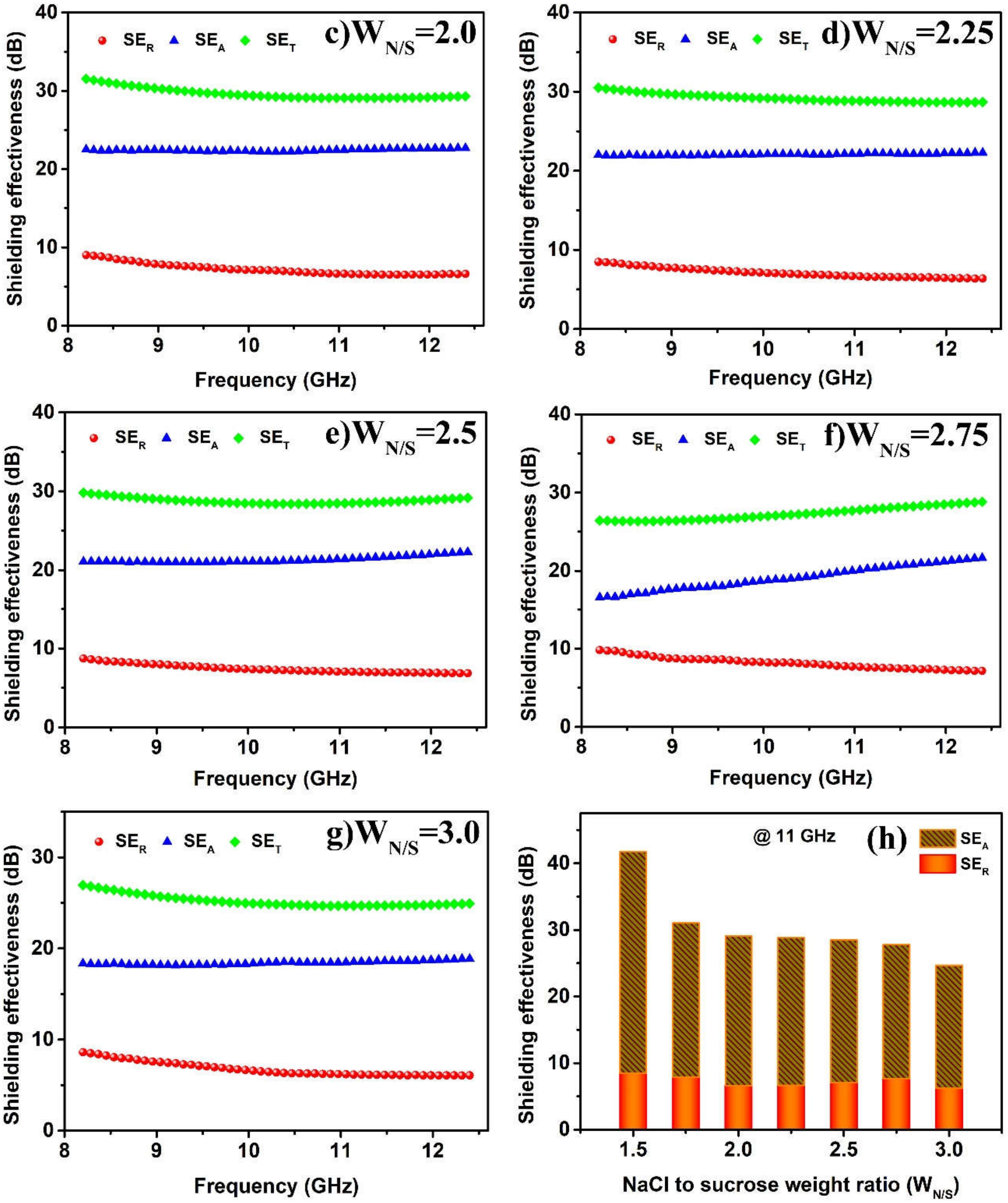

Figure 3.19 EMI shielding effectiveness as a function of frequency (a - g) and SE_T, SE_A and SE_R at 11 GHz (h) of low-density microcellular carbon foams prepared at various **$W_{N/S}$**

The carbon foams with densities of 0.14 and 0.22 g cm^{-3} prepared by thermo-foaming of molten sucrose showed a total EMI SE of 20 and 30 dB, respectively (R Narasimman et al., 2016, 2015). The low-density microcellular carbon foams with a comparable density of 0.138 and 0.214 g cm^{-3} show total EMI SE of 28.47 and 41.7 dB, respectively. That is, the EMI SE value obtained for low-density microcellular carbon foams is nearly 40% higher than that of the carbon foams of similar density prepared by thermo-foaming of molten sucrose. The carbon foam prepared by thermo-foaming of molten sucrose had highly interconnected cells of size nearly 890 µm (R Narasimman et al., 2016, 2015). Therefore, the enhanced EMI shielding effectiveness in microcellular carbon foams is due to the smaller cell sizes (a majority are in the range of 3 to 6 µm) as the smaller cell sizes create large interface area where the attenuation of EM radiation takes place. This will enhance the transfer of EM energy by absorption in the material (Qiulong Li et al., 2016; Shen et al., 2016; Liying Zhang et al., 2016). The mechanism of multiple internal reflections of EM radiation within the microcells as one of the contributions to the higher EM absorption of microcellular foams is proposed by various authors (Y. Li et al., 2016; Shen et al., 2016). In this, the EM radiation enters inside the microcells of the microcellular carbon foams, reflects back and forth due to a large impedance mismatch between air and carbon surface leading to enhanced EM absorption. The specific EMI SE obtained by dividing the SE with the bulk density of the sample increases from 194.8 to 257.3 dB/g/cm^{-3} when the $\mathbf{W_{N/S}}$ increases from 1.5 to 3. The EMI SE and specific EMI SE of low-density microcellular carbon foams are comparable with or higher than that of some of the carbon-based EMI shielding materials reported in the literature. The EMI SE and specific EMI SE of carbon-based EMI shielding materials reported in the literature are given in **Table 3.7**.

3.3.12 Large carbon foam bodies

The low thermal conductivity, relatively high compressive strength, excellent flame resistance and superior EMI shielding effectiveness made the microcellular carbon foam a candidate material for thermal protection and EMI shielding applications. The practical utility of microcellular carbon foams demands fabrication of large carbon foam bodies. The observed low volume shrinkage during carbonization and stability of the bodies against mechanical disintegration during washing was encouraging to fabricate carbon foams of a large size at $\mathbf{W_{N/S}}$ in the range of 1.5 to 3. A large microcellular carbon foam of 20 cm × 20 cm × 2.5 cm size is fabricated using a suitable stainless steel mould. The photograph of a large microcellular carbon foam body prepared at $\mathbf{W_{N/S}}$=2 is shown in **Figure 3.20**. This clearly shows the efficacy of the process to scale up for the production of large carbon foam bodies for practical applications.

Table 3.7 The EMI shielding effectiveness of some carbon-based shielding materials

Material	Density (g/cm^3)	Thickness (mm)	EMI SE (dB)	Specific EMI SE ($dB/g\ cm^{-3}$)	Reference
GN/CNF	0.08-0.1	0.22-0.27	26-28	280	(W.-L. Song et al., 2015)
ALC	0.112	10	~51	455.3	(Y. Q. Li et al., 2015)
Graphene foam	0.06	0.3	~25.2	420	(Shen et al., 2016)
Carbon foam/SiC NW	0.56-0.59	4	19-45	76.2	(Farhan, Wang, & Li, 2016)
Carbon foam/ CNT/Fe_3O_4	0.125	0.2	17-36	288	(Qiulong Li et al., 2016)
Carbon/Graphene foam	0.61-0.72	0.024-0.073	24-51	70.8	(Y. Li et al., 2016)
Carbon/Graphene foam	0.13-0.28	5	21.2-38.6	137.8	(R Narasimman et al., 2015)
Carbon/CNT foam	0.23-0.26	5	26-38	146	(R Narasimman et al., 2016)
Carbon foam	0.214	5	41.7	195	Present work

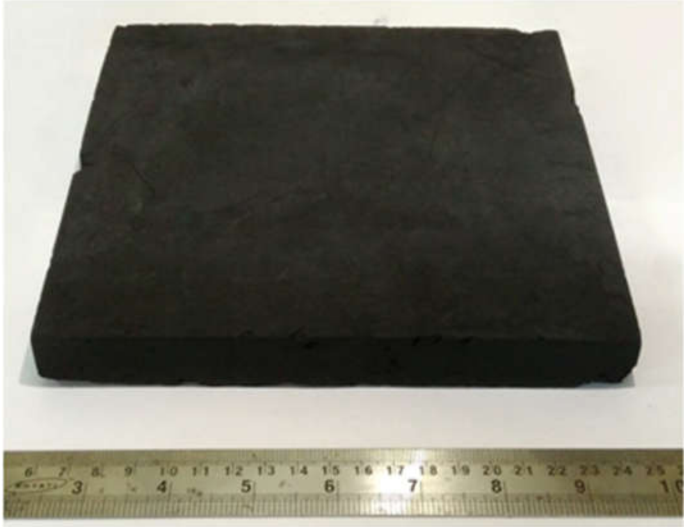

Figure 3.20 Photograph of a large body of low-density microcellular carbon foam prepared at **$W_{N/S}$=2**

3.4 Conclusions

Mouldable NaCl pastes in molten sucrose at NaCl to sucrose weight ratios (**$W_{N/S}$**) in the range of 1.5 to 3 are prepared by using glycerol as a plasticizing additive. The setting of the molten sucrose-NaCl-glycerol pastes is due to the caramelization of sucrose as well as the slow evaporation of glycerol at 160 °C. High setting time (5 to 13 h) is due to the slow caramelization of sucrose in glycerol medium. The linear shrinkage of sucrose polymer-NaCl composites during carbonization at 750 °C decreases from 7.62 to 3.64% whereas the volume shrinkage decreases from 20.65 to 10.02% when the **$W_{N/S}$** increases from 1.5 to 3. The carbon foams obtained by carbonization and NaCl template removal are devoid of macropores as the water vapour produced by slow caramelization of sucrose diffuses out without creating bubbles. The **$W_{N/S}$** higher than 3 results in the disintegration of the carbon-NaCl composites during the NaCl removal by washing with water. The microcell sizes are in the range of 2 to 20 µm with a majority of cells in the size range of 3 to 6 µm. The foam density decreases from 0.214 to 0.096 g cm^{-3} as **$W_{N/S}$** increases from 1.5 to 3. The compressive strength decreases from 4.84 to 0.60 MPa when **$W_{N/S}$** increases from 1.5 to 3. The compressive strength shows a linear relationship with foam density indicating homogeneity of the pore structure in the prepared foams. The carbon-NaCl composites have the adequate compressive strength (6.9 to 17.8 MPa) and Young's modulus (521 to 1964 MPa) to withstand stresses during machining to produce slots, thin-walled fins and holes using conventional machines and tools. The thermal conductivity linearly decreases from 0.235 to 0.088 W m^{-1} K^{-1} as **$W_{N/S}$** increases from 1.5 to 3. The low-density microcellular carbon foams show relatively high EMI SE (24.7 to 41.7 dB) and specific EMI SE (194.8 to 257.3 dB/g cm^{-3}) due to the high EMI absorption caused by the large interface area created due to the microcellular nature.

CHAPTER 4

THERMALLY CONDUCTING MICROCELLULAR CARBON FOAMS USING GRAPHITE AS CONDUCTING FILLER

4.1 Introduction

The amorphous microcellular carbon foam produced from sucrose by NaCl particle templating method have low thermal conductivity and are suitable for high-temperature thermal insulation applications. Carbon foams with relatively high thermal conductivity are used for hosting phase change materials (PCM) for thermal energy storage. Thermally conducting carbon foams produced using coal, coal tar pitch, mesophase pitch, and some of the synthetic organic polymers are used for this purpose (P. Jana et al., 2014; P. Jana, Palomo del Barrio, et al., 2016; H. Ji et al., 2014; M Karthik, Faik, Blanco-Rodríguez, Rodríguez-Aseguinolaza, & D'Aguanno, 2015; Mani Karthik et al., 2017; Lafdi, Mesalhy, & Elgafy, 2008; Lafdi, Mesalhy, & Shaikh, 2007; Mesalhy et al., 2006; Moeini Sedeh & Khodadadi, 2013; Nada & Alshaer, 2015; G. Qi et al., 2017; X. Xiao & Zhang, 2013; Lianbin Zhang, Li, Tang, & Wang, 2016; Zhong et al., 2010). However, these carbon foams are graphitized at high temperatures to attain adequate thermal conductivity which translates to a high cost of production. Moreover, large cell size in these foams severely limits their ability to retain PCM during thermal cycling. In this work, the synthesis process for microcellular carbon foam is augmented by incorporating graphite powder as a thermally conducting filler to prepare thermally conducting microcellular carbon foams. The effect of graphite loading on the compressive strength and thermal conductivity of the foams for the proposed application as a host matrix for wax-based PCM for thermal energy storage is also studied. The narrow confines of micrometre-sized open cells would facilitate retention of molten wax during thermal cycling and also favour rapid heat transport between the conducting matrix and the PCM.

4.2. Experimental

4.2.1 Materials

Analytical grade sucrose was procured from Sisco Research Laboratories, Maharashtra, India. NaCl, glycerol, paraffin wax (Melting range- 58-60 °C) and methanol were procured from Merck India Ltd. Mumbai. Graphite powder was purchased from Sigma Aldrich Co. Ltd. Distilled water was used for NaCl extraction.

4.2.2 Preparation of conducting carbon foam

The flowchart for the preparation of microcellular conducting carbon foams (**MCCF**) is shown in **Figure 4.1**. Sucrose, NaCl, graphite powder and glycerol were mixed in a planetary ball mill (Fritsch, Germany) in methanol medium for 3 h at 200 RPM. The slurries obtained were transferred to a borosilicate glass tray and dried overnight at 70 °C in an air oven. The dried mixtures were then heated at 185 °C to melt the sucrose and thoroughly blended using a wooden ladle until homogeneous pastes were obtained. The pastes were transferred to a stainless steel mould of dimension 10 cm x 10 cm x 2.5 cm and then gently pressed at 160 °C in a hydraulic press for the setting. Once set, composite bodies comprising of sucrose polymer, NaCl particles and graphite powder were carefully extracted from the mould and annealed at 200 °C for 2 h in a muffle furnace. They were then carbonized at 750 °C for 2 h in a box furnace under argon flow. A temperature ramp of 1 °C min^{-1} during heating and natural cooling under constant argon flow was used. The carbonized composite bodies were then washed with distilled water at 90 °C until the entire NaCl was leached out, which was confirmed by titrating the spent water against the aqueous $AgNO_3$ solution. The washed bodies were dried and further annealed at 900 °C for 2 h in the inert atmosphere box furnace to obtain the final **MCCF**s. Foams of various graphite loading and porosities were prepared by varying sucrose, graphite powder and NaCl concentrations in the mixture. The **MCCF** samples were designated as **MCCF-*x*-*y*-*z*** where ***x, y and z*** are the weight in gram of sucrose, graphite powder, and NaCl, respectively, in the compositions used for their preparation. The compositions of the sucrose-NaCl-graphite-glycerol mixtures used are given in **Table 4.1**.

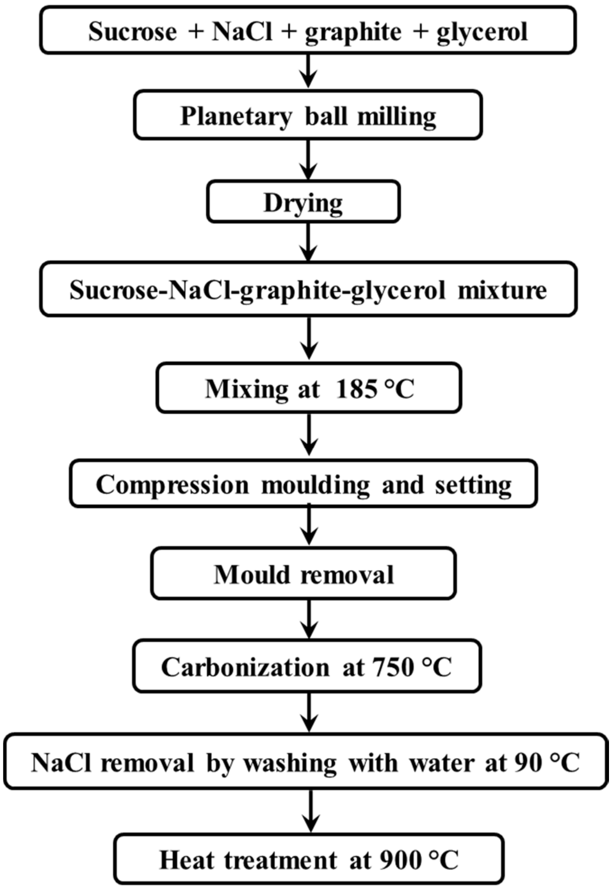

Figure 4.1 Flowchart of the methodology used for the preparation of microcellular conducting carbon foams

4.2.3 Preparation of paraffin wax-conducting carbon foam (PW/MCCF) composites

The rectangular carbon foam pieces of 30 mm x 30 mm x 15 mm were accurately weighed after drying at 150 °C for 6 h. Paraffin wax (PW) was heated in a glass beaker at 120 °C. The carbon foam samples placed into the molten wax. The beaker containing the sample was then placed in a vacuum desiccator for 15 min to ensure complete intrusion of wax in the foam. The wax-infiltrated foam samples removed from the melt was allowed to cool in air. Solidified wax adhering on the surface of the foam sample was removed by scraping with a straight-edged knife. The increase in weight after wax infiltration is taken as the quantity of wax loaded in each sample.

Table 4.1 Compositions and setting time of **MCCF**s

Sample	Sucrose (g)	Graphite (g)	NaCl (g)	Glycerol (g)	Setting time (h)
MCCF-90-10-100	90	10	100	15	4
MCCF-80-20-100	80	20	100	25	4.5
MCCF-70-30-100	70	30	100	60	5
MCCF-60-40-100	60	40	100	75	6
MCCF-50-50-100	50	50	100	90	7
MCCF-90-10-150	90	10	150	25	5.5
MCCF-80-20-150	80	20	150	45	6.5
MCCF-70-30-150	70	30	150	75	8
MCCF-60-40-150	60	40	150	85	9
MCCF-50-50-150	50	50	150	100	10
MCCF-90-10-200	90	10	200	55	7
MCCF-80-20-200	80	20	200	80	8
MCCF-70-30-200	70	30	200	100	9.5
MCCF-60-40-200	60	40	200	125	11
MCCF-50-50-200	50	50	200	140	14
MCCF-90-10-250	90	10	250	75	12
MCCF-80-20-250	80	20	250	100	13.5
MCCF-70-30-250	70	30	250	120	15
MCCF-60-40-250	60	40	250	135	16
MCCF-50-50-250	50	50	250	160	18

4.2.4 Characterisation

4.2.4.1 Density and porosity measurement

Bulk densities of the **MCCF**s were determined from the dimensions and weight of small polished samples. Porosities of the foams were determined using Equation 2.2 (**Chapter 2**). The skeletal density of the **MCCF**s was measured using a helium pycnometer (AccuPyc II 1340 Pycnometer, Micromeritics, USA).

4.2.4.2 Thermogravimetric analysis

Thermal stability of the **MCCF**, **PW** and **PW/MCCF** composites was studied by thermogravimetry technique using a thermogravimetric analyser (TGA, Q-50, TA Instruments, USA). Analysis of samples was performed both under air and N_2 flow at a heating rate of 10 °C min^{-1}.

4.2.4.3 Differential scanning calorimetry measurements

DSC analysis of the **PW** and **PW/MCCF** composites was performed using a differential scanning calorimeter (DSC, TA Instruments, USA) at a heating rate of 2 °C min^{-1}.

4.2.4.4 XRD and Raman analysis

The X-ray diffraction (XRD) analysis of the **MCCF** samples was carried out in an X-ray diffractometer (X'pert Pro, Philips, USA) using Cu Kα radiation.

Raman spectra of the carbon foam samples were obtained using a inVia Raman Microscope, Renishaw, U.K.

4.2.4.5 SEM analysis

High-resolution scanning electron microscope (HRSEM, FEI Quanta FEG 200, USA) was used to examine the microstructure of the foam and composite samples. The microcell sizes were measured from the high-magnification SEM images using the ImageJ software.

4.2.4.6 Compressive strength

The compressive strength of **MCCF** samples was measured using a Universal Testing Machine (Instron 5050, Instron, USA) at a crosshead speed of 0.5 mm min^{-1} following ASTM standard C365/C365M-05. The stress at 10% of strain value is taken as the compressive strength and slope of the initial linear region in the stress-strain graph is taken as Young's modulus.

4.2.4.7 Thermal conductivity measurements

The thermal conductivity measurements of the **MCCF** and **PW/MCCF** composite samples were carried out at room temperature using the transient plane source method (Hot Disk, TPS 2500S, Sweden). Samples of size approximately 40 mm × 40 mm × 15 mm were used for the measurements.

4.2.4.8 Contact angle measurements

Contact angle measurement of the samples by static sessile drop method at room temperature was performed using a contact angle goniometer (Model 290, rame-hart instrument co., USA). 5 µL of water was used for the measurement.

4.3 Results and Discussion

4.3.1 Setting of molten sucrose-NaCl-graphite-glycerol pastes

The setting of the paste to sucrose polymer-NaCl-graphite composite body takes place by the polymerization of sucrose as well as slow evaporation of glycerol. The setting time of each of the composition is determined by separately keeping the paste in a watch glass at 160 °C in an air oven. Time taken for the paste to solidify is taken as the setting time. The observed increase (5 to 18 h) in setting time with an increase in graphite and NaCl loading is due to the presence of a higher concentration of glycerol. During inert atmosphere heat treatment, the carbon produced from the sucrose polymer binds the graphite and NaCl particles to form a carbon-NaCl composite body. It is observed that the linear and volumetric shrinkages during carbonization decrease with an increase in the NaCl particle and graphite filler loading. The linear and volumetric shrinkages observed are in the ranges of 1.4 to 8.1% and 3.19 to 22.5%, respectively. The high-magnification SEM image of the carbon-NaCl composite is presented in **Figure 4.2**. The image shows a uniform distribution of near cuboid NaCl particles with smooth edges and graphite particles of largely irregular morphology within the turbostratic carbon matrix. The size of the NaCl particles, estimated from SEM images using ImageJ software, lies within the range of 2 to 14 µm with a majority in 2 to 8 µm. From the SEM images, it is evident that there are no large macropores in the foams formed by the entrapment of water vapour generated during the polymerization of sucrose. Removal of the NaCl particles by water-washing creates microcells throughout the carbon body.

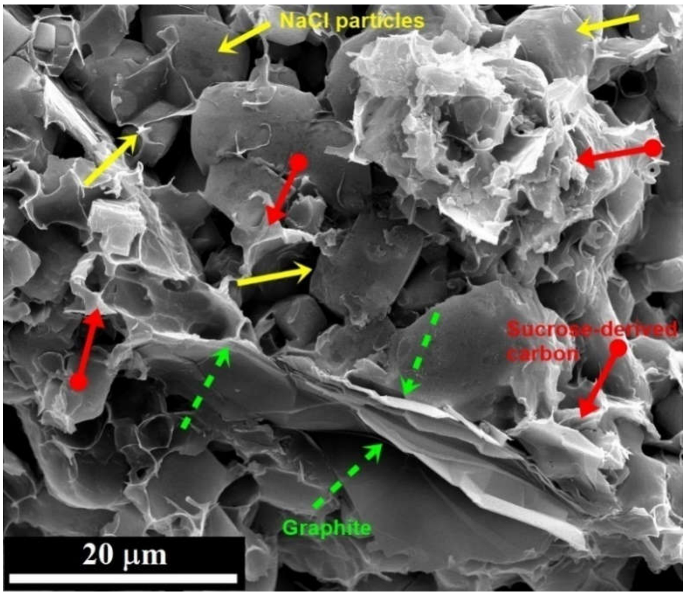

Figure 4.2 High-magnification SEM image of the carbon-NaCl composite (The solid arrow indicates NaCl particles, dash line with arrowhead indicates graphite particles and solid arrow with a dot indicates turbostratic carbon)

4.3.2 Phase analysis

The **MCCF**s obtained after washing and subsequent carbonization at 900 °C contain the disordered carbon and the graphite phases. The XRD analysis of **MCCF-90-10-200** shows three prominent peaks (**Figure 4.3a)**, two sharp peaks at 26.7° and 54.9° corresponding to the reflections from (002) plane and (004) plane of graphite and a broad peak at 44.6° corresponding to the reflection from (101) plane of the disordered carbon (Li Chen, Song, Shi, & Ding, 2018; J. W. Klett et al., 2004; S. Li et al., 2007). Comparison of the XRD diffraction pattern (**Figure 4.3b**) of **MCCF**s with increasing graphite loading shows an increase in the intensity of the peak corresponding to the reflection from (002) plane. Also, the absence of reflections from NaCl confirms the complete extraction of NaCl during water-washing. The presence of crystalline and amorphous phases in the composite carbon foam is further confirmed by the Raman spectrum (**Figure 4.4**). The carbon produced from sucrose shows peaks corresponding to disordered (D band at 1350 cm^{-1} corresponding to sp^3 carbon) and ordered (G band at 1598 cm^{-1} corresponding to sp^2 carbon) structure indicating its turbostratic nature (S. A. Song et al., 2017; Liying Zhang et al., 2016; Zúñiga Ruiz et al., 2015). On the other hand, the pristine graphite exhibits a sharp G band with a very minute D band. However, the Raman spectrum of composite carbon foam shows a relatively intense D band due to sucrose-derived carbon and a sharp G band corresponding to the graphite. The base-broadening observed for the G band of the composite carbon foam is due to the overlap of the G bands of graphite and turbostratic carbon produced from sucrose.

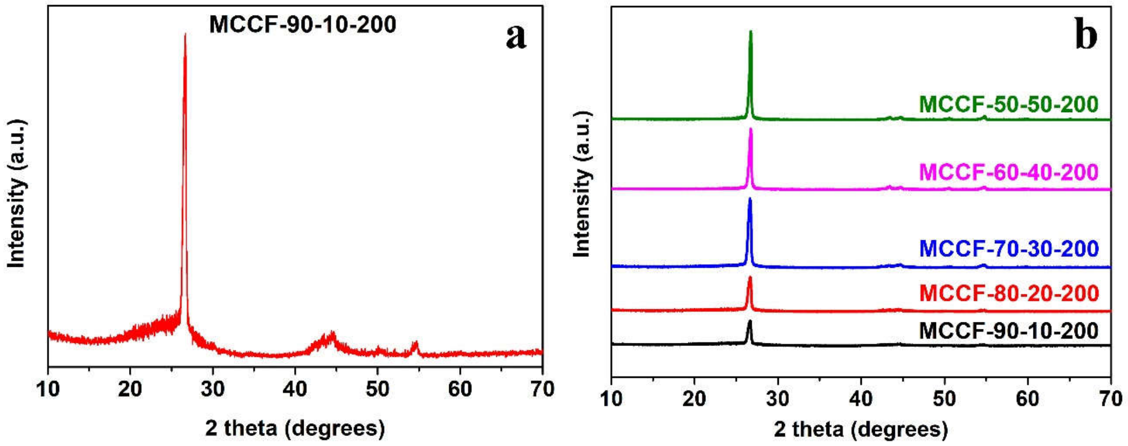

Figure 4.3 (a) XRD diffraction pattern of **MCCF-90-10-200** and (b) comparison of XRD diffraction pattern of **MCCF-x-y-200**

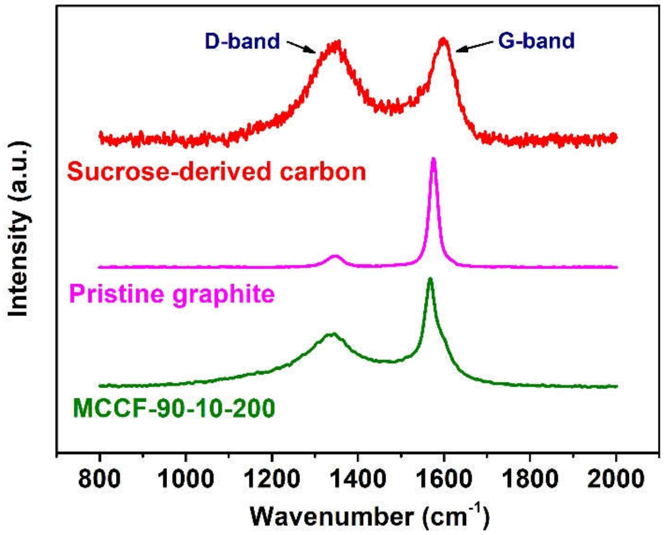

Figure 4.4 Raman spectra of a typical **MCCF**, pristine graphite and sucrose-derived carbon

4.3.3 Microstructure of MCCF

Figure 4.5a and **4.5**b show the high-magnification SEM images of the **MCCF-90-10-200** and **MCCF-50-50-200**. Microcellular carbon foam prepared without graphite filler contained near-uniform cuboidal microcells with predominantly open cell structure

(**Figure 3.10**, **Chapter 3**). Incorporation of graphite filler retains the interconnected cellular structure. The microcell sizes observed in SEM images of all **MCCF-x-y-200** samples are in the range of 2 to 11.7 µm. The decrease in the porosity with an increase in graphite loading is evidenced by the SEM images. On increasing the NaCl particle loading at constant sucrose to graphite ratios, the cell wall becomes progressively thinner while the size distribution of the microcells remains more or less the same. This is clearly evidenced by the SEM images of **MCCF-70-30-100** and **MCCF-70-30-250** shown in **Figure 4.5**c and **4.5**d.

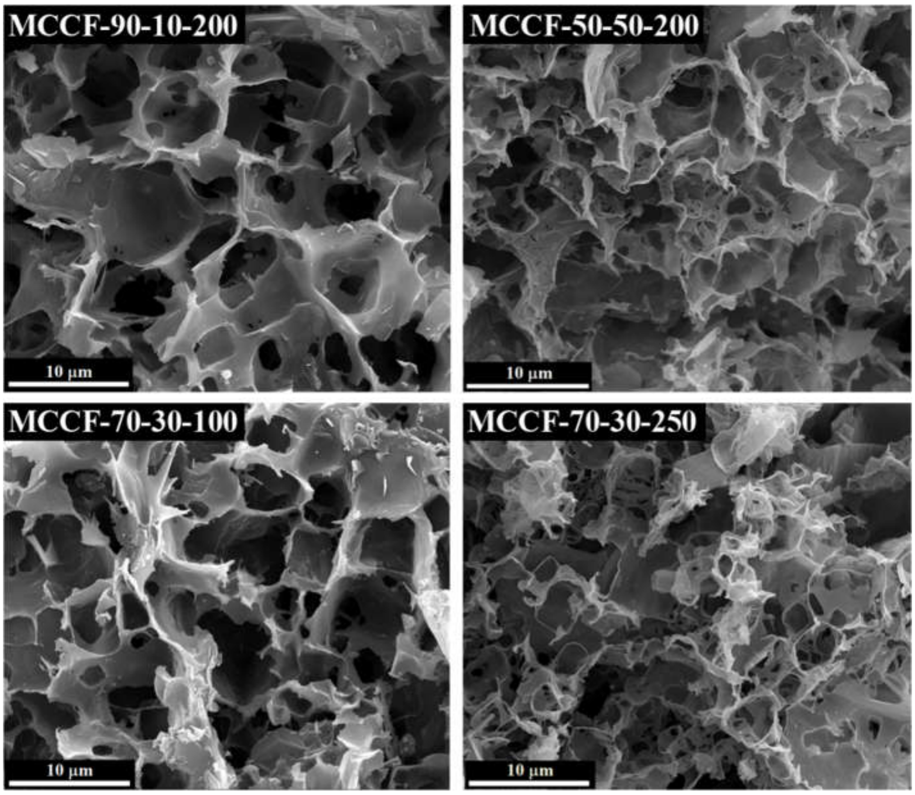

Figure 4.5 High-magnification SEM images of (i) **MCCF-90-10-200**, (ii) **MCCF-50-50-200**, (iii) **MCCF-70-30-100** and (iv) **MCCF-70-30-250**

4.3.4 MCCF density

The density of the **MCCF** is a function of both NaCl and graphite loading. Clearly, the increase in the NaCl particle loading increases the porosity and thus decreases the density of the carbon foam. Whereas, the graphite loading contributes to the increase in the density of the foams by increasing the carbon yield from the sucrose-graphite mixture. The density of the foams is in the range of 0.137 to 0.526 g cm^{-3}. The variation of the density of the foam as a function of graphite and NaCl loading is provided in **Figure 4.6a**. Analysis of the **MCCF-x-y-200** group of samples demonstrated an increase in the skeletal density from 2.09 to 2.22 g cm^{-3} when the value of **y** increases from 10 to 50. The porosity calculated from the bulk and skeletal density is found to be in the range of 76.1 to 93.4% (**Figure 4.6b**).

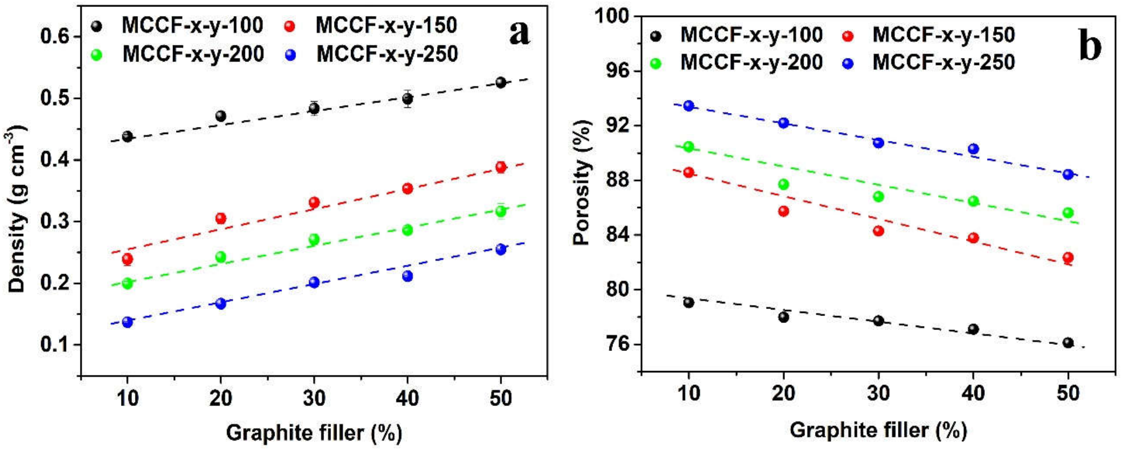

Figure 4.6 (a) Density and (b) porosity of **MCCF-x-y-z** as functions of filler loading and NaCl template loading

4.3.5 Compressive strength and Young's modulus

Typical compressive stress-strain curves of **MCCF**s with respect to varying graphite filler loading and NaCl loading is shown in **Figure 4.7**a & b, respectively. The stress-strain curves are analogous to that of solid foam bodies. It exhibits a linear elastic behaviour at low strain (<10%), followed by a plateau region corresponding to the collapse of microcells. Finally, a region with a sharp rise in the compressive stress at high strains signifies the densification of the foam due to the complete collapse of the cells. The stress corresponding to the 10% strain value is taken as the compressive strength and the slope of the linear region is taken as the Young's modulus. **Figure 4.7**c **and 4.7**d illustrate the compressive strength and Young's modulus of **MCCF**, respectively. It is interesting to observe that the compressive strength of the foams decreases with an increase in the graphite loading except for **MCCF-x-y-250** set of foams even though there is an increase in the density. This is quite prominent for **MCCF-x-y-100** group of foams where the compressive strength decreases from 14.96 to 1.46 MPa when graphite loading increases from 10 to 50%. This behaviour can be explained by the fact that as graphite loading increases there is an obvious decrease in the disordered carbon in the foam which binds the graphite particles, resulting in a weaker structure.

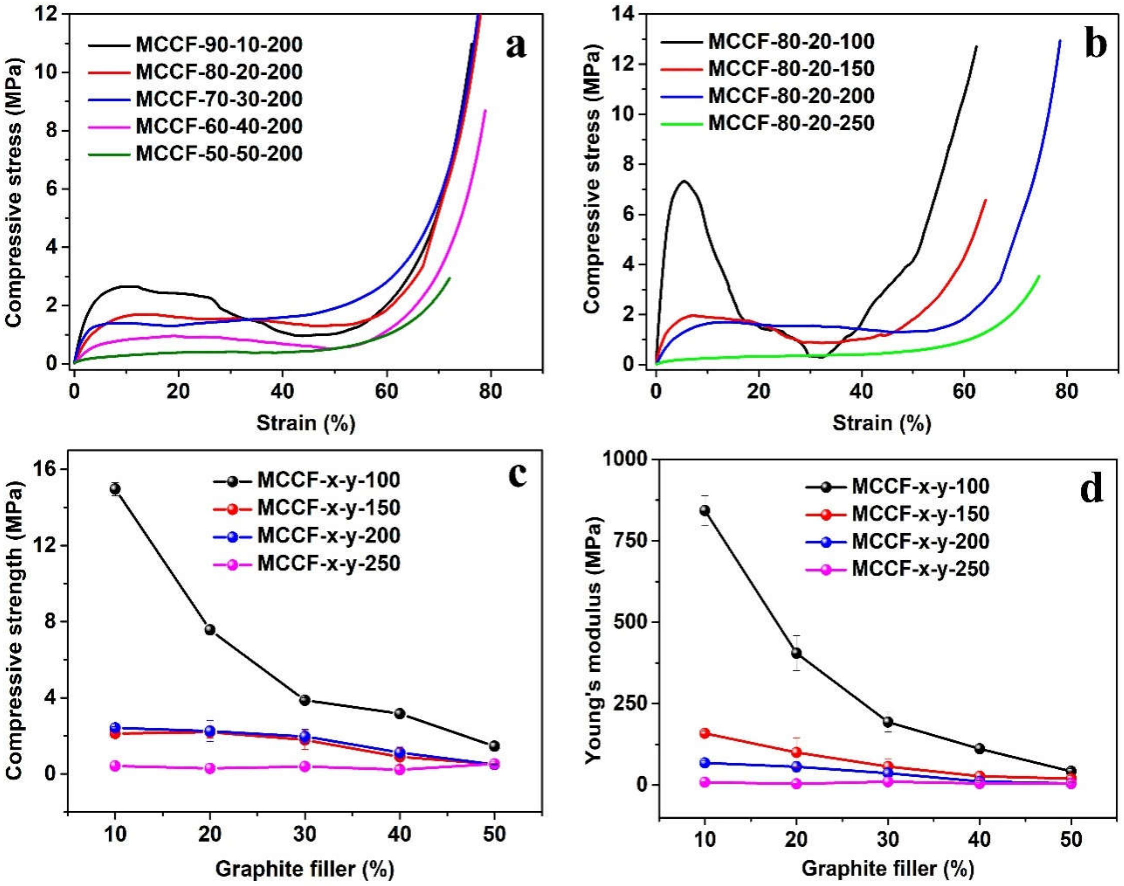

Figure 4.7 Stress-strain plots of **MCCF**s with (a) increasing graphite filler loading and (b) with increasing NaCl loading. Compressive strength (c) and Young's modulus (d) of **MCCF**s as a function of NaCl and graphite loading

However, in the **MCCF-x-y-250** set of foams, this phenomenon is offset by the increase in strength due to the increase in density. The compressive strength of the **MCCF-x-y-200** and **MCCF-x-y-250** remains within a narrow range of 0.5 to 2.25 MPa and 0.225 to 0.53 MPa, respectively. The Young's modulus of **MCCF**s is in the range of 3.5 to 843 MPa.

4.3.6 Thermal conductivity of MCCFs

Figure 4.8a shows the thermal conductivity of the **MCCF**s as a function of the NaCl and graphite loadings. It is observed that the thermal conductivity increases with an increase in the graphite filler loading at any given NaCl template concentration. Alternatively, at any given graphite filler loading, the thermal conductivity decreases with an increase in the NaCl template concentration. **MCCF-50-50-100** shows the highest thermal conductivity of 5.23 W m^{-1} K^{-1} while **MCCF-90-10-250** exhibits the lowest value of 0.282 W m^{-1} K^{-1}. This observation can be ascribed to the bulk density of the **MCCF**s. It is well known that the thermal conductivity of porous bodies increases with an increase in their bulk density as thicker cell walls are conducive for fast heat transport. However, the observed drastic increase in the thermal conductivity is not proportional to the minor increase in the density as a result of graphite filler addition. Jana *et al* showed that graphite filler plays a key role in improving the thermal conductivity of the carbon foams of large cell sizes derived from tannin and sucrose (P. Jana, Fierro, et al., 2016; P. Jana, Fierro, Pizzi, & Celzard, 2015). The contribution of graphite filler is determined by comparing the experimental values of thermal conductivity of the foams with the theoretical values of graphite-free carbon foams of similar densities calculated using the Gibson-Ashby model (Equation 4.1) (Gibson & Ashby, 1997; P. Jana, Fierro, et al., 2016). A similar approach is used to establish the contribution of graphite filler towards the increase in thermal conductivity of **MCCF**.

$$k_f = \frac{1}{3}\left(\frac{\rho_b}{\rho_s}\right)k_c + \left(1 - \frac{\rho_b}{\rho_s}\right)k_a \qquad (4.1)$$

Here, k_f is the thermal conductivity of the foam, ρ_b is the bulk density, and ρ_s is the skeletal density of microcellular carbon foam prepared without graphite filler. k_c and k_a are the thermal conductivities of the sucrose-derived carbon and air at 20 °C, respectively. To derive the thermal conductivity of sucrose-derived carbon, a simple back substitution of the values, k_f= 0.197 W m^{-1} K^{-1}, ρ_b = 0.16 g cm^{-3} and ρ_s = 1.98 g cm^{-3} is used. The thermal conductivity of air at room temperature is taken as k_a = 0.026 W m^{-1} K^{-1}. Upon substitution of these values in Equation 4.1, a thermal conductivity value of 6.8 W m^{-1} K^{-1} for the sucrose-derived carbon (k_c) is obtained. This value is then used to determine the theoretical thermal conductivity of carbon foams (without graphite filler) of density equivalent to the **MCCF**. A comparison of the theoretical and experimental thermal conductivities of **MCCF-x-y-200** is shown in **Figure 4.8**b. This analysis indicates that a significant increase in the thermal conductivity of the **MCCF** is primarily due to the graphite filler addition and to a lower extent due to the increase in density. The thermal conductivity of the **MCCF** increases by an order of one by the addition of conducting graphite fillers.

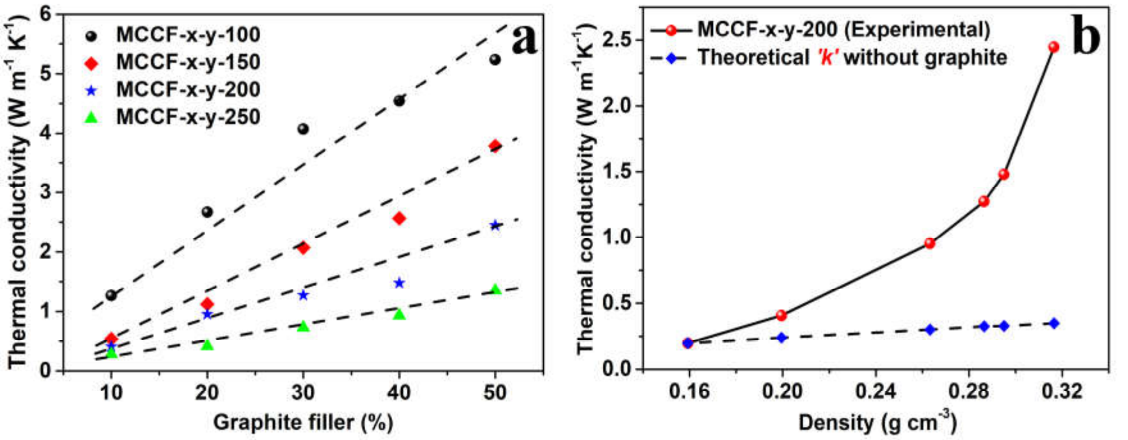

Figure 4.8 (a) Thermal conductivity of **MCCF**s and (b) comparison of the experimental thermal conductivity of **MCCF-x-y-200** with theoretical thermal conductivity of carbon foams of similar density without graphite filler

4.3.7 Contact angle of MCCF

Hydrophobicity of **MCCF**s plays a crucial role in the infiltration of paraffin wax (**PW**) within the pores. The contact angle of the **MCCF** prepared at various NaCl and graphite loadings is shown in **Figure 4.9**a & b. The contact angle measured for the **MCCF-x-y-200** group of foams indicates nearly similar values (125 to 129°) implying that the graphite concentration does not play a major role in determining the hydrophobicity of the foams. However, a large increase in the contact angle is observed with an increase in NaCl template loading. The contact angle of 54° observed for **MCCF-70-30-100** increases to 128° for **MCCF-70-30-250** implying that the contact angle increases with an increase in the porosity of the **MCCF**s. This can be explained by the Cassie-Baxter model (Cassie & Baxter, 1944). The increase in porosity due to increase in NaCl template concentration decreases the cell wall thickness of the microcellular carbon foams. It appears that the microcellular foams with thin cell walls produce micron-level roughness on the fractured surface of the carbon foam body required for creating hydrophobicity. The photographs of water droplets on **MCCF-70-30-100** and **MCCF-70-30-250** are presented in **Figure 4.9** c and d, respectively.

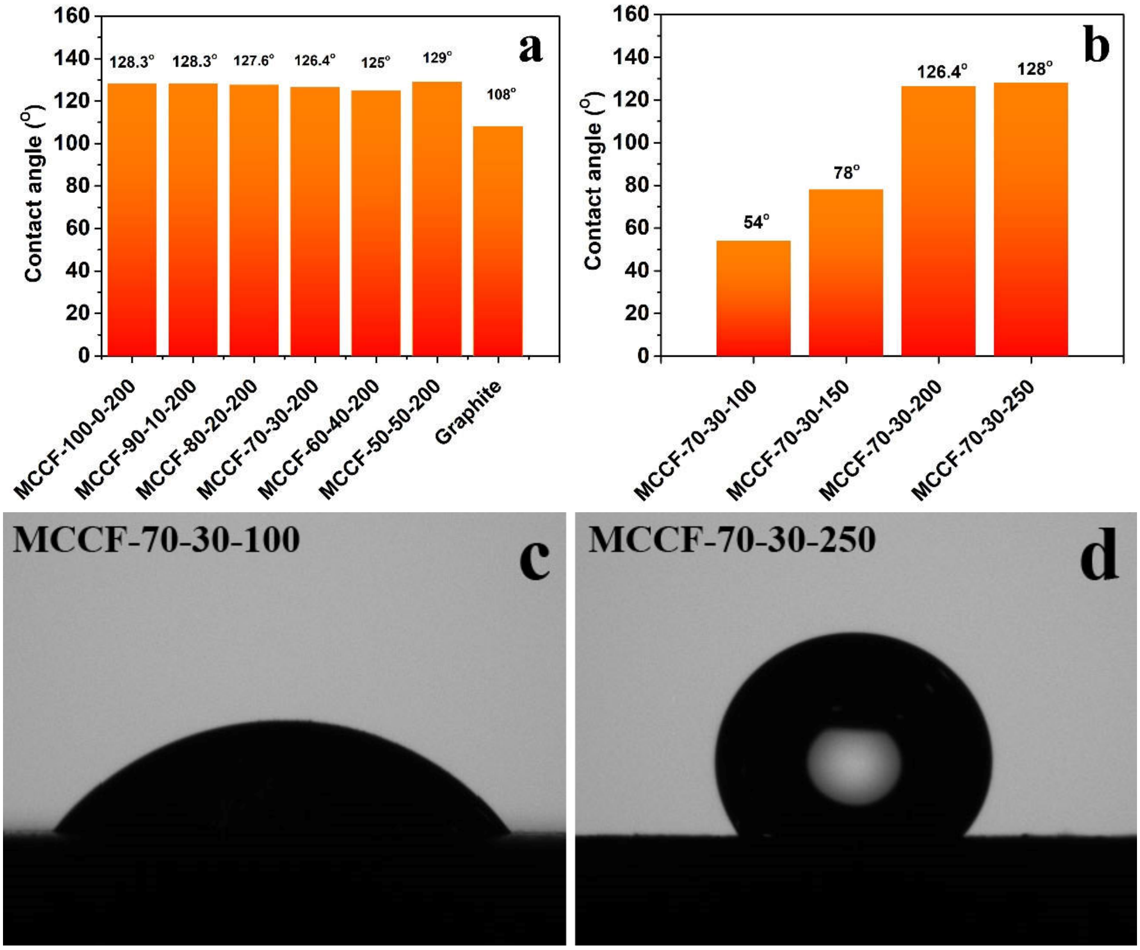

Figure 4.9 Contact angles of (a) **MCCF-x-y-200** series of carbon foams showing the effect of graphite loading, (b) contact angles of **MCCF-70-30-z** indicating the effect of porosity (NaCl loading). (c) and (d) present the photographs of water droplet on the surfaces of **MCCF-70-30-100** and **MCCF-70-30-250**, respectively

4.3.8 MCCF as host for wax-based phase change material

Sustainable energy sources are rapidly gaining importance due to the steady depletion of conventional fossil fuel-based energy sources as well as their inherent polluting nature (Chu, Cui, & Liu, 2017). To improve the efficient utilization of sustainable energy from sources that are characteristically intermittent, it is vital to produce economically viable technologies for absorption, storage, and release of energy when demanded. Thermal energy storage systems using phase change materials (PCM) are one of the technologies employed for this purpose. Organic PCMs such as paraffin wax, fatty acids, glycols; inorganic PCMs such as salts, salt hydrates, metals and alloys; and eutectic organic/inorganic compounds are materials possessing high latent heat of fusion which store and release thermal energy during phase changes at a constant temperature (Y. Lin, Jia, Alva, & Fang, 2018). Though organic PCMs have relatively lower phase change enthalpy compared to inorganic PCMs, their chemical stability, a wide range of melting temperatures, non-corrosive nature, self-nucleating behaviour, non-toxicity and abundance prove advantageous over the latter. However, the poor thermal conductivity of organic PCMs (0.1-0.3 W m^{-1} K^{-1}) is detrimental to the rate of heat transfer thus reducing their performance (Kenisarin, 2014). Physical structures such as fins enhance the heat transfer by increasing the relative surface area in contact with PCM (Y. Zhang & Faghri, 1996). The thermal conductivity of the PCMs can also be improved by using highly conducting additives such as metallic and ceramic nanoparticles such as Cu, Fe_3O_4, Al_2O_3, TiO_2, SiO_2, and ZnO (S. C. Lin & Al-Kayiem, 2016; Şahan, Fois, & Paksoy, 2015; T.-P. Teng & Yu, 2012). Introduction of carbon-based fillers such as carbon fibres (Babapoor, Azizi, & Karimi, 2015), carbon nanotubes (CNT) (Z.-T. Yu et al., 2013), graphene (Xin et al., 2014; Yavari et al., 2011) and graphite flakes (N. Wang, Zhang, Zhu, & Gao, 2012) have also been studied. The use of nanofillers for enhancing the thermal conductivity of PCM has certain limitations of its own: (i) the instability of the nanofillers in PCM causes it to precipitate out consequent to repeated thermal cycles, (ii) the nanofillers do not undergo phase change and displace a large volume of PCM which results in lower heat storage capacity, (iii) thermal resistance between the nanofiller and the PCM significantly lower the heat transfer efficiency.

To overcome these shortcomings, an alternate approach was explored by impregnating PCMs in a thermally conducting lightweight porous matrix. Three-dimensional graphene and CNT aerogels/sponges are used as conducting matrices for PCMs to form composites for thermal energy storage systems (Liangjie Chen et al., 2012; J. Yang et al., 2016). The high porosities of graphene and CNT aerogels (>95%) and their inherent high thermal conductivity allow high PCM loading and enhanced thermal performance. However, the pores that host the PCM in these aerogels are quite large (>100 μm) which impedes the heat transport between the conducting matrix and the PCM. Kholmanov *et al.* explored a method to overcome this problem by growing long CNT networks from the struts of Ultrathin Graphitic Foams (UGF) into the interstitial pore space (Kholmanov, Kim, Ou, Ruoff, & Shi, 2015). The inclusion of the CNT network within the pores effectively enhanced the thermal conductivity of UGF-CNT/erythritol composite over UGF/erythritol composite by over a factor of 1.8. However, the complexity of the synthesis process and the expensive precursors involved in the synthesis of graphene and CNT aerogels restrict their large scale production. Carbon foams with adequate thermal conductivity are also used for hosting phase change materials (P. Jana, Palomo del Barrio, et al., 2016; M Karthik, Faik, Blanco-Rodríguez, et al., 2015; Mani Karthik et al., 2017; Lafdi et al., 2008). However, the large cell size of the carbon foams impede the heat transfer and leads to leakage of the PCM during thermal cycling. Microcellular carbon foams with adequate thermal conductivity would solve these two problems.

4.3.9 Paraffin wax loading

MCCFs with high porosity is an ideal host for accommodating PCM. The microcells in the foam are also favourable in maintaining the form stability during re-melting and solidification thus preventing the leakage of PCM. **Figure 4.10** shows the percentage mass loading of paraffin wax in the **PW/MCCF** composites.

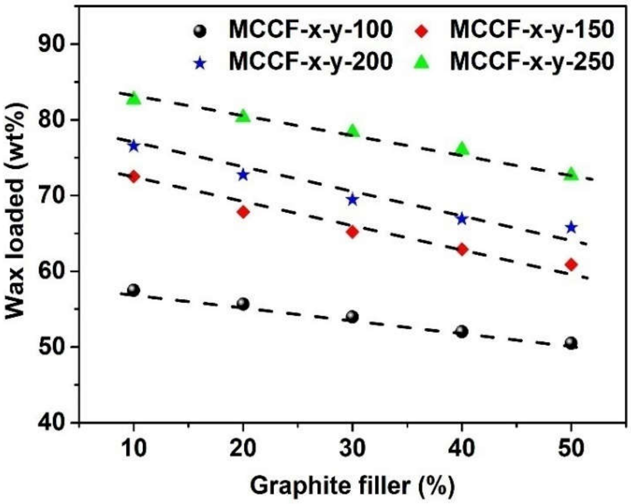

Figure 4.10 Paraffin wax loading (wt%) in **MCCF**

Wax loading is in the range of 50.5 to 82.6 wt% with **MCCF-50-50-100** and **MCCF-90-10-250** showing the lowest and highest values, respectively. It is obvious that the mass loading of wax is dependent on the porosity and pore interconnectivity of the CCF and follows a similar trend to that of porosity. However, the percentage volume of impregnated PW with respect to the volume of foam (V_w/V_f*100) is in the range of 65.35 to 77.41% which is less than the porosity (76.1 to 93.4%) of the foams calculated using Equation 2.2 (**Chapter 2**). It appears that the molten wax completely fills the microcells and the observed lower volume loading of solid wax is due to the shrinkage of wax during freezing.

4.3.10 Thermal studies of PW/MCCF composites

The thermal conductivity of **PW/MCCF** composites measured at room temperature is shown in **Figure 4.11**. The **PW/MCCF** composites show higher thermal conductivity (0.65 to 7.72 W m^{-1} K^{-1}) compared to the corresponding un-filled **MCCFs** by as much as 23 to 130%. This increase is due to the higher thermal conductivity of wax (0.24 W m^{-1} K^{-1}) over the air (0.0257 W m^{-1} K^{-1}) at ambient temperature.

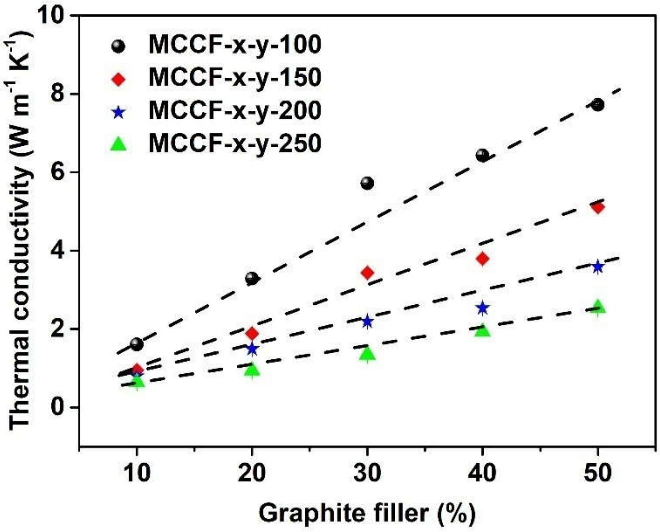

Figure 4.11 Thermal conductivity of **PW/MCCF** composites at room temperature

The SEM image (**Figure 4.12**) of the fractured **PW/MCCF** composite shows that the wax covers the entire carbon matrix surface as well as fills almost the entirety of the pores. The interconnected microcells help in the distribution of the wax through the bulk of the foam thus forming a homogeneous composite. The excellent adhesion of wax on the microcell surface is evident from the lack of large free space in the foam cell wall-wax interface which is otherwise expected during the solidification of molten material in a confined volume. This will enhance the heat transfer from the wax to the carbon foam which is another reason for the higher thermal conductivity of **PW/MCCF** composites compared to unfilled **MCCF**s.

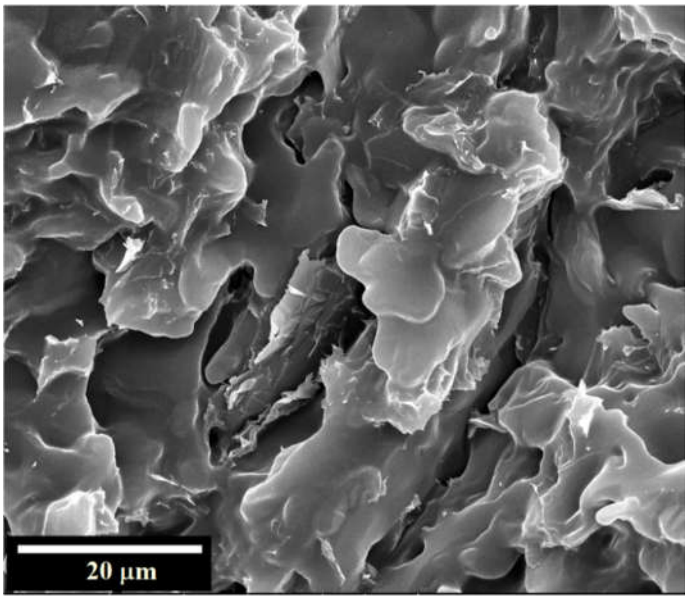

Figure 4.12 High-magnification SEM image of **PW/MCCF-50-50-200** composite

TGA of **MCCF-50-50-200**, wax and **PW/MCCF-50-50-200** composites in air and N_2 is shown in **Figure 4.13**. The foam is stable up to a temperature of 530 °C after which two specific weight-loss regions are observed, the first in the temperature range of 530-650 °C and the second after 650 °C. The first weight-loss is attributed to the decomposition of the disordered carbon present in the foam. The decomposition of the more stable crystalline graphite takes place after 650 °C.

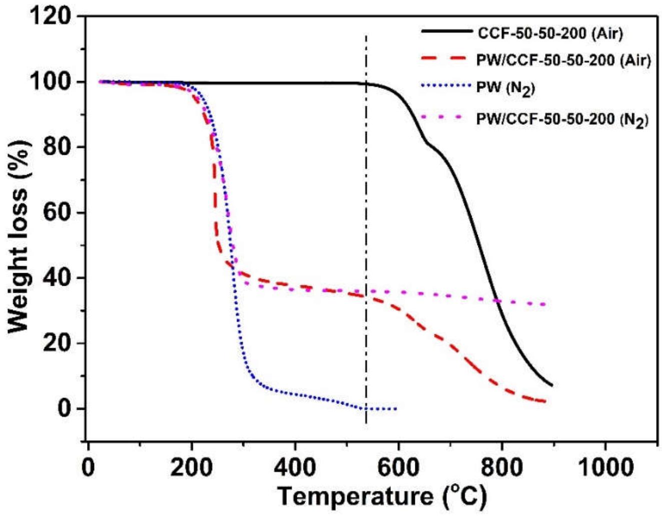

Figure 4.13 TGA curves of **MCCF-50-50-200**, pure paraffin wax, **PW/MCCF-50-50-200** in air and N_2

Nearly, 7.3% residue was obtained at 900 °C which is the maximum temperature limit of our instrument. **PW** shows a weight loss in the range of 190 to 535 °C, largely due to evaporation. The weight-loss curve of **PW/MCCF-50-50-200** composite follows a similar profile up to 530 °C in both air and N_2 atmosphere which is due to the elimination of wax. In the air atmosphere, the weight-loss observed after 530 °C is due to the decomposition of carbon (disordered and graphitic). The mass loading of **PW** obtained from TGA is nearly equal to that calculated from the weight increase during infiltration.

DSC graph of **PW** and **PW/MCCF-90-10-250** composite exhibiting enthalpy change of the **PW** in the pristine form and in the composite during heating and cooling is shown in **Figure 4.14**. The similar profile of the DSC curves for **PW** and **PW/MCCF** implies that there occurs no chemical reaction between the **PW** and the foam. Two distinct peaks, a major and a minor, can be observed in both the curves during heating and cooling processes. The minor peak corresponds to a solid-solid phase transition and the major peak represents the solid-liquid phase transition of the **PW** (B. Li, Liu, Hu, Wang, & Gao, 2013). The melting point of wax in pristine and in a composite form determined from the DSC curves are 58.4 and 59.7 °C, respectively. The onset of melting occurs at 52.7 and 52.4 °C in the pristine wax and **PW/MCCF** composite, respectively.

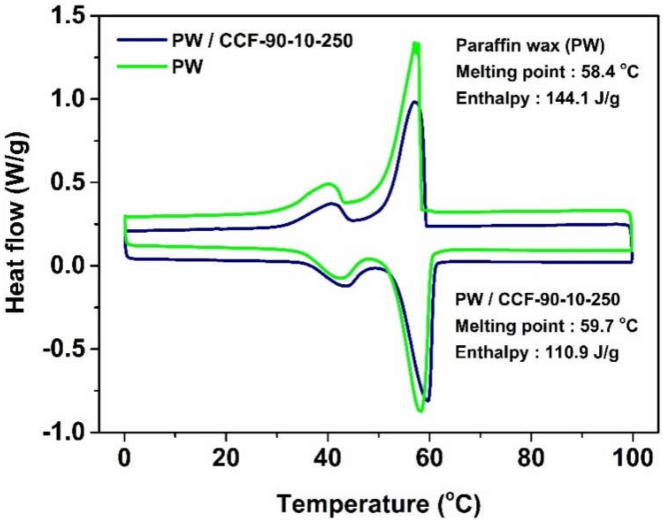

Figure 4.14 DSC curves of Paraffin wax and **PW/MCCF-90-10-250** composites

The melting enthalpy determined from the DSC analysis of pristine **PW** and **PW/MCCF-90-10-250** is 144.1 J g^{-1} and 110.9 J g^{-1}, respectively. Since the conducting carbon foam host is not involved in the phase-change process; the specific enthalpy of the composite is lower than that of the pristine PW. The highest specific enthalpy observed for **PW/MCCF** composite is 76.9% of the pristine **PW**. This value is comparable with that obtained for some of the PW/macrocellular carbon foam composites reported in the literature (Mani Karthik et al., 2017; X. Xiao & Zhang, 2013).

4.3.11 Form stability

Form stability is another important criterion with respect to PCMs. PCM impregnated in conducting carbon foam matrices tends to leak-out during re-melting owing to the low viscosity of the liquid phase, which adversely affects the cyclic operation of the TES devices. This is due to the relatively large cell size of the carbon foams. The microcells in the **MCCF** prevent the leakage of **PW** due to the higher capillary forces (Liangjie Chen et al., 2012; Lianbin Zhang et al., 2016). **Figure 4.15** shows the digital photographs of pristine **PW** and **PW/MCCF-50-50-250** composite on a Teflon coated glass cloth heated over a hotplate at 70 °C. The pristine **PW** melts completely and spreads on the surface of the fabric over a period of time whereas the **PW/MCCF** composite shows only a slight wetting on the surface due to the melting of **PW**. The wax impregnation and retention characteristics of the microcellular **MCCF** is compared with that of the macrocellular conducting carbon foam prepared from sucrose and graphite powder by thermo-foaming. In contrast to the microcellular **MCCF**, carbon foams of large cell sizes (~600 µm), **Figure 4.16**, and high porosity (91.5%) show entirely different impregnation characteristics and form stability.

Both **MCCF** and macrocellular carbon foam prepared by thermo-foaming sink in molten wax during impregnation. However, the time taken for the sinking of macrocellular carbon foam is very high compared to that of microcellular **MCCF** body of a similar size and density. The observed sinking time of the **MCCF** and macrocellular carbon foam are 20 min and 6 h, respectively. This observation is counterintuitive, as the larger pores in the thermo-foamed carbon foam are expected to favour quicker wax impregnation compared to the **MCCF**.

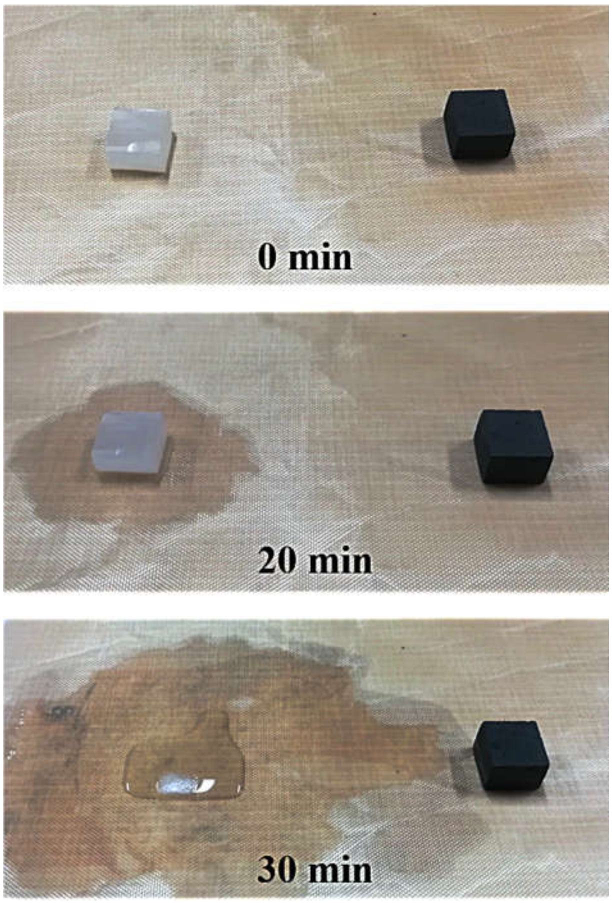

Figure 4.15 Digital photograph of pure paraffin wax and **PW/CCF-50-50-200** composite heated at 70 °C for 30 min

The relation between the capillary rise of a liquid and the capillary radius is given by the Jurin's Law (Rodríguez-Valverde & Tirado Miranda, 2010):

$$h = \frac{2\,\gamma\,cos\varphi}{\rho g r} \qquad (4.2)$$

where, h is the capillary rise, γ is the surface tension of the liquid, φ is the contact angle of the liquid, ρ is the density of the liquid, g is the acceleration due to gravity and r is the capillary radius. Open cellular carbon foam can be considered as a solid body with a large number of capillaries and infiltration of paraffin wax is aided by capillary action. The faster wax infiltration in our microcellular **MCCF** is as a result of the higher capillary forces due to its lower capillary size (cell size). The capillary forces assisted by the hydrophobic nature of the foams improves the rate of wax impregnation. In addition to the difficulty in impregnation, the majority of the wax impregnated in the macrocellular carbon foam drains-out when it is lifted from the molten wax reservoir. The amount of wax retained within the foam is merely 51.5% of its pore volume. Cooling the reservoir until the freezing of the wax by keeping the carbon foam in the immersed condition is necessary to ensure the retention of infiltrated wax. Though an infiltration of 88% of the pore volume could be achieved by this method, however, on re-heating a significant quantity of the impregnated wax seeps out of the composite within 30 min. These contrasting behaviours of the microcellular **MCCF** and the macrocellular conducting carbon foams, with respect to PCM impregnation and retention, highlights the apparent advantages of the microcellular morphology achieved using the reported technique.

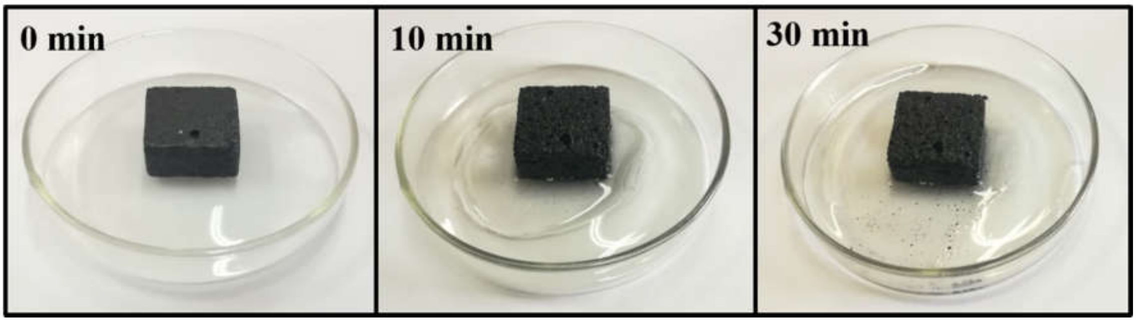

Figure 4.16 Photographs showing poor form stability of a macroporous carbon foam-paraffin wax composite

4.4 Conclusions

Microcellular conducting carbon foams (**MCCF**) with density in the range of 0.137 to 0.526 g cm^{-3} are prepared using NaCl particle templating method using sucrose as a sustainable carbon source and graphite powder as the conducting filler. The compressive strength of **MCCF** lies within the range of 0.225 to 14.96 MPa. The **MCCF**s prepared at a NaCl loading show a decrease in compressive strength as graphite filler loading increases due to a decrease in sucrose-derived amorphous carbon which binds the graphite particles. The thermal conductivity of the **MCCF**s varies from 0.282 to 5.23 W m^{-1} K^{-1}. The thermal conductivity increases with an increase in graphite filler loading and decreases with an increase in NaCl particle template loading. High-magnification SEM images reveal interconnected microcellular morphology with cell size in the range of 2 to 11.7 μm. Hydrophobicity of the **MCCF** increases with an increase in NaCl template loading as evidenced by the contact angle measurements. The hydrophobic nature of **MCCF** enables easy infiltration of wax-based phase change materials. Paraffin wax/conducting carbon foam (**PW/MCCF**) composites with wax loading in the range of 50.5 to 82.6 wt% exhibit higher thermal conductivity (0.65-7.72 W m^{-1} K^{-1}) than the unfilled foams. The highest melting enthalpy of 110.9 J g^{-1} is achieved for **PW/MCCF** composite with 82.6 wt% wax loading. The **PW/MCCF** composites also show good form stability at 70 °C due to the microcellular morphology of the foams which enhances the capillary and surface tension forces.

CHAPTER 5

MICROCELLULAR SILICON CARBIDE FOAMS FROM SUCROSE AND SILICON POWDER BY NaCl PARTICLE TEMPLATING

5.1 Introduction

Silicon carbide (SiC) foams are widely used as gas or molten metal filters, catalyst carriers, lightweight structural components and EMI shielding materials at high temperature owing to properties such as lightweight, good thermal shock resistance, oxidation resistance, excellent chemical stability, semiconductivity and good dielectric property (Afsharvahid et al., 2008; Duan et al., 2014; Duong-Viet et al., 2016; Gianella et al., 2012; Jiao et al., 2012; Quan Li et al., 2013; Caiyun Liang et al., 2017; Ou et al., 2017; Wood & Harris, 2008). Several methods for the processing of SiC foams are reported in the literature. They are broadly classified into the following categories: polymer foam replication, fugitive templating, emulsion templating, freeze-casting and direct foaming (Colombo, 2006; Fukushima & Colombo, 2012; Ge et al., 2014; Hossain et al., 2016; Koh et al., 2006; R Mouazer et al., 2005; Rabah Mouazer, Thijs, Mullens, & Luyten, 2004; Shcherban et al., 2017; Ungureanu et al., 2011; Vijayan, Wilson, Sreeja, & Prabhakaran, 2016; F. Xue et al., 2018; J. Yan, Wang, & Kim, 2006; Z. Zhang et al., 2009). Carbothermal reduction and reaction bonding techniques are also employed to convert carbon foams into SiC foams (Eom, Kim, Song, & Kim, 2007; J. Li, Yuan, Deng, & Zhu, 2017; Lim, Kim, & Song, 2013). Carbothermal reduction involves the reduction of SiO_2, SiO and SiOC with carbon while the reaction bonding technique involves the reaction between carbon and silicon at elevated temperatures. Alumina and yttria are used as additives to promote carbon-silicon reaction and densification of SiC (Eom et al., 2008; Vijayan et al., 2016).

Majority of the above-mentioned preparation methods produces SiC foams of large cell size. However, microcellular SiC foams are beneficial for better mechanical strength, higher EMI shielding effectiveness and lower thermal conductivity (Alvarez et al., 2010; Ameli, Jung, & Park, 2013; Letellier, Delgado-Sanchez, et al., 2017; Sundarram & Li, 2013; Zakiyan, Azizi, & Ghasemi, 2018). Pore templating with PMMA microbeads and carbon dioxide gas blowing methods are used for the preparation of microcellular SiC foams from pre-ceramic polymers (Young Woo Kim, Kim, Song, Kim, & Park, 2005; Young Wook Kim, Kim, & Park, 2005). However, the pre-ceramic polymers are expensive. In this chapter, processing of microcellular SiC foams by NaCl particle templating using sucrose (carbon source) and silicon powder. Microcellular SiC foams show high absorption-dominated EMI shielding properties and possess reasonably high mechanical strength and low thermal conductivity. The use of biomass and NaCl makes it an eco-friendly and sustainable process with scope for industrial-scale production.

5.2 Experimental

5.2.1 Materials

Analytical grade sucrose was procured from Sisco Research Laboratories, Maharashtra, India. NaCl, glycerol and methanol were procured from Merck India Ltd. Silicon powder was procured from Metal Powder Company Ltd (Madurai, India). Alumina and yttria powders were procured from ACC Alcoa (Kolkata, India) and Sigma Aldrich (USA), respectively. The average particle size and specific surface area of silicon, alumina and yttria powders are given **Table 5.1**.

Table 5.1 Average particle size and specific surface areas of the powders used

Powders	**Average particle size (µm)**	**Specific surface area (m^2 g^{-1})**
Silicon	3.3	2.38
Alumina	0.34	10.4
Yttria	0.56	2.9

5.2.2 Preparation of microcellular SiC foams

Flowchart of the preparation of microcellular SiC foams is shown in **Figure 5.1**. Mixtures of sucrose, NaCl, silicon, alumina and yttria powders were ball-milled in a planetary ball mill (Fritsch, Germany) in methanol medium using zirconia balls of 10 mm diameter in a 500 ml zirconia bowl for 2 h at 200 RPM. 58.46 g of silicon powder was used for 100 g of sucrose in all the compositions anticipating a carbon yield of 24 wt% from sucrose (Vijayan et al., 2016). The NaCl to sucrose weight ratio was varied in the range of 1 to 3. The amount of alumina and yttria sintering additives used was 6 and 4 wt%, respectively, of the SiC expected from 58.46 g of silicon powder (Vijayan et al., 2016). The slurries obtained by ball milling were dried in an air oven at 70 °C. The dried powder mixtures were heated in a glass tray at 185 °C in an air oven to melt the sucrose and thoroughly mixed using a wooden ladle. An adequate amount of glycerol is added during mixing to form pastes of mouldable consistency. The composition of the pastes used is given in **Table 5.2**. The paste was transferred to a stainless steel mould of dimension 10 cm × 10 cm × 2.5 cm and then gently pressed at 160 °C in a hydraulic press for setting. After setting, the solid composite body was extracted from the mould and annealed at 200 °C for 2 h. A slow heating rate was used for the annealing. The composite body was then carbonized at 750 °C for 2 h in a box furnace under argon flow. A temperature ramp of 1 °C min^{-1} was used during heating. The furnace was cooled naturally to room temperature. The argon flow was maintained during cooling as well. The carbonized composite body was then washed in distilled water at 90 °C until the entire NaCl was leached out. This was confirmed by titrating the spent water against the aqueous $AgNO_3$ solution. The presence of NaCl in spent water is indicated by the formation of white precipitate (AgCl) on titration with $AgNO_3$ solution. Complete NaCl extraction is indicated by the absence of the white precipitate on titration. The washed body was dried and further sintered at 1500 °C for 2h at a heating rate of 2 °C min^{-1} in an inert atmosphere furnace to obtain the final microcellular SiC foam. The microcellular SiC foams are designated as **MSiCF-x**, where **x** represents the NaCl to sucrose weight ratio used in the composition.

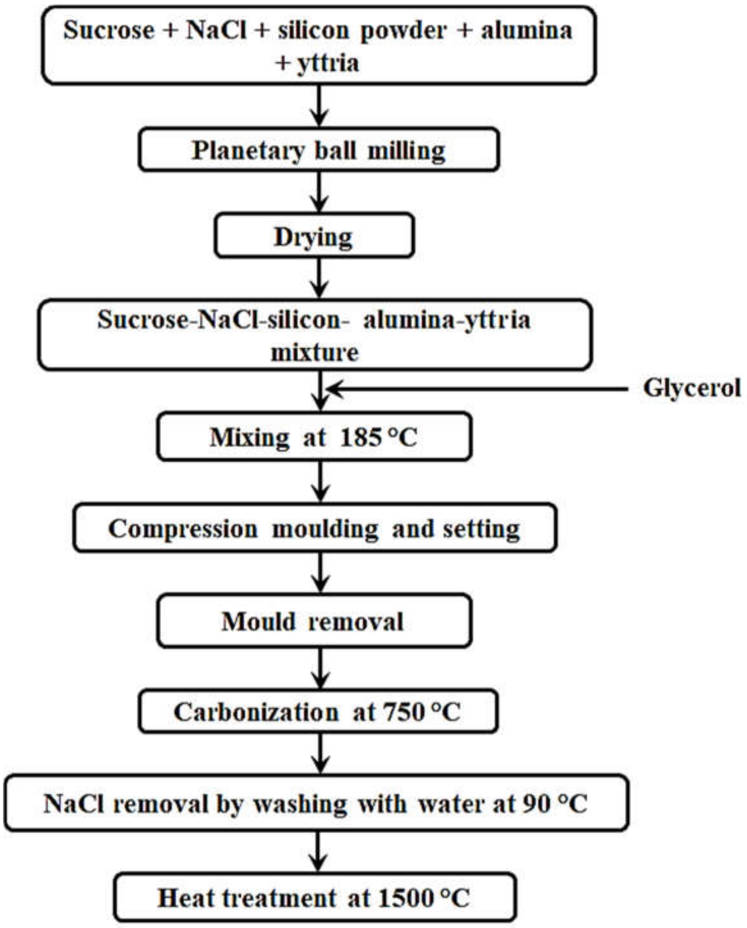

Figure 5.1 Flowchart for the preparation of microcellular SiC foams

Table 5.2 Compositions used for the preparation of **MSiCF**

Sample	Sucrose (g)	NaCl (g)	Silicon (g)	Alumina (g)	Yttria (g)	Glycerol (g)
MSiCF-1	100	100	58.46	5	3.34	2
MSiCF-1.5	100	150	58.46	5	3.34	18
MSiCF-2	100	200	58.46	5	3.34	32
MSiCF-2.5	100	250	58.46	5	3.34	45
MSiCF-3	100	300	58.46	5	3.34	64

5.2.3 Characterization

5.2.3.1 Setting of paste for moulding

The setting characteristics of the pastes were studied by measuring the torque as a function of time in a torque rheometer (Brabender Plasti-Corder, GmbH, Germany) with a rotor speed of 10 RPM at 160 °C. Nearly 50 ml of each composition was used for the study.

5.2.3.2 Carbonization and sintering shrinkage

Carbonization and sintering shrinkages were calculated by measuring the dimensions of the samples before and after heat-treatment for carbonization and sintering, respectively.

5.2.3.3 Density and porosity measurement

Bulk density of the **MSiCF**s was determined from the dimensions and weight of rectangular samples cut with a hacksaw blade and polished using emery sheet. The skeletal density of the **MSiCF**s was measured using a helium pycnometer (AccuPyc II 1340 Pycnometer, Micromeritics, USA). The porosity of the foam samples was calculated using Equation 2.2 (**Chapter 2**)

5.2.3.4 Thermogravimetric analysis

Thermal stability of the carbon-silicon composite foams was studied by thermogravimetry technique using a thermogravimetric analyzer (TGA, Q-50, TA Instruments, USA). Analysis of samples was performed both under air and N_2 flow at a heating rate of 10 °C min^{-1}.

5.2.3.5 XRD analysis

The X-ray diffraction (XRD) analysis of the **MSiCF** samples was carried out in an X-ray diffractometer (X'pertPro, Philips, USA) using Cu Kα radiation.

5.2.3.6 SEM analysis

The microstructure analysis was performed using a scanning electron microscope (SEM; FEI Quanta FEG200, USA). EDAX analysis was performed using (QUANTAX 200 with XFlash®6/30 SDD Detector, Bruker, USA). The cell sizes of the **MSiCF**s and diameter of SiC nanowires grown on the cell wall surfaces are measured from the SEM images using ImageJ software.

5.2.3.7 Compressive strength measurement

The compressive strength of **MSiCF** samples was measured using a Universal Testing Machine (Instron 5050, Instron, USA) at a crosshead speed of 0.5 mm min^{-1} following ASTM standard C365/C365M-05. Compressive strength and Young's modulus were calculated from the stress-strain plots. The stress corresponding to the plateau region of stress-strain plot was taken as the compressive strength and Young's modulus was measured as the slope of the initial linear region.

5.2.3.8 N_2 adsorption-desorption analysis

N_2 adsorption-desorption isotherms at 77 K were obtained using surface area analyser (Micromeritics Tristar II, USA). The samples were degassed under flowing N_2 atmosphere at 300 °C for 12 h before the analyses. The surface area was calculated using the BET (Brunauer-Emmett-Teller) equation in the relative pressure range of 0.05 to 0.25.

5.2.3.9 Thermal conductivity measurement

The thermal conductivity measurement of the **MSiCF** samples was carried out at room temperature using the transient plane source method (Hot Disk, TPS 2500S, Sweden). For measurement, a pair of samples measuring 40 mm × 40 mm ×15 mm from each set was cut and polished to obtain near-perfect flat surfaces to minimize air gap when the sensor is sandwiched in between the samples.

5.2.3.10 Electrical conductivity measurement

The electrical conductivity of **MSiCF**s and carbon-silicon composite foam was recorded using a four probe method. A constant current (I) was applied to the samples using a programmable source (Keithley 6221A). The bulk resistivity (ρ) was calculated from the current and voltage readings using Equation 3.1 (**Chapter 3**).

5.2.3.11 EMI shielding effectiveness measurement

The electromagnetic interference (EMI) shielding effectiveness (SE) and the complex relative permittivity of the **MSiCF**s and the carbon-silicon composite foam were measured in the X-band (8.2–12.4 GHz) of the microwave region using a vector network analyser (VNA) (E5071C) and a corresponding waveguide. Rectangular samples of dimensions 22.7 mm × 10.2 mm × 5 mm were used for the measurement. The scattering parameters were recorded and EMI SE was deduced from the scattering parameters.

5.3 Results and discussion

5.3.1 Preparation and setting of pastes

It has been reported that the sucrose on melting, setting by polymerization, and subsequent carbonization produces 24 wt% carbon (Vijayan et al., 2016). The amount of silicon powder used in the compositions is stoichiometrically equivalent to react with this carbon to produce SiC. Therefore, the sucrose to silicon powder weight ratio is kept constant in all the formulations. The NaCl to sucrose weight ratio is varied from 1 to 3 to modulate the porosity. The resin produced by the melting of sucrose in the sucrose-silicon-NaCl mixture is not sufficient to form a paste of mouldable consistency. Therefore, glycerol is used as a plasticising additive as it does not retain any carbon during pyrolysis and homogeneously mixes with molten sucrose. The amount of glycerol required to achieve pastes of mouldable consistency increases from 2 to 64 g per 100 g sucrose when the NaCl to sucrose weight ratio increases from 1 to 3. The mouldable consistency was ascertained by qualitatively inspecting its deformability at 160 °C with the help of a wooden ladle.

The setting characteristics of the pastes measured as a function of time at 160 °C using a torque rheometer is shown in **Figure 5.2**. The torque initially increases at a slow rate followed by a rapid rise after a certain period of time. It is observed that the onset of the rapid increase in torque is delayed with an increase in the NaCl to sucrose weight ratio. The increase in torque is attributed to the evaporation of glycerol as well as the condensation polymerisation of glucose and fructose anhydride produced from sucrose (**Chapter 3**). The delay in the torque build-up at higher NaCl to sucrose weight ratios is due to the longer time required for the evaporation of the large concentrations of glycerol. The pastes corresponding to NaCl to sucrose weight ratios of 1 and 1.5 reach a torque value of 50 N.m at nearly 50 min. In comparison, the pastes corresponding to NaCl to sucrose weight ratios of 2, 2.5 and 3 reach a torque value of 50 N.m in 81, 136 and 208 min, respectively. It is interesting to note that paste produced from sucrose-NaCl mixture (without silicon powder and glycerol) at NaCl to sucrose weight ratio of 1 takes much longer time (150 min) to reach a torque value of 50 N.m (**Chapter 2**). This indicates that the acidic silica layer on the surface of silicon particles catalyses the –OH condensation between glucose and fructose anhydride leading to faster setting.

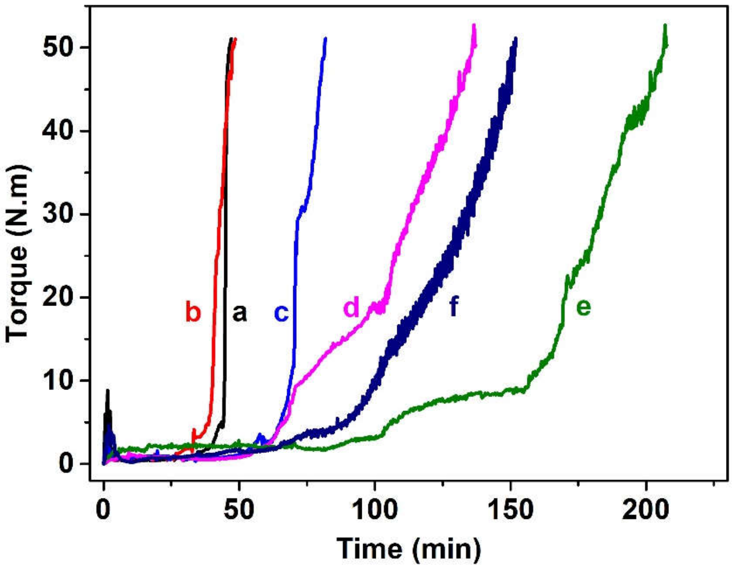

Figure 5.2 Torque-time curves of NaCl–silicon powder pastes in molten sucrose glycerol solution at various NaCl to sucrose ratios of a-1, b-1.5, c-2, d-2.5 & e-3 and paste of NaCl in molten sucrose at NaCl to sucrose weight ratio of 1 (f)

The actual setting time was determined by keeping the pastes prepared at various NaCl to sucrose weight ratios at 160 °C in an air oven and physically inspecting the same after every 30 min. The time at which the soft paste turned into a hard solid is considered as the setting time. The setting time of the pastes prepared at various NaCl to sucrose weight ratios is given in **Table 5.3**.

Table 5.3 Setting time of molten sucrose-silicon-NaCl pastes

Sample	**MSiCF-1**	**MSiCF-1.5**	**MSiCF-2**	**MSiCF-2.5**	**MSiCF-3**
Approximate Setting time (h)	1	1.5	2	2.5	3

5.3.2 Fabrication of microcellular SiC foams

The paste filled in the rectangular mould could be removed as a solid sucrose polymer-silicon-NaCl composite body after heating at 160 °C for the corresponding setting time. The sucrose polymer in the composite body undergoes carbonization during inert atmosphere heat-treatment at 750 °C to form a carbon-silicon-NaCl composite. The composite undergoes shrinkage during the carbonization. There is a decrease in both linear and volumetric shrinkages of the bodies during carbonization from 4 to 1.36% and 10.8 to 5%, respectively, as we increase the NaCl to sucrose weight ratio from 1 to 3. The decrease in shrinkage is due to the fact that the NaCl and silicon particles do not shrink whereas only the sucrose polymer shrinks during carbonization.

The carbon-silicon-NaCl composite has a uniform distribution of NaCl particles of size in the range of 3 to 23 μm as evident from the SEM image of the fractured surface shown in **Figure 5.3**a. These NaCl particles are completely leached out by immersing in the water at 90 °C for ~48 h. The voids created by the removal of NaCl particles remain as microcells in the resulting carbon-silicon composite foam. The SEM image of the fractured surface of carbon-silicon composite foam is shown in **Figure 5.3**b. The uniform distribution of silicon particles in the carbon matrix is evidenced in the high-magnification SEM image (**Figure 3**c). As envisaged from the 24 wt% carbon yield of sucrose, the carbon content in the carbon-silicon composite foam is very close to that required for reaction with the silicon present. The TGA graph of the carbon-silicon composite foams obtained from the paste of various compositions is shown in **Figure 5.4**. The weight loss of 23 to 24% observed up to 600 °C is due to the burnout of carbon and a slight increase in weight after 600 °C is due to the oxidation of silicon in the sample.

The reaction bonding of silicon and carbon in the carbon-silicon composite foam during inert-atmosphere heat-treatment results in the formation of β-SiC foam. This is clearly evidenced by the XRD analysis as well as the change of colour from black to pale green. The XRD pattern of carbon-silicon composite foam before and after high-temperature heat-treatment is shown in **Figure 5.5**. The peaks at 2θ values of 28.7, 47.6, 56.3, 69.4, 76.6 and 88.2° corresponding to the reflections from the planes (111), (220), (311), (400), (331), and (422), respectively, of elemental silicon. These peaks vanish after the high-temperature heat-treatment. On the other hand, peaks at 2θ values of 35.6, 41.3, 59.9 and 71.8° corresponding to reflection from (111), (200), (220) and (311) planes of β-SiC appear (Young Woo Kim et al., 2005; Vijayan et al., 2016).

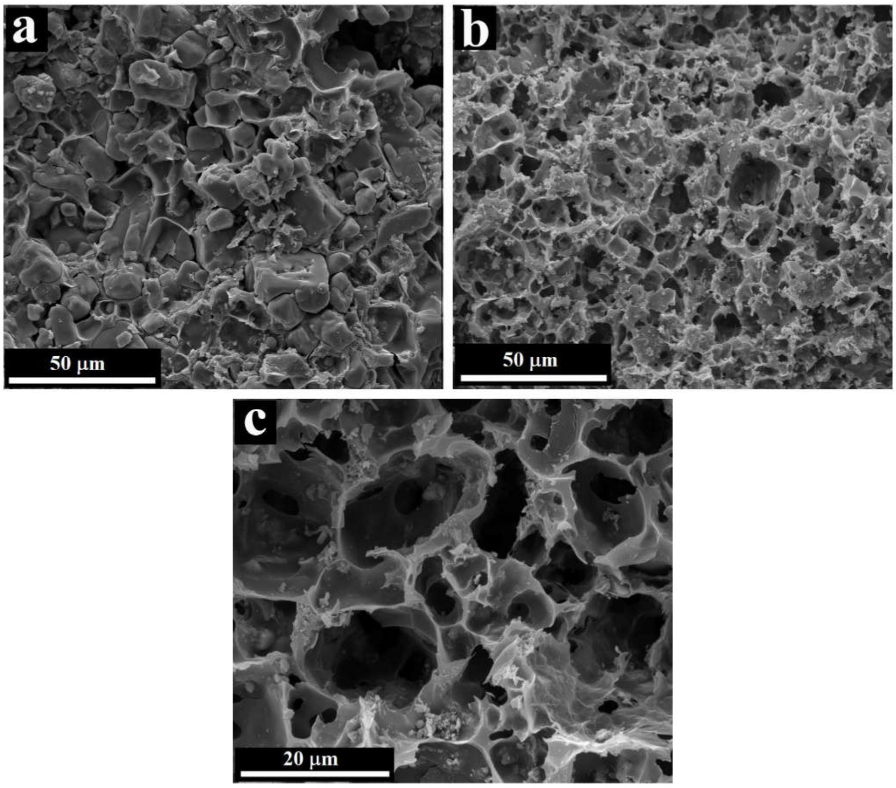

Figure 5.3 SEM images of (a) carbon-silicon-NaCl composite (b) carbon-silicon composite foam and (c) high-magnification SEM image of carbon-silicon composite foam

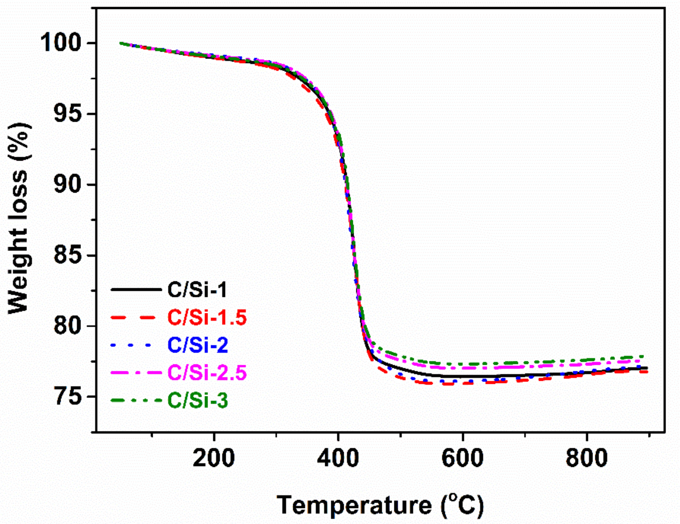

Figure 5.4 TGA performed in air of carbon-silicon composite foams prepared at various NaCl to sucrose weight ratios

The absence of any peak corresponding to carbon in the carbon-silicon composite foam indicates its amorphous nature. Further, the absence of peaks corresponding to silicon after the heat-treatment at 1500 °C indicates the complete conversion of silicon to silicon carbide. The carbon-silicon composite foam sample undergoes marginal shrinkage during the reaction bonding. The linear and volumetric shrinkages during reaction bonding are in the ranges of 0.2 to 2.3% and 1.17 to 7.7%, respectively. A large amount of porosity is expected in struts and cell walls of SiC foam obtained from the carbon-silicon composite foam. The small shrinkage observed is due to the densification of the struts and cell walls. **Figure 5.6** shows a digital photograph of carbon-silicon composite foam and SiC foam obtained by reaction bonding.

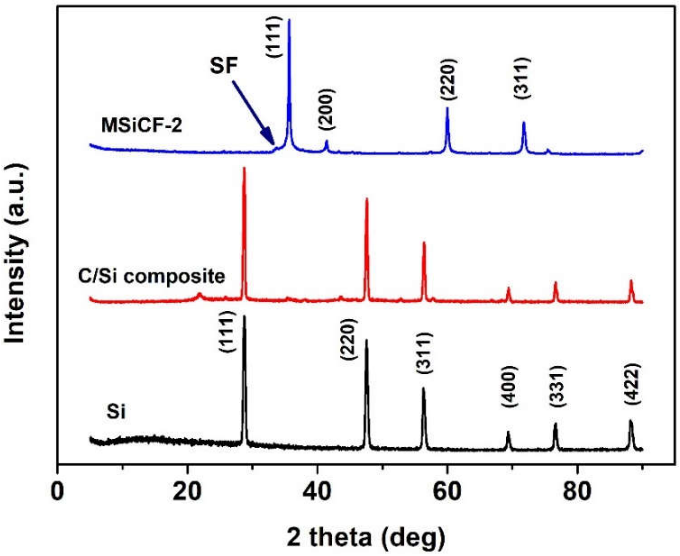

Figure 5.5 XRD diffraction pattern of carbon-silicon composite and **MSiCF-2**. “SF” indicates the peak corresponding to the stacking faults

Figure 5.6 Digital photograph of (a) carbon-silicon composite foam and (b) **MSiCF-2**

5.3.3 Microstructure

The low and high-magnification SEM images of **MSiCF** are shown in **Figure 5.7**. From the low-magnification images, it is observed that **MSiCF-1** and **MSiCF-1.5** contain large macropores which develop when water vapour generated during polymerization of glucose and fructose anhydride through –OH condensation gets entrapped within the molten paste. **MSiCF-2**, **MSiCF-2.5**, and **MSiCF-3** do not show these features since the polymerization is sluggish due to higher glycerol quantities which allows water vapour to diffuse out gradually from the mould. Also, higher concentrations of solid NaCl particles in these compositions restrict the space for the water vapour to accumulate. The **MSiCF**s exhibit a uniform distribution of microcells with open cellular microstructure as observed in the high-magnification SEM images. The cell size determined from the images is in the range of 2 to 22 μm which is consistent in all the studied compositions. A typical cell size distribution of **MSiCF** is shown in **Figure 5.8**. The samples prepared with higher concentrations of NaCl show thinning of the cell walls as the concentration of the carbon and silicon producing SiC correspondingly decreases. At high magnification, the fractured struts of the foams show nano-sized grains (35-110 nm) of near-spherical geometry (**Figure 5.9**).

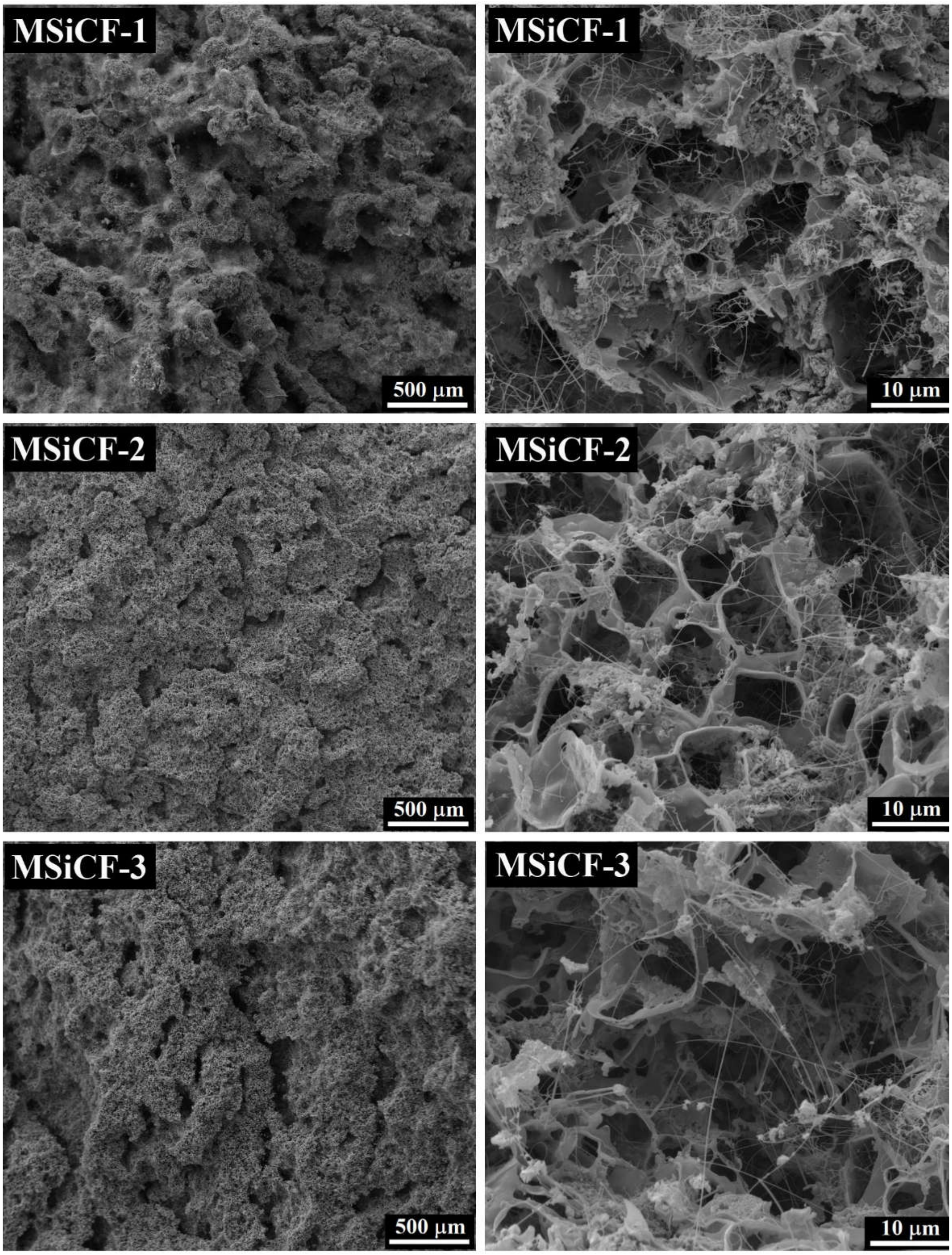

Figure 5.7 Low-magnification (Left) and high-magnification (Right) SEM images of **MSiCF-1**, **MSiCF-2** and **MSiCF-3**

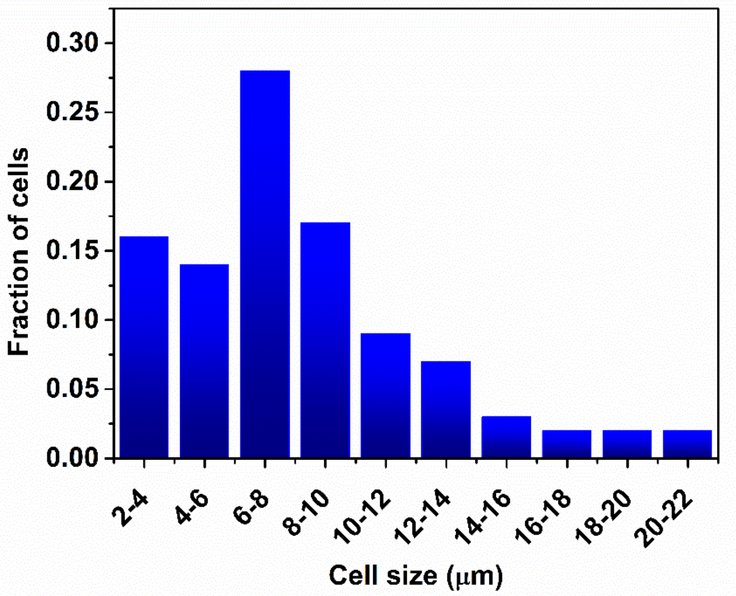

Figure 5.8 Typical cell size distribution determined from SEM images

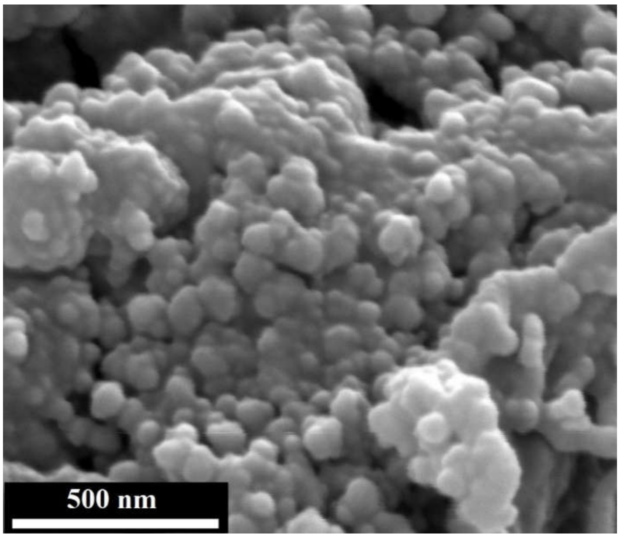

Figure 5.9 High-magnification SEM image of a fractured strut of SiC foam

Interestingly, the high-magnification images also show extensive web-like fibrous nanowires of nearly 30-150 nm diameter occupying the space inside the microcells as well on the surfaces of the cell wall. The EDX analysis of the nanowires confirms the composition as 60.1 wt% of silicon and 31.6 wt% of carbon. In addition, the EDX spectrum also shows the presence of aluminium and oxygen derived from the sintering additives. The carbon to silicon atomic ratio in the nanowires calculated from the EDX data is 1.23. This indicates that the nanowires grown on the cell wall surfaces are carbon-rich SiC. The EDX spectrum of SiC nanowire on the surface of **MSiCF-2** is shown in **Figure 5.10**. A weak diffraction peak at 2θ=33.3° in the XRD diffraction pattern (**Figure 5.4**) of SiC is attributed to the stacking fault in (111) plane in the SiC nanowires (Dai et al., 2015; Farhan, Wang, & Li, 2016). The decoration of SiC and SiOC surfaces with one dimensional SiC nanostructures by chemical vapour infiltration or through carbothermal reduction in the presence of catalysts such as iron and nickel is well established in literature (Duan et al., 2017; X. Qi et al., 2014). In addition, there are numerous reports on the growth of SiC nanowires on SiC and SiOC surfaces without the aid of catalysts through vapour-solid (VS) and vapour-liquid-solid (VLS) mechanisms (Du, He, Shui, Zhang, & Hong, 2019a; Pan et al., 2016; Vakifahmetoglu, Pippel, Woltersdorf, & Colombo, 2010). The VS mechanism is briefly explained thus: trace concentrations of SiO_2 on the surface of Si particles react with carbon producing SiO and CO. This is succeeded by the reaction of 1 mole of SiO with 3 moles of CO producing SiC and 2 moles of CO_2. The CO_2 reacts with carbon to produce CO and drives the positive feedback to reaction (ii) thus sustaining the growth of SiC nanowires. The reactions involved in VS mechanism of SiC nanowire growth are shown below. In the present case, it appears that the growth of SiC nanowire is through the VS mechanism as catalyst such as Fe and Ni is not included in the preparation.

$$SiO_2(s) + C(s) \rightarrow SiO(g) + CO(g) \qquad (i)$$

$$SiO(g) + 3\,CO(g) \rightarrow SiC(s) + 2CO_2(g) \qquad (ii)$$

$$CO_2(g) + C(s) \rightarrow 2CO(g) \qquad (iii)$$

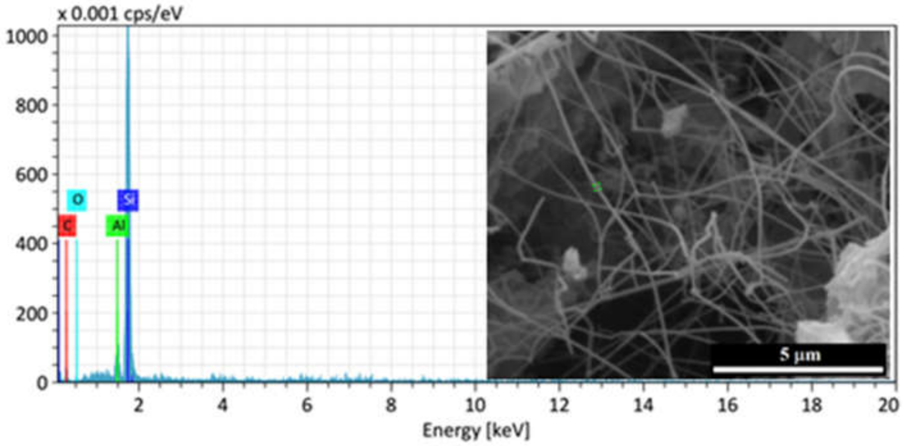

Figure 5.10 EDX spectrum of nanowires grown in **MSiCF-2**

5.3.4 Foam density and surface area

The variation in the bulk density of the **MSiCF** is shown in **Figure 5.11**. The bulk density of the foam is within the range of 0.284 to 0.419 g cm^{-3}. The density of **MSiCF-1.5** (0.419g cm^{-3}) is slightly higher than that of **MSiCF-1** (0.411 g cm^{-3}) even though the former was prepared with a higher concentration of NaCl in its composition. This is due to the large population of macropores in **MSiCF-1** produced by the entrapment of water vapour as evidenced by the SEM image (**Figure 5.7**). The density of the foams decreases from 0.419 to 0.284 g cm^{-3} when the NaCl to sucrose weight ratio increases from 1.5 to 3. The average skeletal density of the **MSiCF** determined from helium pycnometry is 3.19 g cm^{-3}. The porosity calculated from the bulk and skeletal densities using Equation 2.2 (**Chapter 2**) ranges from 86.9 to 91.1%. The effect of porosity and the *in situ* grown nanowires on the surface area of the foams is studied using N_2 adsorption-desorption isotherm. The surface area of **MSiCF**s calculated using the BET equation from the N_2 adsorption-desorption isotherms is in the range of 7.6 to 9.98 m^2 g^{-1} **(Table 5.4)**. **MSiCF-1** has a surface area of 8.03 m^2 g^{-1} while **MSiCF-1.5** exhibits a marginally lower value of 7.6 m^2 g^{-1}. With increasing porosity, we observe a significant increase in the surface area. The increase in the surface area is essentially due to the increase in the area of cell walls as well as higher concentrations of the SiC nanowires at higher porosities.

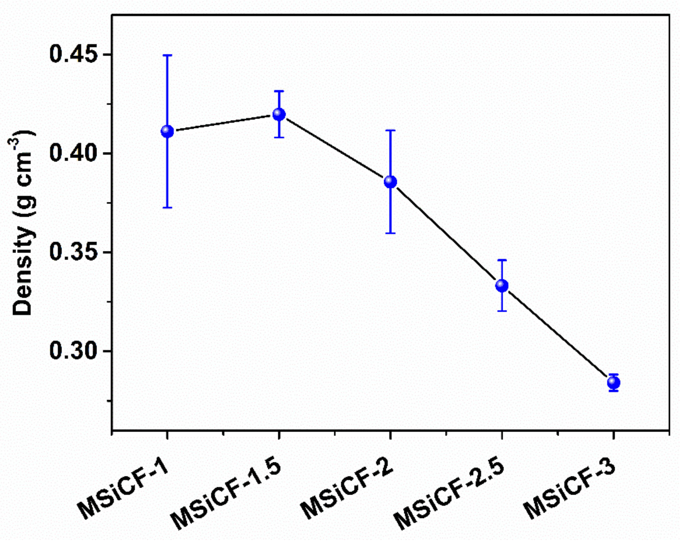

Figure 5.11 Density of **MSiCFs**

Table 5.4 BET Surface area of **MSiCF**s

Sample	**MSiCF-1**	**MSiCF-1.5**	**MSiCF-2**	**MSiCF-2.5**	**MSiCF-3**
BET surface area (m^2g^{-1})	8	7.6	9.6	9.7	10

5.3.5 Compressive strength and thermal conductivity

The SiC foams for EMI shielding and thermal insulation applications requires adequate mechanical strength. The stress-strain plots of **MSiCF**s are shown in **Figure 5.12**a. The graphs are analogous to the stress-strain curves exhibited by brittle cellular foams with an elastic behaviour at low strains represented by the linear section followed by a plateau region signifying the collapse of the cells with increasing strain. At high strains, we observe a rapid rise in the compressive stress which results from the densification of the foams after the complete cellular collapse (Letellier, Delgado-Sanchez, et al., 2017). The compressive strength and Young's modulus of the foams are shown in **Figure 5.12**b. The compressive strength value ranges from 0.97 to 2.38 MPa while Young's modulus is between 52 to 176 MPa. The highest values of compressive strength and Young's modulus are exhibited by **MSiCF-1.5** while the lowest values correspond to **MSiCF-3** which is expected because these samples show the highest and lowest density, respectively. The linear relationship between the compressive strength and bulk density of the foam is presented in **Figure 5.12**c. An R^2 value of 0.9942 reasonably establishes that the compressive strength is a linear function of density.

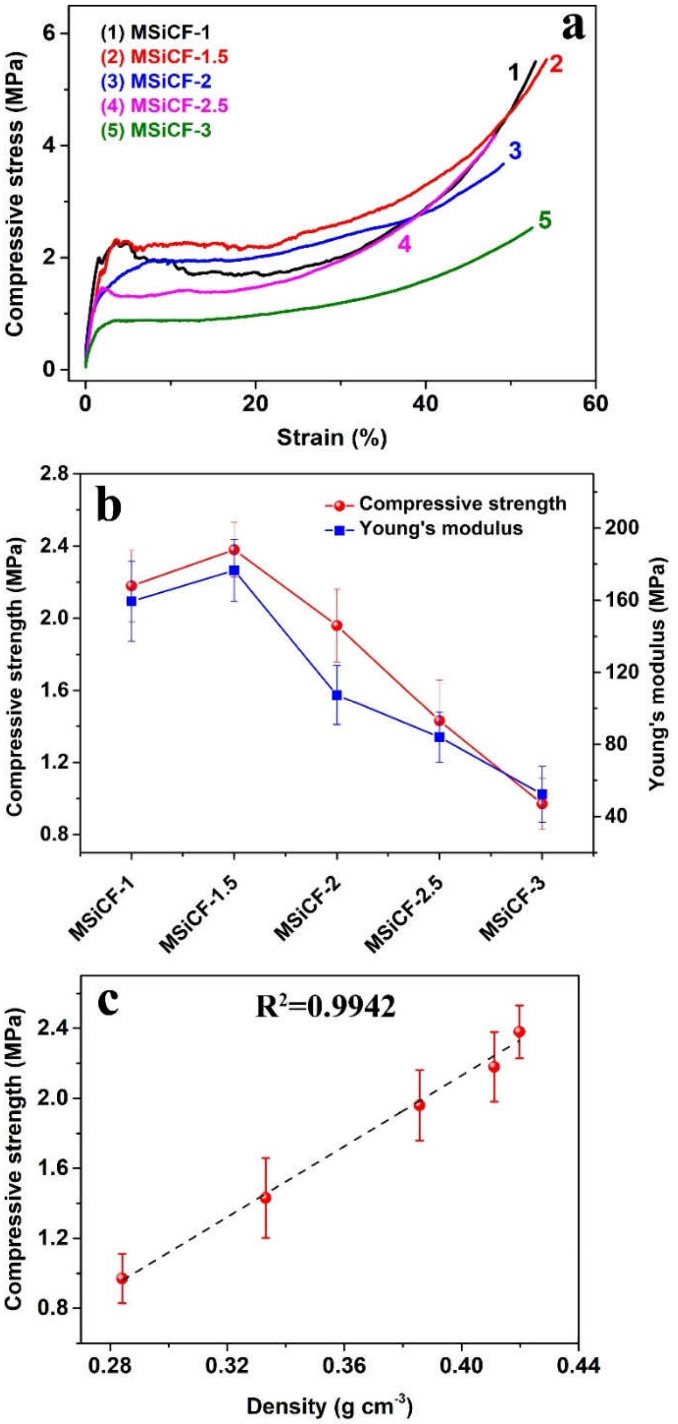

Figure 5.12 (a) Stress-strain graph of **MSiCF**s (b) compressive strength and Young's modulus and (c) compressive strength as a function of the density of **MSiCF**s

The thermal conductivity of the **MSiCF**s lies within the range of 0.334 to 0.758 W m^{-1} K^{-1} (**Figure 5.13**a). It follows a similar trend to that of the bulk density with **MSiCF-1.5** showing a high value of 0.758 W m^{-1} K^{-1} and **MSiCF-3** showing a low value of 0.334 W m^{-1} K^{-1}. It is well known that the thermal conductivity of porous materials is largely dependent on its bulk density (Alvarez et al., 2010; D. C. Jana et al., 2017; Kultayeva et al., 2019; Tondi, Fierro, et al., 2009). High bulk density is indicative of thick cell walls and struts which are amenable to greater heat transport. The high porosity of foams is associated with thin cell walls and narrow struts which results in high tortuosity thus impeding heat transport. **Figure 5.13**b depicts the correlation between the thermal conductivity and density of the **MSiCF**s. Thermal conductivity shows a linear dependence on the density of the foams (R^2=0.9906).

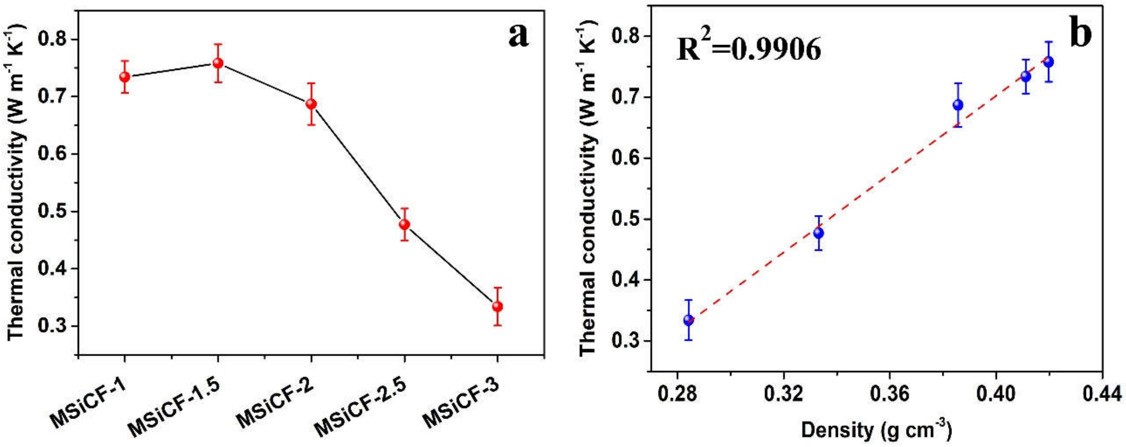

Figure 5.13 (a) Thermal conductivity of **MSiCF**s and (b) the correlation between thermal conductivity and density of **MSiCF**s

5.3.6 Electrical properties

The direct current electrical conductivities of the **MSiCF**s measured using a four probe instrument is shown in **Figure 5.14**. The electrical conductivity of the foams is in the range of 1.02×10^{-4} to 11.1×10^{-4} S cm^{-1}. Contrary to the expected, the electrical conductivity increases with a decrease in the foam density. This effect is explained by the increase in the SiC nanowire population within the microcells with an increase in the porosity of the foams. The one-dimensional nanowires with high carrier concentration form interconnecting networks between cell walls thus contributing to higher electrical conductivity (Duan et al., 2014).

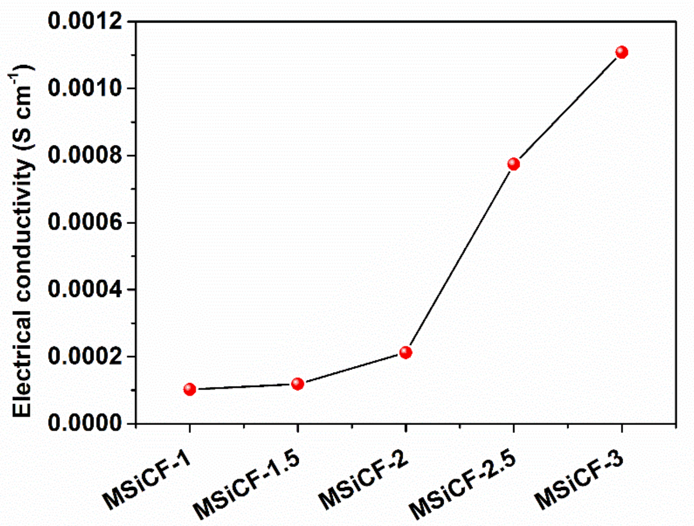

Figure 5.14 Electrical conductivity of **MSiCF**s

The dielectric properties of the **MSiCF**s were measured in the frequency range of 8.2 to 12.4 GHz (X-band). Dielectric materials are characterized by their relative complex permittivity ($\varepsilon=\varepsilon'-j\varepsilon''$) where, ε' is the real component and ε'' is the imaginary component of the complex permittivity representing storage and loss capability, respectively. According to the Debye theory, the real part (ε') of the relative complex permittivity is related to the polarization relaxation and the imaginary part (ε'') is related to the dielectric loss of the material (B. Zhao, Guo, Zhao, et al., 2017; B. Zhao et al., 2016; B. Zhao, Guo, Zhou, et al., 2017). The dielectric loss tangent ($\tan\delta=\varepsilon''/\varepsilon'$) characterizes the microwave attenuation property of the material. Higher $\tan\delta$ indicates superior microwave attenuation capacity. **Figure 5.15** shows the complex permittivity and the dielectric loss of the **MSiCF**s as a function of frequency. It can be seen that the real component (ε') of the complex permittivity of all **MSiCF**s decreases with increase in frequency (**Figure 5.15**a). At high EM wave frequencies, the rearrangement of dipoles is not fast enough to match the alternating electric field causing a decline in the dielectric polarization (Caiyun Liang & Wang, 2019). The average value of ε' of **MSiCF**s lies within the range of 2.5 to 4.0 with **MSiCF-2.5** showing the highest value. Meanwhile, the ε'' values of all but **MSiCF-2.5** also exhibit a declining trend with an increase in the EM wave frequency

(**Figure 5.15**b). The ε'' of **MSiCF-2.5** shows a slight increase with an increase in the frequency. The average value of ε'' ranges from 0.69 to 2.18 and does not follow any obvious trend in relation to porosity with **MSiCF-2.5** exhibiting the highest value of 2.18. The dielectric loss tangent (*tan* δ) of **MSiCF**s varies between 0.25 and 0.55 showing no apparent correlation with porosity either (**Figure 5.15**c). The *tan* δ of **MSiCF-2** and **MSiCF-2.5** increase with an increase of frequency of EM waves. The highest average *tan* δ value of 0.55 is exhibited by **MSiCF-2.5**.

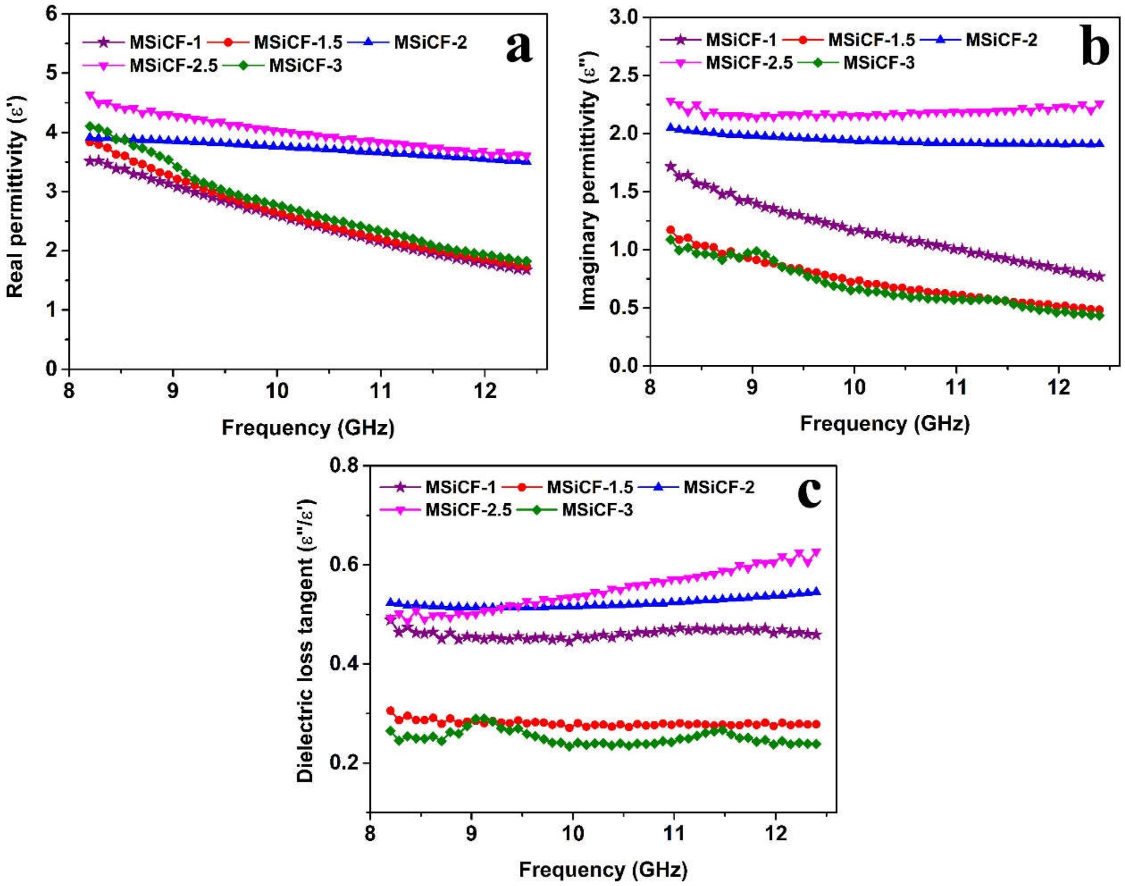

Figure 5.15 The real permittivity (a), imaginary permittivity (b) and the dielectric loss tangent (c) of **MSiCF**s as a function of frequency (8.2–12.4 GHz)

5.3.7 EMI shielding

An ideal EMI shielding material should exhibit high values of shielding effectiveness over the entire range of frequency in the selected band. EMI shielding takes effect through factors such as absorption by attenuation of incident wave (SE_A), reflection from the incident plane (SE_R) and multiple internal reflection (SE_M) within the shielding material (Duan et al., 2014; Caiyun Liang & Wang, 2019; Sreedeviamma Dijith, Vijayan, Prabhakaran, & Peethambharan Surendran, 2019). Reflection of the EM waves occurs when there is an impedance mismatch between the free space and the shielding material. Absorption is explained by the dielectric loss involving conduction and relaxation losses. The relaxation loss is effected by the polarization caused by dipoles, defects, grain boundaries and functional groups in the material while conduction loss occurs due to its electrical conductivity. Multiple internal reflections are caused by porous materials or composites with two or more phases with different dielectric properties. So, the total shielding effectiveness (SE_T) can be summarized using the equation:

$$SE_T = SE_A + SE_R + SE_M \qquad (5.1)$$

In cases where $SE_T > 15$, the multiple internal reflection component is usually neglected. The equation 5.1 can be reorganized as:

$$SE_T \approx SE_A + SE_R \qquad (5.2)$$

Typical graphs showing SE_T, SE_A and SE_R of **MSiCF** and corresponding carbon-silicon composite foam as a function of frequency in the X-band region of the microwave are shown in **Figure 5.16**a & b. The SE_T in **MSiCF**s is more or less independent of frequency. Majority of the reported SiC and SiOC based materials show a large variation in the shielding effectiveness with frequency as the dipoles fail to realign with the EM wave to induce dielectric polarization loss (Caiyun Liang & Wang, 2019). The SE_A and SE_R values observed are in the ranges of 24.9 to 38.8 dB and 3.4 to 6.8 dB, respectively. The SE_T varies in the range of 28.3 to 45.6 dB with a maximum for **MSiCF-2.5** and minimum for **MSiCF-3**. However, the SE_T values of **MSiCF** is found to be lower than that of the carbon-silicon composite foams. This is due to the high electrical conductivity of the carbon-silicon composite foams. For example, the carbon-silicon composite foam prepared at NaCl to sucrose ratio of 2.5 shows a SE_T of 53 dB due to high electrical conductivity of 790 S cm^{-1}. However, the carbon-silicon composite foams are prone to oxidation above 300 °C (**Figure 5.4**) and are not suitable for EMI shielding applications at high temperatures.

We observe that the absorption component of the SE_T of **MSiCF**s is significantly higher than the shielding through reflection with SE_R values showing only a slight variation with the samples. The low reflection component is due to a narrow mismatch in the impedance of the material and free space attributed to microcellular nature of the highly porous (86.8 to 91.1 vol.%) material. Generally, impedance matching is accomplished by incorporating pores in the material. The effective permittivity (ε_{eff}) of the porous absorber material is thus determined by the Maxwell-Garnett (MG) theory:

$$\varepsilon_{eff} = \varepsilon_1 \frac{(\varepsilon_2+2\varepsilon_1)+2f\,(\varepsilon_2-\varepsilon_1)}{(\varepsilon_2+2\varepsilon_1)-f(\varepsilon_2-\varepsilon_1)} \qquad (5.3)$$

where, ε_1 and ε_2 are the permittivity of the solid matrix and air, respectively and f is the volume fraction of the air in the effective medium (Caiyun Liang & Wang, 2019; B. Zhao, Guo, Zhao, et al., 2017; B. Zhao, Liang, et al., 2017). This is a valuable characteristic of a radar-absorbing material used in stealth-based defence application wherein the EM waves have to be absorbed rather than reflected back (C. Wang et al., 2017; Hongtao Zhang, Zhang, & Zhang, 2006, 2007b, 2007a). The SE_T, SE_A and SE_R of **MSiCF**s prepared at various NaCl to sucrose weight ratios is shown in **Figure 5.17**a.

The SE_T values obtained for **MSiCF**s are higher than that reported recently for SiC foams prepared from dough (24.2 dB) and SiOC foams prepared from polysiloxane (18 dB) (Duan et al., 2014; Caiyun Liang et al., 2017). The shielding effectiveness of a material depends on the density and available surface for EMI attenuation. The higher SE_T values obtained for **MSiCF**s is due to their microcellular structure, nanograin size and the presence of vast networks of SiC nanowires within the microcells. Microcells in the foams enhance the microwave absorption through multiple internal reflection mechanism and subsequent dissipation of EM energy as heat (Caiyun Liang & Wang, 2019; Caiyun Liang et al., 2017). In addition, a small amount of free carbon that may be present contribute to the EMI attenuation by ohmic losses. The higher SE_T of **MSiCF-1.5** (41 dB) compared to that of **MSiCF-1** (31 dB) is due to its higher density (D. X. Yan et al., 2012). On the other hand, increase in shielding effectiveness from **MSiCF-1.5** to **MSiCF-2.5** is due to the increase in the available surface for the attenuation of EM radiation due to increase in the number of microcells as well as the population of SiC nanowires with the stacking faults. These SiC nanowires form extensive interfaces with the SiC matrix which induces EM absorption through dipole polarization (Du, He, Shui, Zhang, & Hong, 2019b; Duan et al., 2014, 2017; Haitao Liu, Tian, & Cheng, 2013; Hangyu Zhang et al., 2015). The sample **MSiCF-3** shows the lowest SE_T value of 28.3 dB which can be ascribed to the fact that it has the lowest density of all the studied samples. It appears that the concentration of SiC nanowires in the microcells is insufficient to overcome the effect due to the decrease in density. The specific shielding effectiveness (**Figure 5.17**b) of **MSiCF** calculated on the basis of density of the foams is in the range of 98 to 137 dB $g^{-1}cm^3$. The specific shielding effectiveness obtained is much higher than that reported for SiC foam prepared from dough (24.8 dB g^{-1} cm^3) and SiOC foam prepared from polysiloxane (13.85 dB g^{-1} cm^3) (Duan et al., 2014; Caiyun Liang et al., 2017). With a focus on developing inexpensive, lightweight, thermally and chemically stable material with high EMI shielding properties, the microcellular SiC foams promises great advantage for aerospace and aviation applications.

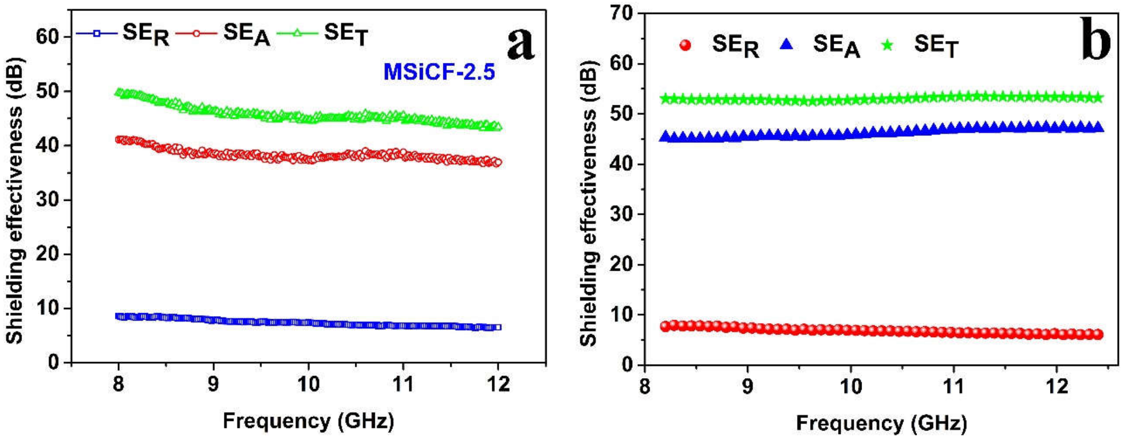

Figure 5.16 (a) The SE_R, SE_A and SE_T of **MSiCF-2.5** and (b) carbon-silicon composite foam prepared at NaCl to sucrose weight ratio of 2.5 over a frequency range of 8.2–12.4 GHz

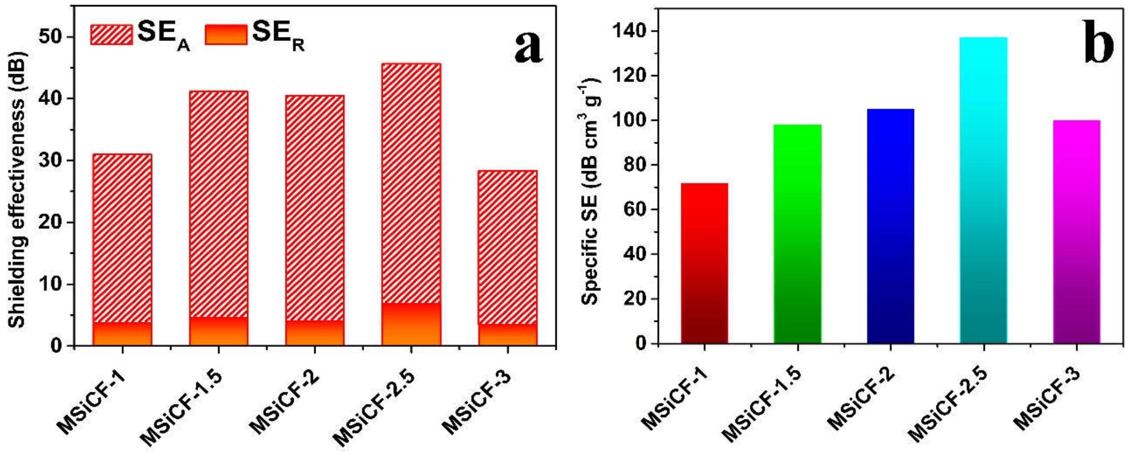

Figure 5.17 (a) EMI shielding effectiveness and (b) specific shielding effectiveness of **MSiCF**s at 11 GHz

5.4 Conclusions

Microcellular SiC foams (**MSiCF**s) are produced from sucrose and silicon powder using NaCl particles as pore template and glycerol as a plasticising additive. The acidic silica on the surface of silicon powder catalyzes the –OH condensation leading to the faster setting of molten sucrose-silicon-NaCl-glycerol pastes during compression moulding at 160 °C to form sucrose polymer-silicon-NaCl composite. Carbonization of sucrose polymer-silicon-NaCl composite followed by NaCl extraction and reaction bonding at 1500 °C results in the formation of **MSiCF**s. The porosity of the **MSiCF** foams is tuned by varying the NaCl particle template to sucrose weight ratio from 1 to 3. The linear and volumetric shrinkages of the sucrose polymer-silicon particle-NaCl composite bodies during carbonization at 750 °C decreases from 4 to 1.36% and 10.8 to 5%, respectively, when NaCl to sucrose weight ratio increases from 1 to 3. The linear and volumetric shrinkages during reaction bonding are in the ranges of 0.2 to 2.3% and 1.17 to 7.7%, respectively. The microcell size formed by the extraction of NaCl particle template is in the range of 2 to 22 μm. Carbon-rich SiC nanowires of diameter in the range of 30-150 nm grow on the cell walls during reaction bonding via a catalyst-free vapour-solid (VS) mechanism. The density and thermal conductivity of the **MSiCF**s are in the ranges of 0.284 to 0.419 g cm^{-3} and 0.334 to 0.758 W m^{-1} K^{-1}, respectively. The thermal conductivity shows a linear relationship with the bulk density of the foams with an R^2

value of 0.9906. The compressive strength (0.97 to 2.38 MPa) linearly increases with foam density. The **MSiCF**s show EMI shielding effectiveness (SE) and specific shielding effectiveness (SSE) as high as 45.6 dB and 137 dB g^{-1} cm^{3}, respectively. The excellent electromagnetic interference shielding property in the X-band frequency of **MSiCF**s is due to the superior impedance matching as a result of high porosity, enhanced polarization at foam-nanowire interfaces and defect sites in the SiC nanowire, internal reflection within the microcell and ohmic losses associated with the presence of a small amount of free carbon. The lightweight and high-absorption dominated shielding effectiveness make the **MSiCF**s suitable candidates for EMI shielding materials in aircraft and aerospace structures.

CHAPTER 6

CONCLUSIONS AND FUTURE WORK

6.1 Conclusions

Carbon foams are three-dimensional macroporous materials composed of solid carbon matrix interspersed with pores called cells. The foams have a porosity greater than 70% and are classified as open celled, closed celled and reticulated. Carbon foams have a wide range of properties such as low density, tunable electrical and thermal conductivity, chemical inertness, high specific surface area, high permeability and high EMI shielding effectiveness. These properties are exploited for various advanced applications such as lightweight thermo-structural components, high-temperature thermal insulation, thermal management, fire-resistant structure, catalyst support, electrode in energy storage devices and sensors, gas and organic solvent absorption and EMI shielding. They are prepared from precursors such as petroleum and coal tar pitches, synthetic polymer resins and natural organic molecules which leave sufficient carbon during pyrolysis. Foaming or blowing of carbon precursor resins, polymer foam replication and sacrificial templating methods are used for their preparation.

Silicon carbide (SiC) foams exhibit superior oxidation resistance in addition to the high surface area, high permeability, high-temperature stability, excellent dielectric property, chemical inertness and high specific strength. They find application as catalyst support, hot-gas and molten metal filters, membrane supports, gas-burner media, and lightweight structural parts for high-temperature applications and high-temperature EMI shielding materials. The SiC foams are prepared from either pre-ceramic polymers or aqueous SiC powder suspensions by foaming and setting, polymer foam replication and sacrificial templating. A detailed review on the preparation, properties and applications of carbon and SiC foams is presented in **Chapter 1**.

Generally, the above processing methods produce foams with relatively large cell sizes. Foams with smaller cell size are reported to possess superior compressive strength compared to foams of similar relative density but of larger cells (>500 μm). Small cell size also restrict conductive heat transfer due to the enhanced phonon scattering in the small struts of the cell resulting in lower thermal conductivity. In addition, smaller cell size facilitates adhesion with facing sheets for the fabrication of sandwich composites using foams as a core for lightweight structural and thermo-structural applications. Foams with cell size less than 100 μm are called microcellular foams. This thesis investigates the preparation of carbon and SiC foams composed of microcells using sucrose as carbon source and NaCl particles as a sacrificial template.

Processing of microcellular carbon foams from molten sucrose-NaCl pastes by compression moulding is discussed in **Chapter 2**. Pastes of molten sucrose and NaCl at NaCl to sucrose weight ratios (**$W_{N/S}$**) ranging from 0.7 to 1.2 is compression moulded in a stainless steel mould. Subsequent setting by polymerization of molten sucrose-NaCl pastes yields a sucrose polymer-NaCl composite bodies. Polymerization of sucrose takes place by intermolecular –OH condensation of glucose and fructose anhydride produced by the decomposition of sucrose. The NaCl particles in the molten sucrose-NaCl pastes are found to catalyse the polymerization of sucrose. The presence of NaCl also aids the intramolecular water elimination reaction during caramelization leading to the carbon-enriched polymeric structures. The sucrose polymer-NaCl composite bodies are carbonized at 750 °C in an inert atmosphere to obtain carbon-NaCl composites. The extraction of NaCl particles by washing with hot water and subsequent heat-treatment at 900 °C produce the microcellular carbon foam. The sucrose polymer-NaCl composites show linear and volumetric shrinkages during carbonization in the ranges of 8.9 to 12% and 24.3 to 28.5%, respectively. The microcellular carbon foams exhibit bulk density within a range of 0.26-0.33 g cm^{-3} where the highest density is shown by the carbon foam prepared at **$W_{N/S}$** of 1. The broad peaks at 2θ values of 25 and 44° in the XRD diffraction pattern corresponding to reflections from (002) and (101) planes indicate the turbostratic nature of the carbon foams. The macropore (70 to 414 μm) and microcells (2 to 13 μm) observed in the SEM images are due to the entrapment of water vapour produced during caramelization and NaCl particle template removal, respectively. The population and size of macropores decrease with an increase in **$W_{N/S}$** whereas the microcell size distribution and average microcell size (5 μm) remains the same. The compressive strength of the carbon foams increases from 2.8 to 8.4 MPa when the **$W_{N/S}$** increases from 0.7 to 1.2. A linear fit of the plot of compressive strength against the density of the foams shows an R^2 value of 0.8919. The thermal conductivity of the carbon foams decreases from 0.348 to 0.257 W m^{-1} K^{-1} when the **$W_{N/S}$** increases from 0.7 to 1.2. The microcellular carbon foams show specific surface area and micropore volume in close ranges of 379-442 m^2 g^{-1} and 0.13-0.15 cm^3 g^{-1}, respectively. The DFT pore size analysis and TEM images reveal micropores of ~1 nm on the cell walls and struts.

To further reduce the density and improve the uniformity of the pore structure of the microcellular carbon foams, it is essential to increase the NaCl particle template concentration. However, pastes of **$W_{N/S}$** higher than 1.2 are highly viscous and are difficult to mould. Glycerol is selected as a plasticizing additive to prepare mouldable pastes containing higher concentrations of NaCl particles. In **Chapter 3**, processing of low-density microcellular carbon foams from sucrose by NaCl particle templating using glycerol as a plasticising additive is discussed. The amount of glycerol required to prepare mouldable pastes increases from 8 to 64 g (per 100 g of sucrose) with an increase in **$W_{N/S}$** from 1.5 to 3. The setting of the molten sucrose-NaCl-glycerol pastes is due to the caramelization of sucrose as well as the slow evaporation of glycerol at 160 °C. The slow setting (setting time: 5 to 13 h) of the molten sucrose-NaCl-glycerol pastes is due to the slow caramelization of sucrose in the presence of glycerol. The linear and volumetric shrinkages during carbonization lie in the range of 3.64 to 7.62% and 10.02 to 20.65%, respectively. It is also evident from the SEM analysis that the carbon foams are devoid of large macropores as the slow caramelization allows the diffusion of water vapour out of the mould without creating bubbles in the paste. Even though pastes of **$W_{N/S}$** higher than 3 could be moulded, the subsequent washing after carbonization results in the disintegration of the carbon-NaCl composites. The study is therefore limited to molten sucrose-NaCl pastes with **$W_{N/S}$** up to 3. The microcell size determined from the SEM images lies within a range of 2 to 20 μm with a majority in a size range of 3 to 6 μm. The foam density and compressive strength decrease from 0.214 to 0.096 g cm^{-3} and 4.84 to 0.60 MPa, respectively, as **$W_{N/S}$** increases from 1.5 to 3. The compressive strength shows a linear relationship with foam density with a high R^2 value of 0.9816 indicating homogeneity of the pore structure in the prepared foams. The thermal conductivity (0.235 to 0.088 W m^{-1} K^{-1}) shows a linear decrease with foam density with an R^2 value of 0.9655.

The low-density microcellular carbon foams show relatively high EMI SE and specific EMI SE ranging from 24.7 to 41.7 dB and 194.8 to 257.3 dB/g cm^{-3}, respectively. The high EMI shielding effectiveness of the foams is largely due to the high interfacial area, porosity and electrical conductivity of the carbon matrix. The carbon-NaCl composites have the adequate compressive strength (6.9 to 17.8 MPa) and Young's modulus (521 to 1964 MPa) to withstand stresses during machining to produce slots, thin-walled fins and holes using conventional machines and tools. The machining of carbon-NaCl composites followed by NaCl extraction by water washing could be the strategy for producing low-density carbon foams with the required contours.

The processing and characterisation of microcellular conducting carbon foams (**MCCF**) are discussed in **Chapter 4**. Compression moulding of molten sucrose-NaCl-graphite-glycerol pastes followed by curing, carbonization, NaCl extraction and heat-treatment produced **MCCF**. Graphite powder is used as a conducting filler and glycerol as a plasticizing additive. In order to prepare foams with a wide range of thermal conductivity and porosity, the concentration of sucrose, graphite powder and NaCl are varied in the composition. The **MCCF**s exhibit bulk density and compressive strength in the ranges of 0.137 to 0.526 g cm^{-1} and 0.225 to 14.96 MPa, respectively. The decrease in observed compressive strength with an increase in graphite filler loading is due to the decrease in the concentration of sucrose derived carbon which binds the graphite filler particles. Thermal conductivity of **MCCF**s (0.282 to 5.23 W m^{-1} K^{-1}) increases with an increase in graphite filler loading and decreases in NaCl particle concentration. Calculations using Gibson-Ashby model indicate that the increase in thermal conductivity due to graphite filler addition outweighs that which occurs due to an increase in foam density. The SEM analysis reveals interconnected microcellular morphology with cell size in the range of 2 to 11.7 μm. It also shows a decrease in the cell wall thickness for **MCCF**s prepared at high NaCl concentrations. Hydrophobicity of the **MCCF**s increases with an increase in NaCl template loading as evidenced by the contact angle measurements. The hydrophobic nature of **MCCF**s enables easy infiltration of wax-based phase change materials. Paraffin wax/conducting carbon foam (**PW/MCCF**) composites with wax loading in the range of 50.5 to 82.6 wt% exhibit higher thermal conductivity (0.65-7.72 W m^{-1} K^{-1}) than the unfilled foams. The highest melting enthalpy of 110.9 J g^{-1} is achieved for **PW/MCCF-90-10-250** composite with 82.6 wt% of wax loading. The **PW/MCCF** composites show good form stability at 70 °C due to the microcellular morphology of the foams which enhances wax retention because of the high capillary forces.

In **Chapter 5**, the processing of microcellular SiC foams (**MSiCF**s) from sucrose and silicon powder using NaCl particles as pore template and glycerol as a plasticising additive is discussed. Glycerol in the range of 2 to 64 g per 100 g sucrose is used as a plasticizing additive depending on the NaCl to sucrose ratio. Molten sucrose-silicon-NaCl-glycerol pastes are compression moulded and cured to obtain sucrose polymer-silicon-NaCl composites. The acidic silica layer on the surface of silicon powder catalyzes the –OH condensation leading to the faster setting (setting time 1 to 3 h) of molten sucrose-silicon-NaCl-glycerol pastes during compression moulding at 160 °C. Carbonization of sucrose polymer-silicon-NaCl composite followed by NaCl extraction and reaction bonding at 1500 °C results in the formation of **MSiCF**s. The NaCl to sucrose weight ratio is varied from 1 to 3 to tune the porosity of the **MSiCF**s. The linear and volumetric shrinkages of sucrose polymer-silicon-NaCl composite bodies during carbonization at 750 °C, decrease from 4 to 1.36 % and 10.8 to 5%, respectively, when the NaCl to sucrose weight ratio increases from 1 to 3. The linear and volumetric shrinkages during reaction bonding are in the ranges of 0.2 to 2.3% and 1.17 to 7.7%, respectively. The microstructure analysis shows microcells with sizes in the range of 2 to 22 μm. The cellular void and cell walls contain carbon-rich SiC nanowires with diameters ranging from 30-150 nm formed via a catalyst-free vapour-solid (VS) mechanism. The density of the **MSiCFs** is in the range of 0.284 to 0.419 g cm^{-3} with a maximum at NaCl to sucrose weight ratio of 1.5. The thermal conductivity (0.334 to 0.758 W m^{-1} K^{-1}) shows a linear relationship with the bulk density of the **MSiCF**s with an R^2 value of 0.9906. The compressive strength (0.97 to 2.38 MPa) of the foams also shows a linear relationship with the foam density. The **MSiCF**s show absorption-dominated EMI shielding and exhibit a total EMI shielding effectiveness (SE) and specific shielding effectiveness (SSE) as high as 45.6 dB and 137 dB g^{-1} cm^3, respectively.

6.2 Future works

The preparation of microcellular carbon foams from sucrose using the NaCl particle templating shows feasibility for large scale production. The ubiquitous precursors and pore template and the simple processing technique are advantageous in exploring the possibility of using the microcellular carbon and SiC foams in several advanced applications, especially in high-temperature thermal protection systems.

The thermal protection system requires carbon foams in the form of sandwich composite structures with ceramic matrix composite (CMC) facing sheets. One of the directions of future research is to prepare microcellular carbon foam-CMC composites and their thermo-structural evaluation.

Another envisaged research is to enhance the microporosity on the cell wall surfaces by CO_2 activation and to study the activated microcellular carbon foam body for the adsorption of CO_2 and other pollutants.

Solar driven steam generation is one of the latest technologies explored for sustainable water purification and desalination of seawater to mitigate global water scarcity. Several porous materials have been studied as a medium for surface-based water evaporation. Microcellular carbon foams could be advantageous for steam generation by suitably improving the surface wettability. The interconnected microcellular structure would allow faster water transport and the inherently dark surface allows superior absorption of the solar spectrum. It is also proposed to study the microcellular carbon foams as a medium for solar-driven steam generation.

References

1 Acharya, R., Kumar, D., & Mathur, G. (2018). Study of Electromagnetic Radiation Effects on Human Body and Reduction Techniques BT - Optical and Wireless Technologies. In V. Janyani, M. Tiwari, G. Singh, & P. Minzioni (Eds.) (pp. 497–505). Singapore: Springer Singapore.

2 Afsharvahid, S., Ashman, P. J., & Dally, B. B. (2008). Investigation of NOx conversion characteristics in a porous medium. *Combustion and Flame*, *152*(4), 604–615. /https://doi.org/10.1016/j.combustflame.2007.06.017

3 Agarwal, P. R., Kumar, R., Kumari, S., & Dhakate, S. R. (2016). Three-dimensional and highly ordered porous carbon–MnO2 composite foam for excellent electromagnetic interference shielding efficiency. *RSC Adv.*, *6*(103), 100713–100722. https://doi.org/10.1039/C6RA23127F

4 Akeiber, H., Nejat, P., Majid, M. Z. A., Wahid, M. A., Jomehzadeh, F., Zeynali Famileh, I., … Zaki, S. A. (2016). A review on phase change material (PCM) for sustainable passive cooling in building envelopes. *Renewable and Sustainable Energy Reviews*, *60*, 1470–1497. https://doi.org/10.1016/j.rser.2016.03.036

5 AL-Hamamre, Z., Diezinger, S., Talukdar, P., Von Issendorff, F., & Trimis, D. (2006). Combustion of Low Calorific Gases from Landfills and Waste Pyrolysis Using Porous Medium Burner Technology. *Process Safety and Environmental Protection*, *84*(4), 297–308. https://doi.org/10.1205/psep.05167

6 Alam, M. M., Miras, J., Pérez-Carrillo, L. A., Vílchez, S., Solans, C., Imae, T., … Esquena, J. (2013). Facile synthesis of dual micro/macroporous carbonaceous foams by templating in highly concentrated water-in-oil emulsions. *Microporous and Mesoporous Materials*, *182*, 102–108. https://doi.org/10.1016/j.micromeso.2013.08.015

7 Alvarez-Lainez, M., Rodriguez-Perez, M. A., & DE Saja, J. A. (2008). Thermal conductivity of open-cell polyolefin foams. *Journal of Polymer Science Part B: Polymer Physics*, *46*(2), 212–221. https://doi.org/10.1002/polb.21358

8 Alvarez, F. X., Jou, D., & Sellitto, A. (2010). Pore-size dependence of the thermal conductivity of porous silicon: A phonon hydrodynamic approach. *Applied Physics Letters*, *97*(3), 33103. https://doi.org/10.1063/1.3462936

9 Amaral-Labat, G., Gourdon, E., Fierro, V., Pizzi, A., & Celzard, A. (2013). Acoustic properties of cellular vitreous carbon foams. *Carbon*, *58*, 76–86. https://doi.org/10.1016/j.carbon.2013.02.033

10 Ameli, A., Jung, P. U., & Park, C. B. (2013). Electrical properties and electromagnetic interference shielding effectiveness of polypropylene/carbon

fiber composite foams. *Carbon*, *60*, 379–391. https://doi.org/10.1016/j.carbon.2013.04.050

11 Amini, N., Aguey-Zinsou, K. F., & Guo, Z. X. (2011). Processing of strong and highly conductive carbon foams as electrode. *Carbon*, *49*(12), 3857–3864. https://doi.org/10.1016/j.carbon.2011.05.022

12 Anderson, D. P., Kearns, K. M., Klett, J. W., & Roy, A. K. (2000). Microcellular graphitic carbon foams for next generation structures and thermal management. In *2000 IEEE Aerospace Conference. Proceedings (Cat. No.00TH8484)* (Vol. 4, pp. 193–200 vol.4). https://doi.org/10.1109/AERO.2000.878406

13 Anyaka, B. O., & Akuru, U. B. (2012). Electromagnetic Wave Effect on Human Health: Challenges for Developing Countries. In *2012 International Conference on Cyber-Enabled Distributed Computing and Knowledge Discovery* (pp. 447–452). https://doi.org/10.1109/CyberC.2012.81

14 Armandi, M., Bonelli, B., Bottero, I., Areán, C. O., & Garrone, E. (2007). Synthesis and characterization of ordered porous carbons with potential applications as hydrogen storage media. *Microporous and Mesoporous Materials*, *103*(1), 150–157. https://doi.org/10.1016/j.micromeso.2007.01.049

15 Arroyo-Gómez, J. J., Villarroel-Rocha, D., de Freitas-Araújo, K. C., Martínez-Huitle, C. A., & Sapag, K. (2018). Applicability of activated carbon obtained from peach stone as an electrochemical sensor for detecting caffeine. *Journal of Electroanalytical Chemistry*, *822*, 171–176. https://doi.org/10.1016/j.jelechem.2018.05.028

16 Aswathi, M. K., Rane, A. V, Ajitha, A. R., Thomas, S., & Jaroszewski, M. (2018, November 16). EMI Shielding Fundamentals. *Advanced Materials for Electromagnetic Shielding*. https://doi.org/doi:10.1002/9781119128625.ch1

17 Aubert, J. H., & Sylwester, A. P. (1991). Morphological characterization of microcellular carbon foams. *Journal of Materials Science*, *26*(21), 5741–5752. https://doi.org/10.1007/BF01130110

18 Babapoor, A., Azizi, M., & Karimi, G. (2015). Thermal management of a Li-ion battery using carbon fiber-PCM composites. *Applied Thermal Engineering*, *82*, 281–290. https://doi.org/10.1016/j.applthermaleng.2015.02.068

19 Bae, G.-S., & Kim, C. Y. (2014). Broadband multilayer radar absorbing coating for RCS reduction. *Microwave and Optical Technology Letters*, *56*(8), 1907–1910. https://doi.org/10.1002/mop.28481

20 Bai, F. (2010). One dimensional thermal analysis of silicon carbide ceramic foam used for solar air receiver. *International Journal of Thermal Sciences*, *49*(12), 2400–2404. https://doi.org/10.1016/j.ijthermalsci.2010.08.010

21 Bao, X., Nangrejo, M. R., & Edirisinghe, M. J. (1999). Synthesis of silicon carbide foams from polymeric precursors and their blends. *Journal of Materials Science*, *34*(11), 2495–2505. https://doi.org/10.1023/A:1004666326039

22 Bao, X., Nangrejo, M. R., & Edirisinghe, M. J. (2000). Preparation of silicon carbide foams using polymeric precursor solutions. *Journal of Materials Science*, *35*(17), 4365–4372. https://doi.org/10.1023/A:1004805023228

23 Baran, D., Yardim, M. F., Atakül, H., & Ekinci, E. (2013). Synthesis of carbon foam with high compressive strength from an asphaltene pitch. *New Carbon Materials*, *28*(2), 127–132. https://doi.org/10.1016/S1872-5805(13)60071-2

24 Biamino, S., Antonini, A., Eisenmenger-Sittner, C., Fuso, L., Pavese, M., Fino, P., … Badini, C. (2010). Multilayer SiC for thermal protection system of space vehicles with decreased thermal conductivity through the thickness. *Journal of the European Ceramic Society*, *30*(8), 1833–1840. https://doi.org/10.1016/j.jeurceramsoc.2010.01.040

25 Biscaro, R. S., Nohara, E. L., Peixoto, G. G., Faez, R., & Rezende, M. C. (2003). Performance evaluation of conducting polymer paints as radar absorbing materials (RAM). In *Proceedings of the 2003 SBMO/IEEE MTT-S International Microwave and Optoelectronics Conference - IMOC 2003. (Cat. No.03TH8678)* (Vol. 1, pp. 355–358 vol.1). https://doi.org/10.1109/IMOC.2003.1244885

26 Bolivar, C. M. V., Antonini, A., Biamino, S., Pavese, M., Fino, P., & Badini, C. (2010). Oxidation resistance of multilayer SiC for space vehicle thermal protection systems. *Advanced Engineering Materials*, *12*(7), 617–622. https://doi.org/10.1002/adem.200900328

27 Bose, P., & Amirtham, V. A. (2016). A review on thermal conductivity enhancement of paraffinwax as latent heat energy storage material. *Renewable and Sustainable Energy Reviews*, *65*, 81–100. https://doi.org/10.1016/j.rser.2016.06.071

28 Brockmeyer, J. W., & Aubrey, L. S. (2008, January 1). Application of Ceramic Foam Filters in Molten Metal Filtration. *Application of Refractories: Ceramic Engineering and Science Proceedings*. https://doi.org/10.1002/9780470320372.ch8

29 Casady, J. B. (2000). 5 - Processing of Silicon Carbide for Devices and Circuits. In S. J. B. T.-P. of W. B. G. S. Pearton (Ed.) (pp. 178–249). Norwich, NY: William Andrew Publishing. https://doi.org/10.1016/B978-081551439-8.50007-9

30 Cassie, A. B. D., & Baxter, S. (1944). Wettability of porous surfaces. *Transactions of the Faraday Society*, *40*(0), 546–551. https://doi.org/10.1039/TF9444000546

31 Celzard, A., Zhao, W., Pizzi, A., & Fierro, V. (2010). Mechanical properties of tannin-based rigid foams undergoing compression. *Materials Science and Engineering A*, *527*(16–17), 4438–4446. https://doi.org/10.1016/j.msea.2010.03.091

32 Chae, S.-H., Kim, Y.-W., Song, I.-H., Kim, H.-D., & Narisawa, M. (2009). Porosity control of porous silicon carbide ceramics. *Journal of the European Ceramic Society*, *29*(13), 2867–2872. https://doi.org/10.1016/j.jeurceramsoc.2009.03.027

33 Chang, C.-F., Chang, C.-Y., & Tsai, W.-T. (2000). Effects of Burn-off and Activation Temperature on Preparation of Activated Carbon from Corn Cob Agrowaste by CO2 and Steam. *Journal of Colloid and Interface Science*, *232*(1), 45–49. https://doi.org/10.1006/jcis.2000.7171

34 Chatterjee, S., & Saito, T. (2015). Lignin-Derived Advanced Carbon Materials. *ChemSusChem*, *8*(23), 3941–3958. https://doi.org/10.1002/cssc.201500692

35 Chen, B., Ma, Q., Tan, C., Lim, T.-T., Huang, L., & Zhang, H. (2015). Carbon-Based Sorbents with Three-Dimensional Architectures for Water Remediation. *Small*, *11*(27), 3319–3336. https://doi.org/10.1002/smll.201403729

36 Chen, C., Kennel, E. B., Stiller, A. H., Stansberry, P. G., & Zondlo, J. W. (2006). Carbon foam derived from various precursors. *Carbon*, *44*(8), 1535–1543. https://doi.org/10.1016/j.carbon.2005.12.021

37 Chen, L., Song, N., Shi, L., & Ding, P. (2018). Anisotropic thermally conductive composite with wood-derived carbon scaffolds. *Composites Part A: Applied Science and Manufacturing*, *112*, 18–24. https://doi.org/10.1016/j.compositesa.2018.05.023

38 Chen, L., Zou, R., Xia, W., Liu, Z., Shang, Y., Zhu, J., … Cao, A. (2012). Electro- and Photodriven Phase Change Composites Based on Wax-Infiltrated Carbon Nanotube Sponges. *ACS Nano*, *6*(12), 10884–10892. https://doi.org/10.1021/nn304310n

39 Chen, S., He, G., Hu, H., Jin, S., Zhou, Y., He, Y., … Hou, H. (2013). Elastic carbon foam via direct carbonization of polymer foam for flexible electrodes and organic chemical absorption. *Energy & Environmental Science*, *6*(8), 2435–2439. https://doi.org/10.1039/C3EE41436A

40 Chen, Y., Chen, B. Z., Shi, X. C., Xu, H., Hu, Y. J., Yuan, Y., & Shen, N. Bin. (2007). Preparation of pitch-based carbon foam using polyurethane

foam template. *Carbon*, *45*(10), 2132–2134. https://doi.org/10.1016/j.carbon.2007.06.004

41 Chollon, G., Delettrez, S., & Langlais, F. (2014). Chemical vapour infiltration and mechanical properties of carbon open-cell foams. *Carbon*, *66*, 18–30. https://doi.org/https://doi.org/10.1016/j.carbon.2013.08.021

42 Chu, S., Cui, Y., & Liu, N. (2017). The path towards sustainable energy. *Nature Materials*, *16*(1), 16–22. https://doi.org/10.1038/nmat4834

43 Chung, D. D. L. (2001). Electromagnetic interference shielding effectiveness of carbon materials. *Carbon*, *39*(2), 279–285. https://doi.org/10.1016/S0008-6223(00)00184-6

44 Colombo, P. (2006). Conventional and novel processing methods for cellular ceramics. *Philosophical Transactions of the Royal Society A: Mathematical, Physical and Engineering Sciences*, *364*(1838), 109–124. https://doi.org/10.1098/rsta.2005.1683

45 Colombo, P., & Bernardo, E. (2003). Macro- and micro-cellular porous ceramics from preceramic polymers. *Composites Science and Technology*, *63*(16), 2353–2359. https://doi.org/10.1016/S0266-3538(03)00268-9

46 Dai, W., Yu, J., Wang, Y., Song, Y., Alam, F. E., Nishimura, K., … Jiang, N. (2015). Enhanced thermal conductivity for polyimide composites with a three-dimensional silicon carbide nanowire@graphene sheets filler. *J. Mater. Chem. A*, *3*(9), 4884–4891. https://doi.org/10.1039/C4TA06417H

47 Daniel, S., & Thomas, S. (2018, November 16). Shielding Efficiency Measuring Methods and Systems. *Advanced Materials for Electromagnetic Shielding*. https://doi.org/doi:10.1002/9781119128625.ch4

48 Darder, M., & Ruiz-Hitzky, E. (2005). Caramel–clay nanocomposites. *Journal of Materials Chemistry*, *15*(35–36), 3913–3918. https://doi.org/10.1039/B505958E

49 Davis, R. F. (2017). Silicon Carbide. In *Reference Module in Materials Science and Materials Engineering*. Elsevier. https://doi.org/10.1016/b978-0-12-803581-8.02445-0

50 De Araújo, M. J. G., Villarroel-Rocha, J., De Souza, V. C., Sapag, K., & Pergher, S. B. C. (2019). Carbon foams from sucrose employing different metallic nitrates as blowing agents: Application in CO2 capture. *Journal of Analytical and Applied Pyrolysis*, *141*, 104627. https://doi.org/10.1016/j.jaap.2019.05.016

51 Delhaes, P. (2002). Chemical vapor deposition and infiltration processes of carbon materials. *Carbon*, *40*(5), 641–657. https://doi.org/10.1016/S0008-6223(01)00195-6

52 Doherty, C. M., Caruso, R. A., Smarsly, B. M., Adelhelm, P., & Drummond, C. J. (2009). Hierarchically Porous Monolithic LiFePO4/Carbon Composite Electrode Materials for High Power Lithium Ion Batteries. *Chemistry of Materials*, *21*(21), 5300–5306. https://doi.org/10.1021/cm9024167

53 Dong, S., Zhang, X., Zhang, D., Sun, B., Yan, L., & Luo, X. (2018). Strong effect of atmosphere on the microstructure and microwave absorption properties of porous SiC ceramics. *Journal of the European Ceramic Society*, *38*(1), 29–39. https://doi.org/10.1016/j.jeurceramsoc.2017.07.034

54 Dong, X., Chen, J., Ma, Y., Wang, J., Chan-Park, M. B., Liu, X., … Chen, P. (2012). Superhydrophobic and superoleophilic hybrid foam of graphene and carbon nanotube for selective removal of oils or organic solvents from the surface of water. *Chemical Communications*, *48*(86), 10660–10662. https://doi.org/10.1039/C2CC35844A

55 Du, B., He, C., Shui, A., Zhang, X., & Hong, C. (2019a). Microwave-absorption properties of heterostructural SiC nanowires/SiOC ceramic derived from polysiloxane. *Ceramics International*, *45*(1), 1208–1214. https://doi.org/10.1016/j.ceramint.2018.09.306

56 Du, B., He, C., Shui, A., Zhang, X., & Hong, C. (2019b). Microwave-absorption properties of heterostructural SiC nanowires/SiOC ceramic derived from polysiloxane. *Ceramics International*, *45*(1), 1208–1214. https://doi.org/10.1016/j.ceramint.2018.09.306

57 Duan, W., Yin, X., Li, Q., Liu, X., Cheng, L., & Zhang, L. (2014). Synthesis and microwave absorption properties of SiC nanowires reinforced SiOC ceramic. *Journal of the European Ceramic Society*, *34*(2), 257–266. https://doi.org/10.1016/j.jeurceramsoc.2013.08.029

58 Duan, W., Yin, X., Luo, C., Kong, J., Ye, F., & Pan, H. (2017). Microwave-absorption properties of SiOC ceramics derived from novel hyperbranched ferrocene-containing polysiloxane. *Journal of the European Ceramic Society*, *37*(5), 2021–2030. https://doi.org/10.1016/j.jeurceramsoc.2016.12.038

59 Dubey, R. J.-C., Nüssli, J., Piveteau, L., Kravchyk, K. V, Rossell, M. D., Campanini, M., … Stadie, N. P. (2019). Zeolite-Templated Carbon as the Cathode for a High Energy Density Dual-Ion Battery. *ACS Applied Materials & Interfaces*, *11*(19), 17686–17696. https://doi.org/10.1021/acsami.9b03886

60 Duong-Viet, C., Ba, H., El-Berrichi, Z., Nhut, J. M., Ledoux, M. J., Liu, Y., & Pham-Huu, C. (2016). Silicon carbide foam as a porous support platform for catalytic applications. *New Journal of Chemistry*, *40*(5), 4285–4299. https://doi.org/10.1039/c5nj02847g

61 Eksilioglu, A., Gencay, N., Yardim, M. F., & Ekinci, E. (2006). Mesophase AR pitch derived carbon foam: Effect of temperature, pressure and pressure

release time. *Journal of Materials Science*, *41*(10), 2743–2748. https://doi.org/10.1007/s10853-006-7079-5

62 El Qada, E. N., Allen, S. J., & Walker, G. M. (2006). Adsorption of Methylene Blue onto activated carbon produced from steam activated bituminous coal: A study of equilibrium adsorption isotherm. *Chemical Engineering Journal*, *124*(1), 103–110. https://doi.org/10.1016/j.cej.2006.08.015

63 Eltmimi, A. H., Barron, L., Rafferty, A., Hanrahan, J. P., Fedyanina, O., Nesterenko, E., … Paull, B. (2010). Preparation, characterisation and modification of carbon-based monolithic rods for chromatographic applications. *Journal of Separation Science*, *33*(9), 1231–1243. https://doi.org/10.1002/jssc.200900845

64 Eom, J. H., Kim, Y. W., & Raju, S. (2013). Processing and properties of macroporous silicon carbide ceramics: A review. *Journal of Asian Ceramic Societies*, *1*(3), 220–242. https://doi.org/10.1016/j.jascer.2013.07.003

65 Eom, J. H., Kim, Y. W., Song, I. H., & Kim, H. D. (2007). Microstructure and properties of porous silicon carbide ceramics fabricated by carbothermal reduction and subsequent sintering process. *Materials Science and Engineering A*, *464*(1–2), 129–134. https://doi.org/10.1016/j.msea.2007.03.076

66 Eom, J. H., Kim, Y. W., Song, I. H., & Kim, H. D. (2008). Processing and properties of polysiloxane-derived porous silicon carbide ceramics using hollow microspheres as templates. *Journal of the European Ceramic Society*, *28*(5), 1029–1035. https://doi.org/10.1016/j.jeurceramsoc.2007.09.009

67 Esposito, L., Sciti, D., Piancastelli, A., & Bellosi, A. (2004). Microstructure and properties of porous β-SiC templated from soft woods. *Journal of the European Ceramic Society*, *24*(2), 533–540. https://doi.org/10.1016/S0955-2219(03)00195-X

68 Fang, Z., Li, C., Sun, J., Zhang, H., & Zhang, J. (2007). The electromagnetic characteristics of carbon foams. *Carbon*, *45*(15), 2873–2879. https://doi.org/10.1016/j.carbon.2007.10.013

69 Farhan, S., Wang, R., Jiang, H., & Li, K. (2016). Use of waste rigid polyurethane for making carbon foam with fireproofing and anti-ablation properties. *Materials and Design*, *101*, 332–339. https://doi.org/10.1016/j.matdes.2016.04.008

70 Farhan, S., Wang, R., Jiang, H., Li, K., & Wang, C. (2016). A novel combination of simple foaming and freeze-drying processes for making carbon foam containing multiwalled carbon nanotubes. *Ceramics International*, *42*(7), 8980–8989. https://doi.org/10.1016/j.ceramint.2016.01.131

71 Farhan, S., Wang, R., & Li, K. (2016). Electromagnetic interference shielding effectiveness of carbon foam containing in situ grown silicon carbide nanowires. *Ceramics International*, *42*(9), 11330–11340. https://doi.org/10.1016/j.ceramint.2016.04.054

72 Farhan, S., Wang, R., & Zhang, D. (2017). Carbon foam with channel like pores prepared from reactive blended allyl novolac with bismaleimide using different cross-linking initiators. *Journal of Analytical and Applied Pyrolysis*, *125*, 328–334. https://doi.org/10.1016/j.jaap.2017.03.008

73 Ferraro, C., Garcia-Tunon, E., Barg, S., Miranda, M., Ni, N., Bell, R., & Saiz, E. (2018). SiC porous structures obtained with innovative shaping technologies. *Journal of the European Ceramic Society*, *38*(3), 823–835. https://doi.org/10.1016/j.jeurceramsoc.2017.09.048

74 Fitzgerald, T. J., Michaud, V. J., & Mortensen, A. (2005). Processing of microcellular SiC foams. *Journal of Materials Science*, *30*(4), 1037–1045. https://doi.org/10.1007/bf01178442

75 Focke, W. W., Badenhorst, H., Ramjee, S., Kruger, H. J., Van Schalkwyk, R., & Rand, B. (2014). Graphite foam from pitch and expandable graphite. *Carbon*, *73*, 41–50. https://doi.org/10.1016/j.carbon.2014.02.035

76 Frind, R., Oschatz, M., & Kaskel, S. (2011). Polymerization of polycarbosilanes in high internal phase emulsions for the synthesis of macroporous silicon carbide catalysts (polyHIPE-SiC). *Journal of Materials Chemistry*, *21*(32), 11936–11940. https://doi.org/10.1039/c1jm10612k

77 Fu, L., Qi, G., Sahore, R., Sougrat, R., DiSalvo, F. J., & Giannelis, E. P. (2013). Facile synthesis and application of a carbon foam with large mesopores. *Physical Chemistry Chemical Physics*, *15*(44), 19134–19137. https://doi.org/10.1039/C3CP53246A

78 Fu, R., Baumann, T. F., Cronin, S., Dresselhaus, G., Dresselhaus, M. S., & Satcher, J. H. (2005). Formation of Graphitic Structures in Cobalt- and Nickel-Doped Carbon Aerogels. *Langmuir*, *21*(7), 2647–2651. https://doi.org/10.1021/la047344d

79 Fukushima, M., & Colombo, P. (2012). Silicon carbide-based foams from direct blowing of polycarbosilane. *Journal of the European Ceramic Society*, *32*(2), 503–510. https://doi.org/10.1016/j.jeurceramsoc.2011.09.009

80 Fukushima, M., Nakata, M., Zhou, Y., Ohji, T., & Yoshizawa, Y. (2010). Fabrication and properties of ultra highly porous silicon carbide by the gelation–freezing method. *Journal of the European Ceramic Society*, *30*(14), 2889–2896. https://doi.org/10.1016/j.jeurceramsoc.2010.03.018

81 Gallego, N. C., & Klett, J. W. (2003). Carbon foams for thermal management. *Carbon*, *41*(7), 1461–1466. https://doi.org/10.1016/S0008-6223(03)00091-5

82 Gandini, A. (1989). 19 - Polymers From Renewable Resources. In G. Allen & J. C. B. T.-C. P. S. and S. Bevington (Eds.) (pp. 527–573). Amsterdam: Pergamon. https://doi.org/10.1016/B978-0-08-096701-1.00237-8

83 Gao, N., Cheng, B., Hou, H., & Zhang, R. (2018). Mesophase pitch based carbon foams as sound absorbers. *Materials Letters*, *212*, 243–246. https://doi.org/10.1016/j.matlet.2017.10.074

84 Garner, R. (2018). Cutting-Edge Heat Shield Installed on NASA's Parker Solar Probe. Retrieved January 16, 2020, from http://parkersolarprobe.jhuapl.edu

85 Ge, H., Wang, G., Yuan, B., Dong, B., & Li, H. (2014). Fabrication and microstructure of porous SiC ceramics using suspension emulsions as pore-forming agents. *Ceramics International*, *40*(8, Part A), 11705–11711. https://doi.org/10.1016/j.ceramint.2014.03.182

86 Ghani, M., Maya, F., & Cerdà, V. (2016). Automated solid-phase extraction of organic pollutants using melamine–formaldehyde polymer-derived carbon foams. *RSC Advances*, *6*(54), 48558–48565. https://doi.org/10.1039/C6RA08230K

87 Gianella, S., Gaia, D., & Ortona, A. (2012). High Temperature Applications of Si-SiC Cellular Ceramics. *Advanced Engineering Materials*, *14*(12), 1074–1081. https://doi.org/10.1002/adem.201200012

88 Gibson, L. J., & Ashby, M. F. (1997). *Cellular Solids: Structure and Properties*. *Cambridge Solid State Science Series* (2nd ed.). Cambridge: Cambridge University Press. https://doi.org/DOI: 10.1017/CBO9781139878326

89 Greil, P., Lifka, T., & Kaindl, A. (1998). Biomorphic Cellular Silicon Carbide Ceramics from Wood: I. Processing and Microstructure. *Journal of the European Ceramic Society*, *18*(14), 1961–1973. https://doi.org/10.1016/S0955-2219(98)00156-3

90 Gross, A. F., & Nowak, A. P. (2010). Hierarchical Carbon Foams with Independently Tunable Mesopore and Macropore Size Distributions. *Langmuir*, *26*(13), 11378–11383. https://doi.org/10.1021/la1007846

91 Guo, S., Peng, J., Li, W., Yang, K., Zhang, L., Zhang, S., & Xia, H. (2009). Effects of CO2 activation on porous structures of coconut shell-based activated carbons. *Applied Surface Science*, *255*(20), 8443–8449. https://doi.org/10.1016/j.apsusc.2009.05.150

92 Gupta, S., & Tai, N.-H. (2016). Carbon materials as oil sorbents: a review on the synthesis and performance. *Journal of Materials Chemistry A*, *4*(5), 1550–1565. https://doi.org/10.1039/C5TA08321D

93 Han, M. S., Choi, S. J., Kim, J. M., Kim, Y. H., Kim, W. N., Lee, H. S., & Sung, J. Y. (2009). Effects of silicone surfactant on the cell size and thermal

conductivity of rigid polyurethane foams by environmentally friendly blowing agents. *Macromolecular Research*, *17*(1), 44–50. https://doi.org/10.1007/BF03218600

94 Hao, G. P., Li, W. C., Qian, D., Wang, G. H., Zhang, W. P., Zhang, T., … Lu, A. H. (2011). Structurally designed synthesis of mechanically stable poly(benzoxazine-co- resol)-based porous carbon monoliths and their application as high-performance CO2 capture sorbents. *Journal of the American Chemical Society*, *133*(29), 11378–11388. https://doi.org/10.1021/ja203857g

95 Hasegawa, G., Ishihara, Y., Kanamori, K., Miyazaki, K., Yamada, Y., Nakanishi, K., & Abe, T. (2011). Facile Preparation of Monolithic LiFePO4/Carbon Composites with Well-Defined Macropores for a Lithium-Ion Battery. *Chemistry of Materials*, *23*(23), 5208–5216. https://doi.org/10.1021/cm2021438

96 He, X., Male, K. B., Nesterenko, P. N., Brabazon, D., Paull, B., & Luong, J. H. T. (2013). Adsorption and Desorption of Methylene Blue on Porous Carbon Monoliths and Nanocrystalline Cellulose. *ACS Applied Materials & Interfaces*, *5*(17), 8796–8804. https://doi.org/10.1021/am403222u

97 Herzog, A., Klingner, R., Vogt, U., & Graule, T. (2004). Wood-Derived Porous SiC Ceramics by Sol Infiltration and Carbothermal Reduction. *Journal of the American Ceramic Society*, *87*(5), 784–793. https://doi.org/10.1111/j.1551-2916.2004.00784.x

98 Hossain, S. S., Sarkar, S., Oraon, N. K., & Ranjan, A. (2016). Pre-ceramic polymer-derived open/closed cell silicon carbide foam: microstructure, phase evaluation, and thermal properties. *Journal of Materials Science*, *51*(21), 9865–9878. https://doi.org/10.1007/s10853-016-0220-1

99 Hu, C., Xue, J., Dong, L., Jiang, Y., Wang, X., Qu, L., & Dai, L. (2016). Scalable Preparation of Multifunctional Fire-Retardant Ultralight Graphene Foams. *ACS Nano*, *10*(1), 1325–1332. https://doi.org/10.1021/acsnano.5b06710

100 Imoto, K., Takahashi, K., Yamaguchi, T., Komura, T., Nakamura, J., & Murata, K. (2003). High-performance carbon counter electrode for dye-sensitized solar cells. *Solar Energy Materials and Solar Cells*, *79*(4), 459–469. https://doi.org/10.1016/S0927-0248(03)00021-7

101 Inagaki, M., Morishita, T., Kuno, A., Kito, T., Hirano, M., Suwa, T., & Kusakawa, K. (2004). Carbon foams prepared from polyimide using urethane foam template. *Carbon*, *42*(3), 497–502. https://doi.org/10.1016/j.carbon.2003.12.080

102 Inagaki, M., Qiu, J., & Guo, Q. (2015). Carbon foam: Preparation and application. *Carbon*, *87*, 128–152. https://doi.org/10.1016/j.carbon.2015.02.021

103 Inagaki, M., Toyoda, M., Soneda, Y., Tsujimura, S., & Morishita, T. (2016). Templated mesoporous carbons: Synthesis and applications. *Carbon*, *107*, 448–473. https://doi.org/10.1016/j.carbon.2016.06.003

104 Jana, D. C., Sundararajan, G., & Chattopadhyay, K. (2017). Effect of Porosity on Structure, Young's Modulus, and Thermal Conductivity of SiC Foams by Direct Foaming and Gelcasting. *Journal of the American Ceramic Society*, *100*(1), 312–322. https://doi.org/10.1111/jace.14544

105 Jana, P., Fierro, V., & Celzard, A. (2013). Ultralow cost reticulated carbon foams from household cleaning pad wastes. *Carbon*, *62*, 517–520. https://doi.org/10.1016/j.carbon.2013.06.020

106 Jana, P., Fierro, V., & Celzard, A. (2016). Sucrose-based carbon foams with enhanced thermal conductivity. *Industrial Crops and Products*, *89*, 498–506. https://doi.org/10.1016/j.indcrop.2016.06.001

107 Jana, P., Fierro, V., Pizzi, A., & Celzard, A. (2014). Biomass-derived, thermally conducting, carbon foams for seasonal thermal storage. *Biomass and Bioenergy*, *67*, 312–318. https://doi.org/10.1016/j.biombioe.2014.04.031

108 Jana, P., Fierro, V., Pizzi, A., & Celzard, A. (2015). Thermal conductivity improvement of composite carbon foams based on tannin-based disordered carbon matrix and graphite fillers. *Materials & Design*, *83*, 635–643. https://doi.org/10.1016/j.matdes.2015.06.057

109 Jana, P., Palomo del Barrio, E., Fierro, V., Medjahdi, G., & Celzard, A. (2016). Design of carbon foams for seasonal solar thermal energy storage. *Carbon*, *109*, 771–787. https://doi.org/10.1016/j.carbon.2016.08.048

110 Jang, W. Y., Park, J. G., Basnet, B., Woo, K. T., Han, I. S., & Kim, I. J. (2017). Highly porous SiC ceramics from particle-stabilized suspension. *Journal of the Australian Ceramic Society*, *53*(2), 657–665. https://doi.org/10.1007/s41779-017-0077-z

111 Ji, C., Zhang, K., Li, L., Chen, X., Hu, J., Yan, D., … He, X. (2017). High performance graphene-based foam fabricated by a facile approach for oil absorption. *Journal of Materials Chemistry A*, *5*(22), 11263–11270. https://doi.org/10.1039/C7TA02613G

112 Ji, H., Sellan, D. P., Pettes, M. T., Kong, X., Ji, J., Shi, L., & Ruoff, R. S. (2014). Enhanced thermal conductivity of phase change materials with ultrathin-graphite foams for thermal energy storage. *Energy & Environmental Science*, *7*(3), 1185–1192. https://doi.org/10.1039/C3EE42573H

113 Ji, H., Zhang, L., Pettes, M. T., Li, H., Chen, S., Shi, L., … Ruoff, R. S. (2012). Ultrathin Graphite Foam: A Three-Dimensional Conductive Network

for Battery Electrodes. *Nano Letters*, *12*(5), 2446–2451. https://doi.org/10.1021/nl300528p

114 Jiang, W., Xin, H., & Li, W. (2016). Microcellular 3D graphene foam via chemical vapor deposition of electroless plated nickel foam templates. *Materials Letters*, *162*, 105–109. https://doi.org/10.1016/j.matlet.2015.09.118

115 Jiao, Y., Jiang, C., Yang, Z., & Zhang, J. (2012). Controllable synthesis of ZSM-5 coatings on SiC foam support for MTP application. *Microporous and Mesoporous Materials*, *162*, 152–158. https://doi.org/10.1016/j.micromeso.2012.05.034

116 Jiao, Y., Yang, X., Jiang, C., Tian, C., Yang, Z., & Zhang, J. (2015). Hierarchical ZSM-5/SiC nano-whisker/SiC foam composites: Preparation and application in MTP reactions. *Journal of Catalysis*, *332*, 70–76. https://doi.org/10.1016/j.jcat.2015.09.002

117 Kamal, M. M., & Mohamad, A. A. (2005). Enhanced radiation output from foam burners operating with a nonpremixed flame. *Combustion and Flame*, *140*(3), 233–248. https://doi.org/10.1016/j.combustflame.2004.12.001

118 Karthik, M., Faik, A., Doppiu, S., Roddatis, V., & D'Aguanno, B. (2015). A simple approach for fabrication of interconnected graphitized macroporous carbon foam with uniform mesopore walls by using hydrothermal method. *Carbon*, *87*(C), 434–443. https://doi.org/10.1016/j.carbon.2015.02.060

119 Karthik, M., Faik, A., Blanco-Rodríguez, P., Rodríguez-Aseguinolaza, J., & D'Aguanno, B. (2015). Preparation of erythritol–graphite foam phase change composite with enhanced thermal conductivity for thermal energy storage applications. *Carbon*, *94*, 266–276. https://doi.org/10.1016/j.carbon.2015.06.075

120 Karthik, M., Faik, A., Doppiu, S., Roddatis, V., & D'Aguanno, B. (2015). A simple approach for fabrication of interconnected graphitized macroporous carbon foam with uniform mesopore walls by using hydrothermal method. *Carbon*, *87*, 434–443. https://doi.org/10.1016/j.carbon.2015.02.060

121 Karthik, M., Faik, A., & D'Aguanno, B. (2017). Graphite foam as interpenetrating matrices for phase change paraffin wax: A candidate composite for low temperature thermal energy storage. *Solar Energy Materials and Solar Cells*, *172*, 324–334. https://doi.org/10.1016/j.solmat.2017.08.004

122 Kenisarin, M. M. (2014). Thermophysical properties of some organic phase change materials for latent heat storage. A review. *Solar Energy*, *107*, 553–575. https://doi.org/10.1016/j.solener.2014.05.001

123 Kershaw, J. R., & Black, K. J. T. (1993). Structural Characterization of Coal-Tar and Petroleum Pitches. *Energy and Fuels*, *7*(3), 420–425. https://doi.org/10.1021/ef00039a014

124 Khan, M., Tiehu, L., Zhao, T. K., Ali, Z., Malik, A., Khan, A., … Xiong, C. (2017). Effect of multi walled carbon nanotubes and diamond nanoparticles on the structure and properties of carbon foams. *Diamond and Related Materials*, *79*, 119–126. https://doi.org/10.1016/j.diamond.2017.09.008

125 Kharisov, B. I., & Kharissova, O. V. (2019). General Data on Carbon Allotropes BT - Carbon Allotropes: Metal-Complex Chemistry, Properties and Applications. In B. I. Kharisov & O. V. Kharissova (Eds.) (pp. 1–8). Cham: Springer International Publishing. https://doi.org/10.1007/978-3-030-03505-1_1

126 Kholmanov, I., Kim, J., Ou, E., Ruoff, R. S., & Shi, L. (2015). Continuous Carbon Nanotube–Ultrathin Graphite Hybrid Foams for Increased Thermal Conductivity and Suppressed Subcooling in Composite Phase Change Materials. *ACS Nano*, *9*(12), 11699–11707. https://doi.org/10.1021/acsnano.5b02917

127 Kim, K., Kwon, Y., Lee, T., Cho, S. J., & Ryoo, R. (2017). Facile large-scale synthesis of three-dimensional graphene-like ordered microporous carbon via ethylene carbonization in CaX zeolite template. *Carbon*, *118*, 517–523. https://doi.org/10.1016/j.carbon.2017.03.082

128 Kim, Y. W., Eom, J.-H., Wang, C., & Park, C. B. (2008). Processing of Porous Silicon Carbide Ceramics from Carbon-Filled Polysiloxane by Extrusion and Carbothermal Reduction. *Journal of the American Ceramic Society*, *91*(4), 1361–1364. https://doi.org/10.1111/j.1551-2916.2008.02280.x

129 Kim, Y. W., Kim, S.-H., Song, I.-H., Kim, H.-D., & Park, C. B. (2005). Fabrication of Open-Cell, Microcellular Silicon Carbide Ceramics by Carbothermal Reduction. *Journal of the American Ceramic Society*, *88*(10), 2949–2951. https://doi.org/10.1111/j.1551-2916.2005.00509.x

130 Kim, Y. W., Kim, S.-H., Wang, C., & Park, C. B. (2003). Fabrication of Microcellular Ceramics Using Gaseous Carbon Dioxide. *Journal of the American Ceramic Society*, *86*(12), 2231–2233. https://doi.org/10.1111/j.1151-2916.2003.tb03641.x

131 Kim, Y. W., & Park, C. B. (2003). Processing of microcellular preceramics using carbon dioxide. *Composites Science and Technology*, *63*(16), 2371–2377. https://doi.org/10.1016/S0266-3538(03)00270-7

132 Kim, Y. W., Kim, S. H., Song, I. H., Kim, H. D., & Park, C. B. (2005). Fabrication of open-cell, microcellular silicon carbide ceramics by carbothermal reduction. *Journal of the American Ceramic Society*. https://doi.org/10.1111/j.1551-2916.2005.00509.x

133 Kim, Y. W., Kim, H. D., & Park, C. B. (2005). Processing of microcellular mullite. *Journal of the American Ceramic Society*, *88*(12), 3311–3315. https://doi.org/10.1111/j.1551-2916.2005.00597.x

134 Klett, J., Hardy, R., Romine, E., Walls, C., & Burchell, T. (2000). High-thermal-conductivity, mesophase-pitch-derived carbon foams: effect of precursor on structure and properties. *Carbon*, *38*(7), 953–973. https://doi.org/10.1016/S0008-6223(99)00190-6

135 Klett, J. W., McMillan, A. D., Gallego, N. C., & Walls, C. A. (2004). The role of structure on the thermal properties of graphitic foams. *Journal of Materials Science*, *39*(11), 3659–3676. https://doi.org/10.1023/B:JMSC.0000030719.80262.f8

136 Koh, Y.-H., Lee, E.-J., Yoon, B.-H., Song, J.-H., Kim, H.-E., & Kim, H.-W. (2006). Effect of Polystyrene Addition on Freeze Casting of Ceramic/Camphene Slurry for Ultra-High Porosity Ceramics with Aligned Pore Channels. *Journal of the American Ceramic Society*, *89*(12), 3646–3653. https://doi.org/10.1111/j.1551-2916.2006.01311.x

137 Koskun, Y., Şavk, A., Şen, B., & Şen, F. (2018). Highly sensitive glucose sensor based on monodisperse palladium nickel/activated carbon nanocomposites. *Analytica Chimica Acta*, *1010*, 37–43. https://doi.org/10.1016/j.aca.2018.01.035

138 Kultayeva, S., Ha, J.-H., Malik, R., Kim, Y.-W., & Kim, K. J. (2019). Effects of porosity on electrical and thermal conductivities of porous SiC ceramics. *Journal of the European Ceramic Society*. https://doi.org/10.1016/j.jeurceramsoc.2019.11.045

139 Kumar, R, Singh, A. P., Chand, M., Pant, R. P., Kotnala, R. K., Dhawan, S. K., … Dhakate, S. R. (2014). Improved microwave absorption in lightweight resin-based carbon foam by decorating with magnetic and dielectric nanoparticles. *RSC Advances*, *4*(45), 23476–23484. https://doi.org/10.1039/C4RA01731E

140 Kumar, R., Dhakate, S. R., Gupta, T., Saini, P., Singh, B. P., & Mathur, R. B. (2013). Effective improvement of the properties of light weight carbon foam by decoration with multi-wall carbon nanotubes. *Journal of Materials Chemistry A*, *1*(18), 5727–5735. https://doi.org/10.1039/C3TA10604G

141 Kumar, R., Dhakate, S. R., & Mathur, R. B. (2013). The role of ferrocene on the enhancement of the mechanical and electrochemical properties of coal tar pitch-based carbon foams. *Journal of Materials Science*, *48*(20), 7071–7080. https://doi.org/10.1007/s10853-013-7518-z

142 Kumar, Rajeev, Dhakate, S. R., Saini, P., & Mathur, R. B. (2013). Improved electromagnetic interference shielding effectiveness of light weight carbon

foam by ferrocene accumulation. *RSC Advances*, *3*(13), 4145–4151. https://doi.org/10.1039/c3ra00121k

143 Kumar, R., Jain, H., Chaudhary, A., Kumari, S., Mondal, D. P., & Srivastava, A. K. (2019). Thermal conductivity and fire-retardant response in graphite foam made from coal tar pitch derived semi coke. *Composites Part B: Engineering*, *172*, 121–130. https://doi.org/10.1016/j.compositesb.2019.05.036

144 Kumar, R., Kumari, S., Mathur, R. B., & Dhakate, S. R. (2015). Nanostructuring effect of multi-walled carbon nanotubes on electrochemical properties of carbon foam as constructive electrode for lead acid battery. *Applied Nanoscience*, *5*(1), 53–61. https://doi.org/10.1007/s13204-014-0291-8

145 Lafdi, K., Mesalhy, O., & Elgafy, A. (2008). Graphite foams infiltrated with phase change materials as alternative materials for space and terrestrial thermal energy storage applications. *Carbon*, *46*(1), 159–168. https://doi.org/10.1016/j.carbon.2007.11.003

146 Lafdi, K., Mesalhy, O., & Shaikh, S. (2007). The effect of surface energy on the heat transfer enhancement of paraffin wax/carbon foam composites. *Carbon*, *45*(11), 2188–2194. https://doi.org/10.1016/j.carbon.2007.06.055

147 Ledoux, M. J., & Pham-Huu, C. (2001). Silicon Carbide: A Novel Catalyst Support for Heterogeneous Catalysis. *CATTECH*, *5*(4), 226–246. https://doi.org/10.1023/A:1014092930183

148 Lee, J., Han, S., & Hyeon, T. (2004). Synthesis of new nanoporous carbon materials using nanostructured silica materials as templates. *Journal of Materials Chemistry*, *14*(4), 478–486. https://doi.org/10.1039/B311541K

149 Lee, J., Kim, J., & Hyeon, T. (2006). Recent progress in the synthesis of porous carbon materials. *Advanced Materials*, *18*(16), 2073–2094. https://doi.org/10.1002/adma.200501576

150 Lee, K. T., Lytle, J. C., Ergang, N. S., Oh, S. M., & Stein, A. (2005). Synthesis and Rate Performance of Monolithic Macroporous Carbon Electrodes for Lithium-Ion Secondary Batteries. *Advanced Functional Materials*, *15*(4), 547–556. https://doi.org/10.1002/adfm.200400186

151 Lei, S., Guo, Q., Shi, J., & Liu, L. (2010). Preparation of phenolic-based carbon foam with controllable pore structure and high compressive strength. *Carbon*, *48*(9), 2644–2646. https://doi.org/10.1016/j.carbon.2010.03.017

152 Letellier, M., Delgado-Sanchez, C., Khelifa, M., Fierro, V., & Celzard, A. (2017). Mechanical properties of model vitreous carbon foams. *Carbon*, *116*, 562–571. https://doi.org/10.1016/j.carbon.2017.02.020

153 Letellier, M., Macutkevic, J., Kuzhir, P., Banys, J., Fierro, V., & Celzard, A. (2017). Electromagnetic properties of model vitreous carbon foams. *Carbon*, *122*, 217–227. https://doi.org/10.1016/j.carbon.2017.06.080

154 Letellier, M., Macutkevic, J., Paddubskaya, A., Klochkov, A., Kuzhir, P., Banys, J., … Celzard, A. (2015). Microwave Dielectric Properties of Tannin-Based Carbon Foams. *Ferroelectrics*, *479*(1), 119–126. https://doi.org/10.1080/00150193.2015.1012036

155 Letellier, M., Macutkevic, J., Paddubskaya, A., Plyushch, A., Kuzhir, P., Ivanov, M., … Celzard, A. (2015). Tannin-Based Carbon Foams for Electromagnetic Applications. *IEEE Transactions on Electromagnetic Compatibility*, *57*(5), 989–995. https://doi.org/10.1109/TEMC.2015.2430370

156 Li, B., Liu, T., Hu, L., Wang, Y., & Gao, L. (2013). Fabrication and properties of microencapsulated paraffin@SiO2phase change composite for thermal energy storage. *ACS Sustainable Chemistry and Engineering*, *1*(3), 374–380. https://doi.org/10.1021/sc300082m

157 Li, J., Yuan, W., Deng, C., & Zhu, H. (2017). Porous SiC/SiCN composite ceramics fabricated by foaming and reaction sintering. *Journal of the European Ceramic Society*, *37*(3), 1131–1134. https://doi.org/10.1016/j.jeurceramsoc.2016.10.025

158 Li, M. Z., Jia, L. C., Zhang, X. P., Yan, D. X., Zhang, Q. C., & Li, Z. M. (2018). Robust carbon nanotube foam for efficient electromagnetic interference shielding and microwave absorption. *Journal of Colloid and Interface Science*, *530*, 113–119. https://doi.org/10.1016/j.jcis.2018.06.052

159 Li, Q., Chen, L., Ding, J., Zhang, J., Li, X., Zheng, K., … Tian, X. (2016). Open-cell phenolic carbon foam and electromagnetic interference shielding properties. *Carbon*, *104*, 90–105. https://doi.org/10.1016/j.carbon.2016.03.055

160 Li, Q., Yin, X., Duan, W., Kong, L., Hao, B., & Ye, F. (2013). Electrical, dielectric and microwave-absorption properties of polymer derived SiC ceramics in X band. *Journal of Alloys and Compounds*, *565*, 66–72. https://doi.org/10.1016/j.jallcom.2013.02.176

161 Li, S., Guo, Q., Song, Y., Shi, J., & Liu, L. (2010). Effects of pitch fluoride on the thermal conductivity of carbon foam derived from mesophase pitch. *Carbon*, *48*(4), 1316–1318. https://doi.org/10.1016/j.carbon.2009.08.004

162 Li, S., Song, Y., Song, Y., Shi, J., Liu, L., Wei, X., & Guo, Q. (2007). Carbon foams with high compressive strength derived from mixtures of mesocarbon microbeads and mesophase pitch. *Carbon*, *45*(10), 2092–2097. https://doi.org/10.1016/j.carbon.2007.05.014

163 Li, S., Tian, Y., Zhong, Y., Yan, X., Song, Y., Guo, Q., … Liu, L. (2011). Formation mechanism of carbon foams derived from mesophase pitch. *Carbon*, *49*(2), 618–624. https://doi.org/10.1016/j.carbon.2010.10.007

164 Li, W. Q., Zhang, H. B., & Xiong, X. (2011). Properties of multi-walled carbon nanotube reinforced carbon foam composites. *Journal of Materials Science*, *46*(4), 1143–1146. https://doi.org/10.1007/s10853-010-5099-7

165 Li, X., Basso, M. C., Braghiroli, F. L., Fierro, V., Pizzi, A., & Celzard, A. (2012). Tailoring the structure of cellular vitreous carbon foams. *Carbon*, *50*(5), 2026–2036. https://doi.org/10.1016/j.carbon.2012.01.004

166 Li, Y. Q., Samad, Y. A., Polychronopoulou, K., & Liao, K. (2015). Lightweight and Highly Conductive Aerogel-like Carbon from Sugarcane with Superior Mechanical and EMI Shielding Properties. *ACS Sustainable Chemistry and Engineering*, *3*(7), 1419–1427. https://doi.org/10.1021/acssuschemeng.5b00340

167 Li, Y., Shen, B., Pei, X., Zhang, Y., Yi, D., Zhai, W., … Zheng, W. (2016). Ultrathin carbon foams for effective electromagnetic interference shielding. *Carbon*, *100*, 375–385. https://doi.org/10.1016/j.carbon.2016.01.030

168 Li, Z. Q., Lu, C. J., Xia, Z. P., Zhou, Y., & Luo, Z. (2007). X-ray diffraction patterns of graphite and turbostratic carbon. *Carbon*, *45*(8), 1686–1695. https://doi.org/10.1016/j.carbon.2007.03.038

169 Liang, B., Guo, S., Zhao, Y., Khan, I. U., Zhang, X., Li, K., & Lv, C. (2020). Single iron atoms anchored on activated carbon as active centres for highly efficient oxygen reduction reaction in air-cathode microbial fuel cell. *Journal of Power Sources*, *450*, 227683. https://doi.org/10.1016/j.jpowsour.2019.227683

170 Liang, C., & Wang, Z. (2019). Eggplant-derived SiC aerogels with high-performance electromagnetic wave absorption and thermal insulation properties. *Chemical Engineering Journal*, *373*, 598–605. https://doi.org/10.1016/j.cej.2019.05.076

171 Liang, C., Wang, Z., Wu, L., Zhang, X., Wang, H., & Wang, Z. (2017). Light and Strong Hierarchical Porous SiC Foam for Efficient Electromagnetic Interference Shielding and Thermal Insulation at Elevated Temperatures. *ACS Applied Materials and Interfaces*, *9*(35), 29950–29957. https://doi.org/10.1021/acsami.7b07735

172 Liang, C., & Dai, S. (2006). Synthesis of Mesoporous Carbon Materials via Enhanced Hydrogen-Bonding Interaction. *Journal of the American Chemical Society*, *128*(16), 5316–5317. https://doi.org/10.1021/ja060242k

173 Liang, C., Dai, S., & Guiochon, G. (2003). A Graphitized-Carbon Monolithic Column. *Analytical Chemistry*, *75*(18), 4904–4912. https://doi.org/10.1021/ac030146r

174 Liang, C., Hong, K., Guiochon, G. A., Mays, J. W., & Dai, S. (2004). Synthesis of a Large-Scale Highly Ordered Porous Carbon Film by Self-Assembly of Block Copolymers. *Angewandte Chemie International Edition*, *43*(43), 5785–5789. https://doi.org/10.1002/anie.200461051

175 Lignin - American Chemical Society. (n.d.). Retrieved February 10, 2020, from https://www.acs.org/content/acs/en/molecule-of-the-week/archive/l/lignin.html

176 Lim, K. Y., Kim, Y. W., & Song, I. H. (2013). Porous sodium borate-bonded SiC ceramics. *Ceramics International*, *39*(6), 6827–6834. https://doi.org/10.1016/j.ceramint.2013.02.014

177 Lin, Q., Luo, B., Qu, L., Fang, C., & Chen, Z. (2013). Direct preparation of carbon foam by pyrolysis of cyanate ester resin at ambient pressure. *Journal of Analytical and Applied Pyrolysis*, *104*, 714–717. https://doi.org/10.1016/j.jaap.2013.05.007

178 Lin, Q., Qu, L., Luo, B., Fang, C., & Luo, K. (2014). Preparation and properties of multiwall carbon nanotubes/carbon foam composites. *Journal of Analytical and Applied Pyrolysis*, *105*, 177–182. https://doi.org/10.1016/j.jaap.2013.11.002

179 Lin, S. C., & Al-Kayiem, H. H. (2016). Evaluation of copper nanoparticles – Paraffin wax compositions for solar thermal energy storage. *Solar Energy*, *132*, 267–278. https://doi.org/10.1016/j.solener.2016.03.004

180 Lin, Y., Jia, Y., Alva, G., & Fang, G. (2018). Review on thermal conductivity enhancement, thermal properties and applications of phase change materials in thermal energy storage. *Renewable and Sustainable Energy Reviews*, *82*, 2730–2742. https://doi.org/10.1016/j.rser.2017.10.002

181 Lin, Y. R., Du, J. H., Wu, W., Chow, L. C., & Notardonato, W. (2010). Experimental Study on Heat Transfer and Pressure Drop of Recuperative Heat Exchangers Using Carbon Foam. *Journal of Heat Transfer*, *132*(9). https://doi.org/10.1115/1.4001625

182 Liu, H., Tian, H., & Cheng, H. (2013). Dielectric properties of SiC fiber-reinforced SiC matrix composites in the temperature range from 25 to 700 °C at frequencies between 8.2 and 18 GHz. *Journal of Nuclear Materials*, *432*(1–3), 57–60. https://doi.org/10.1016/j.jnucmat.2012.08.026

183 Liu, Heguang, Li, T., Huang, T., & Zhao, X. (2015). Effect of multi-walled carbon nanotube additive on the microstructure and properties of pitch-derived carbon foams. *Journal of Materials Science*, *50*(23), 7583–7590. https://doi.org/10.1007/s10853-015-9314-4

184 Liu, H., Wu, J., Zhuang, Q., Dang, A., Li, T., & Zhao, T. (2016). Preparation and the electromagnetic interference shielding in the X-band of carbon foams

with Ni-Zn ferrite additive. *Journal of the European Ceramic Society*, *36*(16), 3939–3946. https://doi.org/10.1016/j.jeurceramsoc.2016.06.017

185 Liu, J., Liu, X., Sun, Y., Sun, C., Liu, H., Stevens, L. A., … Snape, C. E. (2018). High Density and Super Ultra-Microporous-Activated Carbon Macrospheres with High Volumetric Capacity for CO 2 Capture . *Advanced Sustainable Systems*, *2*(2), 1700115. https://doi.org/10.1002/adsu.201700115

186 Liu, M., Gan, L., Zhao, F., Fan, X., Xu, H., Wu, F., … Chen, L. (2007). Carbon foams with high compressive strength derived from polyarylacetylene resin. *Carbon*, *45*(15), 3055–3057. https://doi.org/10.1016/j.carbon.2007.10.003

187 Lorjai, P., Wongkasemjit, S., & Chaisuwan, T. (2009). Preparation of polybenzoxazine foam and its transformation to carbon foam. *Materials Science and Engineering A*, *527*(1–2), 77–84. https://doi.org/10.1016/j.msea.2009.07.032

188 Lua, A. C., & Guo, J. (2000). Activated carbon prepared from oil palm stone by one-step CO2 activation for gaseous pollutant removal. *Carbon*, *38*(7), 1089–1097. https://doi.org/10.1016/S0008-6223(99)00231-6

189 Luo, R., Ni, Y., Li, J., Yang, C., & Wang, S. (2011). The mechanical and thermal insulating properties of resin-derived carbon foams reinforced by K2Ti6O13 whiskers. *Materials Science and Engineering: A*, *528*(4), 2023–2027. https://doi.org/10.1016/j.msea.2010.10.106

190 Ma, Z., Kyotani, T., Liu, Z., Terasaki, O., & Tomita, A. (2001). Very High Surface Area Microporous Carbon with a Three-Dimensional Nano-Array Structure: Synthesis and Its Molecular Structure. *Chemistry of Materials*, *13*(12), 4413–4415. https://doi.org/10.1021/cm010730l

191 Ma, Z., Kyotani, T., & Tomita, A. (2002). Synthesis methods for preparing microporous carbons with a structural regularity of zeolite Y. *Carbon*, *40*(13), 2367–2374. https://doi.org/10.1016/S0008-6223(02)00120-3

192 Maldonado-Hódar, F. J., Moreno-Castilla, C., Rivera-Utrilla, J., Hanzawa, Y., & Yamada, Y. (2000). Catalytic Graphitization of Carbon Aerogels by Transition Metals. *Langmuir*, *16*(9), 4367–4373. https://doi.org/10.1021/la991080r

193 Manawi, M. Y., Ihsanullah, Samara, A., Al-Ansari, T., & Atieh, A. M. (2018). A Review of Carbon Nanomaterials’ Synthesis via the Chemical Vapor Deposition (CVD) Method. *Materials.* https://doi.org/10.3390/ma11050822

194 Matthews, S., Edirisinghe, M. J., & Folkes, M. J. (1999). Effect of pre-pyrolysis heat treatment on the preparation of silicon carbide from a polycarbosilane precursor. *Ceramics International*, *25*(1), 49–60. https://doi.org/10.1016/S0272-8842(97)00088-6

195 McEnaney, B. (1999). Structure and Bonding in Carbon Materials. In T. D. B. T.-C. M. for A. T. Burchell (Ed.), *Carbon Materials for Advanced Technologies* (pp. 1–33). Oxford: Elsevier Science Ltd. https://doi.org/10.1016/b978-008042683-9/50003-0

196 Mesalhy, O., Lafdi, K., & Elgafy, A. (2006). Carbon foam matrices saturated with PCM for thermal protection purposes. *Carbon*, *44*(10), 2080–2088. https://doi.org/10.1016/j.carbon.2005.12.019

197 Mi, H.-Y., Jing, X., Politowicz, A. L., Chen, E., Huang, H.-X., & Turng, L.-S. (2018). Highly compressible ultra-light anisotropic cellulose/graphene aerogel fabricated by bidirectional freeze drying for selective oil absorption. *Carbon*, *132*, 199–209. https://doi.org/10.1016/j.carbon.2018.02.033

198 Ming, J., Wu, Y., Liang, G., Park, J.-B., Zhao, F., & Sun, Y.-K. (2013). Sodium salt effect on hydrothermal carbonization of biomass: a catalyst for carbon-based nanostructured materials for lithium-ion battery applications. *Green Chemistry*, *15*(10), 2722–2726. https://doi.org/10.1039/C3GC40480C

199 Mishra, M. K., Kumar, S., Ranjan, A., & Prasad, N. E. (2018). Processing, properties and microstructure of SiC foam derived from epoxy-modified polycarbosilane. *Ceramics International*, *44*(2), 1859–1867. https://doi.org/10.1016/j.ceramint.2017.10.123

200 Mitome, T., Hirota, Y., Uchida, Y., & Nishiyama, N. (2016). Porous structure and pore size control of mesoporous carbons using a combination of a soft-templating method and a solvent evaporation technique. *Colloids and Surfaces A: Physicochemical and Engineering Aspects*, *494*, 180–185. https://doi.org/10.1016/j.colsurfa.2016.01.009

201 Moeini Sedeh, M., & Khodadadi, J. M. (2013). Thermal conductivity improvement of phase change materials/graphite foam composites. *Carbon*, *60*, 117–128. https://doi.org/10.1016/j.carbon.2013.04.004

202 Moglie, F., Micheli, D., Laurenzi, S., Marchetti, M., & Mariani Primiani, V. (2012). Electromagnetic shielding performance of carbon foams. *Carbon*, *50*(5), 1972–1980. https://doi.org/10.1016/j.carbon.2011.12.053

203 Molina-Sabio, M., Gonzalez, M. T., Rodriguez-Reinoso, F., & Sepúlveda-Escribano, A. (1996). Effect of steam and carbon dioxide activation in the micropore size distribution of activated carbon. *Carbon*, *34*(4), 505–509. https://doi.org/10.1016/0008-6223(96)00006-1

204 Moreau, L., Bindzus, W., & Hill, S. (2011). Influence of salts on starch degradation: Part II – Salt classification and caramelisation. *Starch - Stärke*, *63*(11), 676–682. https://doi.org/10.1002/star.201100032

205 Mouazer, R, Mullens, S., Thijs, I., Luyten, J., & Buekenhoudt, A. (2005). Silicon Carbide Foams by Polyurethane Replica Technique. *Advanced*

Engineering Materials, *7*(12), 1124–1128. https://doi.org/10.1002/adem.200500163

206 Mouazer, Rabah, Thijs, I., Mullens, S., & Luyten, J. (2004). SiC foams produced by gel casting: Synthesis and characterization. *Advanced Engineering Materials*, *6*(5), 340-343. https://doi.org/10.1002/adem.200400009

207 Muehleisen, R. T., Beamer, C. W., & Tinianov, B. D. (2005). Measurements and empirical model of the acoustic properties of reticulated vitreous carbon. *The Journal of the Acoustical Society of America*, *117*(2), 536–544. https://doi.org/10.1121/1.1850343

208 Mukai, S. R., Nishihara, H., Yoshida, T., Taniguchi, K., & Tamon, H. (2005). Morphology of resorcinol–formaldehyde gels obtained through ice-templating. *Carbon*, *43*(7), 1563–1565. https://doi.org/10.1016/j.carbon.2004.12.029

209 Murakami, K., Satoh, Y., Ogino, I., & Mukai, S. R. (2013). Synthesis of a Monolithic Carbon-Based Acid Catalyst with a Honeycomb Structure for Flow Reaction Systems. *Industrial & Engineering Chemistry Research*, *52*(44), 15372–15376. https://doi.org/10.1021/ie400656x

210 Nada, S. A., & Alshaer, W. G. (2015). Comprehensive parametric study of using carbon foam structures saturated with PCMs in thermal management of electronic systems. *Energy Conversion and Management*, *105*, 93–102. https://doi.org/10.1016/j.enconman.2015.07.071

211 Narasimman, R., & Prabhakaran, K. (2012). Preparation of low density carbon foams by foaming molten sucrose using an aluminium nitrate blowing agent. *Carbon*, *50*(5), 1999–2009. https://doi.org/10.1016/j.carbon.2011.12.058

212 Narasimman, R., Vijayan, S., & Prabhakaran, K. (2014). Carbon particle induced foaming of molten sucrose for the preparation of carbon foams. *Materials Science and Engineering B: Solid-State Materials for Advanced Technology*, *189*, 82–89. https://doi.org/10.1016/j.mseb.2014.08.007

213 Narasimman, R, & Prabhakaran, K. (2013). Preparation of carbon foams with enhanced oxidation resistance by foaming molten sucrose using a boric acid blowing agent. *Carbon*, *55*, 305–312. https://doi.org/10.1016/j.carbon.2012.12.068

214 Narasimman, R, Vijayan, S., Dijith, K. S., Surendran, K. P., & Prabhakaran, K. (2016). Carbon composite foams with improved strength and electromagnetic absorption from sucrose and multi-walled carbon nanotube. *Materials Chemistry and Physics*, *181*, 538–548. https://doi.org/10.1016/j.matchemphys.2016.06.091

215 Narasimman, R, Vijayan, S., & Prabhakaran, K. (2014). Carbon foam with microporous cell wall and strut for CO2 capture. *RSC Advances*, *4*(2), 578–582. https://doi.org/10.1039/C3RA46240D

216 Narasimman, R, Vijayan, S., & Prabhakaran, K. (2015). Graphene-reinforced carbon composite foams with improved strength and EMI shielding from sucrose and graphene oxide. *Journal of Materials Science*, *50*(24), 8018–8028. https://doi.org/10.1007/s10853-015-9368-3

217 Narasimman, R., Vijayan, S., & Prabhakaran, K. (2015). Effect of activated carbon particle size on the thermo-foaming of aqueous sucrose resin and properties of the carbon foams. *Journal of Materials Research*, *30*(1), 46–54. https://doi.org/DOI: 10.1557/jmr.2014.294

218 Nishihara, H., Mukai, S. R., & Tamon, H. (2004). Preparation of resorcinol–formaldehyde carbon cryogel microhoneycombs. *Carbon*, *42*(4), 899–901. https://doi.org/10.1016/j.carbon.2004.01.075

219 Ogasawara, T., Ayabe, S., Ishida, Y., Aoki, T., & Kubota, Y. (2018). Heat-resistant sandwich structure with carbon fiber-polyimide composite faces and a carbon foam core. *Composites Part A: Applied Science and Manufacturing*, *114*, 352–359. https://doi.org/10.1016/j.compositesa.2018.08.030

220 Ota, T., Takahashi, M., Hibi, T., Ozawa, M., Suzuki, S., Hikichi, Y., & Suzuki, H. (1995). Biomimetic Process for Producing SiC “Wood.” *Journal of the American Ceramic Society*, *78*(12), 3409–3411. https://doi.org/10.1111/j.1151-2916.1995.tb07988.x

221 Ou, X., Pilitsis, F., Jiao, Y., Zhang, Y., Xu, S., Jennings, M., … Fan, X. (2019). Hierarchical Fe-ZSM-5/SiC foam catalyst as the foam bed catalytic reactor (FBCR) for catalytic wet peroxide oxidation (CWPO). *Chemical Engineering Journal*, *362*, 53–62. https://doi.org/10.1016/j.cej.2019.01.019

222 Ou, X., Zhang, X., Lowe, T., Blanc, R., Rad, M. N., Wang, Y., … Fan, X. (2017). X-ray micro computed tomography characterization of cellular SiC foams for their applications in chemical engineering. *Materials Characterization*, *123*, 20–28. https://doi.org/10.1016/j.matchar.2016.11.013

223 Pan, J., Yan, X., Cheng, X., Shen, W., Li, S., & Cai, X. (2016). In situ synthesis and electrical properties of porous SiOC ceramics decorated with SiC nanowires. *Ceramics International*, *42*(10), 12345–12351. https://doi.org/10.1016/j.ceramint.2016.05.007

224 Patil, U. M., Ghorpade, R. V, Nam, M. S., Nalawade, A. C., Lee, S., Han, H., & Jun, S. C. (2016). PolyHIPE Derived Freestanding 3D Carbon Foam for Cobalt Hydroxide Nanorods Based High Performance Supercapacitor. *Scientific Reports*, *6*(1), 35490. https://doi.org/10.1038/srep35490

225 Pekala, R. W., & Hopper, R. W. (1987). Low-density microcellular carbon foams. *Journal of Materials Science*, *22*(5), 1840–1844. https://doi.org/10.1007/BF01132414

226 Pierson, H. O. (1996). 8 - Characteristics and Properties of Silicon Carbide and Boron Carbide. In H. O. B. T.-H. of R. C. and N. Pierson (Ed.) (pp. 137–155). Westwood, NJ: William Andrew Publishing. https://doi.org/10.1016/B978-081551392-6.50009-X

227 Prabhakaran, K., Singh, P. K., Gokhale, N. M., & Sharma, S. C. (2007). Processing of sucrose to low density carbon foams. *Journal of Materials Science*, *42*(11), 3894–3900. https://doi.org/10.1007/s10853-006-0481-1

228 Prakash Kumar, B. G., Shivakamy, K., Miranda, L. R., & Velan, M. (2006). Preparation of steam activated carbon from rubberwood sawdust (Hevea brasiliensis) and its adsorption kinetics. *Journal of Hazardous Materials*, *136*(3), 922–929. https://doi.org/10.1016/j.jhazmat.2006.01.037

229 Prauchner, M. J., Sapag, K., & Rodríguez-Reinoso, F. (2016). Tailoring biomass-based activated carbon for CH4 storage by combining chemical activation with H3PO4 or ZnCl2 and physical activation with CO2. *Carbon*, *110*, 138–147. https://doi.org/10.1016/j.carbon.2016.08.092

230 Pulci, G., Tirillò, J., Marra, F., Fossati, F., Bartuli, C., & Valente, T. (2010). Carbon–phenolic ablative materials for re-entry space vehicles: Manufacturing and properties. *Composites Part A: Applied Science and Manufacturing*, *41*(10), 1483–1490. https://doi.org/10.1016/j.compositesa.2010.06.010

231 Qi, G., Yang, J., Bao, R., Xia, D., Cao, M., Yang, W., … Wei, D. (2017). Hierarchical graphene foam-based phase change materials with enhanced thermal conductivity and shape stability for efficient solar-to-thermal energy conversion and storage. *Nano Research*, *10*(3), 802–813. https://doi.org/10.1007/s12274-016-1333-1

232 Qi, X., Liang, J., Yu, C., Ma, S., Liu, X., & Xu, B. (2014). Facile synthesis of interconnected SiC nanowire networks on silicon substrate. *Materials Letters*, *116*, 68–70. https://doi.org/10.1016/j.matlet.2013.10.098

233 Qu, J., Han, Q., Gao, F., & Qiu, J. (2017). Carbon foams produced from lignin-phenol-formaldehyde resin for oil/water separation. *New Carbon Materials*, *32*(1), 86–91. https://doi.org/10.1016/S1872-5805(17)60109-4

234 Rashidi, N. A., & Yusup, S. (2016). An overview of activated carbons utilization for the post-combustion carbon dioxide capture. *Journal of CO2 Utilization*, *13*, 1–16. https://doi.org/10.1016/j.jcou.2015.11.002

235 Rasines, G., Lavela, P., Macías, C., Zafra, M. C., Tirado, J. L., Parra, J. B., & Ania, C. O. (2015). N-doped monolithic carbon aerogel electrodes with

optimized features for the electrosorption of ions. *Carbon*, *83*, 262–274. https://doi.org/10.1016/j.carbon.2014.11.015

236 Resmi, V. G., Deepa, J. P., Lakshmi, V., Rajan, T. P. D., Pavithran, C., & Pai, B. C. (2015). Processing of Porous SiC by Aluminum-Derived Binders and Sacrificial Porogen Leaching Method. *International Journal of Applied Ceramic Technology*, *12*(5), 967–975. https://doi.org/10.1111/ijac.12358

237 Rios, R. V. R. A., Martínez-Escandell, M., Molina-Sabio, M., & Rodríguez-Reinoso, F. (2006). Carbon foam prepared by pyrolysis of olive stones under steam. *Carbon*, *44*(8), 1448–1454. https://doi.org/10.1016/j.carbon.2005.11.028

238 Rodríguez-Valverde, M. Á., & Tirado Miranda, M. (2010). Derivation of Jurin's law revisited. *European Journal of Physics*, *32*(1), 49–54. https://doi.org/10.1088/0143-0807/32/1/005

239 Rodríguez, E., Cameán, I., García, R., & García, A. B. (2011). Graphitized boron-doped carbon foams: Performance as anodes in lithium-ion batteries. *Electrochimica Acta*, *56*(14), 5090–5094. https://doi.org/10.1016/j.electacta.2011.03.078

240 Rousseau, B., Guevelou, S., Domingues, G., Vicente, J., Caliot, C., & Flamant, G. (2013). Prediction of the radiative properties of reconstructed alpha-SiC foams used for concentrated solar applications. *MRS Proceedings*, *1545*, mrss13-1545-k01-07. https://doi.org/DOI: 10.1557/opl.2013.1074

241 Rowe, W. B. (2014). 3 - Grinding Wheel Developments. In W. B. B. T.-P. of M. G. T. (Second E. Rowe (Ed.) (pp. 35–62). Oxford: William Andrew Publishing. https://doi.org/10.1016/B978-0-323-24271-4.00003-8

242 Roy, A. K., Zhong, M., Schwab, M. G., Binder, A., Venkataraman, S. S., & Tomović, Ž. (2016). Preparation of a Binder-Free Three-Dimensional Carbon Foam/Silicon Composite as Potential Material for Lithium Ion Battery Anodes. *ACS Applied Materials & Interfaces*, *8*(11), 7343–7348. https://doi.org/10.1021/acsami.5b12026

243 Ryoo, R., Joo, S. H., Kruk, M., & Jaroniec, M. (2001). Ordered Mesoporous Carbons. *Advanced Materials*, *13*(9), 677–681. https://doi.org/10.1002/1521-4095(200105)13:9<677::AID-ADMA677>3.0.CO;2-C

244 Saha, D., Van Bramer, S. E., Orkoulas, G., Ho, H. C., Chen, J., & Henley, D. K. (2017). CO2 capture in lignin-derived and nitrogen-doped hierarchical porous carbons. *Carbon*, *121*(May), 257–266. https://doi.org/10.1016/j.carbon.2017.05.088

245 Şahan, N., Fois, M., & Paksoy, H. (2015). Improving thermal conductivity phase change materials—A study of paraffin nanomagnetite composites. *Solar Energy Materials and Solar Cells*, *137*, 61–67. https://doi.org/10.1016/j.solmat.2015.01.027

246 San Miguel Guillermo, Fowler, G. D., & Sollars, C. J. (2003). A study of the characteristics of activated carbons produced by steam and carbon dioxide activation of waste tyre rubber. *Carbon*, *41*(5), 1009–1016. https://doi.org/10.1016/S0008-6223(02)00449-9

247 Sanchez-Sanchez, A., Izquierdo, M. T., Medjahdi, G., Ghanbaja, J., Celzard, A., & Fierro, V. (2018). Ordered mesoporous carbons obtained by soft-templating of tannin in mild conditions. *Microporous and Mesoporous Materials*, *270*, 127–139. https://doi.org/10.1016/j.micromeso.2018.05.017

248 Sano, Y., Iwase, S., & Nakayama, A. (2012). A Local Thermal Nonequilibrium Analysis of Silicon Carbide Ceramic Foam as a Solar Volumetric Receiver. *Journal of Solar Energy Engineering*, *134*(2). https://doi.org/10.1115/1.4005758

249 Savage, G. (1993). Thermoplastic Matrix Precursors BT - Carbon-Carbon Composites. In G. Savage (Ed.) (pp. 157–191). Dordrecht: Springer Netherlands. https://doi.org/10.1007/978-94-011-1586-5_5

250 Savage, G., & Savage, G. (1993). Thermosetting Resin Matrix Precursors. In G. Savage (Ed.), *Carbon-Carbon Composites* (pp. 117–156). Dordrecht: Springer Netherlands. https://doi.org/10.1007/978-94-011-1586-5_4

251 Seo, J., Park, H., Shin, K., Baeck, S. H., Rhym, Y., & Shim, S. E. (2014). Lignin-derived macroporous carbon foams prepared by using poly(methyl methacrylate) particles as the template. *Carbon*, *76*, 357–367. https://doi.org/10.1016/j.carbon.2014.04.087

252 Shcherban, N. D., Filonenko, S. M., Yaremov, P. S., Sergiienko, S. A., Ilyin, V. G., & Murzin, D. Y. (2017). Carbothermal synthesis of porous silicon carbide using mesoporous silicas. *Journal of Materials Science*, *52*(7), 3917–3926. https://doi.org/10.1007/s10853-016-0652-7

253 Shen, B., Li, Y., Yi, D., Zhai, W., Wei, X., & Zheng, W. (2016). Microcellular graphene foam for improved broadband electromagnetic interference shielding. *Carbon*, *102*, 154–160. https://doi.org/10.1016/j.carbon.2016.02.040

254 Si, W., Zhou, J., Zhang, S., Li, S., Xing, W., & Zhuo, S. (2013). Tunable N-doped or dual N, S-doped activated hydrothermal carbons derived from human hair and glucose for supercapacitor applications. *Electrochimica Acta*, *107*, 397–405. https://doi.org/10.1016/j.electacta.2013.06.065

255 Singh, A. K., Shishkin, A., Koppel, T., & Gupta, N. (2018). A review of porous lightweight composite materials for electromagnetic interference shielding. *Composites Part B: Engineering*, *149*, 188–197. https://doi.org/10.1016/j.compositesb.2018.05.027

256 Somani, P. R., Somani, S. P., & Umeno, M. (2006). Planer nano-graphenes from camphor by CVD. *Chemical Physics Letters*, *430*(1), 56–59. https://doi.org/10.1016/j.cplett.2006.06.081

257 Song, I.-H., Kwon, I.-M., Kim, H.-D., & Kim, Y.-W. (2010). Processing of microcellular silicon carbide ceramics with a duplex pore structure. *Journal of the European Ceramic Society*, *30*(12), 2671–2676. https://doi.org/10.1016/j.jeurceramsoc.2010.04.027

258 Song, S. A., Lee, Y., Kim, Y. S., & Kim, S. S. (2017). Mechanical and thermal properties of carbon foam derived from phenolic foam reinforced with composite particles. *Composite Structures*, *173*, 1–8. https://doi.org/10.1016/j.compstruct.2017.04.001

259 Song, W.-L., Guan, X.-T., Fan, L.-Z., Cao, W.-Q., Wang, C.-Y., & Cao, M.-S. (2015). Tuning three-dimensional textures with graphene aerogels for ultra-light flexible graphene/texture composites of effective electromagnetic shielding. *Carbon*, *93*, 151–160. https://doi.org/10.1016/j.carbon.2015.05.033

260 Sreedeviamma Dijith, K., Vijayan, S., Prabhakaran, K., & Peethambharan Surendran, K. (2019). Conducting La0.5Sr0.5CoO3−δ foams for harsh condition microwave shielding. *Journal of Industrial and Engineering Chemistry*, *78*, 330–337. https://doi.org/10.1016/j.jiec.2019.05.037

261 Stadie, N. P., Wang, S., Kravchyk, K. V, & Kovalenko, M. V. (2017). Zeolite-Templated Carbon as an Ordered Microporous Electrode for Aluminum Batteries. *ACS Nano*, *11*(2), 1911–1919. https://doi.org/10.1021/acsnano.6b07995

262 Sumirat, I., Ando, Y., & Shimamura, S. (2006). Theoretical consideration of the effect of porosity on thermal conductivity of porous materials. *Journal of Porous Materials*, *13*(3), 439–443. https://doi.org/10.1007/s10934-006-8043-0

263 Sundarram, S. S., & Li, W. (2013). On thermal conductivity of micro- and nanocellular polymer foams. *Polymer Engineering & Science*, *53*(9), 1901–1909. https://doi.org/10.1002/pen.23452

264 Szczurek, A., Fierro, V., Pizzi, A., & Celzard, A. (2014). Emulsion-templated porous carbon monoliths derived from tannins. *Carbon*, *74*, 352–362. https://doi.org/10.1016/j.carbon.2014.03.047

265 Szczurek, A., Fierro, V., Pizzi, A., Stauber, M., & Celzard, A. (2013). Carbon meringues derived from flavonoid tannins. *Carbon*, *65*, 214–227. https://doi.org/10.1016/j.carbon.2013.08.017

266 Takikawa, H., Yatsuki, M., Miyano, R., Nagayama, M., Sakakibara, T., Itoh, S., & Ando, Y. (2000). Amorphous Carbon Fibrilliform Nanomaterials

Prepared by Chemical Vapor Deposition. *Japanese Journal of Applied Physics*, *39*(Part 1, No. 9A), 5177–5179. https://doi.org/10.1143/jjap.39.5177

267 Teng, H., Ho, J.-A., & Hsu, Y.-F. (1997). Preparation of activated carbons from bituminous coals with CO2 activation—Influence of coal oxidation. *Carbon*, *35*(2), 275–283. https://doi.org/10.1016/S0008-6223(96)00137-6

268 Teng, T.-P., & Yu, C.-C. (2012). Characteristics of phase-change materials containing oxide nano-additives for thermal storage. *Nanoscale Research Letters*, *7*(1), 611. https://doi.org/10.1186/1556-276X-7-611

269 Thongprachan, N., Yamamoto, T., Chaichanawong, J., Ohmori, T., & Endo, A. (2011). Preparation of macroporous carbon foam using emulsion templating method. *Adsorption*, *17*(1), 205–210. https://doi.org/10.1007/s10450-010-9312-4

270 Tondi, G., Blacher, S., Léonard, A., Pizzi, A., Fierro, V., Leban, J. M., & Celzard, A. (2009). X-Ray Microtomography Studies of Tannin-Derived Organic and Carbon Foams. *Microscopy and Microanalysis*, *15*(5), 384–394. https://doi.org/DOI: 10.1017/S1431927609990444

271 Tondi, G., Fierro, V., Pizzi, A., & Celzard, A. (2009). Tannin-based carbon foams. *Carbon*, *47*(6), 1480–1492. https://doi.org/10.1016/j.carbon.2009.01.041

272 Tondi, G., Pizzi, A., Masson, E., & Celzard, A. (2008). Analysis of gases emitted during carbonization degradation of polyflavonoid tannin/furanic rigid foams. *Polymer Degradation and Stability*, *93*(8), 1539–1543. https://doi.org/10.1016/j.polymdegradstab.2008.05.016

273 Tondi, G., Pizzi, A., Pasch, H., & Celzard, A. (2008). Structure degradation, conservation and rearrangement in the carbonisation of polyflavonoid tannin/furanic rigid foams – A MALDI-TOF investigation. *Polymer Degradation and Stability*, *93*(5), 968–975. https://doi.org/10.1016/j.polymdegradstab.2008.01.024

274 Trimis, D., & Durst, F. (1996). Combustion in a porous medium-advances and applications. *Combustion Science and Technology*, *121*(1–6), 153–168. https://doi.org/10.1080/00102209608935592

275 Truong, V.-V., Turner, B. D., Muscat, R. F., & Russo, M. S. (1997). Conducting-polymer-based radar-absorbing materials. In *Proc.SPIE* (Vol. 3241). Retrieved from https://doi.org/10.1117/12.293483

276 Ungureanu, S., Sigaud, G., Vignoles, G. L., Lorrette, C., Birot, M., Derré, A., … Backov, R. (2011). Tough silicon carbide macro/mesocellular crack-free monolithic foams. *Journal of Materials Chemistry*, *21*(38), 14732–14740. https://doi.org/10.1039/C1JM12084K

277 Vakifahmetoglu, C., Balliana, M., & Colombo, P. (2011). Ceramic foams and micro-beads from emulsions of a preceramic polymer. *Journal of the*

European Ceramic Society, *31*(8), 1481–1490. https://doi.org/10.1016/j.jeurceramsoc.2011.02.012

278 Vakifahmetoglu, C., Pippel, E., Woltersdorf, J., & Colombo, P. (2010). Growth of one-dimensional nanostructures in porous polymer-derived ceramics by catalyst-assisted pyrolysis. Part I: Iron catalyst. *Journal of the American Ceramic Society*, *93*(4), 959–968. https://doi.org/10.1111/j.1551-2916.2009.03448.x

279 Varela-Feria, F. M., Martínez-Fernández, J., De Arellano-López, A. R., & Singh, M. (2002). Low density biomorphic silicon carbide: Microstructure and mechanical properties. *Journal of the European Ceramic Society*, *22*(14–15), 2719–2725. https://doi.org/10.1016/S0955-2219(02)00137-1

280 Vega Bolivar, C. M., Antonini, A., Biamino, S., Pavese, M., Fino, P., & Badini, C. (2010). Oxidation Resistance of Multilayer SiC for Space Vehicle Thermal Protection Systems. *Advanced Engineering Materials*, *12*(7), 617–622. https://doi.org/10.1002/adem.200900328

281 Vijayan, S., Wilson, P., Sreeja, R., & Prabhakaran, K. (2016). Low-Density Open Cellular Silicon Carbide Foams from Sucrose and Silicon Powder. *Journal of the American Ceramic Society*, *99*(12), 3866–3873. https://doi.org/10.1111/jace.14450

282 Vogel, A. I. (1989). *Textbook of Quantitative Chemical Analysis Fifth Edition*. Fifth edition / [revised by ... G.H. Jeffery ... [and others]. Harlow, Essex, England : Longman Scientific & Technical ; New York : Wiley, 1989. Retrieved from https://search.library.wisc.edu/catalog/999612906602121

283 Vogt, U. F., Györfy, L., Herzog, A., Graule, T., & Plesch, G. (2007). Macroporous silicon carbide foams for porous burner applications and catalyst supports. *Journal of Physics and Chemistry of Solids*, *68*(5), 1234–1238. https://doi.org/10.1016/j.jpcs.2006.12.008

284 Wang, C., Chen, M., Lei, H., Yao, K., Li, H., Wen, W., & Fang, D. (2017). Radar stealth and mechanical properties of a broadband radar absorbing structure. *Composites Part B: Engineering*, *123*, 19–27. https://doi.org/10.1016/j.compositesb.2017.05.005

285 Wang, F., Yao, D., Xia, Y., Zuo, K., Xu, J., & Zeng, Y. (2016). Porous SiC ceramics prepared via freeze-casting and solid state sintering. *Ceramics International*, *42*(3), 4526–4531. https://doi.org/10.1016/j.ceramint.2015.11.143

286 Wang, K., Li, Y., Zhang, K., Liu, H., Luo, B., & Lin, Q. (2016). Preparation of near net-shape carbon foams from allyl COPNA-modified bismaleimide resin: Structures and properties. *Journal of Analytical and Applied Pyrolysis*, *117*, 125–131. https://doi.org/10.1016/j.jaap.2015.12.006

287 Wang, M. xian, Wang, C. Y., Li, T. Q., & Hu, Z. J. (2008). Preparation of mesophase-pitch-based carbon foams at low pressures. *Carbon*, *46*(1), 84–91. https://doi.org/10.1016/j.carbon.2007.10.038

288 Wang, N., Zhang, X. R., Zhu, D. S., & Gao, J. W. (2012). The investigation of thermal conductivity and energy storage properties of graphite/paraffin composites. *Journal of Thermal Analysis and Calorimetry*, *107*(3), 949–954. https://doi.org/10.1007/s10973-011-1467-z

289 Wang, S., Luo, R., & Ni, Y. (2010). Preparation and characterization of resin-derived carbon foams reinforced by hollow ceramic microspheres. *Materials Science and Engineering: A*, *527*(15), 3392–3395. https://doi.org/10.1016/j.msea.2010.02.059

290 Wang, X., Zhong, J., Wang, Y., & Yu, M. (2006). A study of the properties of carbon foam reinforced by clay. *Carbon*, *44*(8), 1560–1564. https://doi.org/10.1016/j.carbon.2005.12.025

291 Wang, X., Wei, K., Tao, Y., Yang, X., Zhou, H., He, R., & Fang, D. (2019). Thermal protection system integrating graded insulation materials and multilayer ceramic matrix composite cellular sandwich panels. *Composite Structures*, *209*, 523–534. https://doi.org/10.1016/j.compstruct.2018.11.004

292 Wang, Y., Cao, L., Gao, J., & Wang, Y. (2008). Graphitic Foam with High Strength and High Thermal Conductivity Doped by Tungsten. *Cellular Polymers*, *27*(4), 251–260. https://doi.org/10.1177/026248930802700403

293 Wang, Y., Zuo, S., & Liu, Y. (2018). Ammonia modification of high-surface-area activated carbons as metal-free electrocatalysts for oxygen reduction reaction. *Electrochimica Acta*, *263*, 465–473. https://doi.org/10.1016/j.electacta.2018.01.089

294 Wang, Z., Li, F., Ergang, N. S., & Stein, A. (2006). Effects of Hierarchical Architecture on Electronic and Mechanical Properties of Nanocast Monolithic Porous Carbons and Carbon−Carbon Nanocomposites. *Chemistry of Materials*, *18*(23), 5543–5553. https://doi.org/10.1021/cm062050u

295 Wilson, P., Vijayan, S., & Prabhakaran, K. (2018). Waste-Fish-Derived Nitrogen Self-Doped Microporous Carbon as Effective Sorbent for CO2 Capture. *ChemistrySelect*, *3*(33), 9555–9563. https://doi.org/10.1002/slct.201800842

296 Wolff, F., Ceron Nicolat, B., Fey, T., Greil, P., & Münstedt, H. (2012). Extrusion Foaming of a Preceramic Silicone Resin with a Variety of Profiles and Morphologies. *Advanced Engineering Materials*, *14*(12), 1110–1115. https://doi.org/10.1002/adem.201100351

297 Wolff, F., & Münstedt, H. (2011). Continuous direct melt foaming of a preceramic polymer using carbon dioxide: extrusion device and first results.

Journal of Materials Science, *46*(18), 6162–6167. https://doi.org/10.1007/s10853-011-5679-1

298 Wood, S., & Harris, A. T. (2008). Porous burners for lean-burn applications. *Progress in Energy and Combustion Science*, *34*(5), 667–684. https://doi.org/10.1016/j.pecs.2008.04.003

299 Woodward, R. T., Fam, D. W. H., Anthony, D. B., Hong, J., McDonald, T. O., Petit, C., … Bismarck, A. (2016). Hierarchically porous carbon foams from pickering high internal phase emulsions. *Carbon*, *101*, 253–260. https://doi.org/10.1016/j.carbon.2016.02.002

300 Woodward, R. T., Jobbe-Duval, A., Marchesini, S., Anthony, D. B., Petit, C., & Bismarck, A. (2017). Hypercrosslinked polyHIPEs as precursors to designable, hierarchically porous carbon foams. *Polymer*, *115*, 146–153. https://doi.org/10.1016/j.polymer.2017.03.042

301 Woodward, R. T., Markoulidis, F., De Luca, F., Anthony, D. B., Malko, D., McDonald, T. O., … Bismarck, A. (2018). Carbon foams from emulsion-templated reduced graphene oxide polymer composites: electrodes for supercapacitor devices. *Journal of Materials Chemistry A*, *6*(4), 1840–1849. https://doi.org/10.1039/C7TA09893F

302 Woodward, T. R., De Luca, F., Roberts, D. A., & Bismarck, A. (2016). High-Surface-Area, Emulsion-Templated Carbon Foams by Activation of polyHIPEs Derived from Pickering Emulsions. *Materials*, 9(9), 776. https://doi.org/10.3390/ma9090776

303 Wu, X., Liu, Y., Fang, M., Mei, L., & Luo, B. (2011). Preparation and characterization of carbon foams derived from aluminosilicate and phenolic resin. *Carbon*, *49*(5), 1782–1786. https://doi.org/10.1016/j.carbon.2010.12.065

304 Wu, Y., Fang, S., & Jiang, Y. (1998). Carbon anode materials based on melamine resin. *Journal of Materials Chemistry*, *8*(10), 2223–2227. https://doi.org/10.1039/A805080E

305 Wu, Z., Caliot, C., Flamant, G., & Wang, Z. (2011). Numerical simulation of convective heat transfer between air flow and ceramic foams to optimise volumetric solar air receiver performances. *International Journal of Heat and Mass Transfer*, *54*(7), 1527–1537. https://doi.org/10.1016/j.ijheatmasstransfer.2010.11.037

306 Xia, Y., Yang, Z., Gou, X., & Zhu, Y. (2013). A simple method for the production of highly ordered porous carbon materials with increased hydrogen uptake capacities. *International Journal of Hydrogen Energy*, *38*(12), 5039–5052. https://doi.org/10.1016/j.ijhydene.2013.02.037

307 Xiao, K., Ding, L.-X., Liu, G., Chen, H., Wang, S., & Wang, H. (2016). Freestanding, Hydrophilic Nitrogen-Doped Carbon Foams for Highly

Compressible All Solid-State Supercapacitors. *Advanced Materials*, *28*(28), 5997–6002. https://doi.org/10.1002/adma.201601125

308 Xiao, X., & Zhang, P. (2013). Morphologies and thermal characterization of paraffin/carbon foam composite phase change material. *Solar Energy Materials and Solar Cells*, *117*, 451–461. https://doi.org/10.1016/j.solmat.2013.06.037

309 Xin, G., Sun, H., Scott, S. M., Yao, T., Lu, F., Shao, D., … Lian, J. (2014). Advanced Phase Change Composite by Thermally Annealed Defect-Free Graphene for Thermal Energy Storage. *ACS Applied Materials & Interfaces*, *6*(17), 15262–15271. https://doi.org/10.1021/am503619a

310 Xue, F., Zhou, K., Wu, N., Luo, H., Wang, X., Zhou, X., … Zhang, D. (2018). Porous SiC ceramics with dendritic pore structures by freeze casting from chemical cross-linked polycarbosilane. *Ceramics International*, *44*(6), 6293–6299. https://doi.org/10.1016/j.ceramint.2018.01.019

311 Xue, Y., Liu, J., Chen, H., Wang, R., Li, D., Qu, J., & Dai, L. (2012). Nitrogen-Doped Graphene Foams as Metal-Free Counter Electrodes in High-Performance Dye-Sensitized Solar Cells. *Angewandte Chemie International Edition*, *51*(48), 12124–12127. https://doi.org/10.1002/anie.201207277

312 Yadav, A., Kumar, R., Bhatia, G., & Verma, G. L. (2011). Development of mesophase pitch derived high thermal conductivity graphite foam using a template method. *Carbon*, *49*(11), 3622–3630. https://doi.org/10.1016/j.carbon.2011.04.065

313 Yan, D. X., Ren, P. G., Pang, H., Fu, Q., Yang, M. B., & Li, Z. M. (2012). Efficient electromagnetic interference shielding of lightweight graphene/polystyrene composite. *Journal of Materials Chemistry*, *22*(36), 18772–18774. https://doi.org/10.1039/c2jm32692b

314 Yan, J., Wang, A., & Kim, D. P. (2006). Preparation of ordered mesoporous SiC from preceramic polymer templated by nanoporous silica. *Journal of Physical Chemistry B*, *110*(11), 5429–5433. https://doi.org/10.1021/jp057378+

315 Yang, J.-H., Yang, G.-Z., Yu, D.-G., Wang, X., Zhao, B., Zhang, L.-L., … Zhang, X.-K. (2013). Carbon foams from polyacrylonitrile-borneol films prepared using coaxial electrohydrodynamic atomization. *Carbon*, *53*, 231–236. https://doi.org/10.1016/j.carbon.2012.10.053

316 Yang, J., Qi, G.-Q., Liu, Y., Bao, R.-Y., Liu, Z.-Y., Yang, W., … Yang, M.-B. (2016). Hybrid graphene aerogels/phase change material composites: Thermal conductivity, shape-stabilization and light-to-thermal energy storage. *Carbon*, *100*, 693–702. https://doi.org/10.1016/j.carbon.2016.01.063

317 Yang, J., Shen, Z. M., & Hao, Z. B. (2004). Microwave characteristics of sandwich composites with mesophase pitch carbon foams as core. *Carbon*, *42*(8–9), 1882–1885. https://doi.org/10.1016/j.carbon.2004.03.017

318 Yavari, F., Fard, H. R., Pashayi, K., Rafiee, M. A., Zamiri, A., Yu, Z., … Koratkar, N. (2011). Enhanced Thermal Conductivity in a Nanostructured Phase Change Composite due to Low Concentration Graphene Additives. *The Journal of Physical Chemistry C*, *115*(17), 8753–8758. https://doi.org/10.1021/jp200838s

319 Yoon, B.-H., Lee, E.-J., Kim, H.-E., & Koh, Y.-H. (2007). Highly Aligned Porous Silicon Carbide Ceramics by Freezing Polycarbosilane/Camphene Solution. *Journal of the American Ceramic Society*, *90*(6), 1753–1759. https://doi.org/10.1111/j.1551-2916.2007.01703.x

320 Yoon, B.-H., Park, C.-S., Kim, H.-E., & Koh, Y.-H. (2007). In Situ Synthesis of Porous Silicon Carbide (SiC) Ceramics Decorated with SiC Nanowires. *Journal of the American Ceramic Society*, *90*(12), 3759–3766. https://doi.org/10.1111/j.1551-2916.2007.02037.x

321 Yu, M., Li, C., Ao, X., & Chen, Q. (2019). Fabrication of coal tar pitch–derived reticulated carbon foam as oxidation-resistant thermal insulation. *Journal of Analytical and Applied Pyrolysis*, *141*, 104643. https://doi.org/10.1016/j.jaap.2019.104643

322 Yu, Q., Straatman, A. G., & Thompson, B. E. (2006). Carbon-foam finned tubes in air–water heat exchangers. *Applied Thermal Engineering*, *26*(2), 131–143. https://doi.org/10.1016/j.applthermaleng.2005.06.004

323 Yu, Z.-T., Fang, X., Fan, L.-W., Wang, X., Xiao, Y.-Q., Zeng, Y., … Cen, K.-F. (2013). Increased thermal conductivity of liquid paraffin-based suspensions in the presence of carbon nano-additives of various sizes and shapes. *Carbon*, *53*, 277–285. https://doi.org/10.1016/j.carbon.2012.10.059

324 Zakiyan, S. E., Azizi, H., & Ghasemi, I. (2018). Effect of cell morphology on electrical properties and electromagnetic interference shielding of graphene-poly(methyl methacrylate) microcellular foams. *Composites Science and Technology*, *157*, 217–227. https://doi.org/10.1016/j.compscitech.2018.02.002

325 Zeng, Z., Zhang, Y., Ma, X. Y. D., Shahabadi, S. I. S., Che, B., Wang, P., & Lu, X. (2018). Biomass-based honeycomb-like architectures for preparation of robust carbon foams with high electromagnetic interference shielding performance. *Carbon*, *140*, 227–236. https://doi.org/10.1016/j.carbon.2018.08.061

326 Zhang, H., Xu, Y., Zhou, J., Jiao, J., Chen, Y., Wang, H., … Wang, Z. (2015). Stacking fault and unoccupied densities of state dependence of

electromagnetic wave absorption in SiC nanowires. *Journal of Materials Chemistry C*, *3*(17), 4416–4423. https://doi.org/10.1039/c5tc00405e

327 Zhang, H., Zhang, J., & Zhang, H. (2006). Numerical predictions for radar absorbing silicon carbide foams using a finite integration technique with a perfect boundary approximation. *Smart Materials and Structures*, *15*(3), 759–766. https://doi.org/10.1088/0964-1726/15/3/011

328 Zhang, H., Zhang, J., & Zhang, H. (2007a). Computation of radar absorbing silicon carbide foams and their silica matrix composites. *Computational Materials Science*, *38*(4), 857–864. https://doi.org/10.1016/j.commatsci.2006.05.024

329 Zhang, H., Zhang, J., & Zhang, H. (2007b). Electromagnetic properties of silicon carbide foams and their composites with silicon dioxide as matrix in X-band. *Composites Part A: Applied Science and Manufacturing*, *38*(2), 602–608. https://doi.org/10.1016/j.compositesa.2006.02.014

330 Zhang, L., Li, R., Tang, B., & Wang, P. (2016). Solar-thermal conversion and thermal energy storage of graphene foam-based composites. *Nanoscale*, *8*(30), 14600–14607. https://doi.org/10.1039/C6NR03921A

331 Zhang, L., Liu, M., Roy, S., Chu, E. K., See, K. Y., & Hu, X. (2016). Phthalonitrile-Based Carbon Foam with High Specific Mechanical Strength and Superior Electromagnetic Interference Shielding Performance. *ACS Applied Materials and Interfaces*, *8*(11), 7422–7430. https://doi.org/10.1021/acsami.5b12072

332 Zhang, S. P., Liu, M. X., Gan, L. H., Wu, F. R., Xu, Z. J., Hao, Z. X., & Chen, L. W. (2010). Synthesis of carbon foams with a high compressive strength from arylacetylene. *Xinxing Tan Cailiao/ New Carbon Materials*, *25*(1), 9–14. https://doi.org/10.1016/S1872-5805(09)60012-3

333 Zhang, T., Walawender, W. P., Fan, L. T., Fan, M., Daugaard, D., & Brown, R. C. (2004). Preparation of activated carbon from forest and agricultural residues through CO2 activation. *Chemical Engineering Journal*, *105*(1), 53–59. https://doi.org/10.1016/j.cej.2004.06.011

334 Zhang, Y., & Faghri, A. (1996). Heat transfer enhancement in latent heat thermal energy storage system by using the internally finned tube. *International Journal of Heat and Mass Transfer*, *39*(15), 3165–3173. https://doi.org/10.1016/0017-9310(95)00402-5

335 Zhang, Z., Wang, F., Yu, X., Wang, Y., Yan, Y., Li, K., & Luan, Z. (2009). Porous silicon carbide ceramics produced by a carbon foam derived from mixtures of mesophase pitch and Si particles. *Journal of the American Ceramic Society*, *92*(1), 260–263. https://doi.org/10.1111/j.1551-2916.2008.02842.x

336 Zhao, B., Guo, X., Zhao, W., Deng, J., Fan, B., Shao, G., … Zhang, R. (2017). Facile synthesis of yolk–shell Ni@void@SnO2(Ni3Sn2) ternary composites via galvanic replacement/Kirkendall effect and their enhanced microwave absorption properties. *Nano Research*, *10*(1), 331–343. https://doi.org/10.1007/s12274-016-1295-3

337 Zhao, B., Guo, X., Zhao, W., Deng, J., Shao, G., Fan, B., … Zhang, R. (2016). Yolk-Shell Ni@SnO2 Composites with a Designable Interspace to Improve the Electromagnetic Wave Absorption Properties. *ACS Applied Materials and Interfaces*, *8*(42), 28917–28925. https://doi.org/10.1021/acsami.6b10886

338 Zhao, B., Guo, X., Zhou, Y., Su, T., Ma, C., & Zhang, R. (2017). Constructing hierarchical hollow CuS microspheres: Via a galvanic replacement reaction and their use as wide-band microwave absorbers. *CrystEngComm*, *19*(16), 2178–2186. https://doi.org/10.1039/c7ce00235a

339 Zhao, B., Liang, L., Bai, Z., Guo, X., Zhang, R., Zuo, C., & Deng, J. (2017). Lightweight porous Co3O4 and Co/CoO nanofibers with tunable impedance match and configuration-dependent microwave absorption properties. *CrystEngComm*, *19*(41), 6095–6106. https://doi.org/10.1039/C7CE01464C

340 Zhao, C., Liu, G., Sun, N., Zhang, X., Wang, G., Zhang, Y., … Zhao, H. (2018). Biomass-derived N-doped porous carbon as electrode materials for Zn-air battery powered capacitive deionization. *Chemical Engineering Journal*, *334*, 1270–1280. https://doi.org/10.1016/j.cej.2017.11.069

341 Zhao, W., Pizzi, A., Fierro, V., Du, G., & Celzard, A. (2010). Effect of composition and processing parameters on the characteristics of tannin-based rigid foams. Part I: Cell structure. *Materials Chemistry and Physics*, *122*(1), 175–182. https://doi.org/10.1016/j.matchemphys.2010.02.062

342 Zhong, Y., Guo, Q., Li, S., Shi, J., & Liu, L. (2010). Heat transfer enhancement of paraffin wax using graphite foam for thermal energy storage. *Solar Energy Materials and Solar Cells*, *94*(6), 1011–1014. https://doi.org/10.1016/j.solmat.2010.02.004

343 Zhu, H., Chen, D., An, W., Li, N., Xu, Q., Li, H., … Lu, J. (2015). A Robust and Cost-Effective Superhydrophobic Graphene Foam for Efficient Oil and Organic Solvent Recovery. *Small*, *11*(39), 5222–5229. https://doi.org/10.1002/smll.201501004

344 Zhu, J., Wang, X., Guo, L., Wang, Y., Wang, Y., Yu, M., & Lau, K. (2007). A graphite foam reinforced by graphite particles. *Carbon*, *45*(13), 2547–2550. https://doi.org/10.1016/j.carbon.2007.08.019

345 Zhu, T., Zhou, J., Li, Z., Li, S., Si, W., & Zhuo, S. (2014). Hierarchical porous and N-doped carbon nanotubes derived from polyaniline for electrode

materials in supercapacitors. *Journal of Materials Chemistry A*, *2*(31), 12545–12551. https://doi.org/10.1039/C4TA01465K

346 Zhu, X., Jiang, D., & Tan, S. (2002). Preparation of silicon carbide reticulated porous ceramics. *Materials Science and Engineering: A*, *323*(1), 232–238. https://doi.org/10.1016/S0921-5093(01)01352-1

347 Zhu, X., Jiang, D., Tan, S., & Zhang, Z. (2001). Improvement in the Strut Thickness of Reticulated Porous Ceramics. *Journal of the American Ceramic Society*, *84*(7), 1654–1656. https://doi.org/10.1111/j.1151-2916.2001.tb00895.x

348 Zhu, Y., Hu, H., Li, W., & Zhang, X. (2007). Resorcinol-formaldehyde based porous carbon as an electrode material for supercapacitors. *Carbon*, *45*(1), 160–165. https://doi.org/10.1016/j.carbon.2006.07.010

349 Zu, G., Shen, J., Zou, L., Wang, F., Wang, X., Zhang, Y., & Yao, X. (2016). Nanocellulose-derived highly porous carbon aerogels for supercapacitors. *Carbon*, *99*, 203–211. https://doi.org/10.1016/j.carbon.2015.11.079

350 Zúñiga Ruiz, C. J., Szczurek, A., Martínez De Yuso Arisa, A., Ronda, J. C., Cádiz, V., Fierro, V., & Celzard, A. (2015). Closed-cell carbon foams from diphenolic acid-based polybenzoxazine. *Carbon*, *95*, 919–929. https://doi.org/10.1016/j.carbon.2015.09.012

List of Publications Based on the Thesis

1. Wilson, P., Vijayan, S., & Prabhakaran, K. (2017) Carbon foams with a triplex pore structure by compression molding of molten sucrose-NaCl powder pastes. *Carbon*, 118, 545-555.
2. Wilson, P., Vijayan, S., & Prabhakaran, K. (2018) Low-density microcellular carbon foams from sucrose by NaCl particle templating using glycerol as a plasticizing additive. *Materials and Design*, 139, 25–35.
3. Wilson, P., Vijayan, S., & Prabhakaran, K. (2019) Thermally conducting microcellular carbon foams as a superior host for wax-based phase change materials. *Advanced Engineering Materials*, 21 (4), 1801139.
4. Wilson, P., Vijayan, S., & Prabhakaran, K. (2019) Microcellular SiC foams containing in situ grown nanowires for electromagnetic interference shielding. *Journal of Industrial and Engineering Chemistry*, 80, 401-410.

List of Conferences attended

1. Presented paper on "*Activated carbon monoliths with tailored pore distribution synthesized from compression moulded sucrose-NaCl paste*" at International Conference of Young Researchers on Advanced Materials (IUMRS-ICYRAM 2016), Bangalore, India from 11th–15th December, 2016
2. Presented paper on "*Low-density microcellular carbon foams from sucrose for thermal protection application*" at International Conference on Advanced Materials and Processes (ADMAT-2017 SkyMat), Thiruvananthapuram, India from 14th-16th December 2017
3. Presented paper on "*Sucrose-derived carbon-graphite composite foams for thermal energy storage systems*" at International Conference on Sustainable Chemistry for Health, Environment and Materials (Su-Chem 2018), Hyderabad, India from 5th-8th August 2018

4. Presented paper on "*Conducting carbon foam as host for Phase Change Materials*" at International Conference on Material Science and Technology (ICMST-2018), Thiruvananthapuram, India from 10th-13th October 2018
5. Presented paper on "*Hetero-structured Microcellular SiC Foams by Reaction Sintering of Sucrose-Derived Carbon and Silicon Particles"* at International Conference on Advanced Thermostructural Materials & Thermal Protection Systems (ADTHERM-20), Thiruvananthapuram, India from 20th-21st January 2020